

**UCLA**

**UCLA Electronic Theses and Dissertations**

**Title**

Molecular Engineering of Stabilizers for Water-Air and Water-Water Interfaces

**Permalink**

<https://escholarship.org/uc/item/6nd1q110>

**Author**

Gao, Shang

**Publication Date**

2021

Peer reviewed|Thesis/dissertation

UNIVERSITY OF CALIFORNIA

Los Angeles

Molecular Engineering of Stabilizers for Water-Air and Water-Water Interfaces

A dissertation submitted in partial satisfaction of the requirements for the degree Doctor of  
Philosophy in Chemical Engineering

by

Shang Gao

2021

© Copyright by

Shang Gao

2021

## ABSTRACT OF THE DISSERTATION

Molecular Engineering of Stabilizers for Water-Air and Water-Water Interfaces

by

Shang Gao

Doctor of Philosophy in Chemical Engineering

University of California, Los Angeles, 2021

Professor Samanvaya Srivastava, Chair

This dissertation aims to elucidate the behaviors of interfacially active molecules that self-assemble at fluid-fluid interfaces and stabilize them. Examples of such molecules include amphiphilic surfactant molecules that comprise hydrophobic (oil-loving) and hydrophilic (water-loving) moieties and therefore have a natural affinity for oil-water as well as water-air interfaces. Surfactant molecules are ever present in typical household soaps and detergents, and when dissolved in water, self-assemble at the air water interface as well as into multi-molecule aggregates known as micelles. These assemblies, in turn, facilitate foaming and form the basis of the cleaning actions of the soaps and detergents. The first part of this dissertation examines the role of micellar and interfacially self-assembled surfactants on the stability of thin foam films. Specifically, the correspondence between inter-micellar interactions in bulk solutions and in thin films, and the influence of these interactions on the average lifetime of foam films are investigated. I envision that my studies will inspire colloidal scientists to explore foam film studies as a simple but effective method for characterizing nanoscopic colloidal interactions and forces.

In the second part of this dissertation, development of interfacially active polymers that stabilize water-water interfaces, designed specifically for stabilization of polyelectrolyte complex coacervates, is demonstrated. Complex coacervates form upon electrostatic complexation of oppositely charged macromolecules and their subsequent condensation into aqueous macromolecules-rich phase. This aqueous two-phase system has been demonstrated to exhibit unique capabilities to achieve dynamic spatial compartmentalization as well as spontaneous sequestering of biological molecules. Despite these exciting prospects, their use has been limited owing to our inability to stabilize coacervate droplets and prevent their macro-phase separation. In my research, I have developed block polymers and comb polymers that have successfully stabilized micron-sized coacervate droplets, leading to first demonstrations of stable coacervate emulsions. I have also demonstrated sequestration of proteins (enzymes) into the stabilized coacervate droplets, paving way for these emulsions to be employed as protein-based bioreactors with selective small molecule transport.

The dissertation of Shang Gao is approved.

Panagiotis Christofides

Yoram Cohen

Yunfeng Lu

Gaurav Sant

Vivek Sharma

Samanvaya Srivastava, Committee Chair

University of California, Los Angeles

2021

## TABLE OF CONTENT

Chapter 1. INTRODUCTION .....	1
1.1 OVERVIEW .....	1
1.2. SELF-ASSEMBLY OF AMPHIPHILIC SURFACTANTS .....	5
1.2.1. Characteristics of Surfactant Micelles .....	5
1.2.2. Drainage of Thin Surfactant-laden Foam Films .....	6
1.3. POLYELECTROLYTE COMPLEXATION .....	9
1.3.1. Polyelectrolyte Complexation in Industrial Settings .....	12
1.3.2. Polyelectrolyte Complexes in Biomedicine.....	14
1.3.3. Stabilizing Polyelectrolyte Complex Coacervate Microdroplets.....	19
1.4. OUTLINE OF THIS DISSERTATION.....	21
1.5. REFERENCES .....	23
Chapter 2. INTERMICELLAR INTERACTIONS PROBED IN BULK AQUEOUS SOLUTIONS AND IN FOAM FILMS .....	41
2.1 INTRODUCTION .....	43
2.2. RESULTS .....	48
2.2.1. Intermicellar Interactions in Bulk Aqueous Solutions and Thin Films: Low Concentration Regime ( $25 \text{ mM} \leq C_{SDS} \leq 250 \text{ mM}$ ).....	48
2.2.2. Intermicellar Interactions in Bulk Aqueous Solutions and Thin Films: High Concentration Regime ( $C_{SDS} \leq 600 \text{ mM}$ ) .....	59
2.3. DISCUSSIONS .....	65
2.4. CONCLUSIONS .....	71
2.5. MATERIALS AND METHODS.....	72
2.6. REFERENCES .....	78
Chapter 3. MICELLAR ASSEMBLIES AND FOAM FILM STABILITY: SALT EFFECTS ...	93

3.1 INTRODUCTION .....	95
3.2. RESULTS & DISCUSSIONS .....	98
3.2.1. Influence of Salt on Micellar Assemblies and Foam Film Stability .....	98
3.2.2. An Equivalent Hard-sphere Model to Interpret Interactions Between Ionic Micelles in High Ionic Strength Solutions.....	118
3.3. CONCLUSIONS .....	129
3.4. REFERENCES .....	131
Chapter 4. COMB POLYELECTROLYTE STABILIZED COMPLEX COACERVATE EMULSIONS .....	137
4.1 INTRODUCTION .....	138
4.2. RESULTS & DISCUSSIONS .....	140
4.3. CONCLUSIONS .....	157
4.4. MATERIALS AND METHODS.....	158
4.5. SUPPLEMENTARY FIGURES.....	160
4.6. REFERENCES .....	166
Chapter 5. STABILITY OF STABILIZED COACERVATE DROPLETS AGAINST SALT .	174
5.1 INTRODUCTION .....	176
5.2. RESULTS & DISCUSSIONS .....	178
5.2.1. Comb polyelectrolytes stabilize complex coacervate droplets in salty solutions .....	178
5.2.2. Phase behaviors of stabilized complex coacervate emulsions .....	183
5.2.3. Salt does not impede the encapsulation of proteins in stabilized complex coacervate emulsions .....	191
5.3. CONCLUSIONS .....	194
5.4. REFERENCES .....	195

Chapter 6. INTERACTIONS OF AMPHIPHILIC BLOCK POLYELECTROLYTES WITH COMPLEX COACERVATES .....	200
6.1 INTRODUCTION .....	202
6.2. MATERIALS AND METHODS .....	204
6.3. RESULTS & DISCUSSIONS .....	210
6.4. CONCLUSIONS.....	223
6.5. REFERENCES .....	224
Chapter 7. CONCLUSIONS AND FUTURE DIRECTIONS .....	228

## LIST OF FIGURES

Figure 1-1 Areas of research of this dissertation .....	4
Figure 1-2 Characteristics of oppositely charged macromolecules involved in PE-macroion interactions .....	10
Figure 1-3 F-actin localizes to the periphery of polypeptide coacervates .....	17
Figure 2-1 Schematic of the set-up used for examining stratification using IDIOM (Interferometry Digital Imaging Optical Microscopy) protocols and illustrative examples of stepwise thinning .....	49
Figure 2-2 Coexisting thick-thin regions in stratifying foam films made with 50 and 250 mM SDS solutions .....	52
Figure 2-3 Small angle X-ray scattering (SAXS) results and micelle characteristics .....	56
Figure 2-4 Structure factor and concentration-dependent variation in step size and intermicellar distance .....	58
Figure 2-5 Small Angle X-Ray Scattering (SAXS) measurements for $C_{SDS} = 100 - 600$ mM solutions .....	61
Figure 2-6 Step size $\Delta h$ , intermicellar distance $d$ , and structure factor profiles as a function of SDS concentration $C_{SDS}$ .....	64
Figure 3-1 SAXS intensity $I(q)$ spectra of aqueous SDS solutions with varying SDS concentration $C_{SDS}$ and thickness variations $h(t)$ over time .....	99
Figure 3-2 SAXS intensity $I(q)$ spectra of aqueous SDS solutions with varying SDS concentration $C_{SDS}$ , form factor and structure factor fits .....	101
Figure 3-3 Dimensions of the oblate ellipsoidal SDS micelles .....	102
Figure 3-4 Intermicellar distance $d$ and average step size $\overline{\Delta h}$ .....	103
Figure 3-5 Height of the primary $S(q)$ peak.....	104
Figure 3-6 IDIOM schematic and montages .....	107

Figure 3-7 The number of steps and the layer thickness, $h_i$ as a function of SDS concentration, $C_{SDS}$ for various salt concentration $C_{NaCl}$ in thin foam films undergoing stratified drainage ...	108
Figure 3-8 SAXS intensity $I(q)$ spectra of aqueous SDS solutions with fixed SDS concentration $C_{SDS}$ and the comparisons between $d$ and $\overline{\Delta h}$ .....	110
Figure 3-9 Variations of inter-scatterer distance $d$ with scatterer volume fraction $\phi$ or salt concentration $C_{NaCl}$ at fixed volume fraction or charge .....	113
Figure 3-10 Variations of intermicellar distance $d$ and average step size $\overline{\Delta h}$ of stratifying thin films .....	117
Figure 3-11 SAXS intensity $I(q)$ spectra of SDS solutions with varying SDS concentration $C_{SDS}$ with no added salt and with 80 mM NaCl by Hayter-Penfold structure factor model .....	120
Figure 3-12 SAXS intensity $I(q)$ spectra of SDS solutions with varying SDS concentration $C_{SDS}$ with no added salt and with 80 mM NaCl by equivalent hard-sphere structure factor model ...	121
Figure 3-13 SDS micelle characteristics estimated by Hayter-Penfold structure factor model or equivalent hard-sphere model. ....	124
Figure 3-14 Integrated fits of oblate ellipsoid core-shell form factor and equivalent hard-sphere structure factor .....	126
Figure 3-15 Micelle volume fraction $\phi$ of SDS micelles under $C_{NaCl}$ 0 – 60 mM .....	128
Figure 4-1 Comb polyelectrolytes stabilize complex coacervate droplets .....	142
Figure 4-2 Droplet size in complex coacervate emulsions is controlled by the linear polyelectrolyte and the comb polyelectrolyte concentrations .....	147
Figure 4-3 Proteins partition preferentially in coacervate droplets in the comb polyelectrolyte stabilized coacervate emulsions .....	151
Figure 4-4 Activity of enzymes is markedly enhanced upon localization in stabilized complex coacervate microdroplets .....	155
Figure 4-S1 Comb polyelectrolytes PAA <sub>47-CO</sub> -PEG <sub>25</sub> stabilize complex coacervate droplets ...	160

Figure 4-S2 Complex coacervate emulsions stability is controlled by comb polyelectrolyte PEG lengths and the comb polyelectrolyte concentrations .....	161
Figure 4-S3 Anionic diblock polyelectrolytes PEG <sub>113</sub> -PAGE <sub>30</sub> does not stabilize complex coacervate droplets .....	162
Figure 4-S4 Emulsification can be stimulated by dilution of concentrated single-phase solution of linear polyelectrolytes and comb polyelectrolytes .....	163
Figure 4-S5 Mixing sequences of linear polyelectrolytes and comb polyelectrolytes do not impact the stability of complex coacervate emulsions .....	164
Figure 4-S6 Activity of enzymes is markedly enhanced upon localization in stabilized complex coacervate microdroplets .....	165
Figure 5-1 Comb polyelectrolytes stabilize complex coacervate droplets in salty solutions .....	181
Figure 5-2 Comb polyelectrolytes significantly expand the coacervation window .....	185
Figure 5-3 Comb polyelectrolyte stabilized complex coacervate emulsions can withstand addition of salt .....	189
Figure 5.4 Proteins partition preferentially in coacervate droplets in the comb polyelectrolyte stabilized coacervate emulsions .....	193
Figure 6-1 Polymer NMR, GPC, and FTIR characterizations .....	207
Figure 6-2 Small angle X-ray scattering (SAXS) results and self-assembly characteristics .....	212
Figure 6-3 Mixing sequences impact the stability of amphiphilic micelles stabilized complex coacervate droplets. ....	216
Figure 6-4 Amphiphilic micelle stabilize complex coacervate droplets encapsulated FITC-labelled BSA .....	221
Figure 6-5 Macroscopic and microscopic views of amphiphilic stabilized complex coacervates with 48 hours after mixing. ....	222

## ACKNOWLEDGMENTS

The work in this dissertation would not have been possible without support from many others. I am fortunate to be a Ph.D student in UCLA under the supervision of Prof. Srivastava. The time that I spent here as a graduate student are challenging, fruitful, and will be a never-forgotten memory.

First, foremost, I would like to express my deepest appreciation to my doctoral advisor Professor Samanvaya Srivastava for his conscientious guidance, profound instructions and inspirations, and support throughout my doctoral research. He truly serves as a role model of scientific researcher with passion and professionalism. By the example of him, I learnt how to pursue the solutions to the opening questions in research, how to perform the experimental investigations in an objective manner, and how to present my scientific discoveries in an accurate and profession style. Also, I would like to acknowledge my committee members for their valuable advice and inspirations.

Moreover, I want to express my gratefulness for the assistances from my lab members, my classmates, friends for their insightful comments and beneficial discussions with my lab work. Without the valuable discussions with them, it would have taken me much longer to find out the solutions I encountered during my study and research. I will never forget the days and of course nights we spent together in Argonne. I am again thankful to my committee member and collaborator Prof. Vivek Sharma and Dr. Chrystian Ochoa for their sparkled ideas in foam studies, and instructive comments.

Last but not least, I would like to thank my parents Zhongbao Gao, and Weili Cai, and my husband Dr. Yiu-sun Hung for their endless encouragement, unconditional support and love all the time. My parents grant me the freedom to pursue my dream, support me with any choice I make, and also being the cheerleaders during my study. I met my husband at UCLA, starting from then, he accompanies me through the ups and downs, brings up a solution, and being patient all the time. I am fortunate to have him to go through the PhD journey together.

I am truly blessed to have all of you in my life.

Chapter 1 contains material written by Gao. S from the following publication: (1) C. Ochoa, **S. Gao**, S. Srivastava, V. Sharma, Foam film stratification studies probe intermicellar interactions, *Proceedings of the National Academy of Sciences*, 2021, 118 (25) e2024805118. (2) **S. Gao**, A. Holkar, S. Srivastava, Protein-Polyelectrolyte Complexes and Micellar Assemblies, *Polymers*, 2019 (11) 7, 1097

Chapter 2 contains material written by Gao. S from the following publication: C. Ochoa, **S. Gao**, S. Srivastava, V. Sharma, Foam film stratification studies probe intermicellar interactions, *Proceedings of the National Academy of Sciences*, 2021, 118 (25) e2024805118.

Chapter 3 contains material written by Gao. S from the following publication: **S. Gao**, C. Ochoa, V. Sharma, S. Srivastava, *submitted*.

Chapter 4 contains material written by Gao. S from the following publication: (1) S. Srivastava, **S. Gao**, *US patent 63/187,031, Patent pending*. (2) **S. Gao**, S. Srivastava; *submitted*

Chapter 5 contains material written by Gao. S from the following publication: S. Srivastava, **S. Gao**, *US patent 63/187,031, Patent pending.*

## VITA

- 2013 – 2017            B.S. in Chemical Engineering, Advisor: Prof. Gaohong He  
  
                                 Dalian University of Technology  
  
                                 Dalian, China
- 2017-                    Ph.D in Chemical Engineering, Advisor: Prof. Samanvaya Srivastava  
  
                                 University of California, Los Angeles  
  
                                 Los Angeles, CA

## PUBLICATIONS

1. C. Ochoa, **S. Gao**, S. Srivastava, V. Sharma, Foam film stratification studies probe intermicellar interactions, *Proceedings of the National Academy of Sciences*, 2021, 118 (25) e2024805118
2. S. Srivastava, **S. Gao**, Comb polyelectrolyte stabilized complex coacervate emulsions, US Patent App., May 2021, 63/187,031, *Patent pending*
3. J. Timmons, I. Mehdipour, **S. Gao**, H. Atahan, N. Neithalath, M. Bauchy, E. Garboczi, S. Srivastava, G. Sant., Dispersing nano- and micro-sized portlandite particulates via electrosteric exclusion at short screening length, *Soft Matter*, 16 (14), 2020, 3425
4. **S. Gao**, A. Holkar, S. Srivastava, Protein-Polyelectrolyte Complexes and Micellar Assemblies, *Polymers*, 2019 (11) 7, 1097

5. L. Zhong, C. Tang, B. Wang, HF. Wang, **S. Gao**, Y. Wang, Q. Zhang, SAPO-34 templated growth of hierarchical porous graphene cages as electrocatalysts for both oxygen reduction and evolution, *Carbon*. 2017;32(6):509-16
6. **S. Gao**, S. Srivastava; Comb polyelectrolytes stabilize membraneless complex coacervate microdroplets, *submitted*
7. **S. Gao**, C. Ochoa, V. Sharma, S. Srivastava, Influence of salt on micellar assemblies and foam film stability, *submitted*
8. C. Ochoa, **S. Gao**, S. Srivastava, V. Sharma, Stratification in high concentration micellar SDS foam films, *manuscript in preparation*

#### SELECT PRESENTATIONS

1. **S. Gao**, C. Ochoa, V. Sharma and S. Srivastava, Relationship among phase behavior, micellar structure and thin film drainage in aqueous-salt surfactant solutions [Poster], American Physical Society March Meeting, Virtual, March 2021
2. **S. Gao**, C. Ochoa, V. Sharma and S. Srivastava, Relationship among phase behavior, micellar structure and thin film drainage in aqueous surfactant solutions, American Physical Society March Meeting, Virtual, March 2020
3. **S. Gao**, C. Ochoa, V. Sharma and S. Srivastava, Phase behavior, micelle structure and stepwise drainage of aqueous sodium naphthenate foam films, Annual Meeting of AIChE, Orlando, November 2019
4. **S. Gao**, C. Ochoa, V. Sharma and S. Srivastava, Phase behaviors and structures of sodium naphthenate micelles, American Physical Society March Meeting, Boston, March 2019

## CHAPTER 1

### INTRODUCTION

Contents of section 1.2 are reproduced and reformatted with the permission from Chrystian Ochoa; Shang Gao; Samanvaya Srivastava; Vivek Sharma. “Foam film stratification studies probe intermicellar interactions” *The Proceedings of the National Academy of Sciences* 2021, 118 (25), e2024805118.

Contents of section 1.3 are reproduced and reformatted with the permission from Shang Gao; Advait Holkar; Samanvaya Srivastava. “Protein-Polyelectrolyte Complexes and Micellar Assemblies”, *Polymers* 2019, 11 (7), 1097.

#### 1.1. OVERVIEW

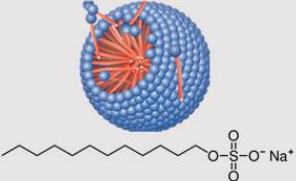
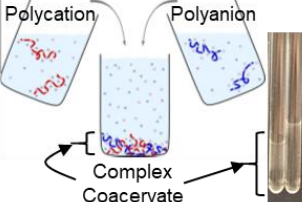
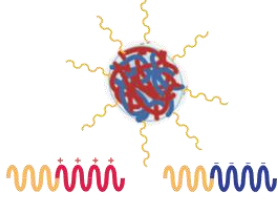
Amphiphilic surfactants are widely employed stabilizers for oil-water or air-water interfaces. They comprise hydrophilic headgroups (that may be neutral or ionic) and hydrophobic carbon chains that enable their adsorption at the hydrophilic-hydrophobic interfaces. Therefore, these molecules play a key role in stabilizing foams and emulsions, comprising immiscible air-water and oil-water mixtures, respectively (Figure 1-1). Amphiphilic surfactants also self-assemble into diverse core-shell micellar structures in aqueous solutions wherein surfactant concentration is above a critical concentration, known as the critical micelle concentration (CMC). These surfactant micelles solubilize oils and oil-soluble dirt in their hydrophobic cores and form the basis of cleaning action of most modern detergents and soaps. Consequently, they are central to molecular formulation of various consumer products in the modern world, including a range of cosmetics (shampoos,

shaving foams, etc.), food products (milk, butter, etc.), soaps and detergents, and pharmaceutical products (ointments, creams, etc.).

Gaining an enhanced understanding the role of surfactants in dictating the stability and lifetime of emulsions and foams is essential towards molecular engineering of improved consumer product formulations as well as controlling foaming and emulsification in industrial processes.<sup>1</sup> In particular, while the surfactant micelles have been long hypothesized to influence emulsion and foam film stability, the fundamental mechanisms behind the role of micelles are not entirely clear yet. The first part of my graduate research has focused on elucidating the influence of micelle morphology, size, concentrations, and intermicellar interactions on stability of thin freestanding liquid films. My results have shown that the liquid drainage in thin liquid films, which directly dictates foam stability, is controlled inherently by the interactions among the micelles in the thin films. Consequently, my work has shown that modulation of intermicellar interactions, by addition of salt, can be employed to markedly influence foam film stability.

The second part of my dissertation focused on stabilization of water-water interfaces present in complex coacervates. Associative phase separation in aqueous solutions of oppositely charged polyelectrolytes (PEs) results in two phases, with one containing both the PEs (coacervates) and the other being primarily water, separated by a membraneless interface. Complex coacervates have been presented as candidates for protocell model and membraneless bioreactors owing to their capability to sequester biomacromolecules and enhance their bioactivity emerging from chemical enrichment and macromolecular crowding the coacervate environment. They are distinct from membranous protocells wherein amphiphilic membranes stabilize the compartments but also limit their functionality by hindering transport. However, the lack of a membrane, that makes complex

coacervate microdroplets distinct, also results in their unrestricted coalescence, influencing their long-term stability which seriously hampers their utility as microcompartments. My graduate research has focused on developing strategies for stabilization of the water-water interface of the complex coacervate microdroplets while retaining their membraneless attributes. My work has shown that small concentrations of comb polyelectrolytes can effectively stabilize complex coacervate microdroplets, in effect creating water-in-water emulsions. The unique comb structure of the comb polyelectrolytes enables their adsorption at the water-water interfaces to prevent the droplets from coalescence and keep the complex coacervate emulsions stable for months while retaining the capabilities of the coacervate microdroplets to sequester biomolecules from solution and enhance their activity. Moreover, my research has enabled precise control of microdroplet sizes, paving the way for complex coacervate-based stable protein carriers and bioreactors.

	Macro-phase Separation	Emulsions	Nanoscale Micelles
<b>Oil-Water Mixture</b>		 Cream: Oil-in-water      Butter: Water-in-Oil	
<b>Polyelectrolyte Complex Coacervate: Aqueous phase comprising polycations and polyanions</b>			

**Figure 1-1 Areas of research of this dissertation.** (First row) Oil-water mixtures and (second row) polyelectrolyte complex coacervates as phase separated mixtures (left column), microemulsions (middle column), and nanoscale micelle assemblies (right column). The “?” represents the current lack of complex coacervate emulsions. The shaded cells represent the areas of research of my dissertation.

## 1.2. SELF-ASSEMBLY OF AMPHIPHILIC SURFACTANTS

### 1.2.1. Characteristics of Surfactant Micelles

Amphiphilic – both (“amphi”), philo (loving) – molecules are surface active agents (surfactants) comprising two parts with opposite natures: a water-soluble, hydrophilic unit referred to as the “head” and an oil-soluble, hydrophobic “tail” unit.<sup>2</sup> At low surfactant concentrations, surfactant molecules tend to adsorb at the liquid-air interfaces leading to a dramatic surfactant-concentration-dependent decrease in surface tension.<sup>1,2</sup> When the surfactant concentrations approach the critical micelle concentration (CMC), it also results in forming small globular or worm-like aggregates called micelles, with (ionic) surfactant heads pointed outwards water and the hydrophobic tails forming the interior.<sup>2</sup> Experimentally, the surface tension of surfactant solution levels off above CMC, and many other properties including scattering intensity, osmotic pressure, solution conductivity, etc. also show a dramatic change at the CMC.<sup>2</sup> The micellar self-assembly of ionic surfactants are driven by a competition between attractive hydrophobic interfacial interactions and the repulsion between the ionic headgroups. The shape, dimension and composition of micelles therefore depend on molecular characteristics of the surfactant molecules as well as on the surfactant concentrations, solution ionic strength and temperature, all of which influence the intermolecular interactions.<sup>2</sup> Further increase in surfactant concentrations much above CMC can also lead to an array of self-assembled structures and phase transitions beyond micellization,<sup>2</sup> although the specific structures and phase transitions depend on strength and nature of intermolecular interactions.

Phase behavior maps of common surfactants are well-documented. For instance, aqueous solutions of sodium dodecyl sulfate (SDS) comprise a rich spectrum of morphologies that arise as a function

of SDS concentration and temperature.<sup>3</sup> The structural micromorphology of SDS solutions have been studied with various characterization techniques, including small angle scattering (X-ray/neutron), electron microscopy (EM),<sup>4,5</sup> NMR,<sup>6-9</sup> fluorescent,<sup>9-11</sup> differential scanning calorimetry and computational approaches.<sup>12-16</sup> Small-angle neutron scattering (SANS), for instance, has been employed to predict the micellar structures, aggregation number and demonstrate the packing of the core of micelles by selectively probing the core and the shell regions of the micelles.<sup>17-22</sup> Selective deuteration of methyl groups in the surfactants as well as manipulation of the background contrast by employing mixtures of water and deuterated water as solvents aid these SANS experiments in enabling selective probing of various regions of the self-assemblies. Further, additives such as lithium chloride and sodium chloride (LiCl and NaCl) have been shown to influence of coulombic intra- and inter-micelle interactions in aqueous SDS solutions resulting in increasing aggregation number with addition of salts; NaCl was shown to stronger screening effect.<sup>23,24</sup> Yet, it must be noted that the micellar assembly in H<sub>2</sub>O-D<sub>2</sub>O mixtures can affect the structure of D<sub>2</sub>O around the ionic headgroups and may not correspond entirely with surfactant assembly in H<sub>2</sub>O, leading to minor variations in the micelle dimensions.<sup>22</sup>

### **1.2.2. Drainage of Thin Surfactant-laden Foam Films**

Instabilities in thin foam films is caused by the Laplace pressure  $P_c$  differences between the films and their plateau borders, resulting in liquid drainage into the plateau borders.<sup>25</sup> Intermolecular interactions and surface forces (DLVO-forces, including steric forces, hydration forces, electrostatic interactions, and van der Waals interactions) jointly contribute to the disjoining pressure  $\Pi(h)$  counterbalancing the Laplace pressure and creating metastable films with thickness

at  $h = 10 - 80$  nm (common black film, CB) or  $h < 10$  nm (Newton black film, NB). The film thickness differences between each metastable state are defined as step size  $\Delta h$ .

Disjoining pressure is also known influenced by the two non-DLVO, medium-mediated interactions arising in multicomponent colloidal dispersions due to structuring of smaller molecules, nanoparticles, micelles, or solvent molecules between larger, dispersed particles, bubbles or drops: (i) depletion-attraction caused by the depletion of smaller species from the confined region,<sup>26-28</sup> and (ii) damped oscillatory structural disjoining pressure term,  $\Pi_{OS}(h)$  contributed by layering in the confined region.<sup>26,27,29-33</sup> For simple fluids, Israelachvili, among others, proposed a phenomenological expression of the form  $\Pi_{OS}(h) = A \exp\left(-\frac{h}{\xi}\right) \cos\left(\frac{2\pi h}{\lambda} + B\right)$ , with periodicity,  $\lambda$  and decay length  $\xi$ , to describe damped oscillations.<sup>1,31,33,34</sup> For relatively short-ranged  $\Pi_{OS}(h)$ , called solvation forces, periodicity and decay length,  $\lambda = \xi = a$  are both set by the molecular size. Such forces can be directly measured using force-based techniques like surface force apparatus (SFA) or colloidal probe AFM (CP-AFM).<sup>1,34</sup> For micellar fluids containing ionic surfactants and charged micelles, the step size,  $\Delta h$  obtained using thickness-time plots from the dynamic stratification experiments, and periodicity,  $\lambda$  directly measured using thin-film balance under equilibrium conditions<sup>35,36</sup> show  $\Delta h = \lambda > a$  and  $\xi > a$  implying that both periodicity (= step size) and decay length exceed micelle size.

Using equilibrium density functional theory, Pollard and Radke<sup>37</sup> showed that oscillatory contribution to disjoining pressure could be computed numerically by treating micelles as hard spheres and interactions between them with screened-Coulomb Yukawa-type interactions. This disjoining pressure counterbalances the Laplace pressure at several film thickness  $h$ , and these

metastable thickness causes the stratification during film drainage. Subsequently, Kralchevsky and Danov used Henderson's theory for bidisperse colloids made up of hard spheres with large size difference to derive an analytical formula for  $\Pi_{OS}(h)$  that depends on micelle number density and uses Carnahan-Starling compressibility factor computed using effective volume fraction (based on  $d_{eff}$ ).<sup>38-40</sup> Yilixiati *et al.*<sup>41</sup> modified the phenomenological model by using step size for periodicity as well as an experimentally determined micelle number density and by computing compressibility factor for effective volume fraction based on  $d_{eff} = 2(l_{SDS} + \kappa^{-1})$  such that  $\kappa^{-1} = 8\pi l_b \left( CMC_{SDS} + \left(\frac{\alpha}{2}\right) (C_{SDS} - CMC_{SDS}) \right)^{-\frac{1}{2}}$  accounts for the influence of both concentration and degree of ionization,  $\alpha$  of micelles. Lastly, there are only a couple of experimental studies that attempt to characterize structure within micellar foam films directly, and these provide support for the intermicellar distance comparable to the step size. Krichevsky and Stavans<sup>42,43</sup> used static and dynamic light scattering, in addition to reflectivity, and comparison with the bulk RMSA calculations to show that the micellar fluid behaves analogous to confined simple fluids, with a step size matched with intermicellar distance. Denkov *et al.*<sup>44</sup> found a lack of order in cryo-electron microscopy of vitrified micellar SDS foam films, even though latex particles formed nicely ordered arrays. Thus, the current state-of-the-art models for oscillatory structural contribution to disjoining pressure in foam films are based on liquid-state theory,<sup>28,33,37,38,41</sup> and these models provide a quantitative analysis of the hydrodynamic processes underlying stratification using thin film equation.<sup>36,45-48</sup> Bruil and coworkers reported that the  $\Delta h$  equals to the step size decreased with increasing sodium dodecyl sulfate (SDS) concentrations following a power law as  $\Delta h \propto c_{soap}^{-\frac{1}{3}}$  and claimed that the step size values "seem to be related to intermolecular distance in the

(unmicellized) bulk solution.” However, this expression was not further supported upon the actual ellipsoidal SDS micelles rather than spherical morphology. Thus, to date, there has been no direct comparisons between multiple length scales, including micelle dimensions, Debye length, intermicellar distances and step sizes, and their relationships with the surfactant concentration and salt concentration. Gaining such comparisons is one of the motivations of this dissertation.

### **1.3. POLYELECTROLYTE COMPLEXATION**

Mixtures of oppositely charged polyelectrolytes (PE) in aqueous milieu interact, assemble together and phase separate to form polyelectrolyte complexes (PECs) (Figure 1-2a).<sup>49-51</sup> Associative phase separation of the results in recruitment of both PEs into the complex phase, driven by a combination of electrostatic interactions and entropy gains from the release of counterions confined in the vicinity of the PE chains. Macroscopic phase separation results in the formation of bulk polyelectrolyte complexes, which can be either solid precipitates, or liquids (also known as complex coacervates).

Charged biomacromolecules, including proteins and nucleic acids, can also participate in complexation and sequester spontaneously into PECs. In this regard, biomacromolecule-PE complexes (Figure 1-2b) are considered to belong to a large class of self-assemblies that form upon complexation of oppositely charged macroions in aqueous solutions, including polyelectrolyte complexes (PECs)<sup>52</sup> that form upon complexation between oppositely charged polyelectrolytes and flocculation of oppositely charged polyelectrolytes and (nano)particles.<sup>53</sup> While the strong partitioning of proteins and the PEs in the complex phase results in high macromolecular concentrations in the complexes, the complexes still are water-rich phases and preserve the native environment for the protein globules which in most cases sustains or even enhances their activities.

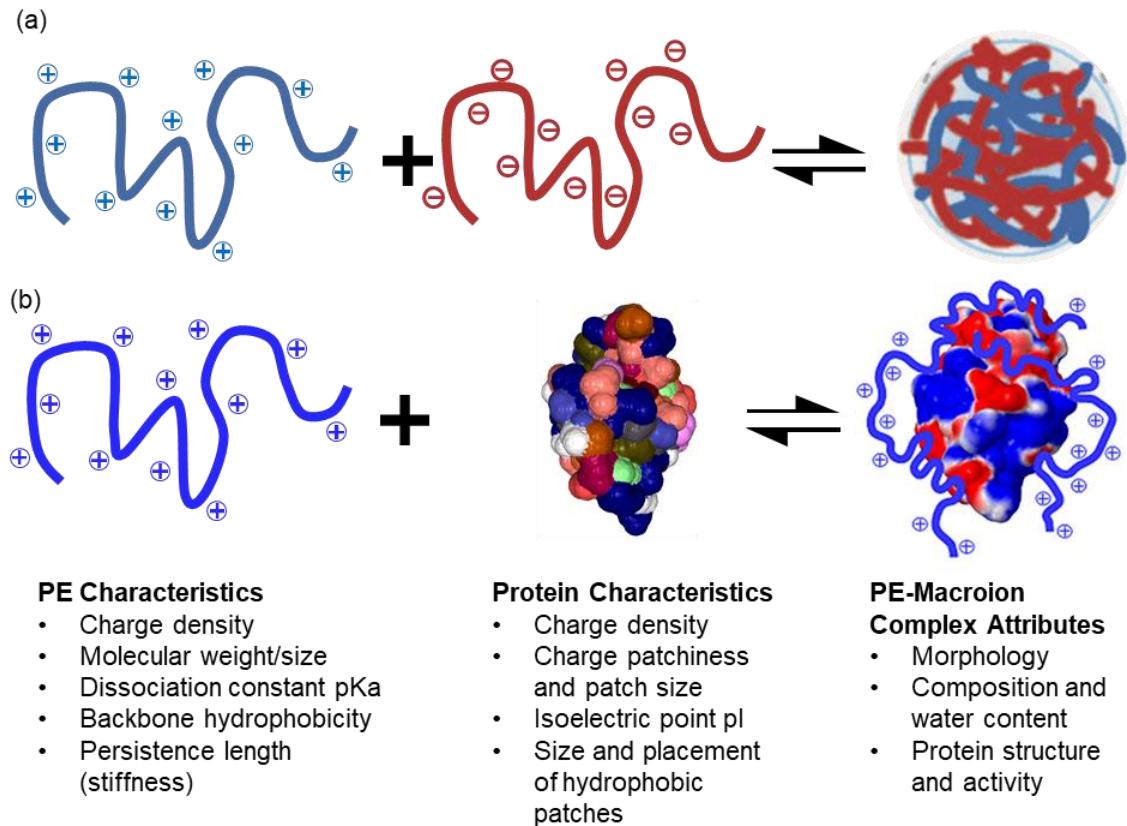


**Figure 1-2 Characteristics of oppositely charged macromolecules involved in PE-macroion interactions.** Schematic depicting complexation of oppositely charged polyelectrolytes to form polyelectrolyte-polyelectrolyte complexes (a) or proteins with polyelectrolytes to form protein–polyelectrolyte complexes (b). The key characteristics of the polyelectrolytes and the proteins that regulate the properties of the complexes are listed. The proteins depicted in the schematics are chicken egg white lysozyme.<sup>54</sup> The three-dimensional rendering of the lysozyme globules also depicts the diversity of the amino acid residues, colored differently, present on the globular surface.

The composition, structure and properties of the PECs are all inherently dictated by the nature and strength of interactions of the PE chains and the encapsulated macroions (proteins, nucleic acids) as well as their surroundings.<sup>49,50,55–57</sup> These interactions, primarily electrostatic in nature, are influenced by a combination of the density, distribution, patchiness and extent of ionization of the ionizable groups on the PE chains and on the surfaces of these macroions. The charge state of PE chains can vary between fully ionized chains and fully deionized neutral chains and can be controlled by the pH of the solution. The degree of ionization of the PE chains can be quantized by using the Henderson–Hasselbalch equation and the dissociation constant pKa of the ionizable groups. Largely, polycations and polyanions can be considered to be fully ionized at  $\text{pH} > \text{pKa} + 1$  and  $\text{pH} < \text{pKa} - 1$ , respectively. Biomacromolecules comprised by amino acids like proteins, in contrast, typically have both positively and negatively charged ionizable moieties on their surfaces. Thus, pH of the aqueous environment influences the extent of ionization of both kinds of charged moieties and consequently controls the net charge of the proteins. The presence of salt ions can also influence the ionization of the charged moieties on both the PE chains and the macroions, influencing the strength of the electrostatic interactions between them. Thus, the structure and properties of the complex can be finely tuned post-complexation externally by varying the ionic strength or pH of the solution.<sup>58,59</sup>

In addition to the placement and extent of ionization of the charged groups, other PEs and macroions characteristics also influence the complex structure and properties. The size and the persistence length (stiffness) of the PE chains both influence the *compactness* of the complexes. Longer PE chains can bridge between protein globules, and floppier chains can conform to adsorb more on the protein surface, both leading to denser complexes.<sup>58,60,61</sup> The concentrations of the PE

chains and the encapsulated protein in the solution also determines the composition and the morphology of the complexes, with higher compositions leading to larger volumes of complexes and inducing morphology transitions from globular to mesh-like complexes.<sup>58</sup> Lastly, hydrophobic interactions between the PE backbones and the hydrophobic patches on the protein surface can in some cases reinforce and in other cases hinder complexation, and their roles need to be considered carefully when designing PEs for specific applications concerning protein–PE complexes.<sup>50,62,63</sup> The key characteristics of PEs and the associated macroions and the tunable attributes of complexes are summarized in Figure 1-2.

### **1.3.1. Polyelectrolyte Complexation in Industrial Settings**

The phenomenon of polyelectrolyte complexation between gelatin and gum arabic was first recorded in 1929 by Bungenberg de Jong and Kruyt.<sup>64</sup> Since 1970s, polyelectrolyte complexation has been applied to the industry development and provided new opportunities for surface engineering in aqueous milieu.

In the paper-making industry, dilute solutions of anionic cellulosic fibers (lignin, charged macroions) are employed to create fibrous networks that eventually form paper. Chemical additives, including calcium carbonate and polymers are added into the aqueous suspensions to improve the paper color and mechanical properties, respectively. Starting in late 1970s, polyelectrolytes such as starch, poly(diallyldimethylammonium chloride) (PDADMAC),<sup>65,66</sup> and carboxymethylcellulose (CMC)<sup>67</sup> have been used to induce densification of anionic cellulosic fibers and improve the mechanical strength of fibril joints as a replacement for mechanical beating,<sup>68</sup> mitigating the side effects of dewetting. The adding sequences, the chemical structures of the polycations, and concentrations of oppositely charged polyelectrolytes have been shown to

greatly influence the quality of the paper produced, and therefore carry great technical and economic impacts in the paper sheet industry.<sup>68</sup> The structure-property relationship between the additional polyelectrolytes with cellulose fibers is still under investigation to further improve the surface adsorption and expand the polyelectrolyte library to create paper with new properties such as antibacterial, thermoresponsive, water-proof functionalities.<sup>69</sup>

Over the past 40 years, the polyelectrolyte complexes have also been applied in flocculation applications of water treatment and mineral processing. Low amount water-soluble polyelectrolytes promote in forming large aggregates to be separated easily and gradually take in place of conventional aluminum or ferrous salts forming small-size unstable flocs.<sup>70,71</sup> A mixture of cationic polyelectrolyte PDADMAC, and anionic surfactant molecules sodium dodecyl sulfate (SDS) is applied to remove silver particles in zeolite, and dye molecules in wastewater,<sup>72</sup> increasing the efficiency to more than 95% by varying the adding sequences. An increasing molar charge ratio between PDADMAC: SDS decreases the net charges of formed complexes, where the surface tension of the complexes approaches to the minimum at 1:1 charge ratio.<sup>73</sup> This formulation tailors stable charged aggregates via electrostatic and hydrophobic interactions. Moreover, the characteristics of polyelectrolytes in terms of hydrophobicity, repeating units, molecular weight, and charge density are manipulated to vary the mechanisms of flocculation formation (electrostatic, chain bridging) for the further purpose of lowering the degree of surface tensions. Lately, environmental-friendly natural polyelectrolytes (modified polysaccharides, chitosan) are of great interest in the drinking water purification markets owing to the advantages of biodegradability and biocompatibility as well as minimal harm to the ecological systems.

Proteins and polysaccharides from food are an important class of water-soluble polyelectrolytes. Electrostatic interactions between milk proteins and polysaccharides are extensively applied into the dairy products, especially for stabilizing the fat-water emulsions and prolonging the product shelf life.<sup>74-76</sup> Polysaccharides (pectin, gum arabic) are utilized to form complex coacervates, protecting casein micelles (phosphoproteins) from precipitations and aggregation against harsh pH condition in acidified milk beverages.<sup>77</sup> Further, the structures of polyelectrolyte complexes with encapsulating bioactive ingredients provide desired mouth feeling during chewing and passaging.<sup>69</sup> Nowadays, plant-based foods as alternatives to traditional foods are extensively under development, where simulating the textures, mouthfeel, and melting behaviors with plant proteins and natural polyelectrolytes through interfacial science is being explored.<sup>78</sup>

### **1.3.2. Polyelectrolyte Complexes in Biomedicine**

Polymers have been used in the shielding of proteins against surrounding environmental changes by the formation of a protective polymer shell around the protein.<sup>79-83</sup> This is especially important in therapeutic protein delivery where proteins may be exposed to proteolytic environments and their uptake into cells may be limited. Encapsulation of proteins in polymer shells by covalent conjugation is shown to be effective in several instances. Complexation of proteins with PEs can also be used for similar purposes. Use of protein-PE complexes for oral delivery of proteins has been explored extensively owing to the ability of the complexes to protect proteins against changes in pH and proteolytic degradation as well as overcoming the mucosal barrier.<sup>79</sup>

*PEC coacervates as protein cargos and enzymatic bioreactors*

Proteins can be incorporated in liquid polyelectrolyte complex coacervates (comprising two oppositely charged homo PEs) with high degrees of partitioning, thus leading to effective encapsulation of the proteins in the complexes. Proteins are minor components in these three-component systems, and thus the inclusion of proteins typically doesn't influence the properties of the bulk complexes much. These complexes are also useful as vehicles for drug delivery and artificial bioreactors. Enzymes alcohol dehydrogenase and trypsin have been reported to retain their activities when complexed with PDADMAC.<sup>84</sup> The concentration of lysozyme encapsulated in coacervate droplets of PAA and poly-(N,N dimethylaminoethyl methacrylate) (PDMAEMA) was observed to be tunable by ionic strength and bulk concentration of lysozyme.<sup>85</sup> Poly(L-lysine) (PLK) and poly(D/L-glutamic acid) (PRE) coacervates were used to reversibly encapsulate BSA for application in drug delivery.<sup>86</sup> BSA loaded coacervate droplets were observed to release the BSA on reducing pH. Coacervate droplets of PAA-polyallylamine hydrochloride (PAH) were also shown to stabilize the *encapsulated* protein against changes in pH and urea concentrations.<sup>87</sup> Furthermore, secondary structure of the proteins was reported to be unchanged in both these studies. Co-encapsulation of BSA and globular actin was recently demonstrated in PLK-PRE coacervates (Figure 1-3(a-c)) with high degrees of partitioning for both the proteins (partition coefficients of ~10 and ~30, respectively; Figure 1-3e).<sup>88</sup> Correspondingly, up to 50-fold increase in the rate of actin filament assembly inside the droplets was reported and was attributed to a combination of high local actin concentrations, macromolecular crowding effects and changes in the local dielectric constants owing to high concentrations of PEs present in the droplets. Surprisingly, the assembled actin filaments were observed to concentrate on the periphery of the

droplet (Figure 1-3(a-c), column 1) as opposed to BSA which was uniformly dispersed (Figure 1-3(a-c), column 2) in the droplets (Figure 1-3d).

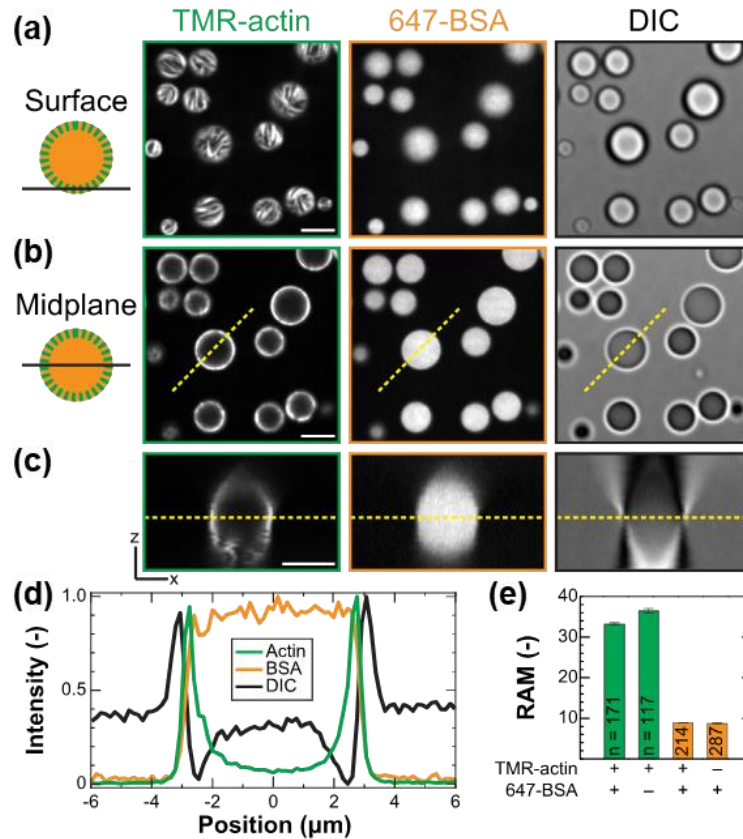


**Figure 1-3 F-actin localizes to the periphery of polypeptide coacervates.** (a-b) Optical and confocal fluorescence micrographs showing PEC droplets (**right**) comprising both actin filaments (**left**) and BSA globules (**middle**). The focal planes are near the droplets-substrate interface (**a**) or near the midplane of the droplets (**b**). (c) An  $x$ - $z$  cross section of the droplets evaluated from multiple images obtained at various  $z$  values. Scale bar, 5  $\mu\text{m}$  in (a-c); (d) uniform distribution of BSA globules and peripheral enrichment of actin filaments in the PEC droplets as depicted from the normalized fluorescence intensity obtained from line scans along the dashed lines shown in (b) and (c); (e) average ratio of fluorescence intestines inside and outside the droplets, indicating a strong degree of partitioning of proteins in PEC droplets, in samples containing 0.5 mM actin, 0.5 mM BSA, or 0.25 mM actin and 0.25 mM BSA together.

Coacervate microdroplets are also actively investigated as artificial cells and protocell models to explore the gaps between the intracellular systems in natural cells and synthetic biological bodies. Rates of bioreactions catalyzed by enzymes can be regulated by controlling the enzyme partitioning in the coacervates. Due to the chemical enrichments in the coacervate droplets, the enzymatic activity is enhanced. PEC coacervates comprising PAA and PEI encapsulate  $\alpha$ -amylase where the complexation does not suppress the enzymatic reaction and prevents the enzymes from denaturation against the acute pH environment.<sup>89</sup> Spatiotemporal organization of coacervate droplets comprising PDADMAC and ATP was regulated by an acoustically two-dimensional pressure field in aqueous solutions.<sup>90</sup> An array of two coacervate droplet systems separately encapsulated glucose oxidase (GOx) and horseradish peroxidase (HRP) was prepared and imposed by a mixture of substrates (o-phenylenediamine (o-PD) and hydrogen peroxide ( $H_2O_2$ )). Under the unidirectional concentration gradients over time or coordinates, the signaling molecules  $H_2O_2$  internally transferred between binary coacervate droplets so that the HRP activity was ignited by the diffusions of  $H_2O_2$  between the neighbor coacervate droplets. This array of established reactors happening cascade enzymatic reactions built up a communicated network between these artificial cells.<sup>90</sup>

#### *PECs as Protein Stabilizers*

High concentration of proteins can be stored in protein–polyelectrolyte complexes.<sup>91</sup> Kurinomaru et al. obtained high concentration of proteins (panitumumab, etanercept, thyroglobulin and others) in complexes by precipitation with cationic and anionic PEs (poly-*L*-lysine and poly-*L*-glutamic acid) followed by redissolution of the complexes in high salt environments without any significant changes in the activities of the proteins and antibodies.<sup>92</sup> The structures of nine redissolved proteins

were analyzed using ultraviolet circular dichroism spectra; only thyroglobulin and *L*-asparaginase were reported to exhibit minor peak shifts, indicating structural rearrangements.<sup>93</sup> Furthermore, precipitation has been proposed as an alternative to lyophilization as it provides thermal, physical and chemical (oxidation) stability, as seen in *L*-asparaginase-PE complexes.<sup>94</sup> Complexation and precipitation of proteins adalimumab and omalizumab with poly-*L*-glutamic acid reduced inactivation due to agitation and heat stresses, thus improving protein stability.<sup>95</sup> Similarly, heparin was shown to suppress and reverse aggregation of both BSA and antithrombin (AT).<sup>96</sup> Even though heparin has a stronger affinity for AT than BSA due to the presence of a more pronounced positive patch, aggregation was inhibited more for BSA than AT, attributed to the higher aggregation of the uncomplex monomers of AT than BSA.

### **1.3.3. Stabilizing Polyelectrolyte Complex Coacervate Microdroplets**

Polyelectrolyte complex coacervates microdroplets form spontaneously upon electrostatic complexation of oppositely charged macromolecules.<sup>52,97,98</sup> As discussed in the previous section, this aqueous microphase paradigm as a liquid-liquid phase separation (LLPS) system has been presented as candidates for artificial cells and protocell models demonstrating dynamic spatial compartmentalization,<sup>99,100</sup> membraneless carriers owing to their capability of sequestering biomacromolecules<sup>86,88,101,102</sup> and bioreactors enhancing bioactivity emerging from chemical enrichment.<sup>103,104</sup> Despite these exciting prospects, their utility microcompartments for biomacromolecules (proteins, nucleic acids) is limited owing to rapid coarsening of coacervate microdroplets into aqueous polymer-rich macrophases through coalescence and Ostwald ripening that limits their shelf life.<sup>105</sup> Thus, stabilization of coacervate microdroplets is imperative to regulate and enhance individual properties at the microscale.

Mechanisms like physical interventions and material modifications have been extensively explored to stabilize coacervate microdroplets. Attempts to utilize typical interfacial stabilizers, including amphiphilic surfactant molecules that comprise hydrophobic (oil-loving) and hydrophilic (water-loving) moieties, that are effective in stabilizing oil-water as well as water-air interfaces have been ineffective. Similarly, charged particles that are utilized to stabilize oil droplets in aqueous phases by forming Pickering emulsions are also not effective to stabilize coacervate microdroplets. Surfactants and charged particles adsorbing at the interfaces both reduce the surface area and bear high desorption energy  $\Delta E = \pi R^2 \gamma_{o-w} > 10^3 k_B T$ . However, owing to low interfacial tension between two aqueous phases in complex coacervates, the desorption energy required for the surfactants/particles to escape the interfaces will be close to thermal energy, resulting in insufficient stabilization of coacervate microdroplets in water.

Novel interfacially active molecules have also been extensively investigated to stabilize coacervate-water interfaces. Mann and coworkers presented a stabilization formulation including fatty acid assemblies that created multilayers around coacervates when below their critical micelle concentration, though limiting the permeability of the coacervate microdroplets.<sup>106</sup> Van Hest and coworkers formulated an amphiphilic terpolymer that undergoes interfacial self-assembly around the coacervates, providing stabilizing enzymatic cargo against coalescence.<sup>107–112</sup> Keating and coworkers demonstrated an intact lipid-vesicle layer stabilized complex coacervates without restricting RNA oligonucleotides diffusion and small molecules uptake restrictions. However, organic solvent involved in the formation of the semi-impermeable membrane perturb the aqueous media.<sup>113,114</sup> Thus, the drawbacks of restricted transport across the amphiphilic semi-permeable membranes and introduction of organic phases have limited the utility of the coacervate

microdroplets accessible through the current stabilization strategies. In the second part of this dissertation, I propose and demonstrate harnessing of an external energy barrier contribution via electrostatic interfacial adsorption to provide the capability of stabilizing cell-sized coacervate microdroplets and create membraneless coacervate emulsions with long shelf-life while preserving transportation of small molecules across the water-water interfaces.

#### **1.4. OUTLINE OF THIS DISSERTATION**

My doctoral dissertation aims to elucidate the behaviors of interfacially active molecules that self-assemble at fluid-fluid interfaces and stabilize them. The first part of my doctoral dissertation examines the role of micellar and interfacially self-assembled surfactants on the stability of thin foam films. Chapter 2 contains the investigations on the contrast between step size obtained from analysis of nanoscopic thickness variations and transitions in stratifying foam films using an optical microscopy protocols that we developed with the intermicellar interactions in bulk solutions using small-angle X-ray scattering, illustrating the stratification driven by the confinement-induced layering of micelles within the liquid-air interfaces of a foam film provides a sensitive probe of non-DLVO supramolecular oscillatory structural forces and micellar interactions. Chapter 3 further discusses the influence of salt on the structures and polydispersity of these self-assemblies and the effects on the intermicellar interactions and the oscillatory structure forces, where the correspondence between bulk liquid phases and liquid-air interfaces diverges. I envision that the correspondence explored here will support the foam film studies as a simple but effective method for characterizing nanoscopic colloidal interactions and forces.

In the second part of my dissertation, I discuss the stabilization mechanism that I have developed by using interfacially active polyelectrolytes that stabilize water-water interfaces, designed

specifically for stabilization of polyelectrolyte complex coacervates. Chapter 4 details the new stabilization mechanism for polyelectrolyte complex coacervate emulsions using comb polyelectrolytes, where the aqueous two-phase system has been demonstrated to exhibit unique capabilities to achieve dynamic spatial compartmentalization, spontaneous sequestering of biological molecules and enhanced biological activity of proteins. Chapter 5 further describes that resistance of polyelectrolyte complex coacervates against salt is improved by stabilizing the complex coacervates with comb polyelectrolytes. Coacervate microdroplets are demonstrated to exist in an enhanced two-phase region while retaining the sequestering capability at high ionic strength at which coacervates typically undergo disassembly. Chapter 6 briefly describes an evaluation of the interactions between amphiphilic block polyelectrolyte self-assembly and the complex coacervates. This research led to the first demonstrations of stable coacervate emulsions via non-covalent bonds, paving way for these emulsions to be employed as feasibly prepared protein encapsulants useful in pharmaceutical, biomedical, food and personal care products.

## 1.5. REFERENCES

- (1) Israelachvili, J. N. *Intermolecular and Surface Forces*; Academic press, 2015.
- (2) Rosen, M. J.; Kunjappu, J. T. *Surfactants and Interfacial Phenomena*; John Wiley & Sons, 2012.
- (3) Laughlin, R. G. *The Aqueous Phase Behavior of Surfactants*; Academic Press, 1996.
- (4) Gawali, S. L.; Zhang, M.; Kumar, S.; Ray, D.; Basu, M.; Aswal, V. K.; Danino, D.; Hassan, P. A. Discerning the Structure Factor of Charged Micelles in Water and Supercooled Solvent by Contrast Variation X-Ray Scattering. *Langmuir* **2019**, *35* (30), 9867–9877. <https://doi.org/10.1021/acs.langmuir.9b00912>.
- (5) Malmberg, C. G.; Maryott, A. A. Dielectric Constants of Aqueous Solutions of Dextrose and Sucrose. *J. Res. Natl. Bur. Stand. (1934)*. **1950**, *45* (4), 299. <https://doi.org/10.6028/jres.045.030>.
- (6) Hedin, N.; Furo, I.; Eriksson, P. O. Fast Diffusion of the Cl<sup>-</sup> Ion in the Headgroup Region of an Oppositely Charged Micelle. A Cl-35 NMR Spin Relaxation Study. *J. Phys. Chem. B* **2000**, *104* (35), 8544–8547. <https://doi.org/10.1021/jp001453t>.
- (7) Morén, A. K.; Nydén, M.; Söderman, O.; Khan, A. Microstructure of Protein–Surfactant Complexes in Gel and Solution an NMR Relaxation Study. *Langmuir* **1999**, *15* (17), 5480–5488. <https://doi.org/10.1021/la9816611>.
- (8) Tedeschi, A. M.; Franco, L.; Ruzzi, M.; Paduano, L.; Corvaja, C.; D’Errico, G. Micellar Aggregation of Alkyltrimethylammonium Bromide Surfactants Studied by Electron

- Paramagnetic Resonance of an Anionic Nitroxide. *Phys. Chem. Chem. Phys.* **2003**, *5* (19), 4204–4209. <https://doi.org/10.1039/b305324p>.
- (9) Griffiths, P. C.; Paul, A.; Heenan, R. K.; Penfold, J.; Ranganathan, R.; Bales, B. L. Role of Counterion Concentration in Determining Micelle Aggregation: Evaluation of the Combination of Constraints from Small-Angle Neutron Scattering, Electron Paramagnetic Resonance, and Time-Resolved Fluorescence Quenching. *J. Phys. Chem. B* **2004**, *108* (12), 3810–3816.
- (10) Pisarcik, M.; Devinsky, F.; Pupak, M. Determination of Micelle Aggregation Numbers of Alkyltrimethylammonium Bromide and Sodium Dodecyl Sulfate Surfactants Using Time-Resolved Fluorescence Quenching. *Open Chem.* **2015**, *13* (1), 922–931. <https://doi.org/10.1515/chem-2015-0103>.
- (11) Almgren, M.; Gimel, J. C.; Wang, K.; Karlsson, G.; Edwards, K.; Brown, W.; Mortensen, K. SDS Micelles at High Ionic Strength. A Light Scattering, Neutron Scattering, Fluorescence Quenching, and CryoTEM Investigation. *J. Colloid Interface Sci.* **1998**, *202* (2), 222–231. <https://doi.org/10.1006/jcis.1998.5503>.
- (12) Floriano, M. A.; Caponetti, E.; Panagiotopoulos, A. Z. Micellization in Model Surfactant Systems. *Langmuir* **1999**, *15* (9), 3143–3151. <https://doi.org/10.1021/la9810206>.
- (13) Rodriguez-Guadarrama, L. A.; Talsania, S. K.; Mohanty, K. K.; Rajagopalan, R. Thermodynamics of Aggregation of Amphiphiles in Solution from Lattice Monte Carlo Simulations. *Langmuir* **1999**, *15* (2), 437–446. <https://doi.org/10.1021/la9806597>.
- (14) Bruce, C. D.; Berkowitz, M. L.; Perera, L.; Forbes, M. D. E. Molecular Dynamics

- Simulation of Sodium Dodecyl Sulfate Micelle in Water: Micellar Structural Characteristics and Counterion Distribution. *J. Phys. Chem. B* **2002**, *106* (15), 3788–3793. <https://doi.org/10.1021/jp013616z>.
- (15) Shelley, J. C.; Shelley, M. Y. Computer Simulation of Surfactant Solutions. *Curr. Opin. Colloid Interface Sci.* **2000**, *5* (1–2), 101–110. [https://doi.org/10.1016/s1359-0294\(00\)00042-x](https://doi.org/10.1016/s1359-0294(00)00042-x).
- (16) Palazzesi, F.; Calvaresi, M.; Zerbetto, F. A Molecular Dynamics Investigation of Structure and Dynamics of SDS and SDBS Micelles. *Soft Matter* **2011**, *7* (19), 9148–9156.
- (17) Bendedouch, D.; Chen, S. H.; Koehler, W. C. Determination of Interparticle Structure Factors in Ionic Micellar Solutions by Small Angle Neutron Scattering. *J. Phys. Chem.* **1983**, *87* (14), 2621–2628. <https://doi.org/10.1021/j100237a030>.
- (18) Bezzobotnov, V. Y.; Borbely, S.; Cser, L.; Farago, B.; Gladkih, I. A.; Ostanevich, Y. M.; Vass, S. Temperature and Concentration Dependence of Properties of Sodium Dodecyl Sulfate Micelles Determined from Small Angle Neutron Scattering Experiments. *J. Phys. Chem.* **1988**, *92* (20), 5738–5743. <https://doi.org/10.1021/j100331a038>.
- (19) Hammouda, B. Temperature Effect on the Nanostructure of SDS Micelles in Water. *J. Res. Natl. Inst. Stand. Technol.* **2013**, *118*, 151–167. <https://doi.org/10.6028/jres.118.008>.
- (20) Hammouda, B. SANS from Pluronic P85 in D-Water. *Eur. Polym. J.* **2010**, *46* (12), 2275–2281. <https://doi.org/10.1016/j.eurpolymj.2010.10.012>.
- (21) Bergstrom, M.; Pedersen, J. S. Structure of Pure SDS and DTAB Micelles in Brine

- Determined by Small-Angle Neutron Scattering (SANS). *Phys. Chem. Chem. Phys.* **1999**, *1* (18), 4437–4446. <https://doi.org/10.1039/a903469b>.
- (22) Cabane, B.; Duplessix, R. t; Zemb, T. High Resolution Neutron Scattering on Ionic Surfactant Micelles: SDS in Water. *J. Phys.* **1985**, *46* (12), 2161–2178.
- (23) Berr, S. S.; Jones, R. R. M. Effect of Added Sodium and Lithium Chlorides on Intermicellar Interactions and Micellar Size of Aqueous Dodecyl Sulfate Aggregates as Determined by Small-Angle Neutron Scattering. *Langmuir* **1988**, *4* (6), 1247–1251. <https://doi.org/10.1021/la00084a005>.
- (24) Hayashi, S.; Ikeda, S. Micelle Size and Shape of Sodium Dodecyl Sulfate in Concentrated Sodium Chloride Solutions. *J. Phys. Chem.* **1980**, *84* (7), 744–751.
- (25) Nikolov, A. D.; Wasan, D. T. Ordered Micelle Structuring in Thin Films Formed from Anionic Surfactant Solutions: I. Experimental. *J. Colloid Interface Sci.* **1989**, *133* (1), 1–12.
- (26) Piech, M.; Walz, J. Y. Direct Measurement of Depletion and Structural Forces in Polydisperse, Charged Systems. *J. Colloid Interface Sci.* **2002**, *253* (1), 117–129. <https://doi.org/10.1006/jcis.2002.8503>.
- (27) James, G. K.; Walz, J. Y. Experimental and Theoretical Investigation of the Depletion and Structural Forces Produced by Ionic Micelles. *Colloids Surfaces A Physicochem. Eng. Asp.* **2014**, *441*, 406–419. <https://doi.org/10.1016/j.colsurfa.2013.09.033>.
- (28) Trokhymchuk, A.; Henderson, D.; Nikolov, A.; Wasan, D. T. Computer Modeling of

- Ionic Micelle Structuring in Thin Films. *J. Phys. Chem. B* **2003**, *107* (16), 3927–3937.  
<https://doi.org/10.1021/jp0210374>.
- (29) Andrieux, S.; Muller, P.; Kaushal, M.; Macias Vera, N. S.; Bollache, R.; Honorez, C.; Cagna, A.; Drenckhan, W. Microfluidic Thin Film Pressure Balance for the Study of Complex Thin Films. *Lab Chip* **2021**, *21* (2), 412–420.  
<https://doi.org/10.1039/D0LC00974A>.
- (30) Tulpar, A.; Van Tassel, P. R.; Walz, J. Y. Structuring of Macroions Confined between Like-Charged Surfaces. *Langmuir* **2006**, *22* (6), 2876–2883.  
<https://doi.org/10.1021/la0530485>.
- (31) Ludwig, M.; Witt, M. U.; von Klitzing, R. Bridging the Gap between Two Different Scaling Laws for Structuring of Liquids under Geometrical Confinement. *Adv. Colloid Interface Sci.* **2019**, *269*, 270–276. <https://doi.org/10.1016/j.cis.2019.04.012>.
- (32) von Klitzing, R.; Thormann, E.; Nylander, T.; Langevin, D.; Stubenrauch, C. Confinement of Linear Polymers, Surfactants, and Particles between Interfaces. *Adv. Colloid Interface Sci.* **2010**, *155* (1–2), 19–31. <https://doi.org/10.1016/j.cis.2010.02.003>.
- (33) Ludwig, M.; von Klitzing, R. Recent Progress in Measurements of Oscillatory Forces and Liquid Properties under Confinement. *Curr. Opin. Colloid Interface Sci.* **2020**, *47* (1), 137–152. <https://doi.org/10.1016/j.cocis.2020.02.002>.
- (34) Israelachvili, J.; Ruths, M. Brief History of Intermolecular and Intersurface Forces in Complex Fluid Systems. *Langmuir* **2013**, *29* (31), 9605–9619.  
<https://doi.org/10.1021/la401002b>.

- (35) Bergeron, V.; Radke, C. J. Equilibrium Measurements of Oscillatory Disjoining Pressures in Aqueous Foam Films. *Langmuir* **1992**, *8* (12), 3020–3026.  
<https://doi.org/10.1021/la00048a028>.
- (36) Zhang, Y.; Sharma, V. Nanoridge Formation and Dynamics of Stratification in Micellar Freestanding Films. *Langmuir* **2018**, *34* (3), 1208–1217.  
<https://doi.org/10.1021/acs.langmuir.7b01871>.
- (37) Pollard, M. L.; Radke, C. J. Density-functional Modeling of Structure and Forces in Thin Micellar Liquid Films. *J. Chem. Phys.* **1994**, *101* (8), 6979–6991.  
<https://doi.org/10.1063/1.468325>.
- (38) Kralchevsky, P. A.; Denkov, N. D. Analytical Expression for the Oscillatory Structural Surface Force. *Chem. Phys. Lett.* **1995**, *240* (4), 385–392. [https://doi.org/10.1016/0009-2614\(95\)00539-G](https://doi.org/10.1016/0009-2614(95)00539-G).
- (39) Danov, K. D.; Basheva, E. S.; Kralchevsky, P. A.; Ananthapadmanabhan, K. P.; Lips, A. The Metastable States of Foam Films Containing Electrically Charged Micelles or Particles: Experiment and Quantitative Interpretation. *Adv. Colloid Interface Sci.* **2011**, *168* (1–2), 50–70.
- (40) Anachkov, S. E.; Danov, K. D.; Basheva, E. S.; Kralchevsky, P. A.; Ananthapadmanabhan, K. P. Determination of the Aggregation Number and Charge of Ionic Surfactant Micelles from the Stepwise Thinning of Foam Films. *Adv. Colloid Interface Sci.* **2012**, *183*, 55–67.
- (41) Yilixiati, S.; Rafiq, R.; Zhang, Y.; Sharma, V. Influence of Salt on Supramolecular

- Oscillatory Structural Forces and Stratification in Micellar Freestanding Films. *ACS Nano* **2018**, *12* (2), 1050–1061. <https://doi.org/10.1021/acsnano.7b05391>.
- (42) Krichevsky, O.; Stavans, J. Micellar Stratification in Soap Films: A Light Scattering Study. *Phys. Rev. Lett.* **1995**, *74* (14), 2752–2755.  
<https://doi.org/10.1103/PhysRevLett.74.2752>.
- (43) Krichevsky, O.; Stavans, J. Confined Fluid between Two Walls: The Case of Micelles inside a Soap Film. *Phys. Rev. E* **1997**, *55* (6), 7260–7266.  
<https://doi.org/10.1103/PhysRevE.55.7260>.
- (44) Denkov, N. D.; Yoshimura, H.; Nagayama, K.; Kouyama, T. Nanoparticle Arrays in Freely Suspended Vitrified Films. *Phys. Rev. Lett.* **1996**, *76* (13), 2354–2357.  
<https://doi.org/10.1103/PhysRevLett.76.2354>.
- (45) Bergeron, V.; Jimenez-Laguna, A. I.; Radke, C. J. Hole Formation and Sheeting in the Drainage of Thin Liquid Films. *Langmuir* **1992**, *8* (12), 3027–3032.  
<https://doi.org/10.1021/la00048a029>.
- (46) Zhang, Y. R.; Sharma, V. Domain Expansion Dynamics in Stratifying Foam Films: Experiments. *Soft Matter* **2015**, *11* (22), 4408–4417. <https://doi.org/10.1039/c5sm00066a>.
- (47) Zhang, Y.; Sharma, V. Thickness-Dependent Phase Transition Drives Nanoridge-to-Mesa Instability in Micellar Freestanding Films. *Langmuir* **2018**, *34* (26), 7922–7931.  
<https://doi.org/10.1021/acs.langmuir.8b01010>.
- (48) Zhang, Y.; Yilixiati, S.; Pearsall, C.; Sharma, V. Nanoscopic Terraces, Mesas, and Ridges

- in Freely Standing Thin Films Sculpted by Supramolecular Oscillatory Surface Forces. *ACS Nano* **2016**, *10* (4), 4678–4683. <https://doi.org/10.1021/acsnano.6b01012>.
- (49) De Kruif, C. G.; Weinbreck, F.; De Vries, R. Complex Coacervation of Proteins and Anionic Polysaccharides. *Curr. Opin. Colloid Interface Sci.* **2004**, *9* (5), 340–349. <https://doi.org/10.1016/j.cocis.2004.09.006>.
- (50) Cooper, C. L.; Dubin, P. L.; Kayitmazer, A. B.; Turksen, S. Polyelectrolyte-Protein Complexes. *Curr. Opin. Colloid Interface Sci.* **2005**, *10* (1–2), 52–78. <https://doi.org/10.1016/j.cocis.2005.05.007>.
- (51) Woitovich Valetti, N.; Brassesco, M. E.; Picó, G. A. Polyelectrolytes–Protein Complexes: A Viable Platform in the Downstream Processes of Industrial Enzymes at Scaling up Level. *J. Chem. Technol. Biotechnol.* **2016**, *91* (12), 2921–2928. <https://doi.org/10.1002/jctb.5050>.
- (52) Srivastava, S.; Tirrell, M. V. Polyelectrolyte Complexation. In *Advances in Chemical Physics*; 2016; Vol. 161, pp 499–544. <https://doi.org/10.1002/9781119290971.ch7>.
- (53) Ulrich, S.; Seijo, M.; Stoll, S. The Many Facets of Polyelectrolytes and Oppositely Charged Macroions Complex Formation. **2006**, *11*, 268–272. <https://doi.org/10.1016/j.cocis.2006.08.002>.
- (54) Nolles, A.; Westphal, A. H.; De Hoop, J. A.; Fokkink, R. G.; Kleijn, J. M.; Van Berkel, W. J. H.; Borst, J. W. Encapsulation of GFP in Complex Coacervate Core Micelles. *Biomacromolecules* **2015**, *16* (5), 1542–1549. <https://doi.org/10.1021/acs.biomac.5b00092>.

- (55) Kayitmazer, A. B.; Koksai, A. F.; Kilic Iyilik, E. Complex Coacervation of Hyaluronic Acid and Chitosan: Effects of PH, Ionic Strength, Charge Density, Chain Length and the Charge Ratio. *Soft Matter* **2015**, *11* (44), 8605–8612. <https://doi.org/10.1039/c5sm01829c>.
- (56) Cummings, C. S.; Obermeyer, A. C. Phase Separation Behavior of Supercharged Proteins and Polyelectrolytes. *Biochemistry* **2018**, *57* (3), 314–323. <https://doi.org/10.1021/acs.biochem.7b00990>.
- (57) Kayitmazer, A. B.; Seeman, D.; Minsky, B. B.; Dubin, P. L.; Xu, Y. Protein-Polyelectrolyte Interactions. *Soft Matter* **2013**, *9* (9), 2553–2583. <https://doi.org/10.1039/c2sm27002a>.
- (58) Cousin, F.; Gummel, J.; Combet, S.; Boué, F. The Model Lysozyme-PSSNa System for Electrostatic Complexation: Similarities and Differences with Complex Coacervation. *Adv. Colloid Interface Sci.* **2011**, *167* (1–2), 71–84. <https://doi.org/10.1016/j.cis.2011.05.007>.
- (59) Cousin, F.; Gummel, J.; Clemens, D.; Grillo, I.; Boué, F. Multiple Scale Reorganization of Electrostatic Complexes of Poly(Styrenesulfonate) and Lysozyme. *Langmuir* **2010**, *26* (10), 7078–7085. <https://doi.org/10.1021/la904398z>.
- (60) Cousin, F.; Gummel, J.; Ung, D.; Boué, F. Polyelectrolyte-Protein Complexes: Structure and Conformation of Each Specie Revealed by SANS. *Langmuir* **2005**, *21* (21), 9675–9688. <https://doi.org/10.1021/la0510174>.
- (61) Gummel, J.; Cousin, F.; Boue, F. Structure Transition in PSS/Lysozyme Complexes: A Chain-Conformation-Driven Process, as Directly Seen by Small Angle Neutron

- Scattering. *Macromolecules* **2008**, *41* (8), 2898–2907. <https://doi.org/10.1021/ma702242d>.
- (62) Sedlák, E.; Fedunová, D.; Veselá, V.; Sedláková, D.; Antalík, M. Polyanion Hydrophobicity and Protein Basicity Affect Protein Stability in Protein-Polyanion Complexes. *Biomacromolecules* **2009**, *10* (9), 2533–2538. <https://doi.org/10.1021/bm900480t>.
- (63) Kamiya, N.; Klibanov, A. M. Controlling the Rate of Protein Release from Polyelectrolyte Complexes. *Biotechnol. Bioeng.* **2003**, *82* (5), 590–594. <https://doi.org/10.1002/bit.10606>.
- (64) Bungenberg de Jong, HG and Kruyt, H. Coacervation (Partial Miscibility in Colloid Systems). *Proc. K. Ned. Akad. Wet* **1929**, *32*, 849–856.
- (65) Hubbe, M. A.; Moore, S. M.; Lee, S. Y. Effects of Charge Ratios and Cationic Polymer Nature on Polyelectrolyte Complex Deposition onto Cellulose. *Ind. Eng. Chem. Res.* **2005**, *44* (9), 3068–3074. <https://doi.org/10.1021/ie048902m>.
- (66) Petzold, G.; Lunkwitz, K. The Interaction between Polyelectrolyte Complexes Made from Poly(Dimethyldiallylammonium Chloride) (PDMDAAC) and Poly(Maleic Acid-Co- $\alpha$ -Methylstyrene) (P(MS- $\alpha$ -MeSty)) and Cellulosic Materials. *Colloids Surfaces A Physicochem. Eng. Asp.* **1995**, *98* (3), 225–233. [https://doi.org/10.1016/0927-7757\(95\)03133-X](https://doi.org/10.1016/0927-7757(95)03133-X).
- (67) Gärdlund, L.; Wågberg, L.; Gernandt, R. Polyelectrolyte Complexes for Surface Modification of Wood Fibres: II. Influence of Complexes on Wet and Dry Strength of Paper. *Colloids Surfaces A Physicochem. Eng. Asp.* **2003**, *218* (1–3), 137–149. [https://doi.org/10.1016/S0927-7757\(02\)00588-5](https://doi.org/10.1016/S0927-7757(02)00588-5).

- (68) Lindström, T.; Wågberg, L.; Larsson, T. On the Nature of Joint Strength in Paper – a Review of Dry and Wet Strength Resins Used in Paper Manufacturing. *13th Fundam. Res. Symp.* **2005**, 32 (May 2005), 457–562. <https://doi.org/10.15376/frc.2005.1.457.ON>.
- (69) Müller, M. *Polyelectrolyte Complexes in the Dispersed and Solid State II Application Aspects*; 2013.
- (70) Swerin, A.; Ödberg, L.; Wågberg, L. An Extended Model for the Estimation of Flocculation Efficiency Factors in Multicomponent Flocculant Systems. *Colloids Surfaces A Physicochem. Eng. Asp.* **1996**, 113 (1–2), 25–38. [https://doi.org/10.1016/0927-7757\(95\)03506-0](https://doi.org/10.1016/0927-7757(95)03506-0).
- (71) Böhm, N.; Kulicke, W. M. Optimization of the Use of Polyelectrolytes for Dewatering Industrial Sludges of Various Origins. *Colloid Polym. Sci.* **1997**, 275 (1), 73–81. <https://doi.org/10.1007/s003960050054>.
- (72) Goddard, E. D. *Interactions of Surfactants with Polymers and Proteins*; Goddard, E. D., Ananthapadmanabhan, K. P., Eds.; CRC Press, 2018. <https://doi.org/10.1201/9781351073783>.
- (73) Naderi, A.; Claesson, P. M.; Bergström, M.; Dedinaite, A. Trapped Non-Equilibrium States in Aqueous Solutions of Oppositely Charged Polyelectrolytes and Surfactants: Effects of Mixing Protocol and Salt Concentration. *Colloids Surfaces A Physicochem. Eng. Asp.* **2005**, 253 (1–3), 83–93. <https://doi.org/10.1016/j.colsurfa.2004.10.123>.
- (74) Ye, A. Complexation between Milk Proteins and Polysaccharides via Electrostatic Interaction: Principles and Applications - A Review. *Int. J. Food Sci. Technol.* **2008**, 43

- (3), 406–415. <https://doi.org/10.1111/j.1365-2621.2006.01454.x>.
- (75) Weinbreck, F.; Nieuwenhuijse, H.; Robijn, G. W.; De Kruif, C. G. Complex Formation of Whey Proteins: Exocellular Polysaccharide EPS B40. *Langmuir* **2003**, *19* (22), 9404–9410. <https://doi.org/10.1021/la0348214>.
- (76) Weinbreck, F.; de Vries, R.; Schrooyen, P.; de Kruif, C. G. Complex Coacervation of Whey Proteins and Gum Arabic. *Biomacromolecules* **2003**, *4* (2), 293–303. <https://doi.org/10.1021/bm025667n>.
- (77) Tromp, R. H.; De Kruif, C. G.; Van Eijk, M.; Rolin, C. On the Mechanism of Stabilisation of Acidified Milk Drinks by Pectin. *Food Hydrocoll.* **2004**, *18* (4), 565–572. <https://doi.org/10.1016/j.foodhyd.2003.09.005>.
- (78) Burgos-Díaz, C.; Wandersleben, T.; Marqués, A. M.; Rubilar, M. Multilayer Emulsions Stabilized by Vegetable Proteins and Polysaccharides. *Curr. Opin. Colloid Interface Sci.* **2016**, *25*, 51–57. <https://doi.org/10.1016/j.cocis.2016.06.014>.
- (79) Bourganis, V.; Karamanidou, T.; Kammona, O.; Kiparissides, C. Polyelectrolyte Complexes as Prospective Carriers for the Oral Delivery of Protein Therapeutics. *Eur. J. Pharm. Biopharm.* **2017**, *111*, 44–60. <https://doi.org/10.1016/j.ejpb.2016.11.005>.
- (80) Harris, J. M.; Chess, R. B. Effect of Pegylation on Pharmaceuticals. *Nat. Rev. Drug Discov.* **2003**, *2* (3), 214–221. <https://doi.org/10.1038/nrd1033>.
- (81) Gu, Z.; Biswas, A.; Zhao, M.; Tang, Y. Tailoring Nanocarriers for Intracellular Protein Delivery. *Chem. Soc. Rev.* **2011**, *40* (7), 3638–3655. <https://doi.org/10.1039/c0cs00227e>.

- (82) Liang, S.; Liu, Y.; Jin, X.; Liu, G.; Wen, J.; Zhang, L.; Li, J.; Yuan, X.; Chen, I. S. Y.; Chen, W.; Wang, H.; Shi, L.; Zhu, X.; Lu, Y. Phosphorylcholine Polymer Nanocapsules Prolong the Circulation Time and Reduce the Immunogenicity of Therapeutic Proteins. *Nano Res.* **2016**, *9* (4), 1022–1031. <https://doi.org/10.1007/s12274-016-0991-3>.
- (83) Zhang, X.; Chen, W.; Zhu, X.; Lu, Y. Encapsulating Therapeutic Proteins with Polyzwitterions for Lower Macrophage Nonspecific Uptake and Longer Circulation Time. *ACS Appl. Mater. Interfaces* **2017**, *9* (9), 7972–7978. <https://doi.org/10.1021/acsami.6b16413>.
- (84) Xia, J.; Mattison, K.; Romano, V.; Dubin, P. L.; Muhoberac, B. B. Complexation of Trypsin and Alcohol Dehydrogenase with Poly(Diallyldimethylammonium Chloride). *Biopolymers* **1997**, *41* (4), 359–365. [https://doi.org/10.1002/\(SICI\)1097-0282\(19970405\)41:4<359::AID-BIP1>3.0.CO;2-L](https://doi.org/10.1002/(SICI)1097-0282(19970405)41:4<359::AID-BIP1>3.0.CO;2-L).
- (85) Lindhoud, S.; Claessens, M. M. A. E. Accumulation of Small Protein Molecules in a Macroscopic Complex Coacervate. *Soft Matter* **2015**, *12* (2), 408–413. <https://doi.org/10.1039/c5sm02386f>.
- (86) Black, K. A.; Priftis, D.; Perry, S. L.; Yip, J.; Byun, W. Y.; Tirrell, M. Protein Encapsulation via Polypeptide Complex Coacervation. *ACS Macro Lett.* **2014**, *3* (10), 1088–1091. <https://doi.org/10.1021/mz500529v>.
- (87) Zhao, M.; Zacharia, N. S. Protein Encapsulation via Polyelectrolyte Complex Coacervation: Protection against Protein Denaturation. *J. Chem. Phys.* **2018**, *149* (16), 163326. <https://doi.org/10.1063/1.5040346>.

- (88) McCall, P. M.; Srivastava, S.; Perry, S. L.; Kovar, D. R.; Gardel, M. L.; Tirrell, M. V. Partitioning and Enhanced Self-Assembly of Actin in Polypeptide Coacervates. *Biophys. J.* **2018**, *114* (7), 1636–1645. <https://doi.org/10.1016/j.bpj.2018.02.020>.
- (89) Kübelbeck, S.; Mikhael, J.; Schoof, S.; Andrieu-Brunsen, A.; Baier, G. Immobilization of  $\alpha$ -Amylase in Polyelectrolyte Complexes. *J. Appl. Polym. Sci.* **2017**, *134* (27), 1–10. <https://doi.org/10.1002/app.45036>.
- (90) Tian, L.; Li, M.; Liu, J.; Patil, A. J.; Drinkwater, B. W.; Mann, S. Nonequilibrium Spatiotemporal Sensing within Acoustically Patterned Two-Dimensional Protocell Arrays. *ACS Cent. Sci.* **2018**, *4* (11), 1551–1558. <https://doi.org/10.1021/acscentsci.8b00555>.
- (91) Kurinomaru, T.; Shiraki, K. Aggregative Protein–Polyelectrolyte Complex for High-Concentration Formulation of Protein Drugs. *Int. J. Biol. Macromol.* **2017**, *100*, 11–17. <https://doi.org/10.1016/j.ijbiomac.2016.06.016>.
- (92) Kurinomaru, T.; Maruyama, T.; Izaki, S.; Handa, K.; Kimoto, T.; Shiraki, K. Protein-Poly(Amino Acid) Complex Precipitation for High-Concentration Protein Formulation. *J. Pharm. Sci.* **2014**, *103* (8), 2248–2254. <https://doi.org/10.1002/jps.24025>.
- (93) Izaki, S.; Kurinomaru, T.; Maruyama, T.; Uchida, T.; Handa, K.; Kimoto, T.; Shiraki, K. Feasibility of Antibody-Poly(Glutamic Acid) Complexes: Preparation of High-Concentration Antibody Formulations and Their Pharmaceutical Properties. *J. Pharm. Sci.* **2015**, *104* (6), 1929–1937. <https://doi.org/10.1002/jps.24422>.
- (94) Maruyama, T.; Izaki, S.; Kurinomaru, T.; Handa, K.; Kimoto, T.; Shiraki, K. Protein-Poly(Amino Acid) Precipitation Stabilizes a Therapeutic Protein L-Asparaginase against

- Physicochemical Stress. *J. Biosci. Bioeng.* **2015**, *120* (6), 720–724.  
<https://doi.org/10.1016/j.jbiosc.2015.04.010>.
- (95) Izaki, S.; Kurinomaru, T.; Handa, K.; Kimoto, T.; Shiraki, K. Stress Tolerance of Antibody-Poly(Amino Acid) Complexes for Improving the Stability of High Concentration Antibody Formulations. *J. Pharm. Sci.* **2015**, *104* (8), 2457–2463.  
<https://doi.org/10.1002/jps.24515>.
- (96) Minsky, B. B.; Zheng, B.; Dubin, P. L. Inhibition of Antithrombin and Bovine Serum Albumin Native State Aggregation by Heparin. *Langmuir* **2014**, *30* (1), 278–287.  
<https://doi.org/10.1021/la4039232>.
- (97) Gucht, J. van der; Spruijt, E.; Lemmers, M.; Cohen Stuart, M. A. Polyelectrolyte Complexes: Bulk Phases and Colloidal Systems. *J. Colloid Interface Sci.* **2011**, *361* (2), 407–422. <https://doi.org/10.1016/j.jcis.2011.05.080>.
- (98) Sing, C. E.; Perry, S. L. Recent Progress in the Science of Complex Coacervation. *Soft Matter* **2020**. <https://doi.org/10.1039/D0SM00001A>.
- (99) Moreau, N. G.; Martin, N.; Gobbo, P.; Tang, T. Y. D.; Mann, S. Spontaneous Membrane-Less Multi-Compartmentalization: Via Aqueous Two-Phase Separation in Complex Coacervate Micro-Droplets. *Chem. Commun.* **2020**, *56* (84), 12717–12720.  
<https://doi.org/10.1039/d0cc05399f>.
- (100) Li, M.; Huang, X.; Tang, T. Y. D.; Mann, S. Synthetic Cellularity Based on Non-Lipid Micro-Compartments and Protocell Models. *Curr. Opin. Chem. Biol.* **2014**, *22*, 1–11.  
<https://doi.org/10.1016/j.cbpa.2014.05.018>.

- (101) Kataoka, K.; Miyata, K.; Nishiyama, N.; Kataoka, K. Rational Design of Smart Supramolecular Assemblies for Gene Delivery: Chemical Challenges in the Creation of Artificial Viruses. *Chem. Soc. Rev.* **2012**, *41* (7), 2718–2739.  
<https://doi.org/10.1039/c2cs15309b>.
- (102) Cabral, H.; Miyata, K.; Osada, K.; Kataoka, K. Block Copolymer Micelles in Nanomedicine Applications. *Chem. Rev.* **2018**, *118* (14), 6844–6892.  
<https://doi.org/10.1021/acs.chemrev.8b00199>.
- (103) Sokolova, E.; Spruijt, E.; Hansen, M. M. K.; Dubuc, E.; Groen, J.; Chokkalingam, V.; Piruska, A.; Heus, H. A.; Huck, W. T. S. Enhanced Transcription Rates in Membrane-Free Protocells Formed by Coacervation of Cell Lysate. *Proc. Natl. Acad. Sci.* **2013**, *110* (29), 11692–11697. <https://doi.org/10.1109/ISSPIT.2006.270766>.
- (104) Elani, Y.; Law, R. V.; Ces, O. Vesicle-Based Artificial Cells as Chemical Microreactors with Spatially Segregated Reaction Pathways. *Nat. Commun.* **2014**, *5* (1), 5305.  
<https://doi.org/10.1038/ncomms6305>.
- (105) Weber, C. A.; Zwicker, D.; Jülicher, F.; Lee, C. F. Physics of Active Emulsions. *Reports Prog. Phys.* **2019**, *82* (6). <https://doi.org/10.1088/1361-6633/ab052b>.
- (106) Dora Tang, T. Y.; Rohaida Che Hak, C.; Thompson, A. J.; Kuimova, M. K.; Williams, D. S.; Perriman, A. W.; Mann, S. Fatty Acid Membrane Assembly on Coacervate Microdroplets as a Step towards a Hybrid Protocell Model. *Nat. Chem.* **2014**, *6* (6), 527–533. <https://doi.org/10.1038/nchem.1921>.
- (107) Mason, A. F.; van Hest, J. C. M. Multifaceted Cell Mimicry in Coacervate-Based

- Synthetic Cells. *Emerg. Top. Life Sci.* **2019**, 3 (5), 567–571.  
<https://doi.org/10.1042/ETLS20190094>.
- (108) Mason, A. F.; Buddingh, B. C.; Williams, D. S.; Van Hest, J. C. M. Hierarchical Self-Assembly of a Copolymer-Stabilized Coacervate Protocell. *J. Am. Chem. Soc.* **2017**, 139 (48), 17309–17312. <https://doi.org/10.1021/jacs.7b10846>.
- (109) Mason, A. F.; Altenburg, W. J.; Song, S.; van Stevendaal, M.; van Hest, J. C. M. Terpolymer-Stabilized Complex Coacervates: A Robust and Versatile Synthetic Cell Platform. In *Methods in Enzymology*; Elsevier Inc., 2021; Vol. 646, pp 51–82.  
<https://doi.org/10.1016/bs.mie.2020.06.008>.
- (110) Mason, A. F.; Yewdall, N. A.; Welzen, P. L. W.; Shao, J.; Stevendaal, M. Van; Hest, J. C. M. V.; Williams, D. S.; Abdelmohsen, L. K. E. A. Mimicking Cellular Compartmentalization in a Hierarchical Protocell through Spontaneous Spatial Organization. *ACS Cent. Sci.* **2019**, 5 (8), 1360–1365.  
<https://doi.org/10.1021/acscentsci.9b00345>.
- (111) van Stevendaal, M. H. M. E.; Vasiukas, L.; Yewdall, N. A.; Mason, A. F.; van Hest, J. C. M. Engineering of Biocompatible Coacervate-Based Synthetic Cells. *ACS Appl. Mater. Interfaces* **2021**, 13 (7), 7879–7889. <https://doi.org/10.1021/acsami.0c19052>.
- (112) Yewdall, N. A.; Buddingh, B. C.; Altenburg, W. J.; Timmermans, S. B. P. E.; Vervoort, D. F. M.; Abdelmohsen, L. K. E. A.; Mason, A. F.; van Hest, J. C. M. Physicochemical Characterization of Polymer-Stabilized Coacervate Protocells. *ChemBioChem* **2019**, 20 (20), 2643–2652. <https://doi.org/10.1002/cbic.201900195>.

- (113) Dewey, D. C.; Strulson, C. A.; Cacace, D. N.; Bevilacqua, P. C.; Keating, C. D. Bioreactor Droplets from Liposome-Stabilized All-Aqueous Emulsions. *Nat. Commun.* **2014**, *5* (May), 1–9. <https://doi.org/10.1038/ncomms5670>.
- (114) Pir Cakmak, F.; Grigas, A. T.; Keating, C. D. Lipid Vesicle-Coated Complex Coacervates. *Langmuir* **2019**, *35* (24), 7830–7840. <https://doi.org/10.1021/acs.langmuir.9b00213>.

## CHAPTER 2

### INTERMICELLAR INTERACTIONS PROBED IN BULK AQUEOUS SOLUTIONS AND IN FOAM FILMS

Contents of section 2.2.1 are reproduced and reformatted with the permission from Chrystian Ochoa; Shang Gao; Samanvaya Srivastava; Vivek Sharma. “Foam film stratification studies probe intermicellar interactions” *The Proceedings of the National Academy of Sciences* 2021, 118 (25) e2024805118.

The thin film stratification studies reported in this Chapter were performed by Chrystian Ochoa.

#### ABSTRACT

Ultrathin foam films containing supramolecular structures like micelles in bulk, and adsorbed surfactant at the liquid-air interface, undergo drainage *via* stratification. At a fixed surfactant concentration, the stepwise decrease in average film thickness of a stratifying micellar film yields a characteristic step size that also describes the quantized thickness difference between coexisting thick-thin flat regions. Even though many published studies claim that step size equals intermicellar distance obtained using scattering from bulk solutions, we found no reports of a direct comparison between the two length scales. It is well-established that step size is inversely proportional to the cubic root of surfactant concentration (in the limit of low surfactant concentration) but cannot be estimated by adding micelle size to Debye length, as the latter is inversely proportional to the square root of surfactant concentration. Moreover, while there are numerous studies that have stratification behavior of foam films stabilized by surfactants or

behavior of surfactant micelles (micelle dimensions, volume fraction, and intermicellar interactions) in bulk, few studies have explored these aspects of surfactant assembly in high surfactant concentration regimes. Understanding the roles of micelles in bulk phase and in foam films in the high concentration regime is expected to provide insightful feedback for consumer product formulations and for controlling undesirable foaming in industrial settings. In this chapter, we first contrast the step size obtained from analysis of nanoscopic thickness variations and transitions in stratifying foam films using Interferometry Digital Imaging Optical Microscopy (IDIOM) protocols with the intermicellar distance obtained using small-angle X-ray scattering in low concentration (25 mM – 250 mM) solutions of a model surfactant, sodium dodecyl sulfate (SDS). Additionally, we extend our study to probe these physical behaviors and transitions in high surfactant concentration range (up to 600 mM). We find that stratification driven by the confinement-induced layering of micelles within the liquid-air interfaces of a foam film provides a sensitive probe of non-DLVO oscillatory forces and micellar interactions in a broad surfactant concentration range.

## 2.1. INTRODUCTION

Molecules in simple liquids and supramolecular structures in complex fluids can stratify or undergo confinement-induced layering induced by symmetry breaking at a solid-liquid or a fluid-fluid interface.<sup>1-6</sup> In freestanding or foam films, the confinement-induced layering of supramolecular structures including micelles,<sup>7-15</sup> lipid layers,<sup>16-17</sup> polyelectrolyte-surfactant complexes,<sup>18-19</sup> nanoparticles,<sup>7, 20</sup> and liquid crystalline assemblies<sup>21</sup> can result in drainage *via* stratification. Due to thin film interference, foam films visualized under white light illumination display iridescent colors for thick films ( $h > 100$  nm),<sup>22-24</sup> but ultrathin films ( $h < 100$  nm) exhibit shades of gray that get progressively darker as the film gets thinner.<sup>7-8, 10-18, 25</sup> In reflected light microscopy, micellar foam films exhibit coexisting thick-thin regions with distinct shades of grey. Interferometry-based measurement of the average film thickness over time decreases in a stepwise fashion yielding a step size,  $\Delta h$ .<sup>7-8, 10-15, 25</sup> Many published studies argue<sup>7-10, 20, 25-30</sup> that foam films containing charged micelles or latex particles stratify analogously due to the formation of “ordered colloidal crystals” and step size  $\Delta h$ , equals the intermicellar distance,  $d$  in bulk solutions. However, a comparison of concentration-dependent  $\Delta h$  obtained from the dynamic foam stratification studies (influenced by confinement effects) with  $d$  measured using small-angle X-ray or neutron scattering (SAXS or SANS) or other direct measurements of static equilibrium structure, and related evidence for or against the formation of “ordered colloidal crystals” in micellar foam films, are lacking in the literature. Thus, the motivations of the studies reported in this chapter are threefold: (i) contrast the step size,  $\Delta h$  obtained via stratification studies with the intermicellar distance,  $d$  and micelle dimensions determined using SAXS, (ii) examine the SAXS data for any evidence of ordered colloidal crystals, and (iii) elucidate the influence of ionic micelles

on foam film stability and topography, as well as on colloidal forces, in multicomponent complex fluids.

Micelles, formed by self-assembly of soaps and detergents, and ever-present in typical household foams, facilitate cleaning and detergent action by solubilizing oils and oil-soluble dirt within their hydrophobic core.<sup>1, 30-31</sup> Micelles formed by biosurfactants like bile salt and rhamnolipids can be used for delivering non-polar, bio-active polyunsaturated oils, flavonoids, vitamins, and hydrophobic drugs.<sup>32-34</sup> Therefore, understanding the stability and lifetime of micellar foams is essential towards molecular engineering of formulations, controlling foams in industrial reactors, rivers, and lakes, and developing bio-surfactants.<sup>32-34</sup> Foam film drainage involves interfacial flows that are influenced both by bulk rheology and interfacial rheology as well as Laplace or capillary pressure,  $P_c = \sigma C$  (set by surface tension and curvature).<sup>24, 35-38</sup> Additionally, thickness transitions and variations in ultrathin ( $h < 100$  nm) freestanding, as well as supported (containing one or two solid boundaries), films<sup>38-40</sup> depend on disjoining pressure,  $\Pi(h) = -(\partial G/\partial h)_{P,T,A,N_i}$  defined as the free energy required to change unit thickness at constant temperature,  $T$ , overall pressure,  $P$ , surface area,  $A$  and mole number,  $N_i$ .<sup>3, 30, 36, 38-39</sup> Intermolecular and surface forces determine the strength and range of disjoining pressure,  $\Pi(h)$  as well as of colloidal interaction forces  $F(h)$ .<sup>2-3, 31, 36, 38-39</sup> Physical properties of surfactant solutions like surface tension and conductivity show distinct change around a critical micelle concentration (CMC) beyond which spherical micelles can form,<sup>30-31</sup> and rod-like micelles, lamellar phases, etc. emerge at higher concentrations.<sup>41-43</sup> In foam films formed with ionic surfactant at  $C_{SDS} < CMC$ , drainage below  $h < 30$  nm often leads to the formation of relatively long-lived common black (CB) film attributed to counterbalancing of  $P_c$  by  $\Pi_{DLVO}(h)$ , the disjoining pressure due to DLVO

(Derjaguin-Landau-Verwey-Overbeek) forces contributed by van der Waals and electrostatic double-layer interactions.<sup>2-3, 31, 35-36</sup> Even thinner Newton black (NB) films attest to the role of shorter-range, non-DLVO surface forces.<sup>12, 22-24, 36, 38</sup> In contrast, in micellar foam films ( $c > \text{CMC}$ ), a non-DLVO, oscillatory structural force,  $\Pi_{OS}(h)$  counterbalances  $P_c$  at multiple flat thicknesses, manifested as distinct shades of grey in reflected light microscopy.<sup>7-8, 10-15, 19, 25, 36, 44-47</sup>

For micellar fluids containing charged micelles, the step size,  $\Delta h$  obtained using thickness-time plots from stratification experiments, and periodicity,  $\lambda$  of  $\Pi_{OS}(h)$  directly measured using thin-film balance<sup>44-45</sup> show that both periodicity and step size exceed micelle size,  $a$  implying  $\lambda > a$  and  $\Delta h > a$ . In 1971, Bruil and Lyklema<sup>48</sup> were the first to report that the concentration-dependent decrease in step size measured for sodium dodecyl sulfate (SDS) solutions followed a power law of the form  $\Delta h \propto c_{\text{soap}}^{-\frac{1}{3}}$  and wrote that step size values “seem to be related to intermolecular distance in the (unmicellized) bulk solution.” In 1988, Nikolov *et al.*<sup>7</sup> reported that foam films containing latex particles stratified in a fashion similar to micellar foam films and argued that diffusion-driven, layer-by-layer removal of micelles or particles from an ordered colloidal crystal structure drives stratification. In their “ordered colloidal crystal” or “micelle-vacancy diffusion” mechanism, they proposed that the effective film viscosity increases with decrease in stratified film thickness<sup>7-9, 26-27, 29</sup>. Contrastingly, in the “hydrodynamic” mechanism, Bergeron and Radke<sup>11, 44</sup> describe stratification using a thin-film equation, by incorporating  $\Pi_{OS}(h)$  and bulk solution viscosity. Nikolov *et al.*<sup>7-9, 26-27</sup> suggested that the step size,  $\Delta h$  was equal to an effective diameter,  $d_{\text{eff}} = 2(l_{\text{SDS}} + \kappa^{-1})$  computed by adding the fixed length of SDS molecules to the Debye length,  $\kappa^{-1}$  that captures the range of screened electrostatic interactions. However, the step size  $\Delta h \propto$

$C_{SDS}^{-\frac{1}{3}}$  and the Debye length  $\kappa^{-1} \propto C_{SDS}^{-\frac{1}{2}}$ , display distinct power laws, and the measured step size exceeds the micelle size,  $a$  as well as the computed effective diameter,  $d_{eff}$  for ionic micellar systems, or typically  $\Delta h > a$  and  $\Delta h > d_{eff}$ .

Studies on charged nanoparticle dispersions find that the periodicity,  $\lambda$  of the oscillatory structural force,  $F(h)$  measured directly with surface force apparatus (SFA), or colloidal probe AFM (or CP-AFM), correlates well with the interparticle distance,  $d$  obtained using scattering and simulations.<sup>4-5, 49-52</sup> Furthermore, the periodicity,  $\lambda \approx d \gg a$  is primarily set by the particle number density,  $\rho$  and is relatively independent of added salt, charge at solid surfaces, and particle size,  $a$ .<sup>4-5, 50-52</sup> Assuming that analogy between  $\lambda \propto \rho^{-\frac{1}{3}}$  in the nanoparticle studies and  $\Delta h \propto C_{SDS}^{-\frac{1}{3}}$  in stratified foam studies arises due to similar underlying physics, Danov *et al.*<sup>28</sup> and Anachkov *et al.*<sup>10</sup> argued that  $\Delta h \approx d$  or step size equals the intermicellar distance,  $d$  in bulk solutions, and hypothesized that step size from stratification studies could be used for determining aggregation number as  $N_{agg} \approx (C_{SDS} - CMC_{SDS})(\Delta h)^3$ . However, Yilixiati *et al.*<sup>15</sup> showed that on salt addition, the measured  $\Delta h$  values for micellar SDS solutions do not collapse onto a single curve even if plotted against micellar number density,  $\rho$  as micelle number and dimensions can change on the addition of salt (or surfactant),<sup>1</sup> whereas nanoparticle dimensions remain constant. Furthermore, solid boundaries that can impact SFA and AFM measurements are absent in stratifying foam films. However, the thickness of stratifying films is rather heterogeneous, and the average thickness changes in a stepwise fashion. Thus, the analogy between stratifying micelles in foam films and stratifying nanoparticle dispersions under confinement between solid surfaces requires further investigation. In particular, a comparison between multiple length-scales including

micelle dimensions, Debye length, intermicellar distance,  $d$  and step size,  $\Delta h$  and the consequences of thickness heterogeneities within foam films are warranted.

In this chapter, we contrast the concentration-dependent changes in step size measured in foam stratification studies with micellar dimensions and intermicellar distances in bulk solutions obtained using small-angle X-ray scattering (SAXS) for aqueous solutions of sodium dodecyl sulfate (SDS). For the range of concentrations ( $25 \text{ mM} \leq C_{SDS} \leq 250 \text{ mM}$ ) explored in section 2.2.1, bulk rheology, interfacial tension, micelle shape and size, and interfacial charge (or potential) are nearly constant. Hence, the observed concentration-dependent changes in step size and nanoscopic topography in stratifying films are dictated by the corresponding changes in intermicellar interactions and the resulting disjoining pressure,  $\Pi_{OS}(h)$ . We visualize and analyze nanoscopic thickness variations and transitions in stratifying foam films using IDIOM (Interferometry Digital Imaging Optical Microscopy) protocols<sup>14</sup> (See Figure 2-1a) that provide requisite spatio-temporal resolution (thickness  $\sim 1 \text{ nm}$ , in-plane  $< 1 \text{ }\mu\text{m}$ , time  $< 1 \text{ ms}$ ). We analyze SAXS data to compute micelle dimensions, volume fraction, and microstructure (order) in bulk solutions and obtain the intermicellar distance from structure factor peak in SAXS data. Finally, we discuss the ramifications of the close comparison between step size from the foam film stratification studies and micellar dimensions and intermicellar distance determined using SAXS analysis, on the intermicellar interactions and the mechanistic basis of stratification. In section 2.2.2, we extend our studies to provide a comparison between the step size and intermicellar distances in higher SDS concentrations ( $100 \text{ mM} \leq C_{SDS} \leq 600 \text{ mM}$ ), highlighting the influences of non-DLVO oscillatory forces and intermicellar interactions on thin film stability and drainage patterns.

## 2.2. RESULTS

### 2.2.1. Intermicellar Interactions in Bulk Aqueous Solutions and Thin Films: Low Concentration Regime ( $25 \text{ mM} \leq C_{SDS} \leq 250 \text{ mM}$ )

#### *Drainage via Stepwise Thinning of Micellar SDS Foam Films*

The IDIOM set-up, shown schematically in Figure 2-1a, is utilized for visualization of a single foam film undergoing drainage, and simultaneously, for quantitative analysis of thickness variations and transitions.<sup>13-15, 45-47</sup> A high-speed camera attached to a microscope captures the pixel-wise reflected light intensity that is determined by interference between light reflected from the two liquid-air interfaces of a single foam film, as sketched in Figure 2-1b. The thickness of micellar foam films is obtained by analyzing average intensity from a square region ( $110 \mu\text{m}^2$ ). Thickness decreases in stepwise fashion, as shown in Figure 2-1c. The thickness profiles obtained for four distinct surfactant concentrations, shifted horizontally to aid clear visualization, feature two characteristic trends: the number of steps increases, whereas the step size decreases with an increase in surfactant concentration. For instance, the number of steps increases from 4 to 7, whereas the step size,  $\Delta h$  decreases from  $\Delta h = 13 \text{ nm}$  to  $\Delta h = 7 \text{ nm}$  when SDS concentration is increased from 50 mM to 250 mM.

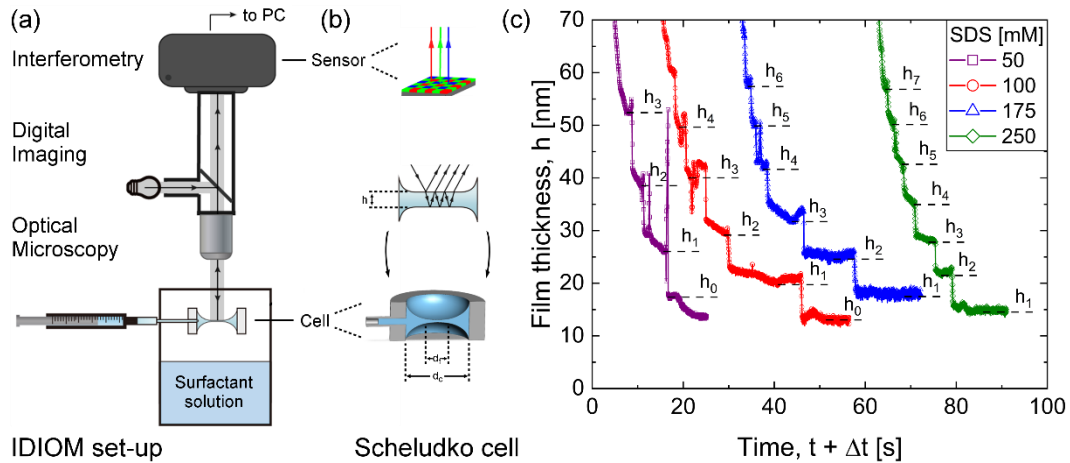


**Figure 2-1 Schematic of the set-up used for examining stratification using IDIOM (Interferometry Digital Imaging Optical Microscopy) protocols and illustrative examples of stepwise thinning.** (a) The Scheludko-like cell contains a plane-parallel film and surrounding meniscus that emulates a single foam film and its Plateau border. The cell is placed in a closed container and stratification is visualized using reflected light microscopy. A finite volume of fluid is inserted into the cell using the side-arm connected to a syringe. No liquid is added or withdrawn during the stratification experiment, and drainage from the film into the meniscus occurs freely and spontaneously. (b) Spatio-temporal variation in interference intensity  $I(x, y, \lambda, t)$  is used for computing thickness transitions and variations in stratifying films. (c) Average film thickness plotted as a function of time shows stepwise thinning for foam films made with aqueous SDS solutions. The spikes and dips in thickness plots appear when mesas or domains emerge in the region selected for computing average thickness. The data are shifted horizontally for clarity.

### *Nanoscopic Topography of Stratifying Films, Characterized Using IDIOM Protocols*

Stratification in horizontal foam films visually manifests as shown in Figure 2-2: regions with distinct thickness appear with contrasting shades of gray, and as thinner regions appear darker, the average thickness of the entire film decreases over time. Sharp contact lines demarcate the coexisting thick-thin regions, and the number of thinner, darker domains nucleated and observed decreases progressively. The concentration-dependent contrast in the number and duration of stepwise transitions and the topography of the films is highlighted in Figure 2-2. In addition to the snapshots that show the contrast in grayscale intensity, here we include representative thickness maps obtained by converting intensity into pixel-wise thickness using IDIOM protocols, as detailed elsewhere.<sup>14, 45-46</sup> Even though the measurements of step size are routinely carried out by using monochromatic light sources and photodiodes as detectors that measure the average reflected light intensity,<sup>24</sup> the visualization and analysis of nanoscopic topographical features shown in Figure 2-2 only began with the advent of IDIOM protocols.<sup>13-15, 45-47</sup>

The increase in the total number of flat regions that have distinct gray color and reflected light intensity values for the two concentrations included here (50 mM and 250 mM) are correlated with increase in the number of steps from 4 to 7 observed in Figure 2-1c. The topographical maps reveal that in addition to flat regions, including circular thinner, darker domains that spontaneously nucleate and grow during the stratification process, a spectrum of non-flat features including nanoridges and mesas also form and grow over time. For example, the necklace of bright, white spots observed in Figure 2-2h turns out to be a chain of mesas in the corresponding thickness map whose the in-plane dimensions are in microns (see scale bar), and thickness is in nm (see colormap). Even though the hydrodynamic mechanisms predict the formation of nanoridge around a growing

domain due to local volume conservation, the direct experimental evidence was lacking before Zhang and Sharma used IDIOM protocols and analysis based on thin-film equation to capture of shape evolution of nanoridges and nanoridge-to-mesa instability.<sup>13-14, 45-46</sup> Zhang and Sharma<sup>45</sup> also showed that the ridge shape in build-up region (going outwards from the thinner domain) exhibits a quasi-steady shape. In contrast, in the leeward region, the shape evolution is captured by a similarity solution, based on thin film equation amended with an oscillatory disjoining pressure term,  $\Pi_{OS}(h)$  with periodicity matched with step size. The topography observed here is dictated by the free drainage from plane-parallel film into the meniscus that occurs at under the influence of capillary pressure, and is described in the creeping flow limit, avoiding the contributions of evaporation or Marangoni stresses on complex flows and fluxes associated with actively-squeezed thin films, evaporating films, deformed films, and films with active-withdrawal of the fluid.<sup>53-61</sup>

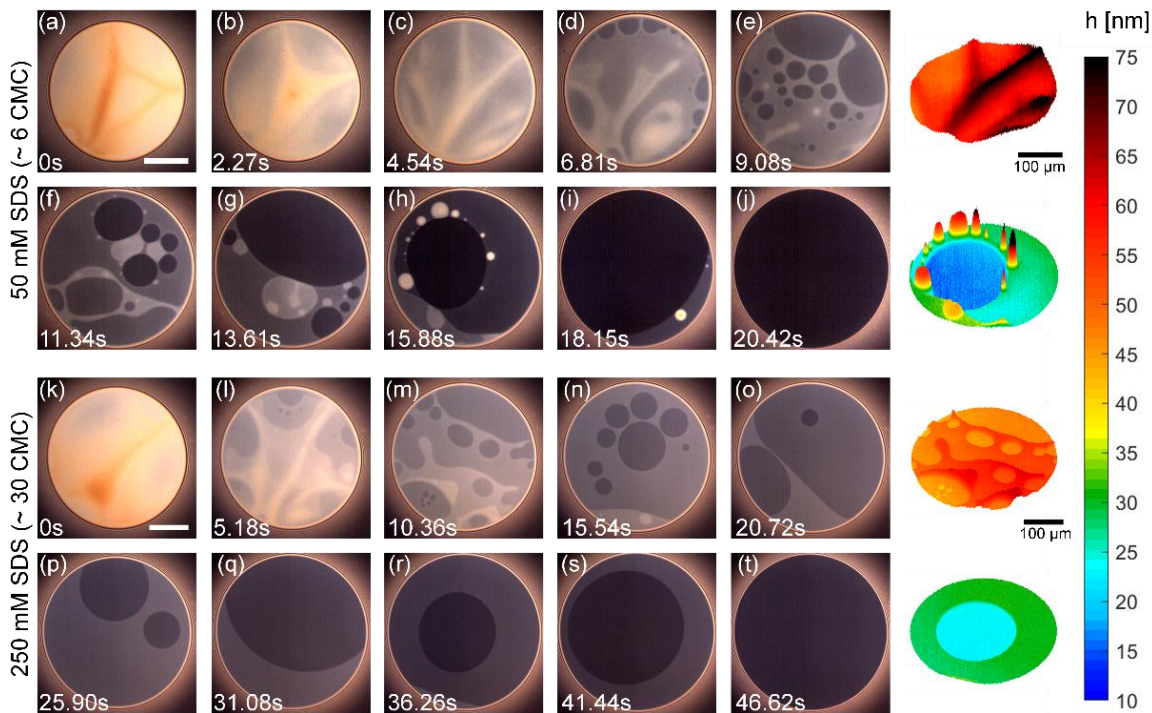


**Figure 2-2 Coexisting thick-thin regions in stratifying foam films made with 50 and 250 mM SDS solutions.** The grayscale snapshots for 50 mM SDS data included in (a) – (j) and for 250 mM SDS in (k) – (t) obtained using reflected-light imaging, and the corresponding thickness maps based on four images (c, h, m, and r) are obtained using IDIOM protocols. Images were acquired in Raw format to enable accurate determination of thickness maps (height is in nm, and the in-plane dimensions are in microns). The brightness and contrast of the grayscale snapshots are enhanced in ImageJ to discern distinct thickness regions easily. Snapshots included here show that the film drainage involves nucleation, growth, and coalescence of thinner, darker domains, as well as the appearance of brighter, white spots. Thickness maps show that domains are thinner, flat regions, whereas white spots can be non-flat and are labeled as mesas. The number of domains

nucleated decreases as the overall film thickness decreases, for example, notice the contrast between images (**m**) and (**r**).

### *Small-Angle X-Ray Scattering (SAXS) of Micellar SDS Solutions*

The background-subtracted one-dimensional SAXS data for the micellar solutions with SDS concentration,  $C_{SDS}$  ranging from 25 mM - 225 mM, are shown in Figure 2-3a. The overall scattering intensity,  $I(q)$  measured as a function of wave vector  $q$ , can be described as a product of a form factor  $P(q)$ , a structure factor  $S(q)$ , and the micelle volume fraction,  $\phi$  such that  $I(q) \propto P(q)S(q)$ . Micelle dimensions (shape and size) can be determined from form factor,  $P(q)$  whereas an analysis of the structure factor,  $S(q)$  reveals information about intermicellar interaction and correlations that depend on charge and micelle number density.<sup>62</sup> For SDS micelles, the hydrophobic core has a lower electron density than water, while the shell comprising the hydrophilic group and counter ions possesses a higher electron density than water. The combined influence of  $P(q)$ ,  $S(q)$ , and the scattering length density differences (between solvent and shell, and between shell and core) create distinct peaks and valleys in the X-ray scattering profiles of SDS micelles in contrast with the neutron scattering profiles.<sup>63</sup> An analysis of the features in  $I(q)$  and their corresponding length scale ( $\sim 1/q$ ) reveal that the  $I(q)$  peaks in the range  $1 \text{ nm}^{-1} < q < 3 \text{ nm}^{-1}$  emerge owing to the contribution of  $P(q)$ , whereas the peaks in the range  $\sim 0.4 \text{ nm}^{-1} < q < 1 \text{ nm}^{-1}$  are the contribution of  $S(q)$ . Upon increasing SDS concentration,  $P(q)$  peak shifts from  $q = 2 \text{ nm}^{-1}$  for  $C_{SDS} = 25 \text{ mM}$  to  $q = 1.7 \text{ nm}^{-1}$  for  $C_{SDS} = 60 \text{ mM}$ , signifying a marginal growth of micelle dimensions in solution. However, the  $P(q)$  peak position remains nearly  $C_{SDS}$ -invariant at  $q \sim 1.7 \text{ nm}^{-1}$  upon further increasing  $C_{SDS}$  up to 225 mM, denoting nearly concentration-independent micelle sizes. Concomitantly, the  $S(q)$  peak that appears in the  $q$  range  $0.4 \text{ nm}^{-1} < q < 1 \text{ nm}^{-1}$  becomes increasingly prominent as  $C_{SDS}$  increases due to the strengthening of intermicellar correlations with an increase in micellar number density,  $\rho \propto \phi$ . This  $S(q)$  peak also

shifts to higher  $q$  with increasing  $C_{SDS}$ , implying that the intermicellar distance,  $d$  decreases with concentration.

Fits to the scattering spectra,  $I(q) \sim \phi P(q)S(q)$  depicted in Figure 2-3a with solid lines were obtained by combining a  $P(q)$  model for oblate ellipsoidal core-shell micelles<sup>64-65</sup> with a  $S(q)$  model proposed by Hayter and Penfold<sup>64, 66-68</sup> based on rescaled mean spherical approximation (RMSA) for particles interacting with screened Coulomb repulsion. The  $P(q)$  fits reveal that SDS molecules self-assemble to form core-shell ellipsoids with the minor and the major axis radii  $R_p \sim 1.3$  nm and  $R_e \sim 2$  nm, respectively (an aspect ratio of  $\sim 0.65$ ) and a shell thickness  $\delta \sim 0.75$  nm (see Figure 2-3b), in good agreement with previous scattering studies on SDS micelles.<sup>43, 62-63, 69-70</sup> The computed values of total charge ( $Q < 30 e^-$ ) show that only a fraction of molecules is ionized. Micelle dimensions and computed charge are nearly independent of surfactant concentration for  $C_{SDS} \geq 60$  mM. The micelle volume fraction,  $\phi$  obtained from the structure factor fit, increases nearly linearly with  $C_{SDS}$ , as shown in Figure 2-3c.

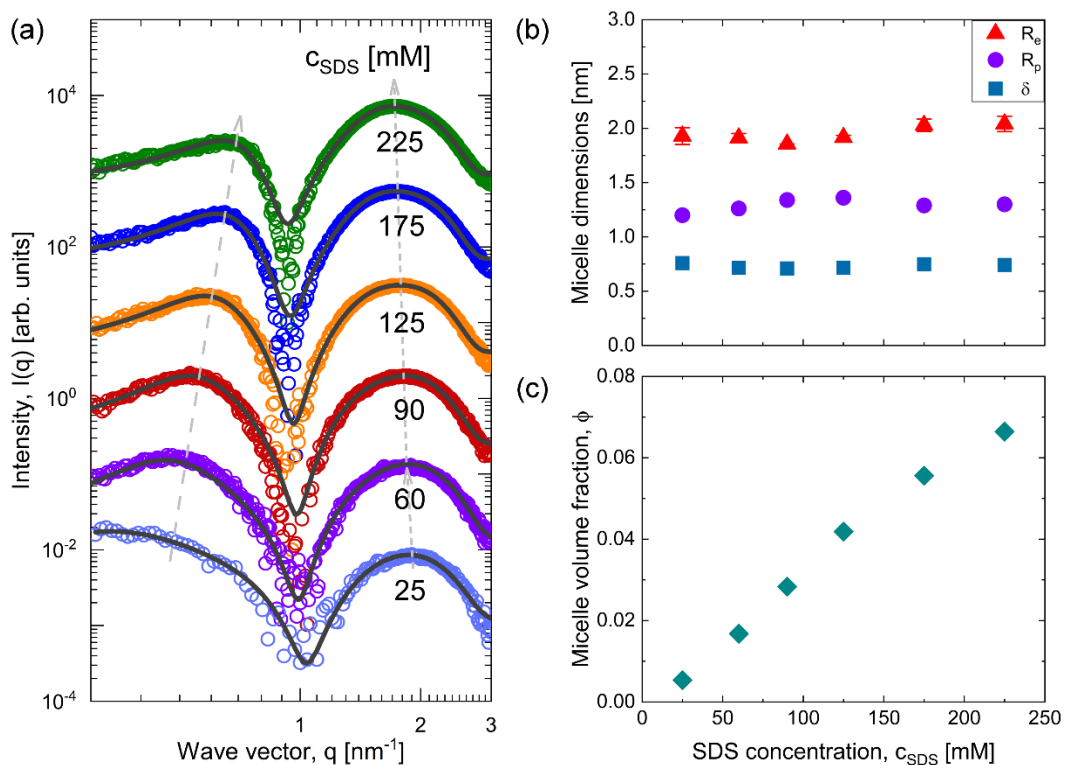


**Figure 2-3 Small angle X-ray scattering (SAXS) results and micelle characteristics.** (a) SAXS intensity patterns and the corresponding typical fits for aqueous SDS solutions with varying SDS concentrations. The fits use the form factor for oblate core-shell ellipsoids and the Hayter-Penfold structure factor, respectively. (b) Dimensions of the oblate SDS micelles: core radius along the major axis,  $R_e$  and core radius along the minor axis,  $R_p$  respectively, and shell thickness  $\delta$ . (c) Micelle volume fraction,  $\phi$ , is rather low ( $\phi < 0.1$ ) and is shown as a function of surfactant concentration,  $C_{SDS}$ .

*Comparison Between Step Size Obtained from Foam Stratification Studies and Intermicellar Distance Obtained from Scattering*

The structure factor,  $S(q)$ , extracted from the fits to  $I(q)$  data shown in Figure 2-4a for a range of SDS concentrations indicate that micelles are arranged in a disordered structure in bulk. The intermicellar correlations, correlated with the primary  $S(q)$  peak amplitude, strengthen with increased concentration. Estimates of intermicellar correlation distance, an indication of the average intermicellar distance,  $d$ , are obtained from the inverse of the position of the primary  $S(q)$  peak,  $q^*$ , as  $d = 2\pi/q^*$  (Figure 2-4a). The magnitude of  $q^*$  steadily increases with increasing  $C_{SDS}$ , denoting a decrease in correlation distance between micelles. The intermicellar distance,  $d$  estimated from the primary  $S(q)$  peaks, is found to be in excellent agreement with the step size,  $\Delta h = h_{n+1} - h_n$  obtained from stratification experiments using IDIOM protocols and both are found to display an inverse cubic root scaling  $\Delta h \propto C_{SDS}^{-\frac{1}{3}}$  and  $d \propto C_{SDS}^{-\frac{1}{3}}$  (denoted by dashed line), as shown in Figure 2-4b. The agreement suggests that even though confining interfaces in thin films lead to layering of micelles, the interactions between micelles and their number density are not different from the bulk solution. The schematics illustrate how micelles distribute themselves self-consistently in bulk (Figure 2-4a) and between interfaces under confinement (Figure 2-4b) for micelles interacting pairwise with screened Coulomb interactions (are not drawn to scale). In spite of these relatively low micelle volume fractions ( $\phi < 0.1$ ), micelles, together with their Debye atmosphere, structure under confinement analogously to confined hard spheres of higher effective size and volume fraction.<sup>2, 71-76</sup> However, as the viscosity depends on the real size and volume fraction of micelles, viscous resistance to drainage flows is not enhanced.<sup>4-5, 73-74</sup>

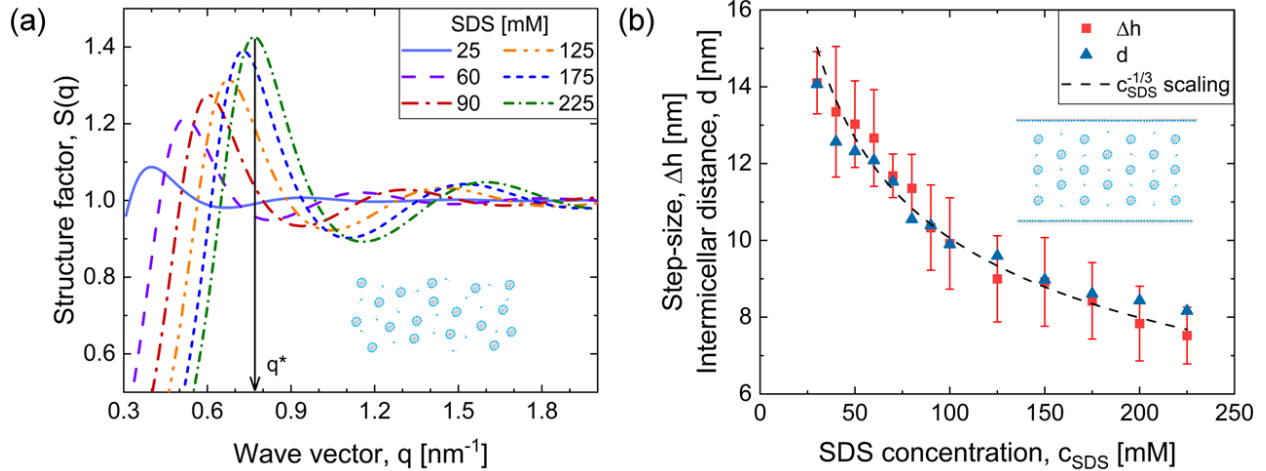


**Figure 2-4 Structure factor and concentration-dependent variation in step size and intermicellar distance.** (a) Structure factor,  $S(q)$  extracted using Hayter-Penfold model shows that the amplitude of the primary peak strengthens and peak position,  $q^*$  shifts to higher  $q$  with SDS concentration. (b) Step size obtained by analyzing stratification in micellar foam films using IDIOM protocols is compared to the intermicellar distance estimated from the inverse of the position of the primary  $S(q)$  peak  $q^*$ , as  $2\pi/q^*$ . Dashed line for  $-1/3$  power law correlates well with the concentration-dependent change in step size and intermicellar distance. Schematics illustrate the distribution of micelles in bulk solution and in the thin film, respectively.

### 2.2.2. Intermicellar Interactions in Bulk Aqueous Solutions and Thin Films: High Concentration Regime ( $C_{SDS} \leq 600$ mM)

The one-dimensional SAXS intensities  $I(q)$ , as a function of wave vector  $q$ , for a series of aqueous SDS solutions with SDS concentration  $C_{SDS}$  ranging from 100 mM to 600 mM ( $\sim 12CMC_{SDS} - \sim 72CMC_{SDS}$ ) are shown in Figure 2-5a. The SAXS spectra for a dispersion of scatterers can be described as a product of form and structure factor,  $I(q) \sim \phi P(q)S(q)$ , corresponding to the scattering contributions from individual scatterers and the spatial correlations between them. The intermediate- $q$  peak, corresponding to smaller length scales, signify the  $P(q)$  contributions and reveal information about the shape and size of the SDS self-assemblies, while the low- $q$  peak, corresponding to larger length scales, signify the  $S(q)$  contributions. The SAXS spectra for SDS solutions at low SDS concentrations ( $C_{SDS} < 300$  mM) exhibit distinct peaks in the low and intermediate  $q$  range ( $q < 0.9 \text{ nm}^{-1}$  and  $1.5 \text{ nm}^{-1} < q < 2.5 \text{ nm}^{-1}$ , respectively) separated by a sharp valley, indicating clear contributions from  $P(q)$  and  $S(q)$ . The dominant structure factor  $S(q)$  peaks starting at values  $q \sim 0.6 \text{ nm}^{-1}$  shifts to higher  $q$  values with increasing  $C_{SDS}$  till 300 mM

For solutions with  $C_{SDS} = 400 - 600$  mM, there is no noticeable peak in the  $q < 1 \text{ nm}^{-1}$  region where  $I(q)$  remains nearly flat. This infers that the shifting structure factor peak is located in the valley region  $q \sim 1 \text{ nm}^{-1}$ , following the shifting trend of  $S(q)$  peaks to higher  $q$  values with increase in  $C_{SDS}$ . A bulge appears at the  $q \sim 1.2 \text{ nm}^{-1}$  values of the primary form factor peak for  $C_{SDS} = 400$  mM, which likely indicates interference between the shifting structure factor peak with the form factor peaks. However, these  $S(q)$  bulges no longer shift between  $C_{SDS} = 500$  and 600 mM, indicating a constant intermicellar distances. With increasing  $C_{SDS}$  concentrations till 500 mM, almost flat intensity  $I(q)$  appear at low  $q$ , and at 600 mM  $C_{SDS}$   $I(q)$  at low  $q$  follows a

slightly steeper negative decay.<sup>69</sup> Although the data can be well fitted with an ellipsoidal form factor model, the slope of the intensity profiles for  $q < 0.5 \text{ nm}^{-1}$  becomes slightly negative at  $C_{SDS} = 600 \text{ mM}$ , indicating a transition from ellipsoidal to rod-like micelles between concentrations  $C_{SDS} = 500 \text{ mM}$  and  $C_{SDS} = 600 \text{ mM}$ . This implies that a minority of the micelles have acquired a cylindrical rod-like shape while the majority of micelles maintain the ellipsoidal morphology in the solution.

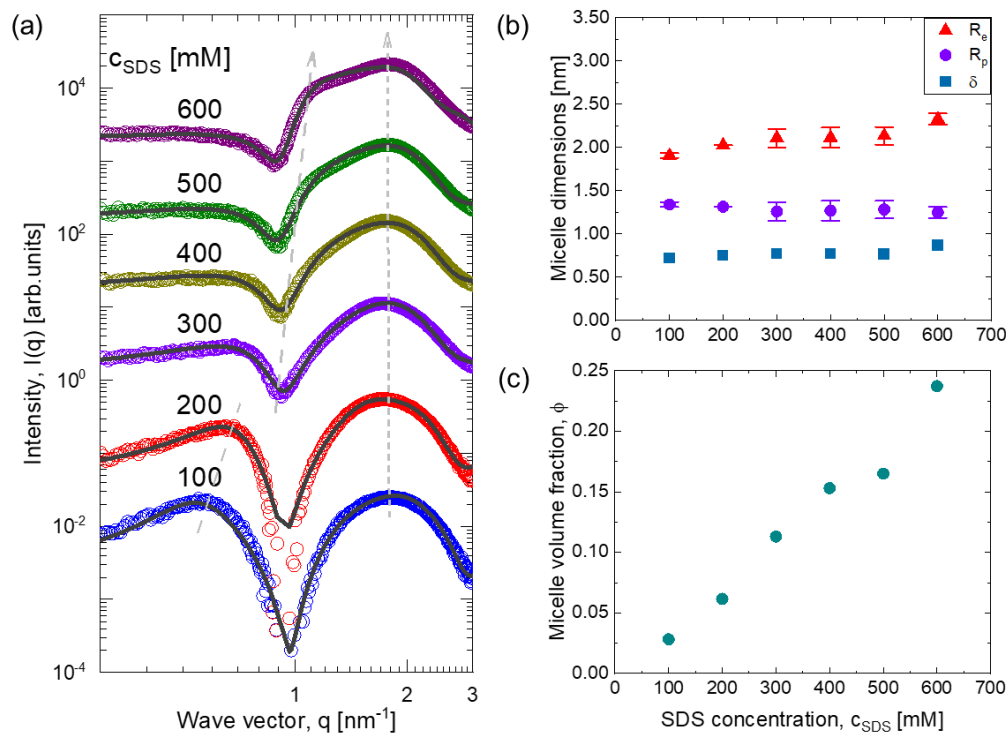


**Figure 2-5 Small Angle X-Ray Scattering (SAXS) measurements for  $C_{\text{SDS}} = 100 - 600$  mM solutions.** (a) SAXS intensity  $I$  as a function of wavevector  $q$ . Intensity patterns are shown in open circles and the corresponding fits are demonstrated in solid lines. The fits correspond to the form and structure factor models of oblate ellipsoids and Hayter-Penfold, respectively. The scattering profiles have been shifted vertically for clarity of viewing. Dashed lines indicate trend of structure and form factor peaks. (b) Micelle dimensions as a function of SDS concentration  $C_{\text{SDS}}$ : core radii along the major axis  $R_e$ , core radii along the minor axis  $R_p$ , and shell thickness  $\delta$ . (c) Micelle volume fraction  $\phi$  as a function of SDS concentration.

The micelle characteristics estimated from fits to the SAXS spectra show good agreement with previous reports in the literature.<sup>77-80</sup> The estimated micelle minor axis radius  $R_p \sim 1.3$  nm for  $C_{SDS} = 100$  and 200 mM match well with the micelle core radius obtained by Bezzobotnov, *et al.*<sup>77</sup> using SANS; the estimated total micelle radii  $R_e + \delta \sim 2.8$  nm for  $C_{SDS} = 300$  mM agree with those obtained by Putra and Ikram<sup>79</sup> using SANS. The estimated total micelle minor axis radius  $R_p + \delta$  values for  $C_{SDS} \leq 500$  mM agree with the total micelle radii with the SANS measurements by Itri and Amaral<sup>81</sup>, and the estimated total micelle minor axis radius  $R_p + \delta$  values for  $C_{SDS} = 300$  and 500 mM agree with the total micelle radii of SAXS measurements by Gubaidullin, *et al.*<sup>80</sup>. The Hayter-Penfold structure factor model fits indicate a monotonic increase in micelle volume fraction from  $\phi = 0.025$  to 0.25 for  $C_{SDS} = 100 - 600$  mM, as shown in Figure 2-5c. The slightly increasing micelle size and elongating micelle, coupled with the linearly increasing volume fraction and decreasing intermicellar distance with SDS concentration, influence the supramolecular oscillatory disjoining pressure in ultra-thin films, which determines metastable thicknesses, number of layers, and step size as a function of SDS concentration.

Figure 2-6a shows the structure factor  $S(q)$  as a function of wave vector  $q$  for six SDS concentrations  $C_{SDS}$  where each profile corresponds to the Hayter-Penfold model fits of the  $I(q)$  data. Each  $S(q)$  profile possesses two peaks, one at values  $q < 1.2$  nm<sup>-1</sup> and one at values  $q > 1.2$  nm<sup>-1</sup>. The intermicellar distance  $d$  is correlated with the inverse of the position of the primary  $S(q)$  peak (at  $q^*$ ) as  $d = 2\pi/q^*$ . The value of  $q^*$  increases from  $C_{SDS} = 100$  to 600 mM, which indicates a decreasing correlation distance  $d$  between micelles. Additionally, the height of the structure factor peak increases from  $C_{SDS} = 400 - 600$  mM, which suggests continuously strengthening intermicellar interactions. Figure 2-6b shows a plot of intermicellar distance  $d$  as a

function of SDS concentration  $C_{SDS}$ , which was measured by using SAXS protocols. The intermicellar distance  $d$  decreases from 10.5 to 6 nm with an increase in SDS concentration from  $C_{SDS} = 100$  to 600 mM.

Figure 2-6b also shows a plot of the step size  $\Delta h = h_{n+1} - h_n$  (except any  $h_1 - h_0$ ) as a function of SDS concentration obtained by using IDIOM protocols. The decrease in step size with SDS concentrations is due to the increasing screening of electrostatic interactions with increasing SDS concentration and corresponds to the decrease in the period of the supramolecular oscillatory disjoining pressure profile. The step size values for concentrations  $C_{SDS} \leq 375$  mM agree with the inverse cubic root scaling of  $\Delta h \propto C_{SDS}^{-\frac{1}{3}}$ , which is characteristic of random close packed spheres, while the step size values for concentrations  $C_{SDS} \geq 400$  mM have small deviation from  $\Delta h \propto C_{SDS}^{-\frac{1}{3}}$ . These deviations can be ascribed to the onset of the transition between spherical to rod-like micelles in SDS solutions at  $C_{SDS} \geq 500$  mM. Importantly, the intermicellar distance  $d$  values agree with those of step size, and with the relatively few intermicellar distance values calculated by other researchers<sup>77, 79-80</sup> with SAXS and SANS methods. Additionally, the intermicellar distance values vs. SDS concentration  $C_{SDS}$  agree with the inverse cubic root law of  $d \sim C_{SDS}^{-\frac{1}{3}}$ , characteristic of random close packed spheres. The correlation of intermicellar distance with step size even in the extended surfactant concentration range indicates that the electrostatic interactions among ionic micelles give rise to structure in bulk solutions, as well as to oscillatory structural disjoining pressure that influences foam film stability and topography.

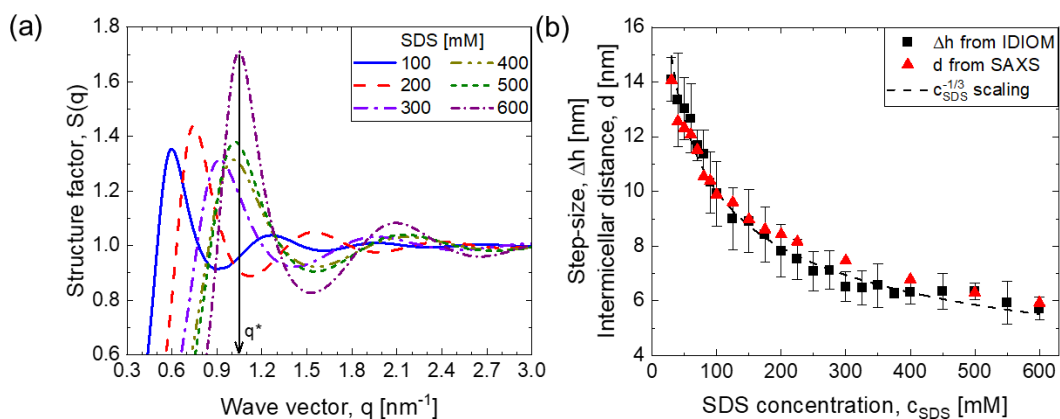


**Figure 2-6 Step size  $\Delta h$ , intermicellar distance  $d$ , and structure factor profiles as a function of SDS concentration  $C_{SDS}$ .** (a) Structure factor  $S(q)$  from Hayter-Penfold model as a function of the wave vector  $q$  for six SDS concentrations. The peak position  $q^*$  increases with SDS concentration,  $C_{SDS}$ . (b) Step size (with corresponding error bar) as a function of SDS concentration  $C_{SDS}$ , measured by using IDIOM protocols. Step size values have reasonable agreement with those in literature. The dashed line denotes the inverse cubic root power law  $\Delta h \propto C_{SDS}^{-\frac{1}{3}}$  fit, which is characteristic of random packed spheres. Intermicellar distance as a function of SDS concentration  $C_{SDS}$ , measured by using SAXS protocols. Values agree with those of step size in (b). The dashed line denotes the inverse cubic root power law  $\Delta h \propto C_{SDS}^{-\frac{1}{3}}$ .

### 2.3. DISCUSSION

The step size obtained from IDIOM protocols, shown in Figure 2-4 and 2-6 shows reasonable agreement with the values obtained using conventional interferometry studies.<sup>14</sup> Here step size is reported for an extended range of concentrations (as high as 600 mM or  $C_{SDS}/CMC_{SDS} \sim 75$ ). In contrast, most of the published studies were restricted to concentrations below 100 mM, except for three measurements, including a report by Krivchevsky and Stavans<sup>75-76</sup> and the 1971 dataset from Bruil and Lyklema that reported  $\Delta h \propto c_{soap}^{-\frac{1}{3}}$ . In the third dataset from 1984, Manev *et al.*<sup>82</sup> postulated that micellar SDS foam films stratify due to liquid crystallinity, following studies in the 1970s that found liquid crystals films display stratification.<sup>21, 83-86</sup> However, there is no evidence for the formation of liquid crystals either in bulk solutions or in stratified films, at low SDS concentrations investigated (including  $C_{SDS}/CMC_{SDS} < 5$ ). Furthermore, for a fixed surfactant concentration, Manev *et al.*<sup>82</sup> reported that the step size varies during progressive thinning. In our study, the step size is found to be relatively constant, consistent with the observations and analysis of Perrin,<sup>87-88</sup> Nikolov *et al.*,<sup>7-9</sup> and other published literature.<sup>7-20, 25-30, 44-47, 87-92</sup>

Though the existence of two black films was well-established by 1893,<sup>93</sup> Johannott first reported the existence of multiple blacks (as many as five) in 1906.<sup>92</sup> After that, Perrin observed stepwise thinning with constant step size and cited stratification as evidence for molecular reality in his Nobel lecture in 1926.<sup>87-88</sup> Even though the concepts underlying DLVO forces and the explanation for the two black films (NB and CB) emerged by the 1950s, a direct comparison between step size determined from stratification in micellar foam films and micellar dimensions and interactions remained unexplored before this study. Here we discuss the import of our contributions on the

longstanding debate between two mechanisms advanced for describing the thermodynamic and hydrodynamic phenomena that drive stratification in micellar foam films. (I) Step-wise thinning due to layer-by-layer removal of micelles from an “ordered colloidal crystal (OCC)” structure, with formation and growth of thinner, darker domains driven by diffusion of micelles and vacancies (“micelle-vacancy diffusion” or OCC mechanism), and increased viscosity of thinner films.<sup>7-9, 26-27, 29</sup> (II) Stratification governed by thin-film equation, the “hydrodynamic” mechanism, wherein bulk viscosity describes fluid behavior, and nanoscopic topography manifests due to an interplay of disjoining pressure and capillary pressure.

In several papers, Nikolov, Wasan, Kralchevsky, and coworkers<sup>7-9, 26-27, 29</sup> argued that ionic micelles undergo a phase transition to form ordered colloidal crystal phases in analogy with the phase transitions reported by Hachishu *et al.*<sup>94</sup> for charged latex particles. Formation of ordered phases by highly charged spheres at relatively low volume fractions compared to hard spheres is observed in innumerable studies<sup>95-99</sup> with evidence from Bragg diffraction,<sup>94</sup> scattering,<sup>97, 100-101</sup> microscopy (optical, total internal reflection and confocal),<sup>101-102</sup> among others. Since SDS micelles are relatively small, visualization of local microstructure using any optical microscopy techniques is ruled out, whereas small-angle X-ray scattering facilitates investigation of the micelle arrangements and correlations. In contrast to the ordered phases observed in charged sphere suspensions, scattering spectra and the corresponding structure factors for SDS solutions obtained in our small-angle X-ray scattering (SAXS) studies (see Figure 2-4a) do not show evidence of ordered colloidal (“micellar”) crystals, and instead indicate disordered micelle arrangements with strengthening intermicellar correlations with increasing  $C_{SDS}$ . Previously published SAXS and

SANS studies for SDS solutions (in the range of concentrations examined here) show a similar liquid-like structure comprising macroions (micelles) and their counterion cloud.<sup>67, 78, 80, 103-107</sup>

Nikolov *et al.*<sup>7-9, 26-27, 29</sup> assumed that interlayer spacing in films was less than the intermicellar distance in bulk and relied on the colloidal crystal picture to advance “micelle-vacancy diffusion” as a mechanism for stratification, arguing that domain expansion dynamics are governed by diffusion of micelles and vacancies. Furthermore, the cell-model used by Nikolov *et al.* model yields a series of disjoining pressures that arise due to the presence of certain layers of micelles, rather than generating a single, oscillatory structural disjoining pressure. Bergeron and Radke<sup>44</sup> first measured the oscillatory structural disjoining pressure,  $\Pi_{OS}(h)$  for SDS solutions and articulated that  $\Pi_{OS}(h)$  is a continuous function of thickness. Bergeron and Radke<sup>44</sup> also showed that the step size obtained from thickness-time plots (dynamic measurement) is correlated with the periodicity,  $\lambda$  measured for  $\Pi_{OS}(h)$  or the supramolecular oscillatory force, measured using a thin film balance. (equilibrium measurement). In contrast with the ordered colloidal crystal model, Bergeron, Jimenez-Laguna, and Radke<sup>44</sup> numerically solved the thin film equation with oscillatory disjoining pressure term included to capture initial domain expansion dynamics, and postulated that non-flat ridges form around growing domains due to mass conservation. Furthermore, Pollard and Radke<sup>74</sup> also showed *via* simulations that viscosity in micellar films is comparable to the bulk value (within 10%). However, using the thin film equation, Langevin and coworkers<sup>91</sup> argued that the domain expansion kinetics for stratifying films containing polyelectrolyte-surfactant complex is effectively determined by how quickly thickness changes diffuse away from a ridge and inferred film viscosity was 60 times higher than bulk viscosity. Recently, Lee, Nikolov and Wasan<sup>25, 89-90</sup>

reiterated the micelle vacancy-diffusion model and postulated that the viscosity of stratified films is itself thickness-dependent and higher than bulk viscosity (nearly by an order of magnitude).

Even though the hydrodynamic models assume or predict that nanoridge forms around a growing domain, characterization, and analysis of such non-flat structures began after the introduction of IDIOM protocols.<sup>13-14, 45-46</sup> The “micelle-vacancy diffusion” or “colloidal crystal” mechanism does not explain the appearance of ridges, observed as brighter halos around growing domains in greyscale images obtained using reflected light microscopy, or in some instances, subsequent appearance of bright circular spots at moving front between expanding domain and its thicker surroundings, identified to be relatively flat, pancake-like structures we called mesas. Though Lee *et al.*<sup>25</sup> utilized the micelle-vacancy diffusion model to discuss domain expansion dynamics, they invoke Rayleigh instability to describe mesa formation, thus ignoring or contradicting their arguments about thickness-dependent viscosity and interaction energy, and micelle-vacancy mechanism. Using IDIOM protocols and thin-film equation amended with disjoining pressure term, Zhang *et al.*<sup>13-14, 45-46</sup> recently showed that the size and shape evolution of non-flat regions including nanoridges and mesas is determined by the magnitude and periodicity of oscillatory structural contribution to disjoining pressure. The dynamics are indeed captured with the bulk viscosity values. Due to the presence of a thickness-dependent oscillatory disjoining pressure (or oscillatory free energy), the linear stability analysis predicts the possibility of a spinodal instability leading to the spontaneous emergence of mesh-like thick-thin regions driven purely by thin-film thermodynamics and hydrodynamics. Yilixiati *et al.*<sup>47</sup> showed that micellar foam films underwent such spinodal stratification and characterized the evolution of nanoscopic hills and gullies experimentally using IDIOM protocols. Thus, additional corroboration for the “hydrodynamic”

mechanism can be attributed to the self-consistent explanation for domain expansion, nanoridge formation, nanoridge-to-mesa instability, and spinodal stratification.<sup>13-15, 45-47</sup> However, as the hydrodynamic models involve a critical role for supramolecular oscillatory structural disjoining pressure contribution, we summarize the key progress made though the detailed studies of stratification.

As discussed in Chapter 1, two non-DLVO, medium-mediated interactions arise in multicomponent colloidal dispersions due to structuring of smaller molecules, nanoparticles, micelles, or solvent molecules between larger, dispersed particles, bubbles or drops: (i) depletion attraction caused by the depletion of smaller species from the confined region,<sup>6, 108-110</sup> and (ii) damped oscillatory structural disjoining pressure term,  $\Pi_{OS}(h)$  contributed by layering in the confined region<sup>4-5, 19, 30, 36, 108-112</sup>. For relatively short-ranged  $\Pi_{OS}(h)$ , called solvation forces, periodicity and decay length,  $\lambda = \xi = a$  are both set by the molecular size. Using equilibrium density functional theory, Pollard and Radke<sup>73</sup> showed that oscillatory contribution to disjoining pressure could be computed numerically by treating micelles as hard spheres and interactions between them with screened-Coulomb Yukawa-type interactions. Subsequently, Kralchevsky and Danov used Henderson's theory for bidisperse colloids made up of hard spheres with large size difference to derive an analytical formula for  $\Pi_{OS}(h)$  that depends on micelle number density and uses Carnahan-Starling compressibility factor computed using effective volume fraction (based on  $d_{eff}$ ).<sup>10, 28, 113</sup>

There are only a couple of experimental studies that attempt to characterize structure within micellar foam films directly, and these provide support for the intermicellar distance comparable to the stepsize. Krichevsky and Stavans<sup>75-76</sup> used static and dynamic light scattering, in addition to

reflectivity, and comparison with the bulk RMSA calculations to show that the micellar fluid behaves analogous to confined simple fluids, with a step size matched with intermicellar distance. Denkov *et al.*<sup>114</sup> found a lack of order in cryoelectron microscopy of vitrified micellar SDS foam films, even though latex particles formed nicely ordered arrays. Thus, the current state-of-the-art models for oscillatory structural contribution to disjoining pressure in foam films are based on liquid-state theory<sup>6, 15, 30, 73, 113, 115</sup>, and these models provide a quantitative analysis of the hydrodynamic processes underlying stratification using thin film equation.<sup>11, 13-14, 45-46</sup>

The close comparison of intermicellar distance and micelle dimensions determined using scattering with step size measured in foam film stratification studies reveals that the micellar solutions can be considered as (disordered) liquids in the concentration range explored here, though step-size appears to deviate marginally from the inverse cubic root law for concentrations  $C_{\text{SDS}} \geq 400$  mM. The corroboration from scattering datasets presented by Figures 2-4 and 2-6 implies that screened Coulomb interactions that describe intermicellar interactions in bulk solutions play the defining role in dictating drainage of foam films as well. The intermicellar distance and interactions present in foam films correlate with those in bulk solutions for aqueous SDS solutions. Thus, the comparison supports mechanistic description of stratification using hydrodynamic models that consider micellar solutions to be liquid-like and incorporate confinement-induced layering via  $\Pi_{OS}(h)$  term.<sup>11, 45-46, 91</sup> The thin-film equation amended with disjoining pressure provides a quantitative and self-consistent description of thickness transitions and variations observed with a high spatio-temporal resolution by IDIOM protocols.<sup>45-47</sup> In the concentration regime explored here for SDS solutions, micelle dimensions, surface tension, interfacial charge, and rheology are all nearly matched. Hence, the stratification studies reveal the

influence of amplitude and range of oscillatory disjoining pressure and underlying intermicellar interactions. Therefore, a concentration-dependent increase in the number of steps, observed in Figures 2-1 and 2-2, implies an increase in the magnitude of supramolecular oscillatory structural disjoining pressure. In contrast, a concentration-dependent decrease in step size can be correlated with the corresponding decrease in periodicity of  $\Pi_{OS}(h)$ . Analogous changes in the magnitude and the periodicity of oscillatory structural force,  $F(h)$  are obtained from SFA or CP-AFM measurements for nanoparticle dispersions and micellar solutions.<sup>4-5, 49-52, 76, 107, 109</sup>

## 2.4. CONCLUSIONS

In this chapter, we utilize foam film stratification studies in combination with small-angle X-ray scattering (SAXS) and address three longstanding, mechanistic questions about stratification in both low SDS concentration ( $25 \text{ mM} \leq C_{SDS} \leq 250 \text{ mM}$ ) and rarely studied high SDS concentration ( $250 \text{ mM} \leq C_{SDS} \leq 600 \text{ mM}$ ) regimes. First, we show that the step size,  $\Delta h$  obtained from foam film stratification studies is equal to the intermicellar distance,  $d$  determined using small-angle X-ray scattering (SAXS) in both concentration regimes. Step size obtained from discrete jumps in average thickness *vs.* time plots as well as from the difference in the thickness of flat regions are correlated with the periodicity of supramolecular oscillatory structural forces. Secondly, we find that the SAXS data does not provide any evidence for the formation of ordered colloidal crystals in the current whole SDS concentration range. The microstructure can be described using Hayter-Penfold liquid-state theory based on the rescaled mean spherical approximation (RMSA). We find that scattering datasets can be described using a model developed for scattering by a disordered suspension of charged spheres. The micelle dimensions (shape and size) remain nearly constant for the concentration range explored in this study. The comparison of scattering and stratification

studies presented here suggests that the electrostatic interactions between ionic micelles give rise to structure in bulk solutions, and oscillatory structural disjoining pressure (and structural forces) influence foam film stability and topography. The comparison also supports the mechanistic description of stratification using hydrodynamic models that consider micellar solutions to be liquid-like and utilize the thin film equation amended with disjoining pressure to quantitatively and self-consistently model thickness transitions and variations, observed with a high spatio-temporal resolution by IDIOM protocols. We anticipate that our results will facilitate the use of foam film stratification studies as a quick, frugal, and robust characterization of the strength and range of interactions between dispersed supramolecular structures, including micelles, macromolecules, and nanoparticles, especially in multicomponent complex fluids, and to provide insights into molecular engineering of formulations.

## **2.5. MATERIALS AND METHODS**

### *Materials*

Freestanding horizontal foam films and samples in quartz capillaries are composed of solutions of sodium dodecyl sulfate (SDS, Sigma-Aldrich Co., St. Louis, MO, L6026, >99.0%). The CMC of SDS is determined with maximum bubble pressure tensiometry and pendant drop tensiometry to be 8.2 mM. All solutions are prepared with deionized water of resistivity 18.2 M $\Omega$ ·cm.

### *IDIOM<sup>13-15, 45-46</sup> Protocols and Thin Film Balance*

Using a syringe pump to control the rate of flow out of a syringe, solution containing SDS is passed through a side-arm connected to an aperture on the side of a roughly 1.25 mm long and 1.6 mm internal diameter horizontal Scheludko-like cell (see Figure 2-1a) until an overhanging drop forms

in the cell. The solution is withdrawn until a plane-parallel region / thin liquid film forms, after which the film freely drains into its only surrounding Plateau border in a closed system. The drainage occurs under constant plane parallel film diameter,  $d_f$  constant cell diameter,  $d_c$  and, therefore, constant Laplace pressure  $P_c = 4\gamma d_c / (d_c^2 - d_f^2)$ , where  $\gamma$  is the surface tension value. A Fiilex P360EX portable LED light source provides roughly 4000K color temperature light to a Navitar Zoom 6000, containing a beam splitter and a 10x microscope objective, magnification system. The white light is directed by the beam splitter into the foam film, which reflects the interference intensity back through the magnification system, and focuses it into the photo-sensor array of a high-resolution, high-speed color camera (FASTCAM Mini UX100), which captures the pixel-wise measurements of spatio-temporal variation of the interference intensity  $I(x, y, \lambda, t)$  (see Figure 2-1a). Every pixel, that altogether give the color image, can be read as a combination of three intensities of red ( $\lambda = 620$  nm), green ( $\lambda = 540$  nm), and blue ( $\lambda = 470$  nm) light, with each intensity ranging from 0 – 4095 for a RAW image with a 12-bit depth. The film thickness  $h(x, y, \lambda, t)$  is obtained from IDIOM protocols, which rely on intensity maps  $I(x, y, \lambda, t)$  and on the interferometry equation

$$h = \left( \frac{\lambda}{2\pi n} \right) \arcsin \left( \sqrt{\frac{\Delta}{1 + \frac{4R(1-\Delta)}{(1-R)^2}}} \right)$$

where  $\lambda$  is the wavelength of light,  $\Delta = (I - I_{min}) / (I_{max} - I_{min})$ , the reflectivity is given by  $R = (n - 1)^2 / (n + 1)^2$ , the light reflected from the film is normal to the film surface, and the foam film gives zeroth order of light interference valid for films with thickness  $h < \frac{\lambda}{2\pi}$  or about  $h < 100$  nm in our case. Here  $I$  is the intensity value measured in each pixel of the high-speed color camera

sensor ( $x$  and  $y$  plane),  $I_{min}$  and  $I_{max}$  are the minimum and maximum intensity values, respectively, in each pixel over time  $t$ , and  $n$  is the refractive index of the SDS solution. We used the refractive index  $n = 1.33$  for all SDS solutions, which gives us an effective thickness  $h$ . The thicknesses separately measured for each of the three camera color channels are found to be in good agreement ( $< 1$  nm difference). The image analysis is completed in MATLAB with specifically developed codes. Using the IDIOM protocols, thickness maps of the foam film can be created, which possess high spatial (thickness  $< 1$  nm, lateral  $\sim 500$  nm) and temporal (up to 1000 fps) resolution.

#### *Intermicellar Distance and Micelle Dimensions using Small Angle X-Ray Scattering (SAXS)*

SAXS measurements were performed at beamline 12-ID-B at the Advanced Photon Source (APS) in Argonne National Laboratory. The solutions were placed in 2 mm thin-walled quartz capillary tubes (Charles Supper Company, Inc.) and were equilibrated at room temperature for at least 24 hours prior to the scattering experiments. The one-dimensional scattering intensity,  $I(q)$  was obtained from the azimuthal averaging of the two-dimensional scattering speckle data. Scattering from the solvent and capillary background was subtracted to obtain  $I(q)$  from the SDS self-assemblies in the solution as a function of the wave vector  $q = \frac{4\pi \sin \theta}{\lambda}$  ranging from  $q = 0.3 - 3$  nm<sup>-1</sup>. Here,  $2\theta$  is the angle between the incident beam and the detector and  $\lambda$  is the wavelength of the radiation. As the intensity,  $I(q)$  profile depends on the structure factor,  $S(q)$  set by intermicellar interference and the form factor,  $P(q)$  set by intramicellar interference. The structural and micelle characteristics are obtained by fitting the product  $\phi P(q)S(q)$  to the experimental  $I(q)$  data using custom written scripts in MATLAB provided as follows.

$P(q)$  is expressed as  $P(q) \sim (1/V_{total})F^2(q)$ , with  $V_{total}$  being the micelle volume and  $F(q) = \iiint dV \rho(r) e^{-iqr}$ ,  $\rho(r)$  being the scattering length density at a point  $r$  in space. For core-shell assemblies like the SDS micelles are expected to form,

$$F^2(q) = \int_0^{\pi/2} [(\rho_s - \rho_{solvent})V_{total}\Phi(q, \alpha, R_e + \delta, R_p + \delta) + (\rho_c - \rho_s)V_c\Phi(q, \alpha, R_1, R_2, \dots)]^2 \sin \alpha d\alpha$$

$$\Phi(q, \alpha, R_e + \delta, R_p + \delta) = 3 \frac{\sin(qR_0) - (qR_0) \cos(qR_0)}{(qR_0)^3}$$

$$R_0 = \sqrt{(R_e + \delta)^2 \sin^2 \alpha + (R_p + \delta)^2 \cos^2 \alpha}$$

with  $\rho_c$ ,  $\rho_s$  and  $\rho_{solvent}$  being the scattering length densities of the core, shell and solvent, respectively,  $V_c$  being the volume of the core,  $R_e, R_p$  being the equatorial radius and polar radius respectively,  $\delta$  being the thickness of the shell, and  $\alpha$  being the angle of orientation for anisotropic particles. With averaging over all randomly oriented micelles in the system, an integration over an orientation variable which is equal to the cosine of the angle between scattering vector  $q$ , and the equatorial axis.

The structure factor  $S(q)$  describes the interscatterer (intermicellar) interactions and is related to the pair-correlation function  $g(r)$  as  $S(q) = 1 + 4\pi n \int_0^\infty [g(r) - 1] r^2 \frac{\sin qr}{qr} dr$ , with  $n$  being the micelle number density and  $r$  being the position vector.<sup>116</sup>  $S(q)$  is unity at sufficiently dilute concentrations where the interactions between scatterers (micelles) are sufficiently weak, and the scattering intensity contains contribution from the form factor only. With growing scatterer concentrations, however, the influence of interscatterer interactions manifest as non-unity structure factors. Interactions between ionic surfactant micelles are described adequately by the structure

factor model proposed by Hayter and Penfold,  $S_{HP}(q)$ , by combining the Ornstein-Zernike equation with the rescaled mean spherical approximation (RMSA) closure relation.<sup>66, 68</sup>  $S_{HP}(q)$  depends on the effective micelle radius, volume fraction and total charge of the micelles, as well as on dielectric constant and ionic strength of the medium and temperature.

Hydrophobic dodecyl chains make up the core of the SDS micelles while the shell consists of the hydrophilic ionic head ( $\text{SO}_3^-$ ) and the coupled counter ions.  $\rho_c$  and  $\rho_s$  both can be calculated from the atomic number and molar volume of the corresponding components and treated as constants during the fitting process using the following equation  $\rho_i = \sum_{i=1}^j \frac{Z_i r_T}{V_m}$  where  $Z_i$  is the atomic number of the  $i$ th of  $j$  atoms in a molecule of molecular volume  $V_m$ , and  $r_T$  is the Thomson scattering length ( $2.8179 \times 10^{-15}$  m, classical electron radius),  $\rho_c$  and  $\rho_s$  are thus calculated as  $7.963 \times 10^{-6} \text{ \AA}^{-2}$  and  $10.81 \times 10^{-6} \text{ \AA}^{-2}$ , respectively.  $\rho_{solvent}$  is  $9.469 \times 10^{-6} \text{ \AA}^{-2}$ .<sup>66, 68</sup> It must be noted here that in calculation of  $\rho_s$ , the nearest  $-\text{CH}_2$  group of the dodecyl chain was assumed to be attached to the sulphate head group. Further, the shell of the micelles formed by the ionic head groups and counter ions have a higher electron density than the aqueous surrounding, which is in turn higher than the hydrophobic core possessing the lowest electron density.

Several software packages are available for fitting of small-angle scattering data. However, none of them allow for (i) the adjustment of the  $R_{eff}$  in the structure factor depending on the micelle shape for non-spherical micelles (ex. for ellipsoid micelles  $R_{eff} = \sqrt{(R_e + \delta)(R_p + \delta)}$ ,  $R_1$ ,  $R_2$  and  $\delta$  being core major and minor axes and shell thickness, respectively), or (ii) for concomitant and/or sequential fitting of scattering data as will be required in this proposed research. Hence, fitting routines are developed as a fundamental ground of this chapter used to obtain a complete control on the data fitting methodology. All 1-D SAXS data shown in this chapter are fitted using

a MATLAB code I have developed.  $P(q)$  and  $S(q)$  is calculated for a given set of initial guesses for the parameters, and the resulting  $I_{fit}(q)$  is based on linear regression fitted the experimental data  $I(q)$ . The root means square error between  $I(q)$  and  $I_{fit}(q)$  is calculated and minimized using the `fmincon` subroutine in MATLAB.

## 2.6 REFERENCES

1. Israelachvili, J. N., *Intermolecular and surface forces*. Academic press: 2015.
2. Israelachvili, J.; Ruths, M., Brief history of intermolecular and intersurface forces in complex fluid systems. *Langmuir* **2013**, *29* (31), 9605-19.
3. Derjaguin, B. V.; Churaev, N. V.; Muller, V. M., *Surface Forces*. Springer: New York, 1987.
4. Ludwig, M.; Witt, M. U.; von Klitzing, R., Bridging the gap between two different scaling laws for structuring of liquids under geometrical confinement. *Adv Colloid Interface Sci* **2019**, *269*, 270-276.
5. Ludwig, M.; von Klitzing, R., Progress in measurements of oscillatory forces and liquid properties under confinement. *Current Opinion in Colloid & Interface Science* **2020**.
6. Trokhymchuk, A.; Henderson, D., Depletion forces in bulk and in confined domains: From Asakura–Oosawa to recent statistical physics advances. *Current Opinion in Colloid and Interface Science* **2015**, *20* (1), 32-38.
7. Nikolov, A. D.; Wasan, D. T.; Kralchevsky, P. A.; Ivanov, I. B. In *Ordered structures in thinning micellar foam and latex films*, Ordering and Organisation in Ionic Solutions, Kyoto, Japan, Sogami, N. I. a. I., Ed. World Scientific, Singapore: Kyoto, Japan, 1988; pp 302-414.
8. Nikolov, A. D.; Wasan, D. T., Ordered micelle structuring in thin films formed from anionic surfactant solutions: I. Experimental. *Journal of Colloid and Interface Science* **1989**, *133* (1), 1-12.

9. Nikolov, A. D.; Kralchevsky, P. A.; Ivanov, I. B.; Wasan, D. T., Ordered micelle structuring in thin films formed from anionic surfactant solutions: II. Model development. *J. Colloid Interface Sci.* **1989**, *133* (1), 13-22.
10. Anachkov, S. E.; Danov, K. D.; Basheva, E. S.; Kralchevsky, P. A.; Ananthapadmanabhan, K. P., Determination of the aggregation number and charge of ionic surfactant micelles from the stepwise thinning of foam films. *Adv Colloid Interface Sci* **2012**, *183-184*, 55-67.
11. Bergeron, V.; Jimenez-Laguna, A. I.; Radke, C. J., Hole formation and sheeting in the drainage of thin liquid films. *Langmuir* **1992**, *8* (12), 3027-3032.
12. Langevin, D.; Sonin, A. A., Thinning of soap films. *Advances in Colloid and Interface Science* **1994**, *51*, 1-27.
13. Zhang, Y.; Sharma, V., Domain expansion dynamics in stratifying foam films: experiments. *Soft Matter* **2015**, *11* (22), 4408-17.
14. Zhang, Y.; Yilixiati, S.; Pearsall, C.; Sharma, V., Nanoscopic Terraces, Mesas, and Ridges in Freely Standing Thin Films Sculpted by Supramolecular Oscillatory Surface Forces. *ACS Nano* **2016**, *10* (4), 4678-83.
15. Yilixiati, S.; Rafiq, R.; Zhang, Y.; Sharma, V., Influence of Salt on Supramolecular Oscillatory Structural Forces and Stratification in Micellar Freestanding Films. *ACS Nano* **2018**, *12* (2), 1050-1061.

16. Lalchev, Z.; Todorov, R.; Exerowa, D., Thin liquid films as a model to study surfactant layers on the alveolar surface. *Current Opinion in Colloid and Interface Science* **2008**, *13* (3), 183-193.
17. Beltramo, P. J.; Vermant, J., Simple optical imaging of nanoscale features in free-standing films. *ACS Omega* **2016**, *1* (3), 363-370.
18. Beltrán, C. M.; Langevin, D., Stratification kinetics of polyelectrolyte solutions confined in thin films. *Physical review letters* **2005**, *94* (21), 217803.
19. Von Klitzing, R.; Thormann, E.; Nylander, T.; Langevin, D.; Stubenrauch, C., Confinement of linear polymers, surfactants, and particles between interfaces. *Advances in colloid and interface science* **2010**, *155* (1-2), 19-31.
20. Basheva, E. S.; Danov, K. D.; Kralchevsky, P. A., Experimental Study of Particle Structuring in Vertical Stratifying Films from Latex Suspensions. *Langmuir* **1997**, *13* (16), 4342-4348.
21. Oswald, P.; Pieranski, P., *Smectic and columnar liquid crystals: concepts and physical properties illustrated by experiments*. CRC Press: 2005.
22. Mysels, K. J.; Frankel, S.; Shinoda, K., *Soap films: Studies of their Thinning and a Bibliography*. Pergamon Press: 1959.
23. Gochev, G.; Platikanov, D.; Miller, R., Chronicles of foam films. *Adv Colloid Interface Sci* **2016**, *233*, 115-125.

24. Cantat, I.; Cohen-Addad, S.; Elias, F.; Graner, F.; Höhler, R.; Pitois, O., *Foams: Structure and Dynamics*. Oxford University Press: 2013.
25. Lee, J.; Nikolov, A.; Wasan, D., Stepwise thinning dynamics of a foam film formed from an anionic micellar solution. *J Colloid Interface Sci* **2017**, *487*, 217-222.
26. Kralchevski, P.; Nikolov, A.; Wasan, D. T.; Ivanov, I., Formation and expansion of dark spots in stratifying foam films. *Langmuir* **2002**, *6* (6), 1180-1189.
27. Wasan, D. T.; Nikolov, A. D.; Kralchevsky, P. A.; Ivanov, I. B., Universality in film stratification due to colloid crystal formation. *Colloids and Surfaces* **1992**, *67*, 139-145.
28. Danov, K. D.; Basheva, E. S.; Kralchevsky, P. A.; Ananthapadmanabhan, K. P.; Lips, A., The metastable states of foam films containing electrically charged micelles or particles: experiment and quantitative interpretation. *Adv Colloid Interface Sci* **2011**, *168* (1-2), 50-70.
29. Wasan, D.; Nikolov, A., Thin liquid films containing micelles or nanoparticles. *Current Opinion in Colloid & Interface Science* **2008**, *13* (3), 128-133.
30. Kralchevsky, P. A.; Danov, K. D.; Denkov, N. D., Chemical physics of colloid systems and interfaces. In *Handbook of Surface and Colloid Chemistry*, 2nd ed.; Birdi, K. S., Ed. CRC Press New York, 1997; Vol. 2.
31. Fennell Evans, D.; Wennerström, H., *The Colloidal Domain: Where Physics, Chemistry, Biology, and Technology Meet*. 2nd ed.; Wiley-VCH: New York: 1999.

32. Ferreira, A.; Vecino, X.; Ferreira, D.; Cruz, J. M.; Moldes, A. B.; Rodrigues, L. R., Novel cosmetic formulations containing a biosurfactant from *Lactobacillus paracasei*. *Colloids Surf B Biointerfaces* **2017**, *155*, 522-529.
33. Bai, L.; Huan, S.; Gu, J.; McClements, D. J., Fabrication of oil-in-water nanoemulsions by dual-channel microfluidization using natural emulsifiers: Saponins, phospholipids, proteins, and polysaccharides. *Food Hydrocolloids* **2016**, *61*, 703-711.
34. Vecino, X.; Cruz, J. M.; Moldes, A. B.; Rodrigues, L. R., Biosurfactants in cosmetic formulations: trends and challenges. *Crit Rev Biotechnol* **2017**, *37* (7), 911-923.
35. Sheludko, A., Thin liquid films. *Advances in Colloid and Interface Science* **1967**, *1* (4), 391-464.
36. Bergeron, V., Forces and structure in thin liquid soap films. *Journal of Physics: Condensed Matter* **1999**, *11* (19), R215-R238.
37. Weaire, D. L.; Hutzler, S., *The Physics of Foams*. Oxford University Press: 1999.
38. Radke, C. J., Film and membrane-model thermodynamics of free thin liquid films. *J Colloid Interface Sci* **2015**, *449*, 462-79.
39. de Gennes, P. G.; Brochard-Wyart, F.; Quéré, D., *Capillarity and Wetting Phenomena: Drops, Bubbles, Pearls, Waves*. Springer-Verlag: New York, 2004.
40. Kalliadasis, S.; Thiele, U., *Thin Films of Soft Matter*. SpringerWien NewYork: 2007.

41. Lutz-Bueno, V.; Liebi, M.; Kohlbrecher, J.; Fischer, P., Intermicellar interactions and the viscoelasticity of surfactant solutions: Complementary use of SANS and SAXS. *Langmuir* **2017**, *33* (10), 2617-2627.
42. Dreiss, C. A., Wormlike micelles: where do we stand? Recent developments, linear rheology and scattering techniques. *Soft Matter* **2007**, *3* (8), 956-970.
43. Reiss-Husson, F.; Luzzati, V., The structure of the micellar solutions of some amphiphilic compounds in pure water as determined by absolute small-angle X-ray scattering techniques. *Journal of Physical Chemistry* **1964**, *68* (12), 3504-3511.
44. Bergeron, V.; Radke, C. J., Equilibrium measurements of oscillatory disjoining pressures in aqueous foam films. *Langmuir* **1992**, *8* (12), 3020-3026.
45. Zhang, Y.; Sharma, V., Nanoridge Formation and Dynamics of Stratification in Micellar Freestanding Films. *Langmuir* **2018**, *34* (3), 1208-1217.
46. Zhang, Y.; Sharma, V., Thickness-Dependent Phase Transition Drives Nanoridge-to-Mesa Instability in Micellar Freestanding Films. *Langmuir* **2018**, *34* (26), 7922-7931.
47. Yilixiati, S.; Wojcik, E.; Zhang, Y.; Sharma, V., Spinodal stratification in ultrathin micellar foam films. *MSDE* **2019**, *4* (3), 626-638.
48. Bruil, H. G.; Lyklema, J., Stratification in Free Liquid Films. *Nature Physical Science* **1971**, *233* (36), 19-20.

49. Klapp, S. H. L.; Grandner, S.; Zeng, Y.; von Klitzing, R., Asymptotic structure of charged colloids between two and three dimensions: the influence of salt. *Journal of Physics: Condensed Matter* **2008**, *20* (49), 494232.
50. Klapp, S. H. L.; Grandner, S.; Zeng, Y.; von Klitzing, R., Charged silica suspensions as model materials for liquids in confined geometries. *Soft Matter* **2010**, *6* (10), 2330.
51. Zeng, Y.; Grandner, S.; Oliveira, C. L. P.; Thünemann, A. F.; Paris, O.; Pedersen, J. S.; Klapp, S. H. L.; von Klitzing, R., Effect of particle size and Debye length on order parameters of colloidal silica suspensions under confinement. *Soft Matter* **2011**, *7* (22), 10899.
52. Zeng, Y.; Schon, S.; von Klitzing, R., Silica nanoparticle suspensions under confinement of thin liquid films. *J Colloid Interface Sci* **2015**, *449*, 522-9.
53. Chatzigiannakis, E.; Vermant, J., Breakup of Thin Liquid Films: From Stochastic to Deterministic. *Phys Rev Lett* **2020**, *125* (15), 158001.
54. Chatzigiannakis, E.; Jaensson, N.; Vermant, J., Thin Liquid Films: where Hydrodynamics, Capillarity, Surface Stresses, and Intermolecular Forces meet. *Current Opinion in Colloid & Interface Science* **2021**, 101441.
55. Suja, V. C.; Rodríguez-Hakim, M.; Tajuelo, J.; Fuller, G. G., Single bubble and drop techniques for characterizing foams and emulsions. *Advances in Colloid and Interface Science* **2020**, 102295.

56. Chandran Suja, V.; Hadidi, A.; Kannan, A.; Fuller, G., Axisymmetry breaking, chaos, and symmetry recovery in bubble film thickness profiles due to evaporation-induced Marangoni flows. *Physics of Fluids* **2021**, *33* (1), 012112.
57. Chevallier, E.; Saint-Jalmes, A.; Cantat, I.; Lequeux, F.; Monteux, C., Light induced flows opposing drainage in foams and thin-films using photosurfactants. *Soft Matter* **2013**, *9* (29), 7054.
58. Suja, V. C.; Kar, A.; Cates, W.; Remmert, S. M.; Savage, P. D.; Fuller, G. G., Evaporation-induced foam stabilization in lubricating oils. *Proceedings of the National Academy of Sciences* **2018**, *115* (31), 7919-7924.
59. Bussonnière, A.; Shabalina, E.; Ah-Thon, X.; Le Fur, M.; Cantat, I., Dynamical coupling between connected foam films: Interface transfer across the menisci. *Physical review letters* **2020**, *124* (1), 018001.
60. Champougny, L.; Miguet, J.; Henaff, R.; Restagno, F.; Boulogne, F.; Rio, E., Influence of Evaporation on Soap Film Rupture. *Langmuir* **2018**, *34* (10), 3221-3227.
61. Andrieux, S.; Muller, P.; Kaushal, M.; Macias Vera, N. S.; Bollache, R.; Honorez, C.; Cagna, A.; Drenckhan, W., Microfluidic thin film pressure balance for the study of complex thin films. *Lab Chip* **2021**, *21* (2), 412-420.
62. Hammouda, B., Temperature Effect on the Nanostructure of SDS Micelles in Water. *J Res Natl Inst Stand Technol* **2013**, *118*, 151-67.

63. Gawali, S. L.; Zhang, M.; Kumar, S.; Ray, D.; Basu, M.; Aswal, V. K.; Danino, D.; Hassan, P. A., Discerning the Structure Factor of Charged Micelles in Water and Supercooled Solvent by Contrast Variation X-ray Scattering. *Langmuir* **2019**, *35* (30), 9867-9877.
64. Kotlarchyk, M.; Chen, S. H., Analysis of small angle neutron scattering spectra from polydisperse interacting colloids. *Journal of Chemical Physics* **1983**, *79* (5), 2461-2469.
65. Berr, S. S., Solvent isotope effects on alkytrimethylammonium bromide micelles as a function of alkyl chain length. *Journal of Physical Chemistry* **1987**, *91* (18), 4760-4765.
66. Hayter, J. B.; Penfold, J., An analytic structure factor for macroion solutions. *Molecular Physics* **1981**, *42* (1), 109-118.
67. Hayter, J., B; Penfold, J., Determination of micelle structure and charge by neutron small-angle scattering. *Colloid and Polymer Science* **1983**, *261* (12), 1022-1030.
68. Hansen, J.-P.; Hayter, J. B., A rescaled MSA structure factor for dilute charged colloidal dispersions. *Molecular Physics* **1982**, *46* (3), 651-656.
69. Schäfer, K.; Kolli, H. B.; Killingmoe Christensen, M.; Bore, S. L.; Diezemann, G.; Gauss, J.; Milano, G.; Lund, R.; Cascella, M., Supramolecular Packing Drives Morphological Transitions of Charged Surfactant Micelles. *Angewandte Chemie International Edition* **2020**.
70. Jensen, G. V.; Lund, R.; Gummel, J.; Narayanan, T.; Pedersen, J. S., Monitoring the transition from spherical to polymer-like surfactant micelles using small-angle X-ray scattering. *Angewandte Chemie* **2014**, *126* (43), 11708-11712.

71. Tarazona, P., Free-energy density functional for hard spheres. *Physical Review A* **1985**, *31* (4), 2672.
72. Bitsanis, I. T. K. M.; Vanderlick, T. K.; Tirrell, M.; Davis, H. T., A tractable molecular theory of flow in strongly inhomogeneous fluids. *Journal of chemical physics* **1988**, *89* (5), 3152-3162.
73. Pollard, M. L.; Radke, C. J., Density-functional modeling of structure and forces in thin micellar liquid films. *J. Chemical Physics* **1994**, *101* (8), 6979-6991.
74. Pollard, M. L.; Radke, C. J., Effective viscosities in thin ionic micellar liquid films. *AICHE journal* **1996**, *42* (7), 2005-2013.
75. Krichevsky, O.; Stavans, J., Micellar Stratification in Soap Films: A Light Scattering Study. *Phys Rev Lett* **1995**, *74* (14), 2752-2755.
76. Krichevsky, O.; Stavans, J., Confined fluid between two walls: The case of micelles inside a soap film. *Physical Review E* **1997**, *55* (6), 7260.
77. Bezzobotnov, V. Y.; Borbely, S.; Cser, L.; Farago, B.; Gladkih, I.; Ostanevich, Y. M.; Vass, S., Temperature and Concentration Dependence of Properties of Sodium Dodecyl Sulfate Micelles Determined from Small Angle Neutron Scattering Experiments. *The Journal of Physical Chemistry* **1988**, *92* (20), 5738-5743.
78. Itri, R.; Amaral, L. Q.; Mariani, P., Structure of the hexagonal phase of the sodium dodecyl sulfate and water system. *Phys Rev E Stat Phys Plasmas Fluids Relat Interdiscip Topics* **1996**, *54* (5), 5211-5216.

79. Putra, E. G. R.; Ikram, A., Nanosize structure of self-assembly sodium dodecyl sulfate: A study by small angle neutron scattering (SANS). *Indonesian Journal of Chemistry* **2006**, *6* (2), 117-120.
80. Gubaidullin, A. T.; Litvinov, I. A.; Samigullina, A. I.; Zueva, O. S.; Rukhlov, V. S.; Idiyatullin, B. Z.; Zuev, Y. F., Structure and dynamics of concentrated micellar solutions of sodium dodecyl sulfate. *Russian Chemical Bulletin* **2016**, *65* (1), 158-166.
81. Itri, R.; Amaral, L., Study of the isotropic-hexagonal transition in the system sodium dodecyl sulfate/water. *Journal of Physical Chemistry* **1990**, *94* (5), 2198-2202.
82. Manev, E. D.; Sazdanova, S. V.; Wasan, D. T., Emulsion and foam stability—The effect of film size on film drainage. *Journal of Colloid and Interface Science* **1984**, *97* (2), 591-594.
83. Friberg, S.; LINDEN, S. E.; Saito, H., Thin films from liquid crystals. *Nature* **1974**, *251* (5475), 494.
84. Young, C. Y.; Pindak, R.; Clark, N. A.; Meyer, R. B., Light-scattering study of two-dimensional molecular-orientation fluctuations in a freely suspended ferroelectric liquid-crystal film. *Physical Review Letters* **1978**, *40* (12), 773.
85. Sirota, E. B.; Pershan, P. S.; Sorensen, L. B.; Collett, J., X-ray and optical studies of the thickness dependence of the phase diagram of liquid-crystal films. *Phys Rev A Gen Phys* **1987**, *36* (6), 2890-2901.
86. Manev, E.; Proust, J. E.; Ter-Minassian-Saraga, L., Structural disjoining pressure in thin films of liquid crystals. *Colloid and Polymer Science* **1977**, *255* (11), 1133-1135.

87. Perrin, J., La stratification des lames liquides. *Annales de Physique (Paris)* **1918**, *10*, 160-184.
88. Perrin, J., Nobel Prize Lecture. Stockholm: 1928.
89. Lee, J.; Nikolov, A.; Wasan, D., Stratification of a Foam Film Formed from a Nonionic Micellar Solution: Experiments and Modeling. *Langmuir* **2016**, *32* (19), 4837-47.
90. Lee, J.; Nikolov, A.; Wasan, D., Stepwise dynamics of an anionic micellar film—Formation of crown lenses. *Journal of Colloid and Interface Science* **2017**, *496*, 60-65.
91. Heinig, P.; Beltran, C. M.; Langevin, D., Domain growth dynamics and local viscosity in stratifying foam films. *Phys Rev E Stat Nonlin Soft Matter Phys* **2006**, *73* (5 Pt 1), 051607.
92. Johonnott, E. S., LXVIII. The black spot in thin liquid films. *The London, Edinburgh, and Dublin Philosophical Magazine and Journal of Science* **2009**, *11* (66), 746-753.
93. Reinold, A. W.; Rucker, A. W., On the thickness and electrical resistance of thin liquid films. *Proceedings of the Royal Society of London* **1893**, *53* (321-325), 394-398.
94. Hachisu, S.; Kobayashi, Y.; Kose, A., Phase separation in monodisperse latexes. *Journal of Colloid and Interface Science* **1973**, *42* (2), 342-348.
95. Robbins, M. O.; Kremer, K.; Grest, G. S., Phase diagram and dynamics of Yukawa systems. *Journal of Chemical Physics* **1988**, *88* (5), 3286-3312.
96. Pieranski, P., Colloidal crystals. *Contemporary Physics* **1983**, *24* (1), 25-73.
97. Monovoukas, Y.; Gast, A. P., The experimental phase diagram of charged colloidal suspensions. *Journal of colloid and interface science* **1989**, *128* (2), 533-548.

98. Murray, C. A.; Grier, D. G., Video microscopy of monodisperse colloidal systems. *Annual review of physical chemistry* **1996**, *47* (1), 421-462.
99. Nägele, G., On the dynamics and structure of charge-stabilized suspensions. *Physics Reports* **1996**, *272* (5-6), 215-372.
100. Sirota, E. B.; Ou-Yang, H. D.; Sinha, S. K.; Chaikin, P. M.; Axe, J. D.; Fujii, Y., Complete phase diagram of a charged colloidal system: A synchro-tron x-ray scattering study. *Phys Rev Lett* **1989**, *62* (13), 1524-1527.
101. Yoshida, H.; Yamanaka, J.; Koga, T.; Koga, T.; Ise, N.; Hashimoto, T., Transitions between ordered and disordered phases and their coexistence in dilute ionic colloidal dispersions. *Langmuir* **1999**, *15* (8), 2684-2702.
102. Van Winkle, D. H.; Murray, C. A., Layering transitions in colloidal crystals as observed by diffraction and direct-lattice imaging. *Physical Review A* **1986**, *34* (1), 562.
103. Itri, R.; Amaral, L. Q., Distance distribution function of sodium dodecyl sulfate micelles by x-ray scattering. *Journal of Physical Chemistry* **1991**, *95* (1), 423-427.
104. Cabane, B.; Duplessix, R.; Zemb, T., High resolution neutron scattering on ionic surfactant micelles: SDS in water. *Journal De Physique* **1985**, *46* (12), 2161-2178.
105. Chevalier, Y.; Zemb, T., The structure of micelles and microemulsions. *Reports on Progress in Physics* **1990**, *53* (3), 279.
106. Aswal, V. K.; Goyal, P. S., Counterions in the growth of ionic micelles in aqueous electrolyte solutions: a small-angle neutron scattering study. *Physical Review E* **2000**, *61* (3), 2947.

107. Tabor, R. F.; Lockie, H.; Chan, D. Y. C.; Grieser, F.; Grillo, I.; Mutch, K. J.; Dagastine, R. R., Structural forces in soft matter systems: unique flocculation pathways between deformable droplets. *Soft Matter* **2011**, 7 (24), 11334-11344.
108. Tuinier, R.; Lekkerkerker, H. N. W., *Colloids and the Depletion Interaction*. Springer Netherlands: 2011.
109. James, G. K.; Walz, J. Y., Experimental and theoretical investigation of the depletion and structural forces produced by ionic micelles. *Colloids and Surfaces A: Physicochemical and Engineering Aspects* **2014**, 441, 406-419.
110. Piech, M.; Walz, J. Y., Direct measurement of depletion and structural forces in polydisperse, charged systems. *J Colloid Interface Sci* **2002**, 253 (1), 117-29.
111. Sharma, A.; Walz, J. Y., Direct measurement of the depletion interaction in a charged colloidal dispersion. *Journal of the Chemical Society, Faraday Transactions* **1996**, 92 (24), 4997-5004.
112. Tulpar, A.; Van Tassel, P. R.; Walz, J. Y., Structuring of macroions confined between like-charged surfaces. *Langmuir* **2006**, 22 (6), 2876-2883.
113. Kralchevsky, P. A.; Denkov, N. D., Analytical expression for the oscillatory structural surface force. *Chemical Physics Letters* **1995**, 240 (4), 385-392.
114. Denkov, N. D.; Yoshimura, H.; Nagayama, K.; Kouyama, T., Nanoparticle arrays in freely suspended vitrified films. *Phys Rev Lett* **1996**, 76 (13), 2354-2357.

115. Trokhymchuk, A.; Henderson, D.; Nikolov, A.; Wasan, D. T., Computer modeling of ionic micelle structuring in thin films. *Journal of Physical Chemistry B* **2003**, *107* (16), 3927-3937.
116. McQuarrie, D., Statistical mechanics University Science Books. *Sausalito, CA* **2000**.

## CHAPTER 3

### MICELLAR ASSEMBLIES AND FOAM FILM STABILITY: SALT EFFECTS

The stratification studies reported in this Chapter were performed by Chrystian Ochoa.

#### ABSTRACT

Micellar foam films formulated with ionic surfactants show dramatic changes in stratification process on salt addition: both the step size and number of stepwise transitions diminish. As stratification process is driven by supramolecular oscillatory structural forces that arise due to confinement-induced structuring of micelles, it is apparent that salt addition reduces both the periodicity and decay length of the oscillatory forces. In contrast, on surfactant addition periodicity decreases but decay length increases, whereas in charge nanoparticle systems the periodicity is found to be independent of added electrolyte concentration. In this chapter, we characterize the changes in micellar size, shape, and interaction on salt addition in bulk using small angle X-ray scattering (SAXS) to understand and elucidate the influence of salt on stratification in micellar foam films and in general on the oscillatory structural forces. We infer that the increase in polydispersity of micelle shape and size, leads to significant reduction in long range correlations, and anticipate the findings are significant for multicomponent soft and biological matter containing self-assembled supramolecular structures as dispersants, wherein weakening of the screened Coulomb interactions govern the self-assembly, interfacial adsorption, interactions, dynamics, and stability. Moreover, we establish an equivalent hard-sphere model to interpret the screened

intermicellar interactions where the standard approach to elucidate interparticle correlations (Hayter-Penfold structure factor model) fail in high salt concentration regime.

### 3.1. INTRODUCTION

Self-assembled sodium dodecyl sulfate (SDS) micelles in aqueous solutions are employed as model nanoscale colloids to explore the interplay of bulk and interfacial intermolecular forces in solutions and in thin freestanding films.<sup>1</sup> When SDS is dissolved in water at concentrations above the critical micelle concentrations (CMC), the surfactant molecules aggregate into micelles with a hydrophobic hydrocarbon (dodecyl) core interfacing a shell comprising the hydrophilic charged (sulfate) headgroups. Within the micelle shells, ionization of the negatively charged headgroups leads to electrostatic repulsion among them, resulting in a strong curvature of the core-shell interface and regulating the surfactant aggregation numbers in micelles.<sup>2</sup> Additionally, ionized headgroups in micellar shells contribute to counterion-mediated electrostatic interactions between the micelles, leading to strong spatial correlations among them.

Structuring of small molecules next to an interface or under confinement leads to oscillatory structural forces that can cause stratification in supported films and in measurement of distance-dependent alternating attractive-repulsive interactions in simulations as well as in surface force apparatus measurements. Analogous structuring of supramolecular structures like micelles, polymers, and nanoparticles creates supramolecular oscillatory structural forces, with periodicity much greater than the size of charged micelles or particle size, that can be observed in simulations, as well as experimentally in surface force apparatus and colloidal probe atomic force microscopy (CP-AFM) measurements.<sup>3-5</sup> In multicomponent colloidal dispersions, smaller supramolecular structures at low concentration (called depletants) are driven away from the region between the larger dispersants causing depletion attraction, driven by entropic factors. However, at high concentration, the interactions, and rearrangements of depletants can lead to oscillatory structural

interactions,  $F_{OS}$  that are often present in foam films that contain micelles. Investigations discussed in Chapter 2 have described the quantitative characterization of intermicellar distances and interactions in aqueous surfactant solutions and contrast the step size obtained from analysis of nanoscopic topographical changes and stepwise thinning in stratifying micellar foam films.<sup>1</sup> Here, we focus on the influence of salt on the micellar dimensions and interactions, as determined by scattering, and compare them with the stratification driven by the confinement-induced layering of micelles in the liquid-air interfaces of foam films.

In this chapter, we also establish an equivalent hard-sphere model to simplify the complex iterative approximations required in the use of Hayter-Penfold structure factor model, particularly in systems with strongly screened interactions. Small-angle X-ray scattering (SAXS) reveals the characteristics of nanoparticles in size, shape and interparticle correlations. The correlation intensity, known as structure factor in scattering analysis, is dependent on particle number density and how particles interact, including steric repulsions for hard sphere particles, sticky pair potentials for attractive particles, and screened electrostatic repulsions for similarly charged particles.<sup>4-10</sup> When surfactant molecules are dissolved in salty solutions with weak charge screening, intermicellar interactions are dominated by repulsive forces between surface charges. This repulsive force is described by the classical Gouy-Chapman double-layer interaction model, influenced by various physical quantities including surface charge density  $z$ , particle volume fraction  $\varphi$ , and the ionic strength  $I$  related with the Debye Length  $\kappa^{-1} = \left[ \frac{\epsilon_r \epsilon_0 k_B T}{2N_A e^2 I} \right]^{1/2}$ , and modeled as Hayter-Penfold structure factor widely used to describe interactions between charged nanoparticles like micelles, also in proteins and oxide particles.

The Hayter-Penfold structure factor model assumes charged spheres of hardcore radius  $R$  with the pair correlation function  $g(r) = 0$  when separation distances  $d < 2R$ , or interacting with the Yukawa pair potential  $u(r) = \frac{u_0}{r} \exp(-\kappa R)$  when  $d > 2R$ .<sup>5-6, 11</sup> The  $S(q)$  is calculated using the solution to the Ornstein-Zernike equation<sup>12</sup> along with a direct correlation function  $c(r) = -\frac{g(r)}{k_B T}$  under the assumption of Mean Spherical Approximation (MSA) when  $d > 2R$ . This universal solution however is impractical in the scenario when the volume fraction of the scatterer is low.<sup>11</sup> In such cases, pair correlation function provides a  $g(r) < 0$  demonstrating a negative probability in finding a scatterer at separation distance  $d$ . This limitation is alleviated by a rescaling of the MSA (RMSA) adjusting  $g(r') = 0$  at same particle volume fraction while the spherical particle dimension is rescaled with a factor  $s = R'/R > 1$ .<sup>7-8</sup> However, the renormalized Hayter-Penfold model with RMSA is still insensitive to predict  $S(q)$  in the limit of low effective charge density, typically encountered in strong charge screening regimes. Strong screening leads to weak interparticle correlations, resulting in broadening of the  $S(q)$  peaks and causes an inaccurate numerical evaluation of volume fraction. When finding the numerical solution to  $g(r) = 0$  from the quintic polynomial equations  $g(r) = 1 + \frac{\int f_1(z)}{f_2(\varphi)}$  through the standard Waisman solution,<sup>8-10</sup> the multiplication function  $\frac{\int f_1(z)}{f_2(\varphi)}$  provided with  $\frac{1}{f_2(\varphi)} \sim \infty$  and  $f_1(z) \sim 0$  is impractical to be accurately interpreted via linear regression.

Thus, an effective hard-sphere model for structure factor is required to overcome the low sensitivity caused by the strong screening effects in Hayter-Penfold structure factor model. In this chapter, we establish such an equivalent hard-sphere model for surfactant solutions with strong screening by assigning an effective hard-sphere radius  $R_{HS}$  and effective volume fractions  $\phi_{HS}$ ,

and model the screened electrostatic double layer into the electro-steric hindrance forces between colloidal particles with low surface charge density. Here, the Coulomb potential under strong screening is modeled as an equivalent electro-steric repulsion. This approach can be of practical implication as an alternate to the Hayter-Penfold structure factor model when predicting interactions between charged colloids in high ionic strength solutions.

## **3.2. RESULTS AND DISCUSSIONS**

### **3.2.1. Influence of Salt on Micellar Assemblies and Foam Film Stability**

The influence of intermolecular and colloidal interactions on the structure of bulk SDS solutions were analyzed through small angle X-ray scattering (SAXS) measurements. The one-dimensional SAXS intensities  $I(q)$ , as a function of wave vector  $q$ , for a series of aqueous SDS solutions with SDS concentration  $C_{SDS}$  ranging from 50 mM to 150 mM ( $\sim 6 \text{ CMC}_{SDS} - \sim 18 \text{ CMC}_{SDS}$ ) are shown in Figure 3-1a. The unique shape of the SAXS spectra of SDS micelles, comprising distinct peaks and valleys, can be attributed to the contributions to  $I(q)$  from the form factor  $P(q)$  and the structure factor  $S(q)$  as  $I(q) \sim P(q)S(q)$ . While  $P(q)$  describes the scattering from a single micelle and is dependent on micelle shape and size,  $S(q)$  describes the  $C_{SDS}$  – dependent intermicellar correlations. The position and the height of the  $I(q)$  peaks in the  $q$ –range  $1-3 \text{ nm}^{-1}$  were found to be largely  $C_{SDS}$  invariant. The individual micelles are expected to retain their shape and size in the  $C_{SDS}$  range considered here,<sup>1</sup> and thus these peaks were attributed to  $P(q)$  contributions to  $I(q)$ . In contrast, the  $I(q)$  peaks in the region  $q < 1 \text{ nm}^{-1}$  were found to grow stronger and shift to higher  $q$  with increasing  $C_{SDS}$ . These peaks were therefore attributed to strengthening intermicellar correlations with increasing  $C_{SDS}$  manifesting as larger  $S(q)$  contributions to  $I(q)$ .

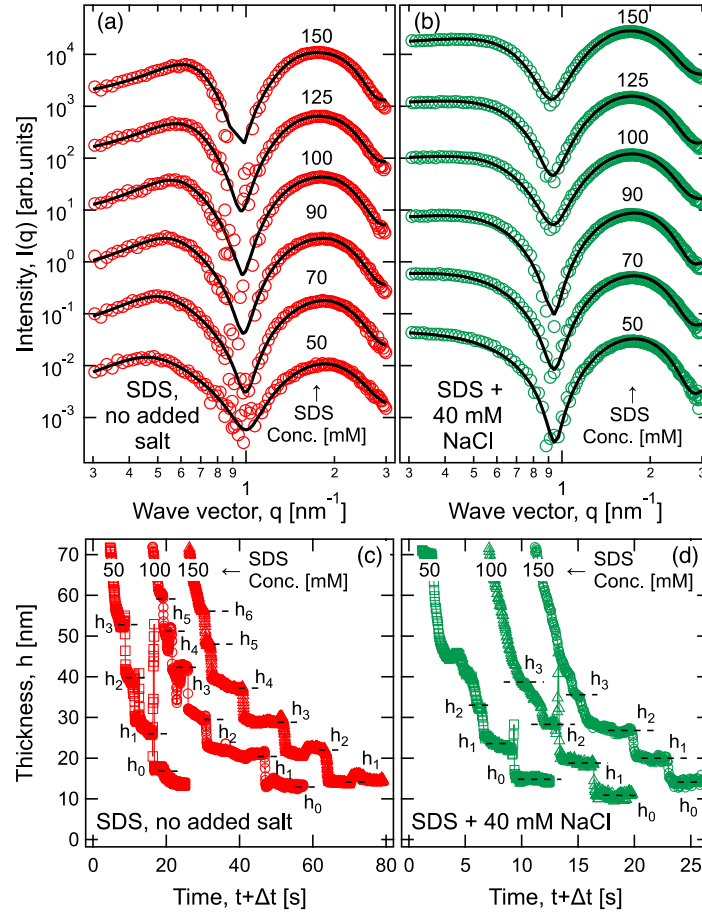


**Figure 3-1:** (a, b) SAXS intensity  $I(q)$  spectra of aqueous SDS solutions with varying SDS concentration  $C_{SDS}$  with (a) no added salt and with (b) 40 mM NaCl. Solid lines depict the fits to  $I(q) \sim P(q)S(q)$  comprising a form factor  $P(q)$  for oblate ellipsoids and Hayter-Penfold structure factor  $S(q)$ , respectively. The spectra are shifted vertically, with a constant shift factor of 12, for clarity. (c, d) Thickness variations,  $h(t)$  of thin aqueous SDS films with varying  $C_{SDS}$  with (c) no added salt and with (d) 40 mM NaCl. Thickness is measured by image analysis using IDIOM.  $h(t)$  profiles of 100 mM and 150 mM SDS solutions are shifted to the right by 13.9 s and 23.6 s in (c) and by 5.35 s and 7.8 s in (d) for clarity. The spikes observed in thickness of certain layers can be attributed to mesas interfering with the thickness measurements.

Further insights into micelle characteristics and intermicellar interactions were obtained by modeling the  $I(q)$  spectra using a  $P(q)$  model for oblate core-shell ellipsoids<sup>7, 13-15</sup> and the Hayter–Penfold  $S(q)$  model with rescaled mean spherical approximation (RMSA) describing the screened Coulomb repulsion.<sup>6, 16</sup> Best fits to the  $I(q)$  data are depicted by solid lines in Figure 3-1a; corresponding  $P(q)$  and  $S(q)$  fits are provided in Figure 3-2.  $P(q)$  fits indicate oblate SDS micelles with core radii along the minor (polar axis) and the major axis (equatorial axis) being  $R_p \sim 1.3$  nm and  $R_e \sim 2$  nm (Figure 3-3), representing a core aspect ratio of  $\sim 0.65$ , and a shell thickness  $\delta$  of  $\sim 0.75$  nm, consistent with previous reports on SDS micelles.<sup>17-19</sup>  $R_p$  values estimated here are also consistent with the length of stretched C<sub>12</sub> tails.<sup>20</sup> Interestingly, these micelles dimensions were found to be largely independent of  $C_{SDS}$  in the range of 50 mM  $< C_{SDS} < 150$  mM.<sup>6, 16</sup> At the same time, the average intermicellar distances, estimated from the inverse of the position of the primary  $S(q)$  peak  $q^*$ , as  $d = 2\pi/q^*$  decreased continually as  $C_{SDS}^{-1/3}$ , indicating progressive crowding of the SDS micelles in solution with increasing  $C_{SDS}$  (Figure 3-4a). This crowding was also complemented by increasing height of the primary  $S(q)$  peak  $S_1$  (Figure 3-5), denoting strengthening intermicellar correlations.

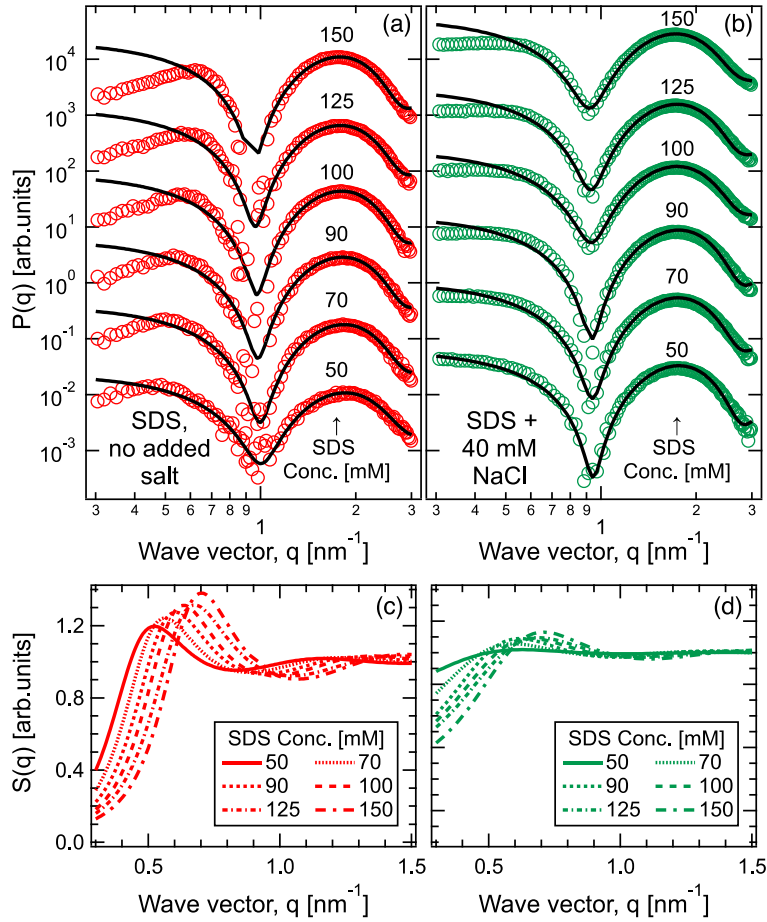


**Figure 3-2:** (a, b) SAXS intensity  $I(q)$  spectra of aqueous SDS solutions with varying SDS concentration  $C_{SDS}$  with (a) no added salt and with (b) 40 mM NaCl. Solid lines depict the form factor  $P(q)$  for oblate ellipsoids. The spectra are shifted vertically, with a constant shift factor of 12, for clarity. (c, d) Hayter-Penfold structure factor  $S(q)$  fits for the corresponding samples from (a) and (b) with (c) no added salt and with (d) 40 mM NaCl.

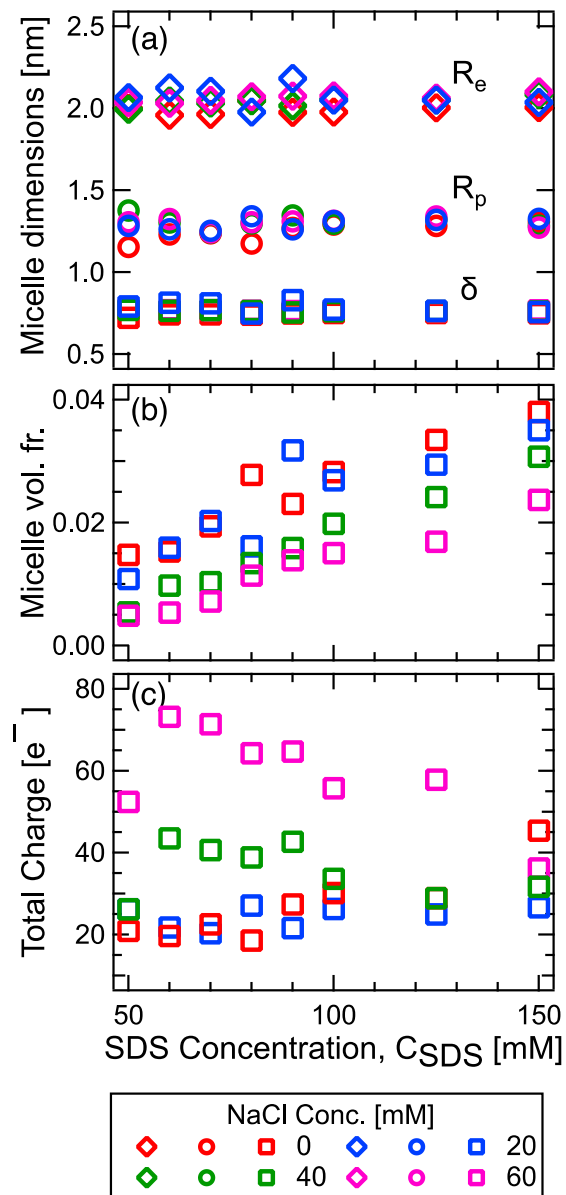


**Figure 3-3.** (a) Dimensions of the oblate ellipsoidal SDS micelles: equatorial (along the major axis) and polar radii (along the minor axis),  $R_e$ , and  $R_p$ , respectively and shell thickness  $\delta$ , as obtained from the  $P(q)$  fits to the SAXS spectra. (b) Micelle volume fraction  $\phi$ , and (c) total charge of the micelles, as estimated from the  $S(q)$  fits to the SAXS spectra.

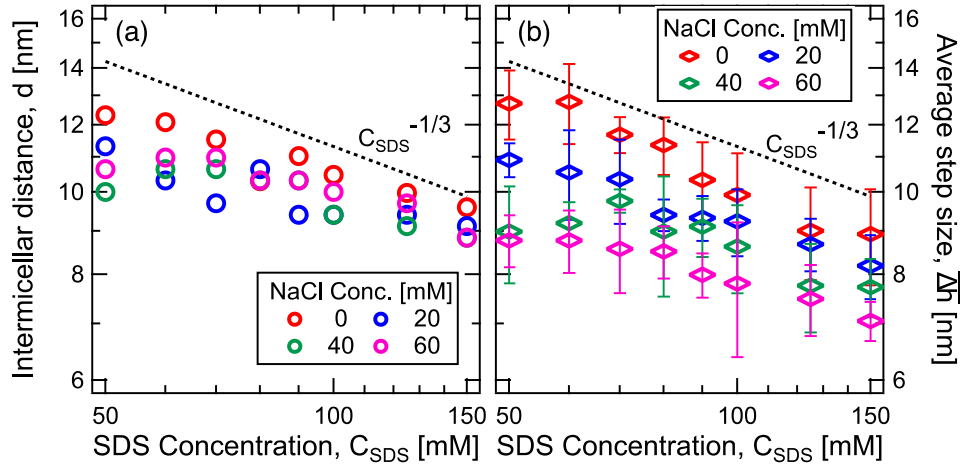


**Figure 3-4.** (a) Intermicellar distance  $d$ , estimated from the inverse of the position of the primary  $S(q)$  peak  $q^*$  as  $d = 2\pi/q^*$ , as a function of SDS concentration  $C_{SDS}$  in bulk SDS solutions with increasing NaCl concentration  $C_{NaCl}$ . (b) Average step size  $\overline{\Delta h}$  observed in thin freestanding micellar SDS films undergoing stratified drainage, determined from IDIOM protocols, as a function of  $C_{SDS}$  with increasing  $C_{NaCl}$ . Dashed lines in (a) and (b) depict a  $C_{SDS}^{-1/3}$  scaling.

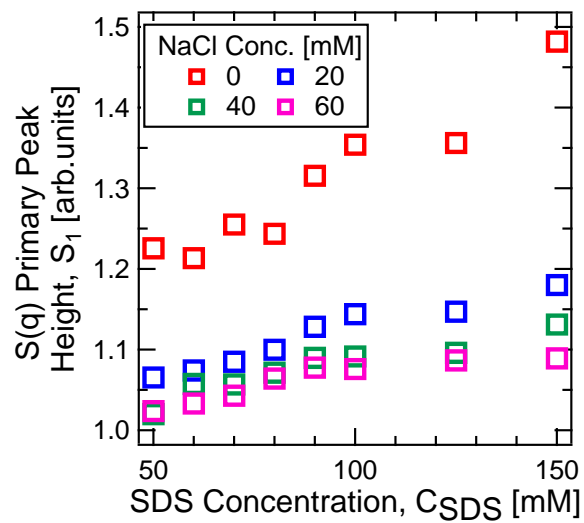


**Figure 3-5.** Height of the primary  $S(q)$  peak,  $S_1$  as a function of SDS concentration  $C_{SDS}$  for various salt concentration  $C_{NaCl}$ .

Introduction of salt led to noticeable changes in the intermicellar interactions while preserving the micellar morphologies, as is evident from a comparison of the  $I(q)$  spectra from SDS solutions with no added salt and with NaCl concentration,  $C_{NaCl} = 40$  mM shown in Figures 3-1a and 3-1b, respectively. The positions and the heights of the  $C_{SDS}$ -invariant  $P(q)$  peaks in  $1 \text{ nm}^{-1} < q < 3 \text{ nm}^{-1}$  range were similar between SDS solutions with and without salt. Correspondingly, the micelle shape and dimensions (Figure 3-3) did not vary up to  $C_{NaCl} = 60$  mM in solution.<sup>21-23</sup> However, the  $S(q)$  peaks in the range  $q < 1 \text{ nm}^{-1}$  weakened and shifted leftwards in presence of salt, indicating weaker correlations among the micelles, and increasing intermicellar distance. These trends are evident in Figure 3-4a, wherein  $d$ , at a constant  $C_{SDS}$ , was found to initially decrease upon salt addition before plateauing with increasing  $C_{NaCl}$ .

Corresponding investigations of the drainage kinetics of thin freestanding micellar films revealed the influence of intermolecular interactions on micellar arrangements in thin films. Micellar thin films undergo stratified drainage with film thickness  $h$  decreasing in a stepwise manner over time  $t$ .<sup>24-28</sup> This stratified drainage is attributed to an interplay of constant capillary pressure, imposed on the film, and the oscillatory disjoining pressure contributed by the bulk and interfacial intermolecular interactions. The disjoining pressure in thin surfactant-laden micellar films has long been hypothesized to depend on micelle number density, and intermicellar distance and interactions.<sup>25, 29-30</sup> Figure 3-1c shows the  $h(t)$  evolution, obtained from IDIOM protocols, for SDS solutions with 50, 100, and 150 mM  $C_{SDS}$ , showing stepwise thinning over time.<sup>24-28</sup> We note that our IDIOM protocols enable measurements of stratification kinetics for an extended range of surfactant concentrations while other reports in the literature have been limited to surfactant concentrations below 100 mM (Figure 3-6).<sup>25, 31-34</sup> The thickness of each quasi-stable layer

depicted as  $h_i$ <sup>24-25, 29, 31-33, 35-37</sup> and are in agreement with the values obtained from conventional interferometry studies.<sup>32-34, 38-40</sup> With increasing  $C_{SDS}$ , the number of steps comprising the stratified drainage increased while the layer thickness,  $h_i$ , decreased (Figure 3-7). For example,  $h_3$  decreased from 51 nm to 40 nm to 33 nm with  $C_{SDS}$  increasing from 50 mM to 100 mM to 150 mM, respectively. These trends could be attributed to tighter intermicellar packings leading to concomitant decrease of periodicity and increase of the decay length and the amplitude (of periodicity) of the oscillatory disjoining pressure in the thin films.

The step size  $\Delta h$ , defined as the thickness difference between two successive layers,  $\Delta h = h_i - h_{i-1}$  was found to be remarkably consistent between the stepwise transitions in draining films. The average step size  $\overline{\Delta h}$ , corresponding to the periodicity of disjoining pressure in the thin films,<sup>29</sup> decreased with increasing  $C_{SDS}$  and, analogous to  $d$ , also followed a  $C_{SDS}^{-1/3}$  scaling (Figure 3-4b) in the range  $50 \text{ mM} \leq C_{SDS} \leq 150 \text{ mM}$ .

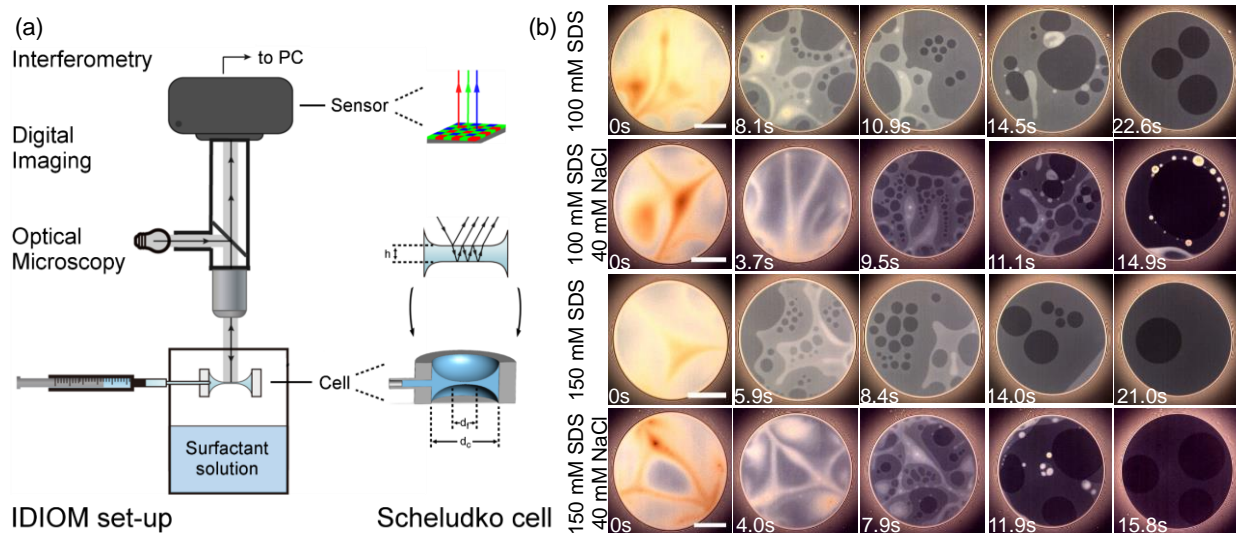


**Figure 3-6. IDIOM schematic and montages.** Schematic of thin film balance and IDIOM set-up, and snapshots for visualizing stratification for SDS/NaCl solutions. **(a)** Schematic of the IDIOM setup used for measuring thickness variations and transitions of a circular plane-parallel film surrounded by a thicker meniscus. Pixelwise thickness measurement relies on the spatiotemporal variation in interference intensity captured by the photosensor array of a digital camera. **(b)** Brightness-enhanced snapshots for foam films with  $C_{SDS}$  and  $C_{NaCl}$  as follows: 100 mM and 0 (first row), 100 mM and 40 mM (second row), 150 mM and 0 (third row), and 150 mM and 40 mM (fourth row). The first snapshot in each row corresponds to the time of maximum interference intensity of red wavelength light. Snapshots with times  $t > 0$  s show multiple coexisting shades of gray (including domains). The average interference intensity/thickness as well as number of coexisting domains decreases with time. Relatively brighter white spots, mesas, surround some domains in the concentrations shown, except for  $C_{SDS} = 150$  mM. The scale bar represents a length scale of 100  $\mu\text{m}$ .

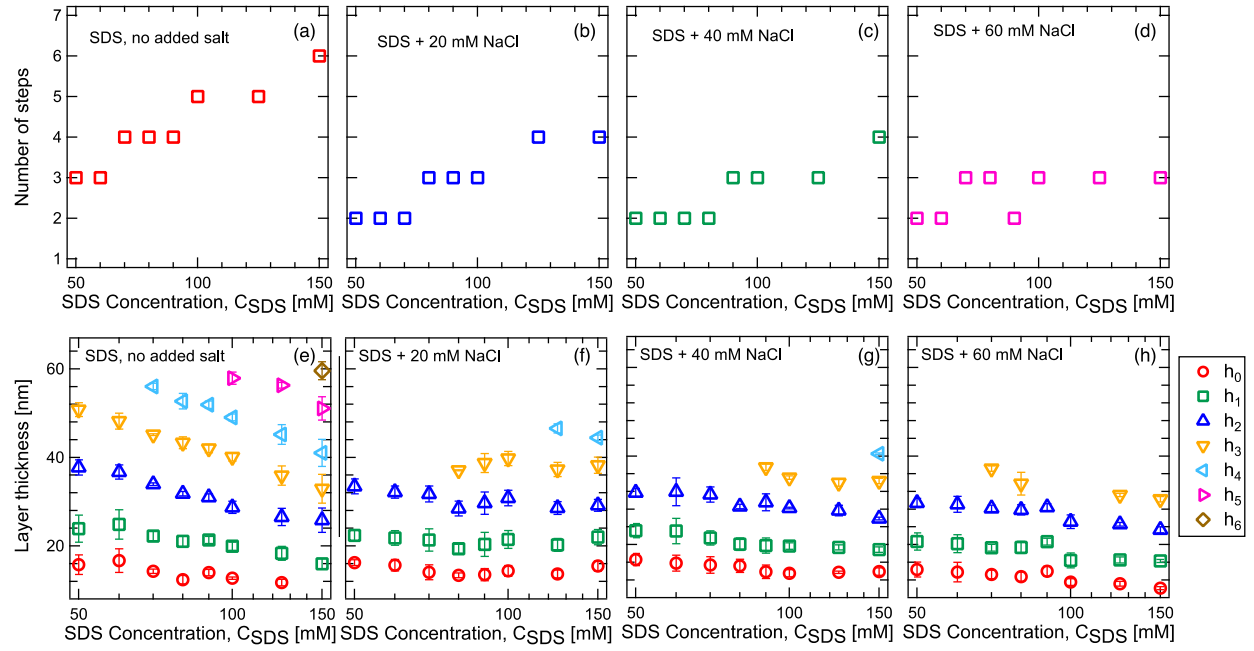


**Figure 3-7.** The number of steps (**a-d**) and the layer thickness,  $h_i$  (**e-h**) and as a function of SDS concentration,  $C_{SDS}$  for various salt concentration  $C_{NaCl}$  in thin foam films undergoing stratified drainage, as obtained from IDIOM experiments.

Similar to the bulk SDS solutions, introduction of salt led to significant changes in the drainage profiles of the thin SDS films. Figure 3-1c and 3-1d compare the stratification profiles for SDS thin films with varying  $C_{SDS}$  in absence or presence of salt. In presence of 40 mM NaCl, thinner SDS films with fewer steps were observed as compared to SDS films without any salt (see also Figure 3-7). These observations point towards a prominent influence of salt in screening intermicellar electrostatic interactions and thus decreasing the decay length of the disjoining pressure, in turn affecting the stratified drainage of the SDS films.<sup>25, 32, 41</sup> Average step size  $\overline{\Delta h}$  also decreased with increasing  $C_{NaCl}$ , as depicted in Figure 3-4b, pointing towards decreasing periodicity of the disjoining pressure with increasing salt concentrations in solution. The  $\overline{\Delta h} \sim C_{SDS}^{-1/3}$  scaling was maintained up to  $C_{NaCl} = 60$  mM. However, variations in  $\overline{\Delta h}$  increased when approaching low  $C_{SDS}$  at high  $C_{NaCl}$  owing to severe damping of the disjoining pressure oscillations in the thin liquid films.

The influence of salt on the micelle morphology, interactions, and arrangements is further illustrated in the SAXS intensity profiles in Figures 3-8a and 3-8b. The form factor peak ( $q \sim 2$  nm<sup>-1</sup>) stays relatively unaffected while the primary structure factor peak ( $q < 1$  nm<sup>-1</sup>) weakens, broadens, and shifts to higher  $q$  with increasing  $C_{NaCl}$ , in both 50 mM and 150 mM SDS solutions. However, the influence of salt diminished as the screening of the electrostatic interactions (Debye length) decreased below 2 nm. Therefore, the average intermicellar distance  $d$  decreased upon initial introduction of salt, but then plateaued upon further addition of salt (Figures 3-8c, d).

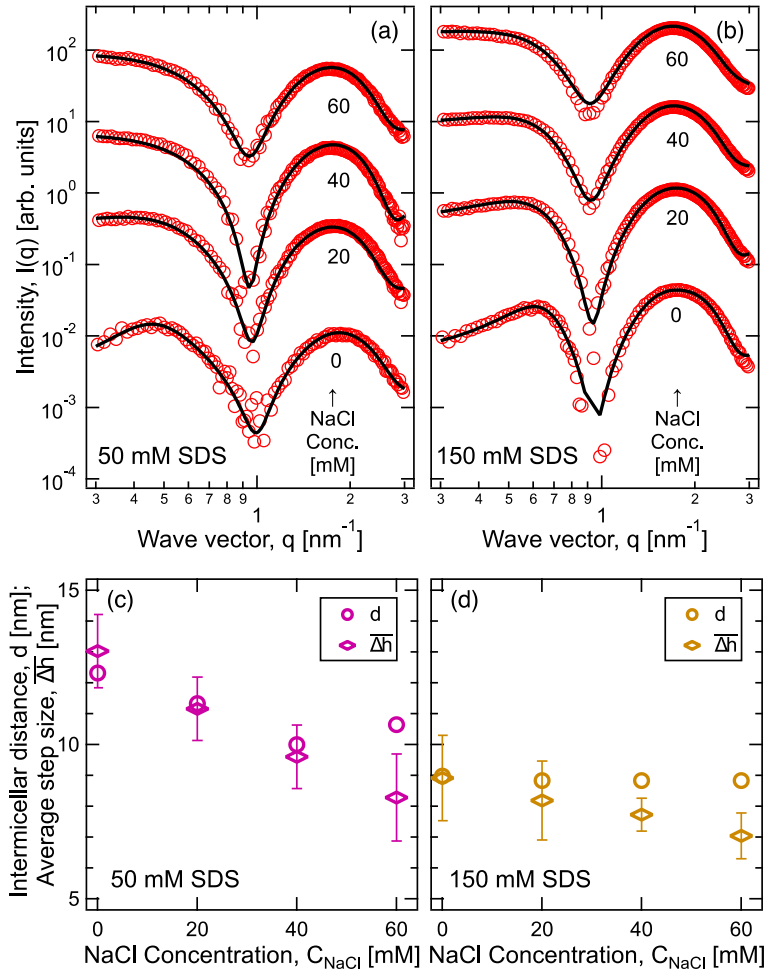


**Figure 3-8.** (a, b) SAXS intensity  $I(q)$  spectra of aqueous SDS solutions with constant SDS concentration  $C_{\text{SDS}}$  ((a) 50 mM and (b) 150 mM) and varying NaCl concentration  $C_{\text{NaCl}}$ . Solid lines depict the fits to  $I(q) \sim P(q)S(q)$  comprising a form factor  $P(q)$  for oblate ellipsoids and Hayter-Penfold structure factor  $S(q)$ , respectively. The spectra are shifted vertically for clarity; the shift factors are reported in the SI. (c, d) Variations of intermicellar distance  $d$  and average step size of stratifying thin films,  $\overline{\Delta h}$ , with  $C_{\text{NaCl}}$  at constant  $C_{\text{SDS}}$  ((c) 50 mM and (d) 150 mM).

The plateauing of  $d$  with increasing  $C_{NaCl}$  can be attributed to a combination of reasons. Firstly, stronger screening of the intermicellar interactions leads to weaker intermicellar correlations. Since  $S(q)$  is the Fourier transform of the three-dimensional radial distribution function of micelles, the primary peak of  $S(q)$  may not correspond to the average intermicellar distance in the case of weakened intermicellar interactions. However, a mapping of  $d$  against volume fraction  $\phi$  of scatterers interacting with screened Yukawa potential shows a monotonic correlation that holds until very small scatterer volume fraction for systems with minimally (Figure 3-9a) and with strongly screened electrostatic interactions (Figure 3-9b), ruling out this possibility. Secondly, screening of electrostatic repulsion with increasing  $C_{NaCl}$  reduces the spatial correlation among the micelles, manifesting as diminishing  $S_1$  (Figure 3-5). The configurational entropy of the system thus increases, leading to a decrease in the average intermicellar spacing with increasing  $C_{NaCl}$ . A mapping of  $d$  against  $C_{NaCl}$  at various volume fraction  $\phi$  and surface charge density of scatterers interacting with screened Yukawa potential, shown in Figures 3-9c – 3-9e, corroborates with these expectations. Lastly, increasing  $C_{NaCl}$  significantly reduces the entropy gains from the counterion release following the ionization of the SDS head groups, resulting in lower headgroup ionization and reduced electrostatic repulsion among them. Thus, micellization occurs at smaller SDS concentrations and micelle can accommodate more SDS molecules, leading to lower  $CMC$ , higher aggregation number ( $N_{agg}$ ) and micellar charge (Figure 3-3c) and smaller micelle volume fractions (Figure 3-3b) at comparable micelle sizes. The micelle number density is therefore expected to decrease with increasing  $C_{NaCl}$  at constant  $C_{SDS}$ , leading to larger intermicellar distances. Both intermicellar repulsion and inter-headgroup repulsion are expected to reduce sharply upon initial addition of salt before gradually plateauing with progressively increasing

$C_{NaCl}$ , and we hypothesize a competition between the two phenomena to result in the observed plateauing of  $d$  with increasing  $C_{NaCl}$ .

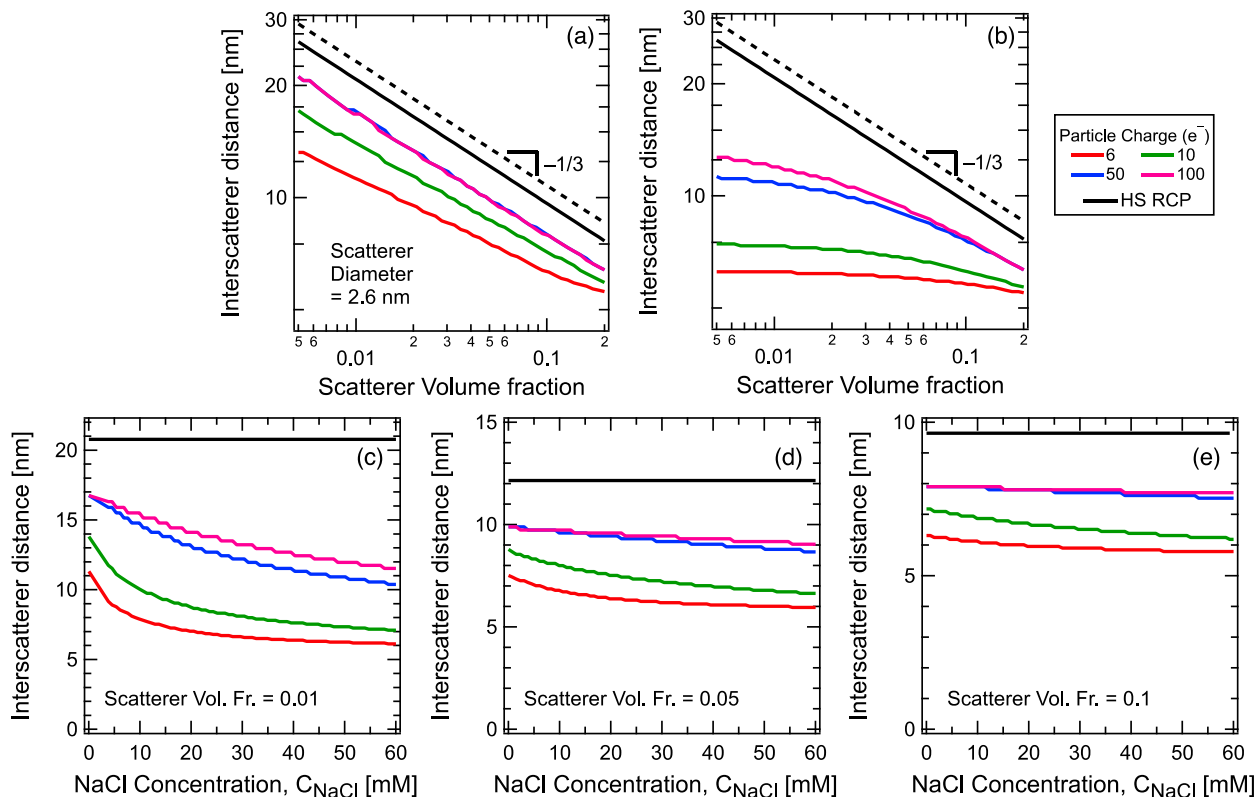


**Figure 3-9.** (a, b) Variations of inter-scatterer distance  $d$  with scatterer volume fraction  $\phi$  with (a) no added salt and (b) NaCl concentration  $C_{NaCl} = 50$  mM, and (c - e) with NaCl concentration  $C_{NaCl}$  for constant  $\phi$ , as calculated for spherical charged scatterers by Hayter-Penfold structure factor at a constant scatterer size  $R \sim 2.6$  nm. Different colors correspond to different scatterer charge ranging from 6 to 100  $e^-$ . Theoretical inter-scatterer distances obtained from random close packing of scatterers, estimated as  $d = 2R(0.638/\phi)^{1/3}$  are shown in black line. In (a, b), dashed lines represent a  $\phi^{-1/3}$  scaling.

The average step size  $\overline{\Delta h}$  of the stratified drainage of thin SDS films also decreased steadily with increasing  $C_{NaCl}$ . In SDS solutions with no added salt, a reasonable agreement between  $\overline{\Delta h}$  and  $d$  is observed (Figure 3-8a and 3-8b, see also Figure 3-4), consistent with earlier results<sup>1</sup> and hypotheses<sup>29</sup> that intermicellar interactions and micelle number density dictate both  $\overline{\Delta h}$  and  $d$  and suggesting that even though the confining interfaces in thin films lead to micelle layering and stratified drainage, the interlayer spacings are dictated largely by the repulsive intermicellar interactions in thin surfactant films without added salt. This agreement between  $\overline{\Delta h}$  and  $d$ , however, worsens with increasing  $C_{NaCl}$  (Figure 3-8c and 3-8d) –  $d$  plateaued while  $\overline{\Delta h}$  continued to decrease at high  $C_{NaCl}$ . Interestingly, this divergence between  $\overline{\Delta h}$  and  $d$  was more apparent at higher  $C_{SDS}$ . Screening of the intermicellar interactions and increasing polydispersity of micelle shape and size upon addition of salt decreases both the amplitude and the decay length of the disjoining pressure, weakening the layered micellar arrangements in the thin films.

Further insights on the influence of  $C_{SDS}$  and  $C_{NaCl}$  on both  $\overline{\Delta h}$  and  $d$  were gained by evaluating their evolutions with variations in the micelle number density,  $\rho$ , estimated as  $\rho = \phi_{mic}/V_{mic}$ . Here  $\phi_{mic}$  is the micelle volume fraction estimated from  $S(q)$  fits (Figure 3-3b) while  $V_{mic}$  is the volume of an individual micelle, estimated from  $P(q)$  fits as (Figure 3-4a). Increasing  $C_{SDS}$  led to an increase in  $\rho$  and results in a decrease in both  $\overline{\Delta h}$  and  $d$ , as evident from the constant  $C_{NaCl}$  data sets in Figure 3-10. Increasing  $C_{NaCl}$  led to a decrease in  $\rho$  resulting from an increase in  $N_{agg}$ . However, if this was the only influence of increasing  $C_{NaCl}$ ,  $d$  should have increased with increasing  $C_{NaCl}$  (Figure 3-4a) and  $d$  for all SDS solutions should have collapsed onto a single curve when plotted against  $\rho$ . We attribute the deviation from these expectations, as evident in Figure 3-10a, to the increase in configurational entropy of the micelles upon weakening

intermicellar interactions and correlations, leading to decreasing  $d$ . This loss of correlation is most evident upon the initial addition of salt and then saturate with increasing  $C_{NaCl}$ , and is correspondingly reflected in the near collapse of the  $d$  vs.  $\rho$  trends for all SDS solutions with added salt. In contrast, the  $\overline{\Delta h}$  trends do not exhibit any such collapse (Figure 3-10b) and signify the growing influence of weakened interactions and increasing polydispersity of micelle shape and size on the micellar layering in thin films.

In salt-free SDS solutions, the surface tension remains nearly constant above  $CMC$ ,<sup>42</sup> and the experiments reported here were carried out with comparable foam size under nearly matched capillary pressure and interfacial charge or potential.<sup>1</sup> On salt addition, the equilibrium surface tension  $CMC$  as well as surface charge decrease,<sup>43</sup> and any change in the latter weakens the confinement effect. More significantly, a substantial increase in polydispersity in size and shape of micelles is observed on salt addition. Polydispersity in size of nanoparticles is known to significantly reduce the ordering for charged spheres in confined and bulk systems<sup>44-47</sup> and here, it leads to both weakening of the magnitude of structural disjoining pressure and decrease in correlations, leading to smaller decay length. More substantial increase in polydispersity occurs on an increase in salt concentration than prompted by change in surfactant concentration. We have examined stratification in foam films formed by bile salts, where polydispersity of micelle sizes is much larger than present in typical head-to-tail surfactants like SDS. Consistent with the observations for SDS with salt, the bile salt films show fewer transitions and lower amplitude of disjoining pressure than observed for SDS at the matched  $CMC$  values.

Even though Anachkov et al.<sup>29</sup> and Danov et al.<sup>34</sup> had postulated that step size provides a quantitative measure of intermicellar distance and aggregation number for micellar solutions,

stratification studies with salt added SDS solutions (and with bile salts films) show that challenges arise for the inherently polydisperse systems. In Yilixiati et al.,<sup>25</sup> the impact of salt on stratification was explained partially by the use of a phenomenological expression for  $\Pi_{OS}(h)$  wherein amplitude was determined by micelle number density and Carnahan-Starling compressibility factor for hard spheres, computed at an effective volume fraction. The effective volume fraction computation relied on an effective size obtained by adding the computed value of Debye length to micelle size. In contrast, the present study considers screened Coulomb interactions between charged micelles, reveals the intermicellar distances as well as structure factor computed using RMSA, and also provides information on change in size and shape with increase in salt content.

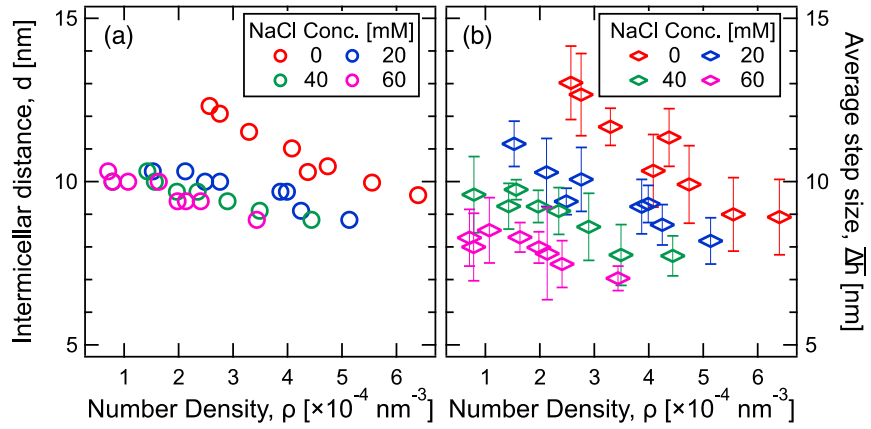


**Figure 3-10.** Variations of (a) intermicellar distance  $d$  and (b) average step size of stratifying thin films,  $\overline{\Delta h}$  with micelle number density  $\rho$ . Different colors correspond to SDS solutions with increasing  $C_{NaCl}$ .

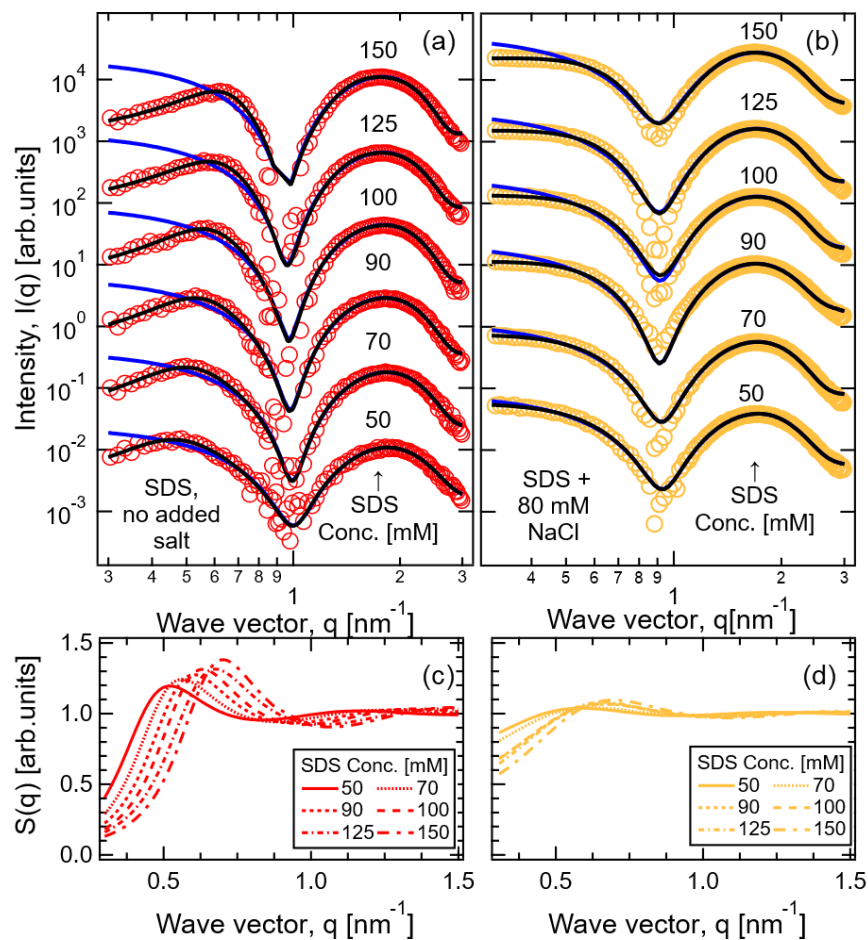
### 3.3.2. An Equivalent Hard-sphere Model to Interpret Interactions Between Ionic Micelles in High Ionic Strength Solutions

Figure 3-11a shows one-dimensional SAXS spectra obtained from SDS solutions with  $C_{SDS}$  ranging from 50 mM to 150 mM ( $\sim 6 \text{ CMC}_{SDS} - \sim 18 \text{ CMC}_{SDS}$ ) and no added salt fitted with the form factor model for oblate ellipsoid core-shell assemblies (demonstrated in blue lines) and rescaled Hayter-Penfold structure factor model (Figure 3-11c). Here, the contrast between the  $I(q)$  fits and the form factor highlights the significant correlations between micelles in the weak screening regime. Structure factor extracted from these fits facilitated estimation of micelle volume fraction, surface charge density, and interparticle distances (Figures 3-3 and 3-4a).

Figure 3-11b shows the SAXS spectra for SDS solutions with  $C_{SDS}$  ranging from 50 mM to 150 mM ( $\sim 6 \text{ CMC}_{SDS} - \sim 18 \text{ CMC}_{SDS}$ ) but also containing salt at high concentration ( $C_{NaCl} = 80 \text{ mM}$ ) along with the corresponding fits (yellow dots as raw data, blue lines as form factor, black lines as integrated fits). In this case,  $I(q)$  peaks in the high  $q$  region ( $\sim 1 - 3 \text{ nm}^{-1}$ ), contributed by the form factor, remain nearly  $C_{SDS}$  and  $C_{NaCl}$  invariant, depicting concentration-independent and screening-independent micelle dimensions. In contrast, in the low  $q$  range ( $\sim 0.4 - 1 \text{ nm}^{-1}$ ), peaks contributed by  $S(q)$  appear as broad plateaus without apparent sharp peaks. Correspondingly, the difference between the integrated fits and the form factor is negligible at low  $C_{SDS}$  while growing marginally at high  $C_{SDS}$ . This suggests that the repulsive interactions between micelles are strongly screened by added salt, leading to weak intermicellar correlations. Structure factors for these solutions are shown in Figure 3-11d and depict minor differences between each profile. The height of the primary peak remains nearly constant, while its position shifts to marginally higher wave vector  $q$  with increasing  $C_{SDS}$ , denoting a closer packing between micelles.

Typical characteristics of the surfactant micelles in solutions containing high salt concentration is demonstrated in Figure 3-13. Oblate SDS micelles are observed in low  $C_{NaCl}$  solutions with core radii along the minor and the major axis being  $R_p \sim 1.3$  nm and  $R_e \sim 2$  nm (Figure 3-13a), representing the core aspect ratio of  $\sim 0.65$ , and the shell thickness  $\delta$  of  $\sim 0.75$  nm. With increasing  $C_{NaCl}$ , an enlarging core radius  $R_e \sim 2.1$  nm represents a lowering of the core aspect ratio to  $\sim 0.59$ , while dimensions in the polar axis and shell thickness remain similar.  $R_p$  indicates the length of stretched  $C_{12}$  tails. Thus, the decreasing aspect ratio depicts the tendency of SDS micelles to adopt a disk-like shape in high salt concentration solutions due to weak repulsive forces between headgroups. The micelle volume fraction  $\varphi$  and total charges per micelle  $z$  can be only obtained from the broad structure factor peaks (Figure 3-13b-c). The aggregation number  $N_{agg}$  are reported in the range of 80-120<sup>29</sup> with the degree of ionization 0.25-0.4 so that the total charge density is predicted to be  $\sim 30$ . Theoretically, aggregation number  $N_{agg}$  increases with increasing  $C_{SDS}$  at a fixed salt concentration  $C_{NaCl}$ , estimated by  $N_{agg} \sim \left(\frac{C_{SDS}}{CMC}\right)^{1/4}$ . However, calculated total charges per micelle undergoes a decrease with increasing SDS concentration  $C_{SDS}$  at a fixed salt concentration  $C_{NaCl}$  (Figure 3-13c). Thus, the charge density currently provided by Hayter-Penfold structure factor is unphysical (Figure 3-13c).

Hayter-Penfold model has been shown to break down in describing inter-micelle correlations in LiCl concentrations as high as 1 M, but not larger than 200 mM for SDS solutions. Steric repulsions become dominant between low charge colloids in the limit of strong screening, such that the hard-sphere model with an effective core radius  $R_{HS}$  is proposed to describe this equivalent electrosteric repulsion.



**Figure 3-11:** (a, b) SAXS intensity  $I(q)$  spectra of SDS solutions with varying SDS concentration  $C_{SDS}$  with (a) no added salt and with (b) 80 mM NaCl. Black solid lines depict the fits to  $I(q) \sim P(q)S(q)$  comprising a form factor  $P(q)$  (in blue solid lines) for oblate ellipsoids and Hayter-Penfold structure factor  $S(q)$ , respectively. The spectra are shifted vertically, with a constant shift factor of 12, for clarity. (c, d) Extracted Hayter-Penfold structure factor varies with SDS concentration  $C_{SDS}$  corresponds to (a, b), respectively.

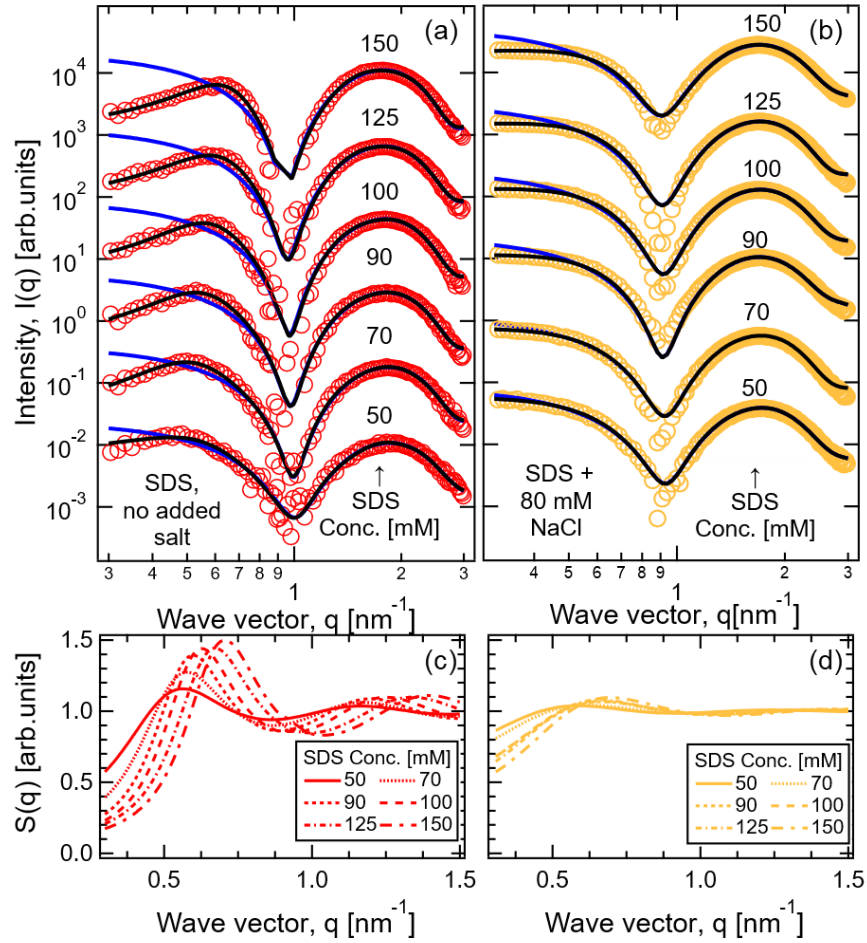


**Figure 3-12:** (a, b) SAXS intensity  $I(q)$  spectra of SDS solutions with varying SDS concentration  $C_{SDS}$  with (a) no added salt and with (b) 80 mM NaCl. Black solid lines depict the fits to  $I(q) \sim P(q)S(q)$  comprising a form factor  $P(q)$  (in blue solid lines) for oblate ellipsoids and equivalent hard-sphere structure factor  $S(q)$ , respectively. The spectra are shifted vertically, with a constant shift factor of 12, for clarity. (c, d) Extracted equivalent hard-sphere structure factor varies with SDS concentration  $C_{SDS}$  corresponds to (a, b), respectively.

Fits to the scattering spectra,  $I(q)$ , using the  $P(q)$  model (in blue lines) for oblate ellipsoidal core-shell micelles together with the hard-sphere model for  $S(q)$  (Figure 3-12c-d) are shown in Figure 3-12a-b with black solid lines. This model combination depicts adequately well both aqueous SDS solutions and salty SDS solutions with 80 mM  $C_{NaCl}$ . Micelle dimensions obtained from these fits reveal similar trends of evolution of micelle characteristics and aspect ratio (Figure 3-13d) as obtained from fits using the Hayter-Penfold  $S(q)$  model (Figure 3-13a). The effective hard-sphere radius  $R_{HS}$  (Figure 3-13e) represents the apparent dimension of the equivalent hard sphere including the steric repulsion between micelles and the screened double layer owing to the added salt. A decreasing  $R_{HS}$  (from  $\sim 5$  nm to  $\sim 4.2$  nm) is revealed with increasing  $C_{SDS}$ , influenced by the increasing micelle number density  $\rho$ . At the same time,  $R_{HS}$  decreases with increasing  $C_{NaCl}$  at fixed  $C_{SDS}$ , depicting the transition from thick electrostatic double-layer to thin double-layer caused by stronger screening.

The difference between  $R_{HS}$  and micelle radial dimensions  $R_{tot}$  ( $= R_e + \delta$ ) decreases with increasing  $C_{SDS}$  at fixed  $C_{NaCl}$  (Figure 3-14(a-b)). This difference is expected to be the Debye length  $\kappa^{-1}$ , elucidating the double layer thickness caused by the screened electrostatic interaction. By computing the  $R_{tot}$  with  $\kappa^{-1}$  at fixed  $C_{SDS}$  and  $C_{NaCl}$ ,  $R_{tot} + \kappa^{-1}$  (filled circles) is juxtaposed against the equivalent  $R_{HS}$  (open circles) with good agreements at  $C_{SDS} = 20$  mM. The increasing differences between the  $R_{tot} + \kappa^{-1}$  and  $\phi_{HP}$  in high salt solutions ( $C_{SDS} = 80$  mM) imply the accuracy of Hayter-Penfold structure factor in interpreting the intermicellar interactions in high salt SDS solutions. The Debye length at low SDS concentration  $C_{SDS}$  but at high salt concentration is imprecise computed in the Hayter-Penfold structure factor model due to the increasing polydispersity of micelle shape and size (Figure 3-14d).

Micelle volume fraction  $\phi$  is manipulated by the electrosteric repulsion at high salt concentration and can be predicted by the effective volume fraction  $\phi_{HS}$ , the equivalent steric hindrance dimensions  $R_{HS}$ , and the real micellar dimensions  $R_{tot}$  by  $\phi = \phi_{HS} \left( \frac{R_{tot}}{R_{HS}} \right)^3$  (Figure 3-14c-d) under the assumption of same micelle number density at fixed  $C_{SDS}$ . Effective volume fraction  $\phi_{HS}$  determined by the equivalent hard-sphere fits increases linearly with  $C_{SDS}$  in both aqueous and salty solutions shown in Figure 3-14c-d. Volume fraction with an excellent agreement, suggesting that the equivalent hard-sphere model well elucidates repulsive forces by the electrosteric hindrances.

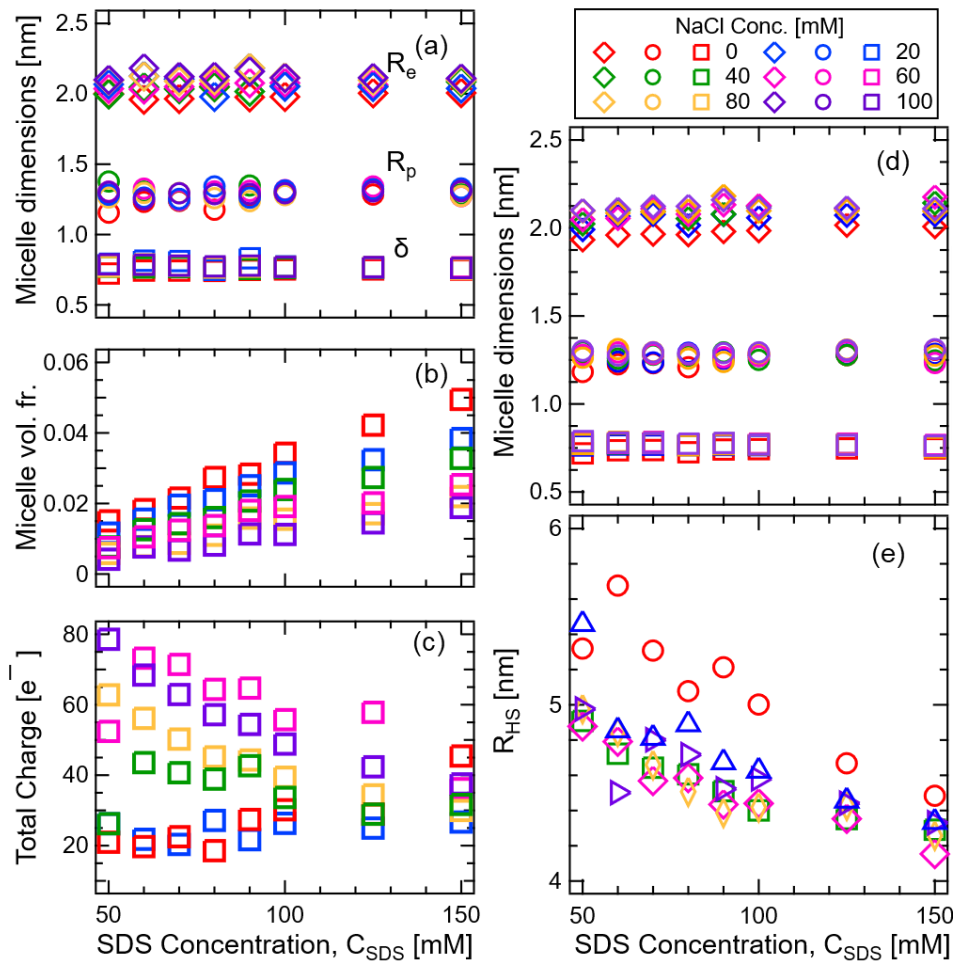


**Figure 3-13. SDS micelle characteristics estimated by Hayter-Penfold structure factor model and equivalent hard-sphere model.** (a) Dimensions of the oblate ellipsoidal SDS micelles: equatorial (along the major axis) and polar radii (along the minor axis),  $R_e$ , and  $R_p$ , respectively and shell thickness  $\delta$ , as obtained from the  $P(q)$  fits to the SAXS spectra. (b) Micelle volume fraction  $\phi$ , and (c) unphysical total charge of the micelles, as estimated from the Hayter-Penfold  $S(q)$  fits to the SAXS spectra. Integrated fits of oblate ellipsoid core-shell form factor and equivalent hard-sphere structure factor: (d) Dimensions of the oblate ellipsoidal SDS micelles: equatorial (along the major axis) and polar radii (along the minor axis),  $R_e$ , and  $R_p$ , respectively

and shell thickness  $\delta$ , as obtained from the  $P(q)$  fits to the SAXS spectra. (e) Effective radius  $R_{HS}$  varies with SDS concentration  $C_{SDS}$  at different salt concentration,  $C_{NaCl}$ .

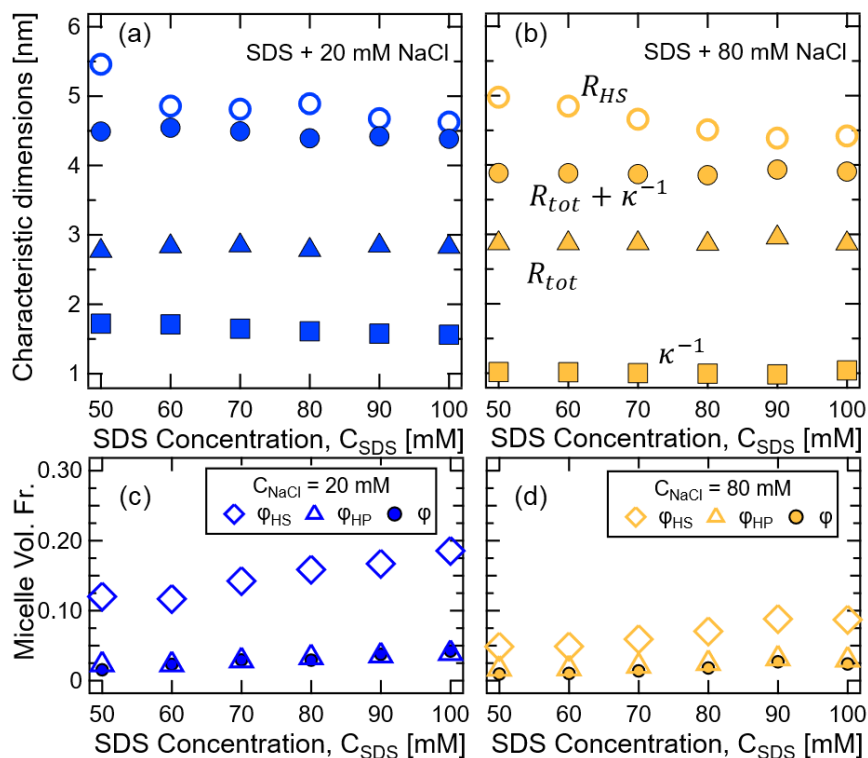


**Figure 3-14. Integrated fits of oblate ellipsoid core-shell form factor and equivalent hard-sphere structure factor. (a-b)** The radial total dimensions of SDS micelles in 20 mM (a) and in 80 mM salt solutions analyzed by core-shell oblate ellipsoidal form factor as  $R_{tot}$ , the effective radius  $R_{HS}$  demonstrating the equivalent hard sphere radius, and  $\kappa^{-1}$  demonstrating the corresponding Debye length. **(c-d)** Effective micelle volume fraction  $\phi_{HS}$  predicted from equivalent hard-sphere structure factor are demonstrated linear proportional to  $C_{SDS}$  at fixed salt concentration  $C_{NaCl} = 20$  mM (a) and 80 mM (b). Similarly, the micelle volume fraction computed by equivalent hard-sphere structure factor model is shown also proportional to  $C_{SDS}$ .

The computed volume fraction  $\phi$  is predicted to demonstrate a proportional relationship with  $C_{SDS}$ . Volume fractions are estimated by Hayter-Penfold structure factor model below  $C_{NaCl} = 60$  mM, while the micelle volume fractions  $\phi$  are computed by equivalent hard-sphere in high salt system (Figure 3-15).

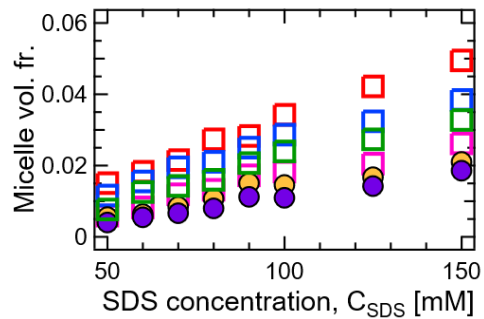


**Figure 3-15.** Micelle volume fraction  $\phi$  of SDS micelles in 0 – 60 mM calculated by Hayter-penfold structure factor model (open squares), and 80-100 mM estimated by the equivalent hard-sphere model (filled circles).

### 3.3. CONCLUSIONS

The size, shape and interactions of micelles formed by sodium dodecyl sulfate (SDS), characterized using small-angle X-ray scattering (SAXS), reveal the addition of salt leads to micelles in bulk that are less spherical, more polydisperse in size, and separated by smaller intermicellar distance. The influence of changing surfactant and salt concentration on micelle interactions and structuring under confinement is examined here by visualizing and analyzing thickness transitions in stratifying foam films. The step size obtained from foam film studies appears to be comparable to the intermicellar distance for salt-free SDS case, but the often-repeated analogy between confinement-induced layering and stratification of charged micelles and charged nanoparticles is found to be inadequate in the presence of salt. The SAXS studies provide careful examination of the influence of salt on the micellar dimensions and screened Coulomb interactions, micelle number density and volume fraction. Additional considerations of salt-induced changes in *CMC*, surface tension, and interfacial charge suggest that the decrease in step size is primarily a manifestation of both a faster decay of correlations and weaker interactions. Addition of salt leads to an increase in polydispersity of size and shape, in addition to a decrease in screening length for electrostatic interactions. Due to an increase in polydispersity, under similar confinement conditions and matched number density, salt-added systems show a lower step size. In contrast with charged micelles, charged nanoparticles preserve their size, shape, and number on addition of salt, and hence exhibit interparticle distances are only a function of particle number density but not the electrolyte concentration. It is well-established that salt addition weakens the screened Coulomb interactions that govern the self-assembly, dynamics, and stability of soft and biological

matter containing charged particles, macromolecules (polyelectrolytes like DNA, proteins), and self-assembled structures (like micelles and vesicles).

Further, we have demonstrated an equivalent hard-sphere model for interpreting intermicellar interactions in both low and high ionic strength. At low ionic strength, the estimated volume fraction from equivalent hard-sphere model shows comparable Hayter-Penfold structure factor model with simplified numerical calculations. At high ionic strength, the equivalent hard-sphere model estimates the micelle volume fraction with the effective hard-sphere radius  $R_{HS}$ , and effective volume fractions  $\phi_{HS}$  gained from electrosteric repulsion interpretations. This approach implies a practical alternative to Hayter-Penfold structure factor model when evaluating the charged colloids volume fraction with the addition of salt.

### 3.4. REFERENCES

1. Ochoa, C.; Gao, S.; Srivastava, S.; Sharma, V., Foam film stratification studies probe intermicellar interactions. *Proc Natl Acad Sci U S A* **2021**, *118* (25).
2. Tanford, C., *The hydrophobic effect: formation of micelles and biological membranes 2d ed.* J. Wiley.: 1980.
3. Klapp, S. H. L.; Grandner, S.; Zeng, Y.; von Klitzing, R., Asymptotic structure of charged colloids between two and three dimensions: the influence of salt. *Journal of Physics: Condensed Matter* **2008**, *20* (49), 494232.
4. Zeng, Y.; Grandner, S.; Oliveira, C. L. P.; Thünemann, A. F.; Paris, O.; Pedersen, J. S.; Klapp, S. H. L.; von Klitzing, R., Effect of particle size and Debye length on order parameters of colloidal silica suspensions under confinement. *Soft Matter* **2011**, *7* (22), 10899.
5. Ludwig, M.; Witt, M. U.; von Klitzing, R., Bridging the gap between two different scaling laws for structuring of liquids under geometrical confinement. *Adv Colloid Interface Sci* **2019**, *269*, 270-276.
6. Hayter, J. B.; Penfold, J., An analytic structure factor for macroion solutions. *Molecular Physics* **1981**, *42* (1), 109-118.
7. Berr, S. S.; Jones, R. R. M., Effect of added sodium and lithium chlorides on intermicellar interactions and micellar size of aqueous dodecyl sulfate aggregates as determined by small-angle neutron scattering. *Langmuir* **1988**, *4* (6), 1247-1251.
8. Bendedouch, D.; Chen, S. H.; Koehler, W. C., Determination of interparticle structure factors in ionic micellar solutions by small angle neutron scattering. *Journal of Physical Chemistry* **1983**, *87* (14), 2621-2628.

9. Kotlarchyk, M.; Chen, S. H., Analysis of small angle neutron scattering spectra from polydisperse interacting colloids. *Journal of Chemical Physics* **1983**, 79 (5), 2461-2469.
10. Bendedouch, D.; Chen, S. H.; Koehler, W. C., Structure of ionic micelles from small angle neutron scattering. *Journal of Physical Chemistry* **1983**, 87 (1), 153-159.
11. Hansen, J.-P.; Hayter, J. B., A rescaled MSA structure factor for dilute charged colloidal dispersions. *Molecular Physics* **1982**, 46 (3), 651-656.
12. Ornstein, L. S.; Zernike, F., Accidental deviations of density and opalescence at the critical point of a simple substance. *PROCEEDINGS OF THE KONINKLIJKE AKADEMIE VAN WETENSCHAPPEN TE AMSTERDAM* **1914**, 17, 793-806.
13. Gawali, S. L.; Zhang, M.; Kumar, S.; Ray, D.; Basu, M.; Aswal, V. K.; Danino, D.; Hassan, P. A., Discerning the Structure Factor of Charged Micelles in Water and Supercooled Solvent by Contrast Variation X-ray Scattering. *Langmuir* **2019**, 35 (30), 9867-9877.
14. Hassan, P. A.; Fritz, G.; Kaler, E. W., Small angle neutron scattering study of sodium dodecyl sulfate micellar growth driven by addition of a hydrotropic salt. *J Colloid Interface Sci* **2003**, 257 (1), 154-62.
15. Itri, R.; Amaral, L. Q., Distance distribution function of sodium dodecyl sulfate micelles by x-ray scattering. *The Journal of Physical Chemistry* **1991**, 95 (1), 423-427.
16. Hayter, J. B.; Zemb, T., Concentration-dependent structure of sodium octanoate micelles. *Chemical Physics Letters* **1982**, 93 (1), 91-94.
17. Espinosa, Y. R.; Grigera, R. J.; Ferrara, C. G., Mechanisms associated with the effects of urea on the micellar structure of sodium dodecyl sulphate in aqueous solutions. *Prog Biophys Mol Biol* **2018**, 140, 117-123.

18. Pisárčik, M.; Devínsky, F.; Pupák, M., Determination of micelle aggregation numbers of alkyltrimethylammonium bromide and sodium dodecyl sulfate surfactants using time-resolved fluorescence quenching. *Open Chemistry* **2015**, *13* (1), 922-931.
19. Hammouda, B., Temperature Effect on the Nanostructure of SDS Micelles in Water. *J Res Natl Inst Stand Technol* **2013**, *118*, 151-67.
20. Nagarajan, R.; Ruckenstein, E., Critical micelle concentration: A transition point for micellar size distribution. *Journal of Colloid and Interface Science* **1977**, *60* (2), 221-231.
21. Bergstrom, M.; Pedersen, J. S., Small-angle neutron scattering (SANS) study of aggregates formed from aqueous mixtures of sodium dodecyl sulfate (SDS) and dodecyltrimethylammonium bromide (DTAB). *Langmuir* **1998**, *14* (14), 3754-3761.
22. Bergstrom, M.; Pedersen, J. S., Structure of pure SDS and DTAB micelles in brine determined by small-angle neutron scattering (SANS). *Physical Chemistry Chemical Physics* **1999**, *1* (18), 4437-4446.
23. Bezzobotnov, V. Y.; Borbely, S.; Cser, L.; Farago, B.; Gladkih, I. A.; Ostanevich, Y. M.; Vass, S., Temperature and Concentration Dependence of Properties of Sodium Dodecyl Sulfate Micelles Determined from Small Angle Neutron Scattering Experiments. *The Journal of Physical Chemistry* **1992**, *92* (20), 5738-5743.
24. Zhang, Y.; Sharma, V., Domain expansion dynamics in stratifying foam films: experiments. *Soft Matter* **2015**, *11* (22), 4408-17.
25. Yilixiati, S.; Rafiq, R.; Zhang, Y.; Sharma, V., Influence of Salt on Supramolecular Oscillatory Structural Forces and Stratification in Micellar Freestanding Films. *ACS Nano* **2018**, *12* (2), 1050-1061.

26. Zhang, Y.; Sharma, V., Nanoridge Formation and Dynamics of Stratification in Micellar Freestanding Films. *Langmuir* **2018**, *34* (3), 1208-1217.
27. Zhang, Y.; Sharma, V., Thickness-Dependent Phase Transition Drives Nanoridge-to-Mesa Instability in Micellar Freestanding Films. *Langmuir* **2018**, *34* (26), 7922-7931.
28. Yilixiati, S.; Wojcik, E.; Zhang, Y.; Sharma, V., Spinodal stratification in ultrathin micellar foam films. *MSDE* **2019**, *4* (3), 626-638.
29. Anachkov, S. E.; Danov, K. D.; Basheva, E. S.; Kralchevsky, P. A.; Ananthapadmanabhan, K. P., Determination of the aggregation number and charge of ionic surfactant micelles from the stepwise thinning of foam films. *Adv Colloid Interface Sci* **2012**, *183-184*, 55-67.
30. Nikolov, A. D.; Kralchevsky, P. A.; Ivanov, I. B.; Wasan, D. T., Ordered micelle structuring in thin films formed from anionic surfactant solutions: II. Model development. *J. Colloid Interface Sci.* **1989**, *133* (1), 13-22.
31. Zhang, Y.; Yilixiati, S.; Pearsall, C.; Sharma, V., Nanoscopic Terraces, Mesas, and Ridges in Freely Standing Thin Films Sculpted by Supramolecular Oscillatory Surface Forces. *ACS Nano* **2016**, *10* (4), 4678-83.
32. Nikolov, A. D.; Wasan, D. T., Ordered micelle structuring in thin films formed from anionic surfactant solutions: I. Experimental. *Journal of Colloid and Interface Science* **1989**, *133* (1), 1-12.
33. Bergeron, V.; Jimenez-Laguna, A. I.; Radke, C. J., Hole formation and sheeting in the drainage of thin liquid films. *Langmuir* **1992**, *8* (12), 3027-3032.
34. Danov, K. D.; Basheva, E. S.; Kralchevsky, P. A.; Ananthapadmanabhan, K. P.; Lips, A., The metastable states of foam films containing electrically charged micelles or particles:

experiment and quantitative interpretation. *Advances in colloid and interface science* **2011**, 168 (1-2), 50-70.

35. Nikolov, A. D.; Wasan, D. T.; Kralchevsky, P. A.; Ivanov, I. B. In *Ordered structures in thinning micellar foam and latex films*, Ordering and Organisation in Ionic Solutions, Kyoto, Japan, Sogami, N. I. a. I., Ed. World Scientific, Singapore: Kyoto, Japan, 1988; pp 302-414.

36. Lee, J.; Nikolov, A.; Wasan, D., Stepwise thinning dynamics of a foam film formed from an anionic micellar solution. *J Colloid Interface Sci* **2017**, 487, 217-222.

37. Langevin, D.; Sonin, A. A., Thinning of soap films. *Advances in Colloid and Interface Science* **1994**, 51, 1-27.

38. Krichevsky, O.; Stavans, J., Micellar Stratification in Soap Films: A Light Scattering Study. *Phys Rev Lett* **1995**, 74 (14), 2752-2755.

39. Bergeron, V.; Radke, C. J., Equilibrium measurements of oscillatory disjoining pressures in aqueous foam films. *Langmuir* **1992**, 8 (12), 3020-3026.

40. Kralchevski, P.; Nikolov, A.; Wasan, D. T.; Ivanov, I., Formation and expansion of dark spots in stratifying foam films. *Langmuir* **1990**, 6 (6), 1180-1189.

41. Krichevsky, O.; Stavans, J., Confined fluid between two walls: The case of micelles inside a soap film. *Physical Review E* **1997**, 55 (6), 7260.

42. Israelachvili, J. N., *Intermolecular and surface forces*. Academic press: 2015.

43. Corrin, M.; Harkins, W. D., The effect of salts on the critical concentration for the formation of micelles in colloidal electrolytes<sup>1</sup>. *Journal of the American Chemical Society* **1947**, 69 (3), 683-688.

44. Sharma, A.; Walz, J. Y., Direct measurement of the depletion interaction in a charged colloidal dispersion. *Journal of the Chemical Society, Faraday Transactions* **1996**, 92 (24), 4997-5004.
45. Piech, M.; Walz, J. Y., Direct measurement of depletion and structural forces in polydisperse, charged systems. *J Colloid Interface Sci* **2002**, 253 (1), 117-29.
46. Tulpar, A.; Van Tassel, P. R.; Walz, J. Y., Structuring of macroions confined between like-charged surfaces. *Langmuir* **2006**, 22 (6), 2876-2883.
47. James, G. K.; Walz, J. Y., Experimental and theoretical investigation of the depletion and structural forces produced by ionic micelles. *Colloids and Surfaces A: Physicochemical and Engineering Aspects* **2014**, 441, 406-419.

**CHAPTER 4**  
**COMB POLYELECTROLYTE STABILIZED COMPLEX COACERVATE**  
**EMULSIONS**

Contents of this chapter are adapted from a manuscript in preparation. Shang Gao; Samanvaya Srivastava; *Manuscript submitted*

Contents of this chapter are adapted from a pending patent. Samanvaya Srivastava; Shang Gao; US 63/187,031, *Patent pending*

**ABSTRACT**

Complex coacervates assemble spontaneously, achieve spatial compartmentalization, and selectively sequester biological molecules while maintaining a membraneless interface with their surroundings. Yet, their use as protocell models and bioreactors have been limited owing to our inability to stabilize coacervate microdroplets and prevent their uncontrolled coalescence. Herein, we introduce a new approach to stabilize complex coacervate microdroplets using comb polyelectrolytes while retaining their membraneless interface, creating membraneless complex coacervate emulsions. Anchoring of comb polyelectrolytes at the coacervate-water interfaces is hypothesized to engender steric repulsion among the coacervate microdroplets and mitigate their coalescence. Tunability of microdroplet size and stability is achieved by regulation of comb polyelectrolyte concentration and molecular weight. Importantly, the comb polyelectrolyte-stabilized coacervate microdroplets spontaneously sequester and retain proteins over extended periods. Moreover, enhanced catalytic activity of proteins and significant (up to 10-fold) acceleration of bioreactions is achieved in stabilized complex coacervate dispersions, even when stored for up to 48 hours. Our findings are expected to expand the utility of complex coacervate

microdroplets as artificial protocells, encapsulants, and bioreactors, and further facilitate their use in pharmaceutical, agricultural, food, and cosmetics formulations.

#### **4.1. INTRODUCTION**

Complex coacervates microdroplets have emerged as attractive protocell models in bottom-up synthetic biology approaches. These self-assembled microdroplets form upon associative phase separation of oppositely charged macromolecules in aqueous solutions, maintain a dynamic equilibrium with their surroundings through a membraneless interface, and remain stable across a wide range of physiochemical conditions (temperature, pH, and ionic strength). The self-assembly processes that drive complex coacervation also result in spontaneous selective sequestration of (bio)molecules into crowded aqueous coacervate environments. Concomitant rapid transport of small molecules across the membraneless coacervate-water interface result in significant acceleration of bioreactions in the coacervate microdroplets. These attributes of coacervate microdroplets distinguish them from membrane-stabilized vesicular protocell models, and have also contributed to their growing utility as protein stabilizers and carriers<sup>1-4</sup> and self-assembled bioreactors.<sup>5,6</sup>

However, the membraneless coacervate-water interface that facilitates many of their bio(techno)logical functions also results in their rapid coarsening through coalescence and Ostwald ripening.<sup>7,8</sup> Synthetic complex coacervate formulations typically condense into aqueous polymer-rich and polymer-lean macro-phases within minutes to hours of mixing.<sup>9</sup> Such macro-phase separation results in restricted transport of small molecules owing to reduced interfacial area between the coacervates and their surroundings. Thus, typical deployment of complex coacervates

as protocell models and bioreactors have been limited to low concentration formulations where droplet coalescence remains restricted.<sup>10,11</sup>

Recent attempts to stabilize complex coacervates have been inspired by strategies adopted to stabilize hydrophobic phases (oils, lipids, etc.) in water. Conjugation of the polyelectrolytes with a neutral block restrict the coarsening of the coacervates at the nanoscale, resulting in complex coacervate micelles.<sup>3,4,12–14</sup> While these micelles have been successfully employed as delivery vehicles for charged biomacromolecules, including nucleic acids<sup>15,16</sup> and proteins,<sup>13,17,18</sup> their small size and relatively low loading capacity for biomolecules have limited their use as viable protocell models and bioreactors. Efforts to stabilize coacervate microdroplets have primarily relied on introduction of additional membranous interfaces around the droplets. For instance, fatty acids,<sup>19</sup> amphiphilic terpolymers,<sup>10,20–24</sup> and lipid-vesicle layers have been incorporated in the complex coacervate formulations that assemble into amphiphilic interfaces around the coacervate droplets, providing steric stabilization against coalescence. However, these approaches achieve stabilization at the expense of introducing a hydrophobic region around the droplets that limit the transport of small hydrophilic molecules across them, require cumbersome preparation steps, and are markedly sensitive to the mixing protocols.<sup>11,25</sup> Hitherto, viable strategies for stabilization of membraneless complex coacervate droplets have not been demonstrated.

Herein, we introduce a new paradigm for stabilization of complex coacervate microdroplets while retaining the membraneless coacervate-water interfaces. Our approach relies on interfacial anchoring of comb polyelectrolytes that introduces steric repulsions among the microdroplets and imparts long-term stability to the microdroplet dispersions. In effect, we create membraneless complex coacervate emulsions. We highlight the simplicity, the versatility, and the robustness of

the stabilization approach and illustrate the tunability of microdroplet size and stability by varying the comb polyelectrolyte characteristics and concentrations. Moreover, we demonstrate that the comb polyelectrolyte-induced stabilization approach does not interfere with spontaneous sequestration of proteins into the coacervate microdroplets. A coupling of macromolecular crowding in the coacervate environment and unhindered transport of small molecule facilitated by large area of the stabilized microdroplet interfaces is shown to enhance the catalytic activity of proteins substantially, and more importantly, retain the enhanced activity over extended time periods. Taken together, our stabilization approach for complex coacervate microdroplets and the advantageous attributes of their stabilized dispersions promise to usher the next generation of complex coacervate-based protocells, encapsulants, stabilizers, and bioreactors.

## 4.2. RESULTS AND DISCUSSIONS

### *Comb Polyelectrolytes Stabilize Complex Coacervate Microdroplets*

Figure 4-1 presents a visual comparison between unstable and stable dispersions of model complex coacervates. Both the complex coacervate dispersions comprise a charge-matched mixture of oppositely charged polyelectrolytes, poly(acrylic acid sodium salt) (PAA,  $MW = 5100$  g/mol) and poly(diallyldimethylammonium chloride) (PDADMAC,  $MW = 8500$  g/mol), along with small amount of polyacrylic acid-comb-polyethylene glycol (PAA-*c*-PEG,  $MW = 39467$  g/mol,  $26 e^-$  at pH = 6, PEG  $MW = 3000$  g/mol) comb polyelectrolytes in the stabilized dispersions. The dispersions are turbid upon initial mixing of their constituents (Figure 4-1A and 4-1B), owing to the presence of complex coacervate microdroplets. Rapid coalescence of the microdroplets and gravity-induced sedimentation in the unstable dispersions resulted in clear solutions with distinct complex coacervate and supernatant phases within a few hours (Figure 4-1A). In contrast,

stabilized coacervate droplets remained dispersed up to 48 hours (Figure 4-1B), with turbidity levels staying nearly constant (Figure 4-1C). Micrographs of the as-mixed unstable and stable formulations both show spherical complex coacervate microdroplets, as expected upon spontaneous mixing of the constituents (Figure 4-1A and 4-1B, respectively). However, while the unstable droplets coalesced into a homogenous phase, spherical microdroplets were still clearly visible in the stable dispersions after 48 hours.

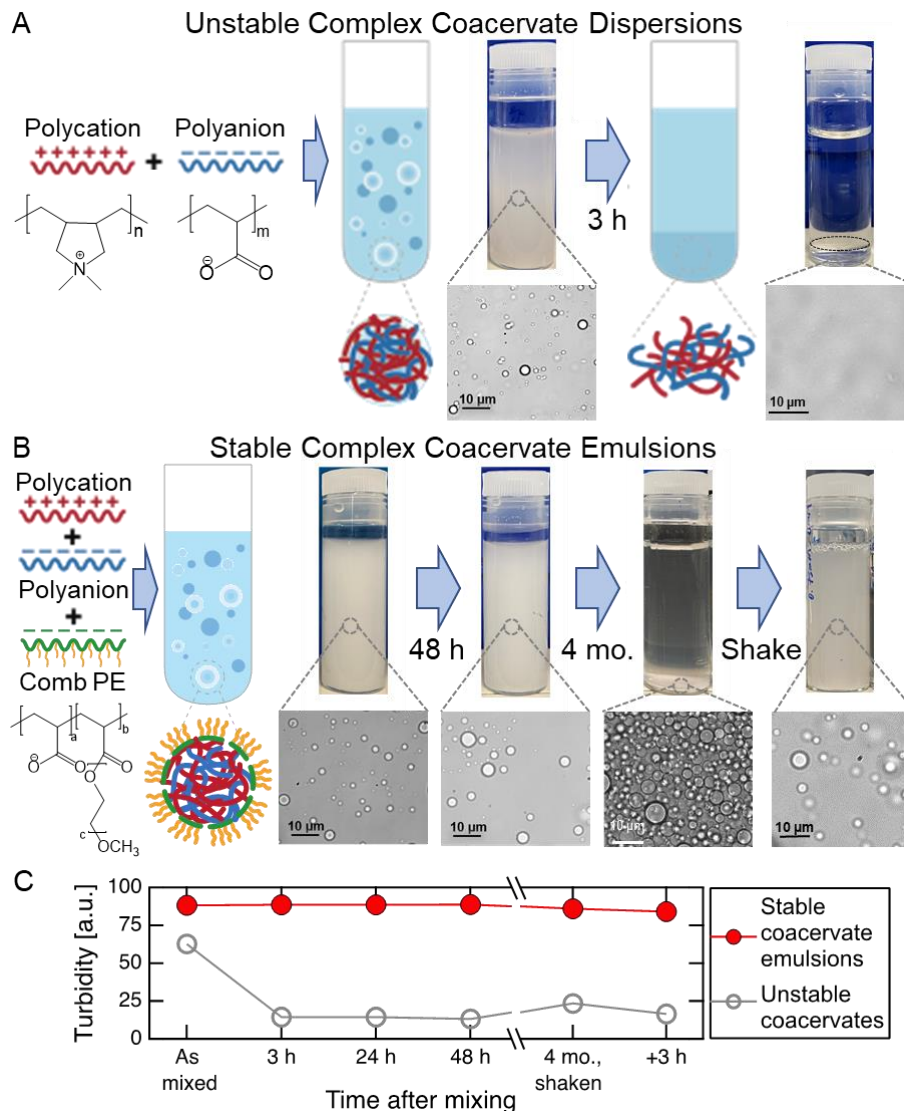


**Figure 4-1: Comb polyelectrolytes stabilize complex coacervate droplets.** (A) Mixing of solutions of oppositely charged polyelectrolytes (38.8 mM ionizable groups, 1:1 charge ratio) lead to formation of turbid dispersions of complex coacervate droplets. The coacervate droplets coalesce readily (within 3 hours) to form a homogenous transparent coacervate phase. The black dashed line denotes the location of the interface between the polymer dense coacervate phase (at the bottom) and the polymer-lean supernatant phase (at the top). Corresponding micrographs

depict coacervate droplets in the as mixed formulations that coalesce into a homogenous coacervate phase within 3 hours. **(B)** Stable complex coacervate emulsions obtained by preparing the same solutions as in (A) with an additional component – anionic comb polyelectrolytes (4.8 mM ionizable groups). The stable complex coacervate emulsions are turbid when prepared and remained turbid for up to 48 hours. Corresponding micrographs reveal distinct micron-sized droplets in the emulsions. Over 4 months, the coacervate droplets settle to the bottom of the vial but do not coalesce, leading to a dense emulsion at the bottom of the vial as revealed from the micrograph of the emulsions taken from the bottom of the vials. Gentle shaking of the vial led to re-dispersion of the coacervate microdroplets, resulting in turbid emulsions. In (A) and (B), scale bars are provided in each micrograph. **(C)** Turbidity is a key indicator of the stability of the emulsions. Turbidity in unstable coacervate dispersions decreased readily within 3 hours, resulting in clear solutions. In contrast, turbidity in the stable coacervate emulsions did not decay up to 48 hours. 4-month aged emulsions, exhibit similar levels of turbidity upon shaking as the freshly prepared samples, and remained turbid for up to 3 hours after shaking.

Comb polyelectrolytes imparted exceptional stability to the coacervate microdroplets. Over 4 months, the coacervate droplets sediment, owing to their large size, yielding clear solutions (Figure 4-1B). Yet, the microdroplets did not coalesce and maintained their spherical morphology, as is evident from micrographs of the dense dispersion of coacervate microdroplets, highlighting the effectiveness of comb polyelectrolytes in preventing microdroplets coalescence (Figure 4-1B). Moreover, the sedimented droplets readily dispersed upon gentle shaking of the vials (Figure 4-1B). Correspondingly, turbidity in the shaken vials recovered to levels similar to the as-mixed emulsions and persisted for a few hours after shaking (Figure 4-1C).

Typical liquid-liquid interfaces, such as oil-water interface, possess a high interfacial tension, and thus provide a strong driving force for interfacially active molecules to self-assemble at the interfaces. In contrast, coacervate-water interfaces are characterized by low interfacial tensions,<sup>26</sup> thus requiring multipoint anchoring to localize the polymeric stabilizers at the interface. The unique architecture of the comb polyelectrolytes, consisting of multiple PEO chains attached to the PAA backbone, is posited to enable such multipoint anchoring of the backbone on the surface of the coacervate droplets while the neutral side chains remain in the supernatant and restrict the complete assimilation of the backbone in the coacervate phase. The PEO side chains, with a Flory radius of  $\sim 5$  nm, are thus hypothesized to form a dense corona around the microdroplets, providing steric repulsion among them and restricting their coalescence, thus imparting long-term stability to the dispersions.

Reducing the strength of the multipoint anchoring of the charge-bearing backbone of the comb polyelectrolytes can therefore be anticipated to hinder their interfacial assembly and resulting stabilization of the coacervate microdroplets. This was consistent with our observations that while

comb polyelectrolytes with varying lengths of the PAA backbone and the PEG side chains were all effective at inhibiting droplet coalescence (Figures S1 and S2), decreasing the PEG length of the comb polyelectrolyte backbone led to poorer stabilization of the coacervate droplets and enhanced settling in the coacervate emulsions (Figure S2, same charge density at pH = 6,  $\sim 25 e^-$ ). Similarly, diblock polymers comprising a charge-bearing block and a neutral block did not impart stability to coacervate droplets, ascribable to their insufficient interfacial absorption resulting in their assimilation of the polymers in the coacervate droplets (Figure S3). At the same time, the sterically hindered inability of the comb polyelectrolytes to assimilate into the coacervate phase also meant that, when mixed with oppositely charged polyelectrolytes, comb polyelectrolytes did not form any self-assembled structures while diblock polyelectrolytes readily formed polyelectrolyte complex micelles (Figure S3).

#### *Relative Concentrations of Linear and Comb Polyelectrolytes Dictate Complex Coacervate Microdroplets Size and Stability*

Both the extent of stabilization and the size of the stabilized complex coacervate droplets is controllable by tuning the relative concentrations of the comb and the linear polyelectrolytes. As shown in Figure 4-2A, increasing the comb polyelectrolyte concentration,  $C_{CPE}$  in formulations containing a constant concentration of the constituent polyelectrolytes (PAA and PDADMAC)  $C_{PE}$  resulted in reduced settling of the complex coacervate droplets. Concomitantly, the mean diameter of the droplets  $D$  in as-mixed formulations containing a constant  $C_{PE}$  decreased initially before increasing marginally and plateauing with increasing  $C_{CPE}$  (Figure 4-2(B-D)). The total interfacial area that can be stabilized is expected to be proportional to  $C_{CPE}$ . Thus, upon increasing  $C_{CPE}$ ,  $D$  decreased until all droplets possessed a monolayer of comb polyelectrolytes on their

surfaces. Further increasing  $C_{CPE}$  resulted in multilayer adsorption on the droplets surfaces, resulting in slight increase of the droplets sizes, followed by saturation of the droplet surfaces, and plateauing of the droplet size. The extent of saturation of the droplet surfaces also dictated their temporal stability. While marginal coarsening of the droplets and settling was observed over 48 hours at low  $C_{CPE}$  (Figure 4-2E and 4-2F), droplet size distribution remained nearly unchanged at high  $C_{CPE}$  (Figure 4-2G).

At the same time, the total volume of the complex coacervate phase is expected to be proportional to  $C_{PE}$ .<sup>27</sup> Therefore, larger  $C_{CPE}$  were required to stabilize formulations with high  $C_{PE}$ . Correspondingly,  $D$  was found to increase linearly with increasing  $C_{PE}$  at a constant  $C_{CPE}$  (Figure 4-2(E-G)). In formulations with low  $C_{CPE}$  and high  $C_{PE}$  (Figure 4-2E), the comb polyelectrolytes were insufficient to stabilize the larger volume of the coacervate phase into small droplets that remain suspended in the emulsions, resulting in unstable formulations.

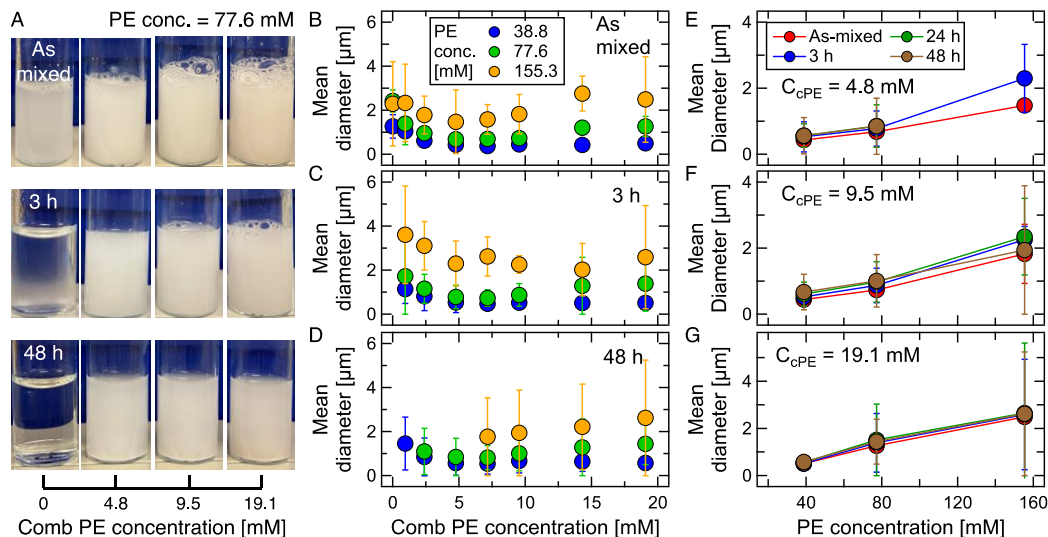


**Figure 4-2: Droplet size in complex coacervate emulsions is controlled by the linear polyelectrolyte and the comb polyelectrolyte concentrations.** (A) Stable complex coacervate emulsions comprising oppositely charged polyelectrolytes (77.6 mM ionizable groups, 1:1 charge ratio) with increasing concentration, expressed in mM of ionizable groups, of comb polyelectrolyte stabilizers. Photographs are taken from different times, indicated as “as mixed”, 3 hours, and 48 hours after mixing. Turbidity in the samples is a key factor for indicating the stability of the emulsions. (B-D) Evolution of the mean diameter (by volume) of the complex coacervate droplets with comb polyelectrolyte concentration (expressed in mM of ionizable groups) in formulations comprising polyelectrolyte concentrations (expressed in concentration of ionizable groups, 1:1 charge ratio) ranging from 38.8 mM to 155.3 mM measured at different times, indicated as “as mixed” (B), 3 hours (C), and 48 hours (D) after mixing. Droplet size underwent a nonmonotonic trend – decreasing initially before increasing and finally plateauing – with comb polyelectrolyte concentration. (E-G) Evolution of the mean diameter (by volume) of the complex coacervate droplets with increasing polyelectrolyte concentrations (expressed in concentration of ionizable

groups, 1:1 charge ratio) and time after mixing, at constant comb polyelectrolyte concentration (expressed in mM of ionizable groups) of 4.8 mM (E), 9.5 mM (F), and 19.1 mM (G). Droplet sizes increase almost linearly with PE concentration. Temporal coarsening of droplets reduced with increasing comb polyelectrolyte concentrations. In (D) and (E), settling occurred within 24 hours for samples with the highest polyelectrolyte concentration and low comb polyelectrolyte concentrations, and therefore droplet sizes are not shown. In (B-G), droplet sizes were measured using dynamic light scattering and averaged from triplicate samples at each concentration and three measurement trials for each sample. Filled symbols denote data measured from unperturbed samples. Errors are calculated through the mean standard deviations of the measurements. Error bars are shown when they are larger than the symbols. We note that the size distribution of the coacervate droplets was obtained by dynamic light scattering (DLS) operated in backscattering mode since optical microscopy depicts only the large droplets that sediment to the bottom of the vials.

Dilution of the stabilized dispersions did not undermine the stability of the complex coacervate microdroplets. Dilution from concentrated homogenous mixtures of the linear and comb polyelectrolytes resulted simultaneous coacervation of the linear polyelectrolytes and interfacial absorption of the comb polyelectrolytes. Thus, a single-phase mixture of the oppositely charged linear polyelectrolytes and the comb polyelectrolytes, when diluted 12-, 24-, 30-, 48-, and 120-fold by addition of water, resulted in stable complex coacervate emulsions that remained turbid up to 48 hours after dilution (Figure S4).

Order of mixing of the linear and comb polyelectrolytes also did not affect the stability of the microdroplets. The results shown in in Figures 4-1 and 4-2 followed a mixing order wherein the comb polyelectrolyte was introduced in the mixture after the polycation but before the polyanion. Other mixing sequences, including mixing of the polycation and the polyanion before the addition of the comb polyelectrolyte and introduction of the comb polyelectrolyte first followed by the addition of the polycation and the polyanion also led to stable dispersions of the complex coacervate droplets (see Figure S5). These results, when combined with resilience against dilution, demonstrate the strong interfacial affinity of the comb polyelectrolytes in aqueous complex coacervate dispersions and highlighting the versatility of the approach demonstrated here to produce stable coacervate emulsions.

### *Spontaneous Sequestration of Proteins in Stabilized Complex Coacervate Microdroplets*

Proteins sequester spontaneously into the comb polyelectrolyte-stabilized complex coacervate microdroplets.<sup>28</sup> Mixing of fluorescein isothiocyanate labeled bovine serum albumin (FITC-BSA) with the linear and comb polyelectrolytes resulted in strong localization of the proteins inside the stabilized droplets, as monitored by fluorescence imaging. BSA, with a net negative charge of  $18 e^-$  at pH  $\sim 6$ , was found to distribute uniformly inside the droplets, as indicated by the overlaid brightfield and fluorescent images (Figure 4-3A, rows 1 and 2). Moreover, the microdroplet morphology (Figure 4-3A, rows 1 and 2) and sizes (Figure 4-3B) in as-mixed formulations were similar in unstable and stabilized dispersions. Yet, while the unstable protein-loaded coacervate droplets (Figure 4-3A, row 1) coalesced readily, resulting in clear solutions with distinct coacervate and supernatant phases, the stabilized coacervate microdroplets maintained their stability up to 48 hours (Figure 4-3A, row 3). The microdroplets coarsened marginally (Figure 4-3B), akin to coacervate microdroplets without proteins (Figure 4-2(E-G)). Moreover, FITC-BSA remained localized within the stabilized microdroplets up to 48 hours (Figure 4-3A, row 3).

The extent of protein localization inside the microdroplets was quantified by estimating the ratio of the fluorescent intensity inside and outside the droplets. A strong partitioning of FITC-BSA inside the stabilized coacervate microdroplets was revealed (Figure 4-3C), in agreement with previous studies.<sup>1</sup> Nominal loss of protein from the stabilized microdroplets was observed; the protein partitioning coefficient in the stable microdroplets after 48 hours of preparation were comparable with freshly prepared unstable complex coacervate formulations (Figure 4-3C).

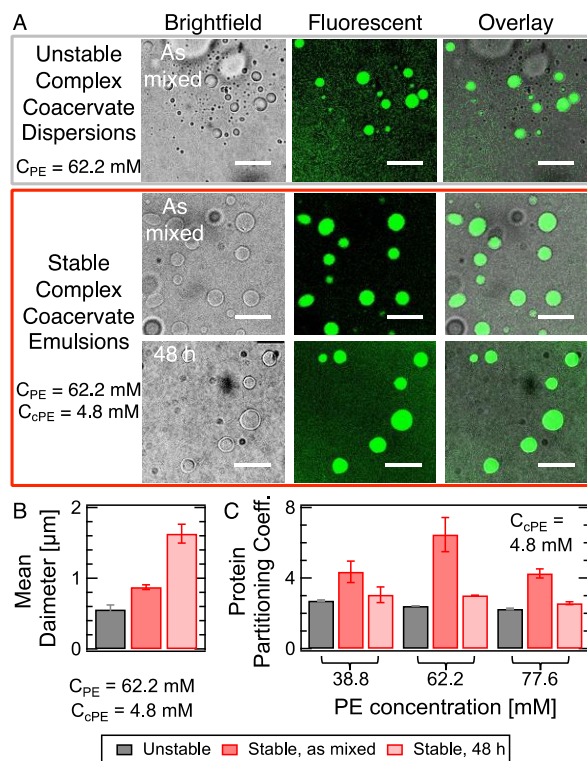


**Figure 4-3: Proteins partition preferentially in coacervate droplets in the comb polyelectrolyte stabilized coacervate emulsions.** (A) Confocal brightfield (left), fluorescence (middle) and overlaid (right) micrographs showing FITC-labelled BSA localized in unstable coacervates droplets in as mixed formulations (row 1) and in stabilized complex coacervate droplets in as mixed formulations (row 2) and after 48 hours of aging (row 3). The droplets were visualized upon settling on nonadherent substrates. FITC-BSA concentration was 1 mM (charge concentration). (B) Mean diameter of FITC-BSA loaded unstable and stable coacervate droplets in formulations corresponding to those depicted in (A). Volume mean diameters were estimated from measurements on triplicate samples and three measurement trials for each sample. (C) The protein partitioning coefficient for FITC-BSA into the coacervate phase, as estimated by the ratio of the fluorescence intensity inside and outside the droplets, for as mixed unstable dispersions, as

mixed stable emulsions, and stable emulsions aged 48 hours of complex coacervate droplets as a function of polyelectrolyte concentration.

#### *Enhanced Catalytic Activity of Proteins in Stabilized Complex Coacervate Microdroplets*

Lipase mediated degradation of *p*-nitrophenyl butyrate to *p*-nitrophenol (Figure 4-4A) was carried out in stabilized complex coacervate microdroplets to highlight their utility as membraneless protocells and bioreactors. The evolution of the absorbance spectra of *p*-nitrophenol (at ~ 405 nm) provided a facile route to quantify its production rate and the catalytic activity of lipase (Figure 4-4C).<sup>29-31</sup> Aqueous mixtures of lipase, oppositely charge linear polyelectrolytes and comb polyelectrolytes formed stable complex coacervate microdroplets wherein lipase, bearing 14  $e^-$  at pH = 6, co-localized with the linear polyelectrolytes. Enzymatic degradation of *p*-nitrophenyl butyrate in such dispersions occurred rapidly, manifesting as a fast growth of the absorbance spectra before plateauing (Figure 4-4C, see also Figure S6). Expectedly, the growth of the absorbance spectra in the stabilized dispersions was significantly faster than the corresponding spectra evolution in lipase solutions. However, surprisingly, the spectra evolution in the stabilized dispersions were faster than even the unstable complex coacervate dispersions.

Going beyond the results suggesting co-localization of FITC-BSA (Figure 4-3) demonstrating that comb polyelectrolytes do not interfere with the co-localization of proteins in the coacervate microdroplets, these results indicate that comb polyelectrolytes that are anchored on the droplet surfaces (i) do not impede with the transport of small molecule substrate (*p*-nitrophenyl butyrate) or product (*p*-nitrophenyl) in and out of the droplets, respectively, (ii) do not interfere with the catalytic action of lipase, and (iii) promote the biodegradation reaction. Moreover, increasing the comb polyelectrolyte concentration led to a faster evolution of the absorbance spectra, indicating

even further acceleration of the biodegradation of *p*-nitrophenyl butyrate to *p*-nitrophenol in the stabilized coacervate microdroplets.

An estimation of the enzymatic reaction rate ( $1/t_{1/2}$ ) was obtained as the inverse of half of the time required for the plateauing of the absorbance spectra. Depicted in Figure 4-4D, it is evident that localization of lipase in complex coacervates led to a two-fold increase in the *p*-nitrophenol production rate. This enhancement is consistent with previous reports<sup>29,30</sup> and has been attributed to enhanced macromolecular crowding in the coacervate environments.<sup>30,32,33</sup> Stabilizing the coacervate droplets by addition of comb polyelectrolytes led to a further increase in *p*-nitrophenol production rates, with up to 5-fold increase and 10-fold increase as compared to reaction rates in complex coacervates and freely suspended lipase in solution, respectively (Figure 4-4D). The reaction rates were also tunable by varying the comb polyelectrolyte concentrations, with higher  $C_{CPE}$  resulting in smaller droplets (Figure 4-4B) and higher reaction rates (Figure 4-4D). We posit that the coacervate microdroplets maintain a large membraneless interfacial area in the stabilized dispersions while the comb polyelectrolytes do not interfere with the transport of small molecules, resulting in swift transport of small molecules in and out of the coacervate droplets, facilitating the bioreaction.

Temporal stability of the coacervate-water interface had a distinct influence on the bioreaction rate in the complex coacervates. As the coacervate droplets coalesced into a homogenous coacervate phase in the unstable formulations, the bioreaction rate declined markedly to approach reaction rates in aqueous protein solutions (Figures 4-4E and 4-4F), thus relinquishing all the advantages of carrying out the bioreaction in a coacervate environments. In contrast, the stabilized coacervate microdroplets remained in dispersed state up to 48 hours (with minor coarsening of droplets, see

Figure 4B), enabling unmitigated transport of substrate and product molecules and preserving the *p*-nitrophenyl butyrate biodegradation rates (Figures 4-4E and 4-4F).

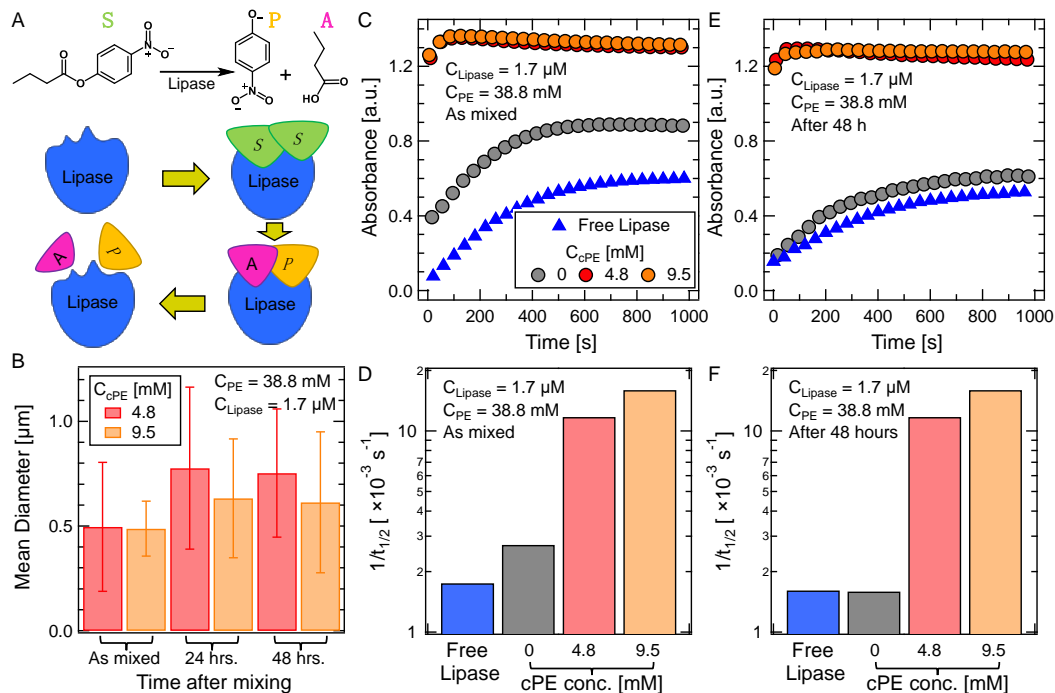


**Figure 4-4: Activity of enzymes is markedly enhanced upon localization in stabilized complex coacervate microdroplets.** (A) Schematics depicting the lipase-mediated degradation of *p*-nitrophenyl butyrate to produce *p*-nitrophenol. (B) Temporal evolution of the mean diameter of stabilized coacervate droplets with co-localized lipase. Volume mean diameters were estimated from measurements on triplicate samples and three measurement trials for each sample. (C) Temporal evolution of the absorbance at  $405 \text{ nm}^{-1}$  upon addition of *p*-nitrophenyl butyrate to an aqueous solution of lipase, unstable complex coacervates dispersions with lipase localized in the unstable coacervate droplets, and complex coacervate emulsions where lipase is localized in stabilized microdroplets. The activity of lipase is revealed by the temporal evolution of the absorbance spectra of the *p*-nitrophenol produced upon enzymatic degradation of *p*-nitrophenyl butyrate. The absorbance spectra for coacervate emulsions evolved at a significantly faster rate as compared to lipase solution or unstable coacervate dispersions, denoting enhanced reaction rates

in solutions where enzymes were localized in stabilized microdroplets. **(D)** The reaction rate ( $1/t_{1/2}$ ), estimated from the absorbance spectra, in formulations corresponding to (C). **(E and F)** Temporal evolution of the absorbance at  $405\text{ nm}^{-1}$  and the reaction rate ( $1/t_{1/2}$ ) in formulations corresponding to (C) but aged for 48 hours before addition of *p*-nitrophenyl butyrate.

### 4.3. CONCLUSIONS

In summary, we have introduced a methodology to abate coalescence of complex coacervate microdroplets by employing comb polyelectrolyte stabilizers. The stabilized microdroplets retain their membraneless interface with their surroundings yet remain stable for months and do not coalesce even when placed in proximity of other microdroplets. Moreover, we have demonstrated that microdroplet stabilization is independent of the formulation processing routes and a facile tuning of the microdroplet size and stability can be achieved by varying the comb polyelectrolyte size and concentrations.

Proteins, when introduced in the formulations, partitioned spontaneously into the stabilized microdroplets, and remained localized in them up to 48 hours. Macromolecular crowding in the coacervate environment enhanced the catalytic activity of proteins by enhancing diffusion of substrate molecules and their binding affinity with protein. The stabilized coacervate-water interfaces further accelerated protein catalyzed reactions by up to 10-fold by promoting rapid transport of the small molecule substrate and products in and out of the coacervate microdroplets. The stabilization of proteins in the microdroplets and of the microdroplets against coalescence also meant that protein-containing formulations retained their ability to catalyze and accelerate biochemical reactions even days after preparation. Thus, the comb polyelectrolyte-stabilized coacervate microdroplets can be envisioned as stable protein storage platforms that retain the biomolecules partitioned into them and conserve their activity over extended durations.

We envision that the long-term stability and the protein encapsulation attributes of the complex coacervate microdroplets will be key in their development as synthetic protocells<sup>34</sup> and colloidal self-assembled microreactors<sup>22,33,35</sup> sustaining and supporting cell-free biosynthesis. Furthermore,

we anticipate that the stabilization approach demonstrated here provides a platform for developing complex coacervate emulsions as protein encapsulants,<sup>1</sup> stabilizers, and delivery vehicles<sup>36</sup> in pharmaceutical,<sup>37</sup> biomedical,<sup>38</sup> agricultural,<sup>39–42</sup> food,<sup>43</sup> and cosmetics<sup>44,45</sup> formulations.

#### **4.4. MATERIALS AND METHODS**

##### *Preparation of stock polyelectrolyte solutions*

Poly(acrylic acid sodium salt) (PAA, molecular weight 5100 g/mol, in powder form), bovine serum albumin (BSA, molecular weight 66kDa, lyophilized powder), lipase from *Candida rugosa* (molecular weight 58kDa, lyophilized powder), *p*-nitrophenyl butyrate, and fluorescein isothiocyanate (FITC) were purchased from Millipore Sigma. Poly(diallyldimethylammonium chloride) (PDADMAC) (molecular weight 8500 g/mol) was purchased from Polysciences, Inc. as a 28 wt% aqueous solution. Comb polyelectrolytes (MasterGlenium7500, MVA2808, MVA2500 and MVA2453) were obtained from BASF. FITC-labelled BSA (FITC-BSA) was synthesized following previously published protocols.<sup>46</sup>

##### *Preparation of Complex Coacervate Dispersions*

Stock solutions of the linear polyelectrolytes, the comb polyelectrolyte and water were mixed in appropriate amounts to produce complex coacervate dispersions. All dispersions contained charge-matched amounts of the oppositely charged linear polyelectrolytes. In dispersions containing proteins (FITC-BSA or lipase), protein stock solutions were also added to the dispersions following the adding sequence: PDADMAC, water, comb polyelectrolyte, protein, and PAA.

##### *Optical and Fluorescence Microscopy*

Confocal microscopy Inverted confocal microscope (Leica, Confocal SP8-STED/FLIM/FCS) with a 100-X oil-immersion objective was employed to obtain brightfield and fluorescence images of complex coacervate dispersions. A small aliquot (~6  $\mu\text{L}$ ) of the complex coacervate dispersions was sandwiched between silanized glass cover slips prior to imaging.

#### *Turbidity measurements*

Turbidity measurements of all dispersions were carried out using a plate reader equipped with a UV spectrophotometer (Tecan Infinite M1000 Pro). 250  $\mu\text{L}$  dispersions were prepared in a 96-well plate (flat bottom, transparent, Costar). The well-plate was shaken for 10 seconds before turbidity measurements. Turbidity scale was defined by  $100\% - T_{580\text{nm}}\% = 10^{(2-\text{Absorbance})}$ .

#### *Absorbance Measurements*

Absorbance at 405 nm of these samples were measured using UV spectrophotometer (Tecan Infinite M1000 Pro). 50  $\mu\text{L}$  of samples (complex coacervates or controls) were placed in the 96-well plate. 150  $\mu\text{L}$  of *p*-nitrophenyl butyrate solutions, prepared in pH = 7.4 PBS buffer, were added into each well (yielding 0.1 mM *p*-nitrophenyl butyrate in each well) before measuring the absorbance at 405 nm for 60 mins at 40 s intervals.

#### *Droplet size measurements with Dynamic Light Scattering*

Dynamic light scattering (DLS) analysis was carried out on Malvern Zetasizer Nano to assess the hydrodynamic radius of the microdroplets in all the dispersions. Three samples of each dispersion were prepared, and three trials were carried out on each sample. Standard deviations on the particle sizes of each condition were calculated on the triplicate samples and three measurements of each sample.

#### 4.5. SUPPLEMENTARY FIGURES

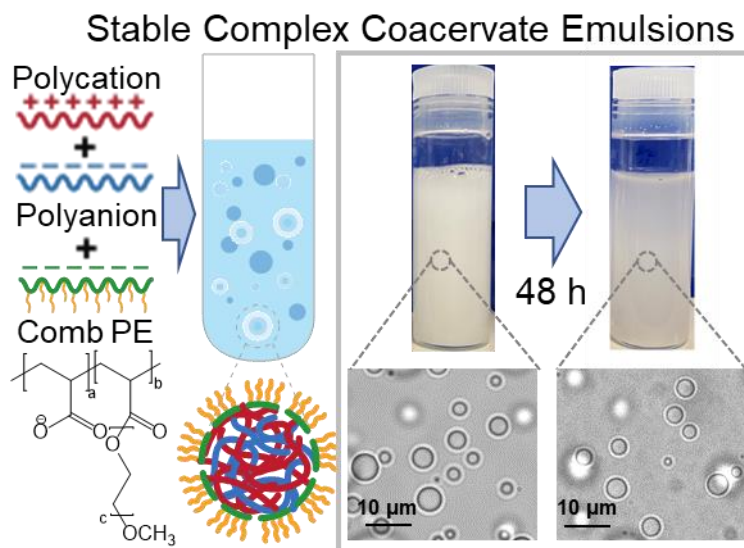


**Figure 4-S1: Comb polyelectrolytes PAA<sub>47-co</sub>-PEG<sub>25</sub> stabilize complex coacervate droplets.**

Stable complex coacervate emulsions obtained by mixing of solutions of oppositely charged polyelectrolytes (38.8 mM ionizable groups, 1:1 charge ratio) with an additional component – anionic comb polyelectrolytes (4.8 mM ionizable groups). The stable complex coacervate emulsions are turbid when prepared and remained turbid for up to 48 hours. Corresponding micrographs reveal distinct micron-sized droplets in the emulsions.

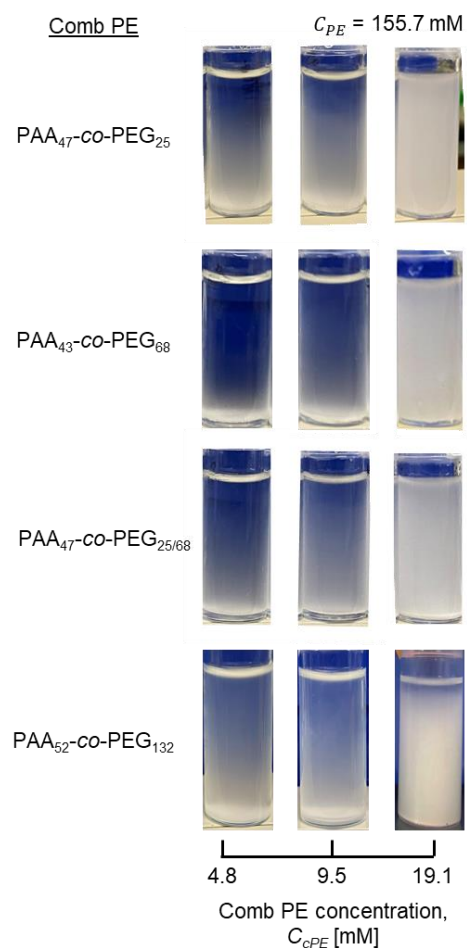


**Figure 4-S2: Complex coacervate emulsions stability is controlled by comb polyelectrolyte PEG lengths and the comb polyelectrolyte concentrations.** Stable complex coacervate emulsions comprising oppositely charged polyelectrolytes (155.7 mM ionizable groups, 1:1 charge ratio) with increasing concentration, expressed in mM of ionizable groups, of comb polyelectrolyte stabilizers PAA<sub>52</sub>-co-PEG<sub>132</sub> and PAA<sub>43</sub>-co-PEG<sub>68</sub>, PAA<sub>47</sub>-co-PEG<sub>25</sub>, PAA<sub>47</sub>-co-PEG<sub>25/68</sub>. Charge density of PAA<sub>52</sub>-co-PEG<sub>132</sub> and PAA<sub>43</sub>-co-PEG<sub>68</sub> two comb polyelectrolyte stabilizers are  $\sim 25 e^-$  at pH = 6. Charge density of PAA<sub>47</sub>-co-PEG<sub>25</sub> and PAA<sub>47</sub>-co-PEG<sub>25/68</sub> two comb polyelectrolyte stabilizers are  $\sim 32, \sim 33 e^-$  at pH = 6. Photographs are taken from 48 hours after mixing.

## Unstable Complex Coacervate Dispersions

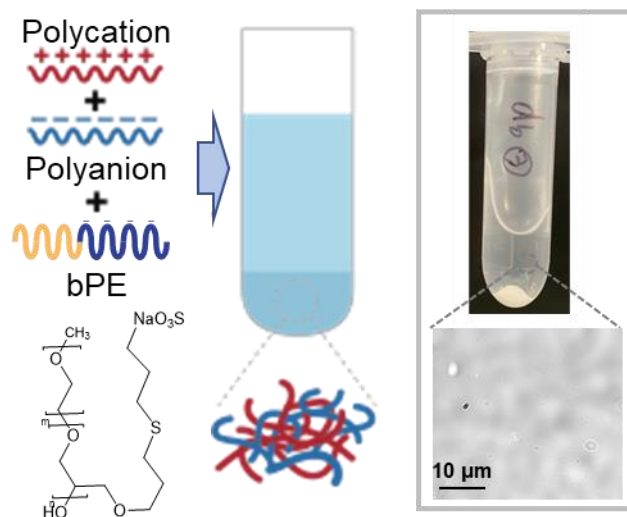


**Figure 4-S3: Anionic diblock polyelectrolytes PEG<sub>113</sub>-PAGE<sub>30</sub> does not stabilize complex coacervate droplets.** Unstable precipitates are obtained by mixing of solutions of oppositely charged polyelectrolytes (38.8 mM ionizable groups, 1:1 charge ratio) with anionic diblock polyelectrolytes PEG<sub>113</sub>-PAGE<sub>30</sub> (4.8 mM ionizable groups). Corresponding micrographs reveal no micron-size droplets in the supernatant.

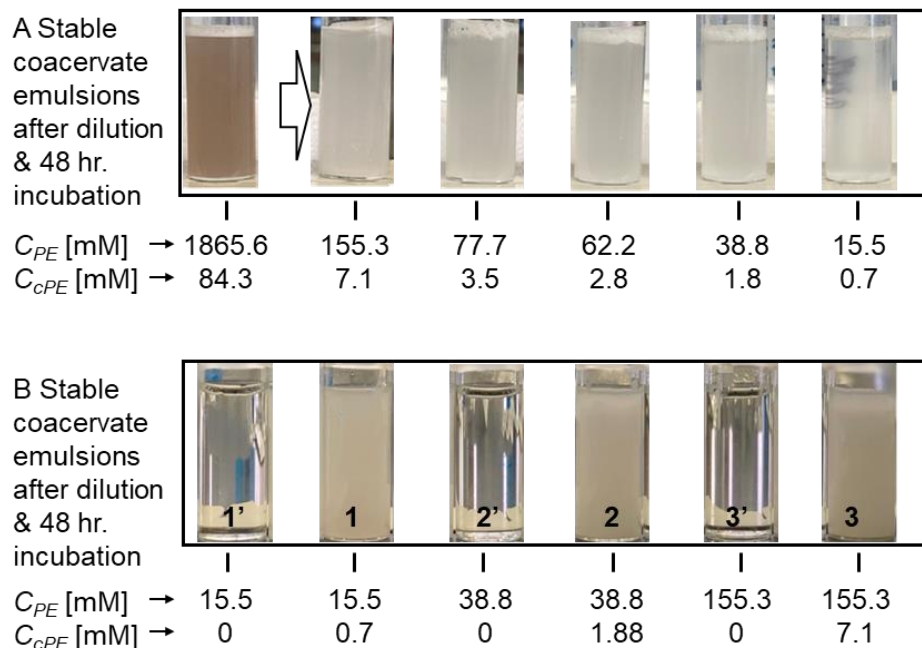


**Figure 4-S4: Emulsification can be stimulated by dilution of concentrated single-phase solution of linear polyelectrolytes and comb polyelectrolytes.** (A) Dilution of single-phase solution comprising oppositely charged linear polyelectrolyte and anionic comb polyelectrolyte into stable complex coacervate emulsions following 12-, 24-, 30-, 48-, and 120-fold dilutions. Photographs are taken 48 hours after dilution. Total linear polyelectrolyte concentration and comb polyelectrolyte concentration of the diluted samples are indicated. (B) A comparison of diluted unstabilized (1'-3') and stabilized (1-3) complex coacervate formulations, beginning with single-phase solution comprising oppositely charged linear polyelectrolyte (1865.6 mM charge concentration) and a single-phase solution comprising a mixture of oppositely charged linear polyelectrolyte (1865.6 mM charge concentration) and anionic comb polyelectrolyte (84.3 mM charge concentration). Photographs taken 48 hours after dilution.

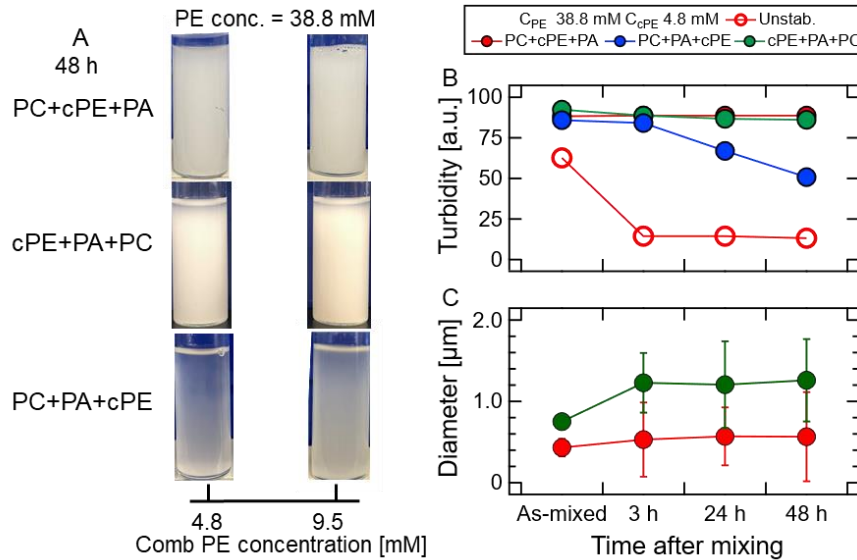


**Figure 4-S5: Mixing sequences of linear polyelectrolytes and comb polyelectrolytes do not impact the stability of complex coacervate emulsions.** Stable complex coacervate emulsions with the mixing sequence as PC+cPE+PA, cPE+PA+PC, PC+PA+cPE comprising oppositely charged polyelectrolytes (38.8 mM ionizable groups, 1:1 charge ratio) with increasing concentration, expressed in mM of ionizable groups, of comb polyelectrolyte stabilizers. Photographs are taken from different times, indicated as “as mixed”, and 48 hours after mixing. **(B)** Evolution of turbidity with time of different mixing sequences. Turbidity in unstable coacervate dispersions decreased readily within 3 hours, resulting in clear solutions. In contrast, turbidity in the stable coacervate emulsions did not decay up to 48 hours with different mixing sequences including PC+cPE+PA (red), PC+PA+cPE (blue), cPE+PA+PC (green). **(C)** Evolution of the mean diameter (by volume) of the complex coacervate droplets with time indicated as “as mixed”, 3 hours, 24 hours and 48 hours after mixing in formulations comprising polyelectrolyte concentrations (38.8 mM ionizable groups, 1:1 charge ratio) of two different mixing sequences.

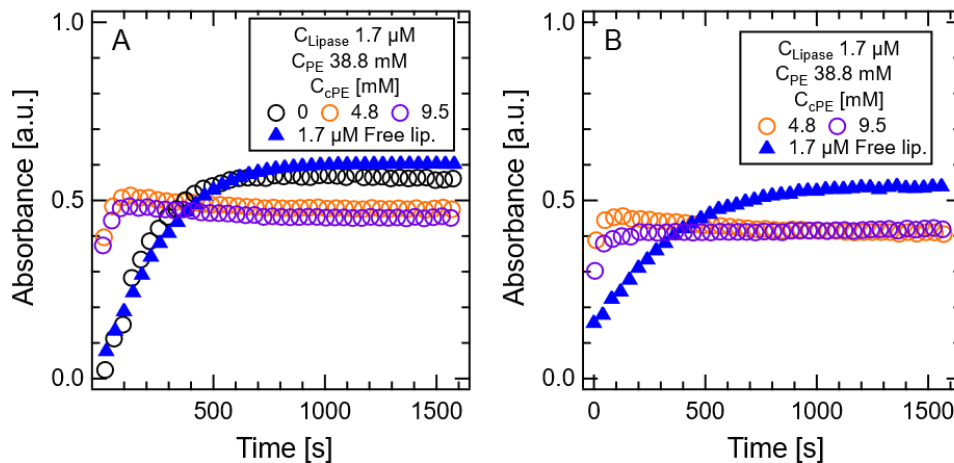


**Figure 4-S6: Activity of enzymes is markedly enhanced upon localization in stabilized complex coacervate microdroplets.** (A) Temporal evolution of the absorbance at 405 nm<sup>-1</sup> upon addition of *p*-nitrophenyl butyrate to an aqueous solution of lipase, unstable complex coacervates dispersions with lipase localized in the unstable coacervate droplets, and complex coacervate emulsions where lipase is localized in stabilized microdroplets. The absorbance values of stabilized complex coacervates undergoing enzymatic reactions (depicted in orange and purple) are obtained by subtracting from their backgrounds (the same formulations without substrates). The activity of lipase is revealed by the temporal evolution of the absorbance spectra of the *p*-nitrophenol produced upon enzymatic degradation of *p*-nitrophenyl butyrate. The absorbance spectra for coacervate emulsions evolved at a significantly faster rate as compared to lipase solution or unstable coacervate dispersions, denoting enhanced reaction rates in solutions where enzymes were localized in stabilized microdroplets. (B) Temporal evolution of the absorbance at 405 nm<sup>-1</sup> and the reaction rate ( $1/t_1$ ) in formulations corresponding to (A) but aged for 48 hours before addition of *p*-nitrophenyl butyrate.

#### 4.6. REFERENCES

- (1) Black, K. A.; Priftis, D.; Perry, S. L.; Yip, J.; Byun, W. Y.; Tirrell, M. Protein Encapsulation via Polypeptide Complex Coacervation. *ACS Macro Lett.* **2014**, *3* (10), 1088–1091. <https://doi.org/10.1021/mz500529v>.
- (2) McCall, P. M.; Srivastava, S.; Perry, S. L.; Kovar, D. R.; Gardel, M. L.; Tirrell, M. V. Partitioning and Enhanced Self-Assembly of Actin in Polypeptide Coacervates. *Biophys. J.* **2018**, *114* (7), 1636–1645. <https://doi.org/10.1016/j.bpj.2018.02.020>.
- (3) Kataoka, K.; Miyata, K.; Nishiyama, N.; Kataoka, K. Rational Design of Smart Supramolecular Assemblies for Gene Delivery: Chemical Challenges in the Creation of Artificial Viruses. *Chem. Soc. Rev.* **2012**, *41* (7), 2718–2739. <https://doi.org/10.1039/c2cs15309b>.
- (4) Cabral, H.; Miyata, K.; Osada, K.; Kataoka, K. Block Copolymer Micelles in Nanomedicine Applications. *Chem. Rev.* **2018**, *118* (14), 6844–6892. <https://doi.org/10.1021/acs.chemrev.8b00199>.
- (5) Sokolova, E.; Spruijt, E.; Hansen, M. M. K.; Dubuc, E.; Groen, J.; Chokkalingam, V.; Piruska, A.; Heus, H. A.; Huck, W. T. S. Enhanced Transcription Rates in Membrane-Free Protocells Formed by Coacervation of Cell Lysate. *Proc. Natl. Acad. Sci.* **2013**, *110* (29), 11692–11697. <https://doi.org/10.1109/ISSPIT.2006.270766>.
- (6) Elani, Y.; Law, R. V.; Ces, O. Vesicle-Based Artificial Cells as Chemical Microreactors with Spatially Segregated Reaction Pathways. *Nat. Commun.* **2014**, *5* (1), 5305. <https://doi.org/10.1038/ncomms6305>.

- (7) Nakashima, K. K.; van Haren, M. H. I.; André, A. A. M.; Robu, I.; Spruijt, E. Active Coacervate Droplets Are Protocells That Grow and Resist Ostwald Ripening. *Nat. Commun.* **2021**, *12* (1), 3819. <https://doi.org/10.1038/s41467-021-24111-x>.
- (8) Larson, R. G. *The Structure and Rheology of Complex Fluids*. New York: Oxford university press 1999.
- (9) Weber, C. A.; Zwicker, D.; Jülicher, F.; Lee, C. F. Physics of Active Emulsions. *Reports Prog. Phys.* **2019**, *82* (6). <https://doi.org/10.1088/1361-6633/ab052b>.
- (10) Mason, A. F.; Buddingh, B. C.; Williams, D. S.; Van Hest, J. C. M. Hierarchical Self-Assembly of a Copolymer-Stabilized Coacervate Protocell. *J. Am. Chem. Soc.* **2017**, *139* (48), 17309–17312. <https://doi.org/10.1021/jacs.7b10846>.
- (11) Dewey, D. C.; Strulson, C. A.; Cacace, D. N.; Bevilacqua, P. C.; Keating, C. D. Bioreactor Droplets from Liposome-Stabilized All-Aqueous Emulsions. *Nat. Commun.* **2014**, *5* (May), 1–9. <https://doi.org/10.1038/ncomms5670>.
- (12) Jaturanpinyo, M.; Harada, A.; Yuan, X.; Kataoka, K. Preparation of Bionanoreactor Based on Core-Shell Structured Polyion Complex Micelles Entrapping Trypsin in the Core Cross-Linked with Glutaraldehyde. *Bioconjug. Chem.* **2004**, *15* (2), 344–348. <https://doi.org/10.1021/bc034149m>.
- (13) Gao; Holkar; Srivastava. Protein–Polyelectrolyte Complexes and Micellar Assemblies. *Polymers (Basel)*. **2019**, *11* (7), 1097. <https://doi.org/10.3390/polym11071097>.
- (14) Kataoka, K.; Togawa, H.; Harada, A.; Yasugi, K.; Matsumoto, T.; Katayose, S.

- Spontaneous Formation of Polyion Complex Micelles with Narrow Distribution from Antisense Oligonucleotide and Cationic Block Copolymer in Physiological Saline. *Macromolecules* **1996**, *29* (26), 8556–8557. <https://doi.org/10.1021/ma961217+>.
- (15) Katayose, S.; Kataoka, K. Water-Soluble Polyion Complex Associates of DNA and Poly(Ethylene Glycol)-Poly(L-Lysine) Block Copolymer. *Bioconjug. Chem.* **1997**, *8* (5), 702–707. <https://doi.org/10.1021/bc9701306>.
- (16) Lueckheide, M.; Vieregge, J. R.; Bologna, A. J.; Leon, L.; Tirrell, M. V. Structure-Property Relationships of Oligonucleotide Polyelectrolyte Complex Micelles. *Nano Lett.* **2018**, *18* (11), 7111–7117. <https://doi.org/10.1021/acs.nanolett.8b03132>.
- (17) Lee, Y.; Ishii, T.; Cabral, H.; Kim, H. J.; Seo, J.-H.; Nishiyama, N.; Oshima, H.; Osada, K.; Kataoka, K. Charge-Conversional Polyionic Complex Micelles-Efficient Nanocarriers for Protein Delivery into Cytoplasm. *Angew. Chemie Int. Ed.* **2009**, *48* (29), 5309–5312. <https://doi.org/10.1002/anie.200900064>.
- (18) Harada, A.; Kataoka, K. On-off Control of Enzymatic Activity Synchronizing with Reversible Formation of Supramolecular Assembly from Enzyme and Charged Block Copolymers [12]. *J. Am. Chem. Soc.* **1999**, *121* (39), 9241–9242. <https://doi.org/10.1021/ja9919175>.
- (19) Dora Tang, T. Y.; Rohaida Che Hak, C.; Thompson, A. J.; Kuimova, M. K.; Williams, D. S.; Perriman, A. W.; Mann, S. Fatty Acid Membrane Assembly on Coacervate Microdroplets as a Step towards a Hybrid Protocell Model. *Nat. Chem.* **2014**, *6* (6), 527–533. <https://doi.org/10.1038/nchem.1921>.

- (20) Mason, A. F.; van Hest, J. C. M. Multifaceted Cell Mimicry in Coacervate-Based Synthetic Cells. *Emerg. Top. Life Sci.* **2019**, *3* (5), 567–571.  
<https://doi.org/10.1042/ETLS20190094>.
- (21) Mason, A. F.; Altenburg, W. J.; Song, S.; van Stevendaal, M.; van Hest, J. C. M. Terpolymer-Stabilized Complex Coacervates: A Robust and Versatile Synthetic Cell Platform. In *Methods in Enzymology*; Elsevier Inc., 2021; Vol. 646, pp 51–82.  
<https://doi.org/10.1016/bs.mie.2020.06.008>.
- (22) Mason, A. F.; Yewdall, N. A.; Welzen, P. L. W.; Shao, J.; Stevendaal, M. Van; Hest, J. C. M. V.; Williams, D. S.; Abdelmohsen, L. K. E. A. Mimicking Cellular Compartmentalization in a Hierarchical Protocell through Spontaneous Spatial Organization. *ACS Cent. Sci.* **2019**, *5* (8), 1360–1365.  
<https://doi.org/10.1021/acscentsci.9b00345>.
- (23) van Stevendaal, M. H. M. E.; Vasiukas, L.; Yewdall, N. A.; Mason, A. F.; van Hest, J. C. M. Engineering of Biocompatible Coacervate-Based Synthetic Cells. *ACS Appl. Mater. Interfaces* **2021**, *13* (7), 7879–7889. <https://doi.org/10.1021/acscami.0c19052>.
- (24) Yewdall, N. A.; Buddingh, B. C.; Altenburg, W. J.; Timmermans, S. B. P. E.; Vervoort, D. F. M.; Abdelmohsen, L. K. E. A.; Mason, A. F.; van Hest, J. C. M. Physicochemical Characterization of Polymer-Stabilized Coacervate Protocells. *ChemBioChem* **2019**, *20* (20), 2643–2652. <https://doi.org/10.1002/cbic.201900195>.
- (25) Pir Cakmak, F.; Grigas, A. T.; Keating, C. D. Lipid Vesicle-Coated Complex Coacervates. *Langmuir* **2019**, *35* (24), 7830–7840. <https://doi.org/10.1021/acs.langmuir.9b00213>.

- (26) Qin, J.; Priftis, D.; Farina, R.; Perry, S. L.; Leon, L.; Whitmer, J.; Hoffmann, K.; Tirrell, M.; De Pablo, J. J. Interfacial Tension of Polyelectrolyte Complex Coacervate Phases. *ACS Macro Lett.* **2014**, *3* (6), 565–568. <https://doi.org/10.1021/mz500190w>.
- (27) Priftis, D.; Tirrell, M. Phase Behaviour and Complex Coacervation of Aqueous Polypeptide Solutions. *Soft Matter* **2012**, *8* (36), 9396–9405. <https://doi.org/10.1039/c2sm25604e>.
- (28) Johnston, B. M.; Johnston, C. W.; Letteri, R. A.; Lytle, T. K.; Sing, C. E.; Emrick, T.; Perry, S. L. The Effect of Comb Architecture on Complex Coacervation. *Org. Biomol. Chem.* **2017**, *15* (36), 7630–7642. <https://doi.org/10.1039/c7ob01314k>.
- (29) Lindhoud, S.; De Vries, R.; Schweins, R.; Cohen Stuart, M. A.; Norde, W. Salt-Induced Release of Lipase from Polyelectrolyte Complex Micelles. *Soft Matter* **2009**, *5* (1), 242–250. <https://doi.org/10.1039/b811640g>.
- (30) Lindhoud, S.; Norde, W.; Stuart, M. A. C.; Cohen Stuart, M. A. Effects of Polyelectrolyte Complex Micelles and Their Components on the Enzymatic Activity of Lipase. *Langmuir* **2010**, *26* (12), 9802–9808. <https://doi.org/10.1021/la1000705>.
- (31) Bassani, G.; Farruggia, B.; Picó, G. Cationic Polyelectrolytes-Lipases Complexes Formation as Tool for Recovery of These Enzymes from Their Natural Sources. *Int. J. Biol. Macromol.* **2011**, *49* (3), 351–355. <https://doi.org/10.1016/j.ijbiomac.2011.05.012>.
- (32) Lindhoud, S.; Claessens, M. M. A. E. Accumulation of Small Protein Molecules in a Macroscopic Complex Coacervate. *Soft Matter* **2015**, *12* (2), 408–413. <https://doi.org/10.1039/c5sm02386f>.

- (33) Love, C.; Steinkühler, J.; Gonzales, D. T.; Yandrapalli, N.; Robinson, T.; Dimova, R.; Tang, T. Y. D. Reversible PH-Responsive Coacervate Formation in Lipid Vesicles Activates Dormant Enzymatic Reactions. *Angew. Chemie - Int. Ed.* **2020**, *59* (15), 5950–5957. <https://doi.org/10.1002/anie.201914893>.
- (34) Moreau, N. G.; Martin, N.; Gobbo, P.; Tang, T. Y. D.; Mann, S. Spontaneous Membrane-Less Multi-Compartmentalization: Via Aqueous Two-Phase Separation in Complex Coacervate Micro-Droplets. *Chem. Commun.* **2020**, *56* (84), 12717–12720. <https://doi.org/10.1039/d0cc05399f>.
- (35) Reichhart, C.; Czeslik, C. A Quantitative Study of the Enzymatic Activity of Horseradish Peroxidase at a Planar Poly(Acrylic Acid) Brush. *Colloids Surfaces B Biointerfaces* **2010**, *75* (2), 612–616. <https://doi.org/10.1016/j.colsurfb.2009.10.017>.
- (36) Li, J.; Liu, X.; Abdelmohsen, L. K. E. A.; Williams, D. S.; Huang, X. Spatial Organization in Proteinaceous Membrane-Stabilized Coacervate Protocells. *Small* **2019**, *15* (36), 1902893. <https://doi.org/10.1002/sml.201902893>.
- (37) Pippa, N.; Pispas, S.; Demetzos, C. Polymer Self-Assembled Nanostructures as Innovative Drug Nanocarrier Platforms. *Curr. Pharm. Des.* **2016**, *22* (19), 2788–2795. <https://doi.org/10.2174/1381612822666160217141232>.
- (38) Bourganis, V.; Karamanidou, T.; Kammona, O.; Kiparissides, C. Polyelectrolyte Complexes as Prospective Carriers for the Oral Delivery of Protein Therapeutics. *Eur. J. Pharm. Biopharm.* **2017**, *111*, 44–60. <https://doi.org/10.1016/j.ejpb.2016.11.005>.
- (39) Panova, I. G.; Khaydapova, D. D.; Ilyasov, L. O.; Umarova, A. B.; Yaroslavov, A. A.

- Polyelectrolyte Complexes Based on Natural Macromolecules for Chemical Sand/Soil Stabilization. *Colloids Surfaces A Physicochem. Eng. Asp.* **2020**, 590 (November 2019), 124504. <https://doi.org/10.1016/j.colsurfa.2020.124504>.
- (40) Panova, I. G.; Ilyasov, L. O.; Khaidapova, D. D.; Bashina, A. S.; Smagin, A. V.; Ogawa, K.; Adachi, Y.; Yaroslavov, A. A. Soil Conditioners Based on Anionic Polymer and Anionic Micro-Sized Hydrogel: A Comparative Study. *Colloids Surfaces A Physicochem. Eng. Asp.* **2021**, 610 (June 2020), 125635. <https://doi.org/10.1016/j.colsurfa.2020.125635>.
- (41) Liu, B.; Fan, Y.; Li, H.; Zhao, W.; Luo, S.; Wang, H.; Guan, B.; Li, Q.; Yue, J.; Dong, Z.; Wang, Y.; Jiang, L. Control the Entire Journey of Pesticide Application on Superhydrophobic Plant Surface by Dynamic Covalent Trimeric Surfactant Coacervation. *Adv. Funct. Mater.* **2021**, 31 (5), 2006606. <https://doi.org/10.1002/adfm.202006606>.
- (42) Huang, B.; Chen, F.; Shen, Y.; Qian, K.; Wang, Y.; Sun, C.; Zhao, X.; Cui, B.; Gao, F.; Zeng, Z.; Cui, H. Advances in Targeted Pesticides with Environmentally Responsive Controlled Release by Nanotechnology. *Nanomaterials* **2018**, 8 (2), 102. <https://doi.org/10.3390/nano8020102>.
- (43) Schmitt, C.; Turgeon, S. L. Protein/Polysaccharide Complexes and Coacervates in Food Systems. *Adv. Colloid Interface Sci.* **2011**, 167 (1–2), 63–70. <https://doi.org/10.1016/j.cis.2010.10.001>.
- (44) Hossel, S. N.-K. M. W. Cosmetic and Pharmaceutical Substances Based on Polyelectrolyte Complexes, 2006.
- (45) Binks, B. P.; Shi, H. Phase Inversion of Silica Particle-Stabilized Water-in-Water

Emulsions. *Langmuir* **2019**, *35* (11), 4046–4057.

<https://doi.org/10.1021/acs.langmuir.8b04151>.

- (46) Ke, C. Y.; Wu, Y. T.; Tseng, W. L. Fluorescein-5-Isothiocyanate-Conjugated Protein-Directed Synthesis of Gold Nanoclusters for Fluorescent Ratiometric Sensing of an Enzyme-Substrate System. *Biosens. Bioelectron.* **2015**, *69*, 46–53.

<https://doi.org/10.1016/j.bios.2015.02.002>.

## CHAPTER 5

### STABILITY OF STABILIZED COACERVATE DROPLETS AGAINST SALT

Contents of this chapter are adapted from a pending patent. Samanvaya Srivastava; Shang Gao; US 63/187,031, *Patent pending*.

#### ABSTRACT

Polyelectrolyte complex (PEC) coacervates have been suggested as protocells and carriers for biomacromolecules including proteins and enzymes. Yet, their applications have been limited due to the spontaneous coalescence, phase separation, and the low resistance to harsh environment like high ionic strength. In Chapter 4, we introduced a stabilization strategy involving comb polyelectrolytes to overcome the rapid coalescence of complex coacervate microdroplets in salt free environments. In this chapter, we expand our investigation on this stabilization approach in improving the resistance of stabilized coacervate emulsions upon the addition of salt. Typically, addition of salt results in dissolution of the complex coacervate phase above a critical salt concentration. However, comb polyelectrolyte-stabilized complex coacervate formulations exhibit stability against the addition of salt above the critical salt concentration corresponding to the unstable coacervates. Consequently, the critical salt concentration and the critical total linear polyelectrolyte concentration at which the complex coacervate phase vanishes both increases upon incorporation of comb polyelectrolytes in the formulations. The stabilized microdroplets remain stable up to 48 hours against coalescence in presence of ~ 300 mM salt, signifying that the stabilizing mechanism is robust and can withstand the presence of high concentrations of salt. Moreover, salt concentrations up to 200 mM do not impede the partitioning of proteins into the complex coacervate microdroplets. Enabled by the comb polyelectrolyte stabilizers, such stable

complex coacervate emulsions that can withstand salt may broaden the applications of coacervates in the fields of biotechnology and pharmaceutical sciences.

## 5.1. INTRODUCTION

Complex coacervation is a liquid-liquid phase separation phenomenon that occurs through electrostatic complexation of oppositely charged polyelectrolytes<sup>1-3</sup> and subsequent condensation into a macromolecule-rich phase. Upon mixing of oppositely charged macromolecules in an aqueous solution, complex coacervate microdroplets appear spontaneously. These droplets possess a distinct water-water interface with the ambient aqueous environments and have a strong propensity to partition and encapsulate charge-bearing molecules (proteins,<sup>1,4,5</sup> nucleic acids, DNA<sup>6-9</sup> and RNA,<sup>10,11</sup> multivalent ions, etc.). As such, they have been presented as minimalistic membraneless protocells and artificial bioreactors exhibiting dynamic spatial compartmentalization that are capable of efficiently and spontaneously sequestering biological molecules and enhancing their activity.<sup>10,12,13,14</sup> Complex coacervates are also utilized in hair conditioner formulations to improve wet and dry hair compatibility,<sup>15</sup> and have been demonstrated as effective anti-erosion agents for environmental protection of agricultural land.<sup>16,17</sup> However, the lack of a membrane around the coacervate droplets, that promotes transport and spontaneous sequestration of biomolecules, also makes the coacervate microdroplets prone to coalescence and Ostwald ripening, leading to macrophase separation. The lack of long-term stability significantly hampers the use of complex coacervates as protocells, bioreactors, or encapsulants.

PEC coacervates are capable of encapsulating more charged loadings compared to PEC micelles in aqueous solutions owing to their high charge density per droplets and large droplet sizes. However, the dissociation of the complexations including PEC micelles and PEC coacervates can be alleviated at even low ionic strengths.<sup>1,18,19</sup> Studies on improving the stability of PEC micelles against salt have proposed by harnessing additional stabilization resulting from the cooperativity

of molecular interactions, such as hydrophobic interaction, in conjunction with electrostatic interaction<sup>20,21</sup> and chemical crosslinking<sup>22–25</sup> while maintaining the durability and activity of loadings. Jaturanpinyo et al. reported stabilization of trypsin/PEG-*b*-P(Asp) micelles by introducing glutaraldehyde as a crosslinker for the core. The aldehyde groups on glutaraldehyde and the primary amine groups on trypsin form a Schiff base, thus improving core stability in high ionic strength solutions.<sup>22</sup> The average diameter (70 nm–90 nm) of adequately crosslinked micelles stayed constant in high relative glutaraldehyde concentrations (GR > 10), GR defined as the total number of aldehyde groups in the glutaraldehyde solution versus the total number of Lys residues in trypsin, and high salt concentrations (NaCl 0–0.6 M). It must be noted that, at GR values below 4, micelles were still destabilized upon exposure to salt beyond 0.15 M owing to incomplete crosslinking between trypsin and the primary amino group. Both free and encapsulated trypsin naturally denatured within a week, while core-stabilized trypsin in the PEC micelles retained its enzymatic activity for >3 weeks. It must be noted, though, that this approach of using glutaraldehyde crosslinkers is not very feasible for biomedical applications owing to glutaraldehyde toxicity and irreversible crosslinking. Introduction of hydrophobic groups, phenyl (Phe), naphthyl (Nap), and pyrenyl (Py), to the  $\omega$ -end of PEG-*b*-P(Asp) increased the association between lysozymes and PEG-*b*-P(Asp), leading to significantly lower critical association concentrations and improved stabilities in high ionic strength environments, albeit with deviations from the spherical shape of the micelles.<sup>20</sup> Micelles comprising PEG-*b*-P(Asp) with Py groups were reported to exhibit smallest variations in size upon exposure to NaCl concentrations up to 0.1 M; micelles with unfunctionalized PEG-*b*-P(Asp) dissociated at ~ 0.05M NaCl. Similarly, quaternization of the amine groups in PEG-*b*-PAMA polymers improved the stability of the  $\alpha$ -

amylase/PEG-*b*-PAMA micelles in 50 mM NaCl solutions.<sup>26</sup> Most of the published literature has focused on the stability of PEC micelles, however, the enhanced stability strategy for the PEC coacervate droplets against salt screening effects was unexplored. Thus, we focus on building up a novel approach of physical associations to support a more potential biomacromolecule cargo.

In chapter 4, we have demonstrated a novel stabilization strategy to create membraneless complex coacervate emulsions, stabilized by commercial comb polyelectrolytes comprising a polyacrylic acid backbone grafted with neutral side chains. This anionic comb polyelectrolyte stabilizer supports the stability of the water-water interfaces in these aqueous emulsions. Following with these investigations, we target on investigating the stabilization mechanism to forfeit the salt-sensitive stabilized coacervate emulsions from high ionic strength.

## **5.2. RESULTS & DISCUSSION**

### **5.2.1. Comb Polyelectrolytes Stabilize Complex Coacervate Droplets in Salty Solutions**

A comparison between unstable and stable polyelectrolyte complex coacervate dispersions comprising charge-matched oppositely charged linear polyelectrolytes, poly(acrylic acid sodium salt) (PAA,  $MW = 5100$  g/mol) and poly(diallyldimethylammonium chloride) (PDADMAC,  $MW = 8500$  g/mol), (1:1 charge ratio, 62.2 mM charge concentration) demonstrate different solution characteristics upon the addition of NaCl. The unstable coacervate dispersions are turbid upon initial mixing of their constituents (Figure 5-1A) in low salt solutions owing to the presence of micron-size coacervate droplets. Electrostatic screening by salt ions induce weaker interactions between polyelectrolyte chains yet is not sufficient to disrupt coacervation entirely. However, induced by the spontaneous coalescence of the microdroplets and sedimentation, the unstable

dispersions resulted in clear solutions with distinct phase boundaries between polymer-dense phase and polymer-lean phases within a few hours (Figure 5-1A). In contrast, coacervate droplets in a low salt solution stabilized by addition of a small amount (4.8 mM charge concentration) of polyacrylic acid-comb-polyethylene glycol (PAA-*co*-PEG,  $MW = 39467$  g/mol,  $26 e^-$  at pH = 6, PEG  $MW = 3000$  g/mol) comb polyelectrolytes retained their turbidity over 48 hours (Figure 5-1B). Micrographs of the as-mixed unstable and stable formulations both show a broad distribution of complex coacervate droplets with similar spherical morphology. The unstable coacervate dispersions contain  $10\times$  larger droplets than stabilized droplets upon spontaneous mixing of the components (Figure 5-1A and 5-1B, respectively). The larger size of unstable coacervate droplets in low salt solutions can be attributed to the weakened interactions between the polyelectrolyte chains, influenced by the addition of salt, which caused fast coalescence of the droplets.

Stabilization of the coacervate droplets against coalescence is hypothesized to arise from the adsorption of the comb polyelectrolytes at the water-water interfaces. The adsorption is anchored by the anionic backbones positioning onto the droplet surfaces, while the neutral side chains spread into surrounding polymer-lean phase to induce steric repulsion between the microdroplets. Owing to the net neutral charges at the surfaces, we expect that the steric repulsions between the coacervate droplets promote droplet stability even in presence of salt.

Mixing of the oppositely charged polyelectrolytes in aqueous solutions with high salt concentration ( $\sim 400$  mM) resulted in clear one-phase solutions. Strong screening of the electrostatic interactions by salt ions results in complete inhibition of coacervation. A homogenous transparent solution without any distinct phase separation is obtained. At medium salt concentration ( $\sim 200$  mM), coacervation still occurred yet was diminished and was accompanied

with faster droplet coalescence and macro-phase separation. In contrast, in presence of comb polyelectrolytes, coacervate microdroplets formed and persisted even in presence of salt. The stabilized formulations remained turbid for at least 48 hours, with micron-size droplets visualized in the solutions (Figure 5-1B). We note that the droplet number density and the droplet sizes both decreased with time in the stabilized formulations, indicating faster coalescence which could be attribute to higher water content in the coacervate droplets.

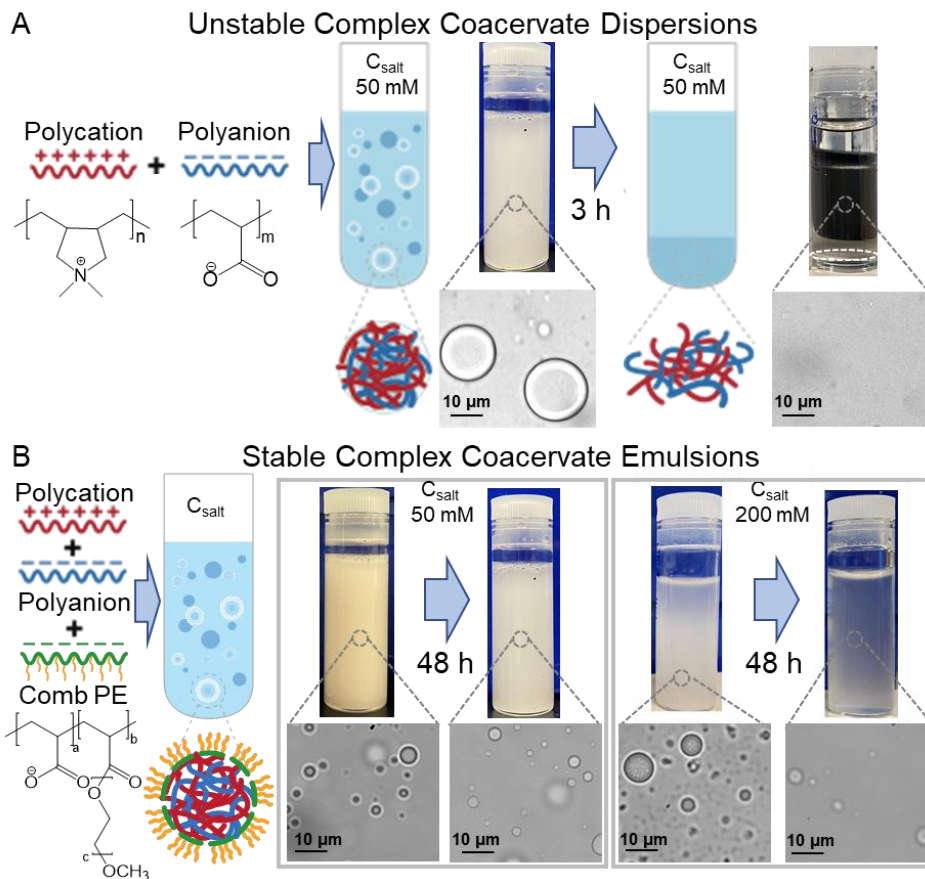


**Figure 5-1: Comb polyelectrolytes stabilize complex coacervate droplets in salty solutions.**

(A) Mixing of solutions of oppositely charged polyelectrolytes (38.8 mM ionizable groups, 1:1 charge ratio) lead to formation of turbid dispersions of complex coacervate droplets. The coacervate droplets in 50 mM salt solution coalesce spontaneously (within 3 hours) to form a homogenous transparent coacervate phase. The white dashed line denotes the location of the interface between the polymer dense coacervate phase (at the bottom) and the polymer-lean supernatant phase (at the top). Corresponding micrographs depict coacervate droplets in the as mixed formulations that coalesce into a homogenous coacervate phase within 3 hours. (B) Stable complex coacervate emulsions obtained by preparing the same solutions as in (A) with an

additional component – anionic comb polyelectrolytes (4.8 mM ionizable groups). The stable complex coacervate emulsions with the addition of 50 mM salt solutions are turbid when prepared and remained turbid for up to 48 hours. Corresponding micrographs reveal distinct micron-sized droplets in the emulsions. With further addition of 200 mM salt solutions, the solutions are turbid when prepared and maintained turbid for up to 48 hours yet proceed phase separation. Corresponding micrographs reveal distinct micron-sized droplets in the emulsions. In (A) and (B), scale bars are provided in each micrograph.

### 5.2.2. Phase Behaviors of Stabilized Complex Coacervate Emulsions

Next, we focused on mapping the phase behavior of the charge-matched mixture of oppositely charged polyelectrolytes delineating the boundary between the one-phase and two-phase regions with using the turbidity measurements. Turbidity of formulations containing a constant total polyelectrolyte concentration  $C_{PE}$  remained constant initially upon increasing salt concentration  $C_{salt}$  before decreasing drastically at critical salt concentration  $C_{salt}^*$ , indicating a two-phase (turbid) to one-phase (clear) transition (Figure 5-2A). This critical salt concentration for the coacervate formulations was found to increase upon stabilization of the coacervate microdroplets (Figure 5-2B-E). Moreover,  $C_{salt}^*$  increased with increasing the comb polyelectrolyte concentration  $C_{CPE}$  (Figure 5-2B-D) and became larger than 1 M at  $C_{CPE} \sim 0.5 C_{PE}$  (Figure 5-2E). Additionally, the turbidity gradient signifying the two-phase to one-phase transition at the critical salt concentration  $C_{salt}^*$  decreased with increasing comb polyelectrolyte concentration  $C_{CPE}$ . This suggested that the stability of the coacervate droplet emulsions against salt increased with increasing  $C_{CPE}$ . Here, we note that the turbidity values of 25% was chosen as the boundary between the turbid two-phase and clear one-phase solutions.

Phase maps for unstable and stabilized complex coacervate formulations depicting the  $C_{PE} - C_{salt}$  region in which coacervation occurs, constructed based on turbidity measurements, are shown in Figures 5-2F-H. In these maps, red, yellow, and black symbols denote formulations with greater than 50%, between 25% and 50%, and less than 25% turbidity levels, respectively. The phase map of unstable complex coacervates (Figures 5-2F) emerges as the characteristic inverted-U shape, with two-phase solutions forming only between the critical total polyelectrolyte concentration boundaries between  $\sim 10$  mM and 800 mM.  $C_{salt}^* \sim 300$  mM was found for  $C_{PE}$  ranging from 10

– 300 mM;  $C_{salt}^*$  decreased upon increasing  $C_{PE}$  beyond 400 mM and approached 0 at  $C_{PE} \sim 800$  mM. Above  $C_{PE} = 800$  mM, the coacervate phase vanished. Outside of this coacervation window, one-phase clear solutions without coacervate droplets were obtained.

Phase maps of stabilized formulations comprising the anionic comb polyelectrolyte stabilizers (Figure 5-2G and H) depict a distinct expansion, both upward and rightward, of the two-phase region. At low  $C_{PE}$ ,  $C_{salt}^*$  for the stabilized coacervates increased significantly as compared to the unstable coacervates. Moreover, the two-phase systems were found to exist at higher  $C_{PE}$  and resisted higher concentrations of salt. The excess macromolecular charge introduced in the form of comb polyelectrolyte is insufficient, in comparison to the linear polyelectrolytes, to influence the thermodynamic equilibrium of the solution. We hypothesize that this expansion of the two-phase region is ascribable to the kinetic stabilization of the coacervate microdroplets against coalescence. Concomitantly, higher comb polyelectrolyte concentration led to smaller coacervate microdroplets that are more stable against coalescence, can form at higher  $C_{PE}$ , and can resist higher  $C_{salt}$ .

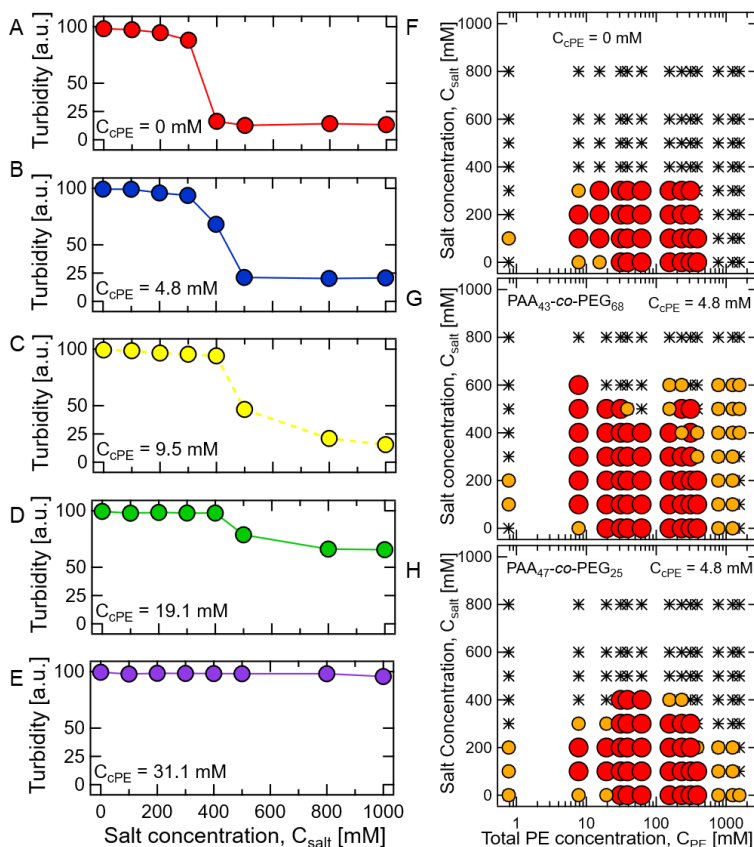


**Figure 5-2: Comb polyelectrolytes significantly expand the coacervation window. (A-E)**

Turbidity measurements indicating stability of the complex coacervate emulsions as a function of salt concentration. With increasing comb polyelectrolyte concentration (at constant linear polyelectrolyte concentration), larger salt concentrations are required to reduce the turbidity of the emulsions. **(F-H)** Mapping phase behaviors by turbidity measurements. **(F)** demonstrates the coacervation formation window of unstabilized coacervate dispersions. The phase behaviors of the oppositely polyelectrolyte pair with the addition of 4.8 mM comb polyelectrolyte stabilizers (PAA<sub>43</sub>-co-PEG<sub>68</sub>) **(G)** and with the addition of 4.8 mM comb polyelectrolyte stabilizers (PAA<sub>47</sub>-co-PEG<sub>25</sub>) are demonstrated. . Turbidity maps of formulations comprising varying concentrations of oppositely charged linear polyelectrolytes (1:1 charge ratio) and salt concentration (NaCl) for

three different anionic comb polyelectrolyte concentrations ( $C_{CPE} = 0, 4.8$  and  $9.5$  mM) highlight this expansion of the coacervation window. Black crosses represent for the clear phase systems. The solid red circles represent turbid solutions (arbitrary turbidity  $> 50$ ) while yellow circles represent partially turbidity solutions (arbitrary turbidity  $> 25$ ).

In chapter 4, the comb polyelectrolyte concentration was shown to tune the properties of polyelectrolyte coacervate microdroplets, including their stability and the microdroplet size. Here, we demonstrate that salt concentration provided as another handle to tune the extent of stabilization and the size of the coacervate microdroplets. As shown in Figure 5-3A, increasing the salt concentration resulted in a decreased stabilization and promoted droplet sedimentation. This decrease can be attributed to a combination of increasing water content in the coacervates, increasing volume of the coacervate phase, and weaker adsorption of comb polyelectrolytes on the coacervate-water interfaces owing to stronger screening of electrostatic interactions upon addition of salt.

The evolution of the coacervate microdroplet size was obtained by dynamic light scattering (DLS) operated in backscattering mode. Introduction of comb polyelectrolytes in as-mixed salt-free coacervate dispersions led to a decrease in the mean diameter (by volume) of the microdroplets  $D$ . Similar trends were shown in aqueous emulsions, where the size of the droplets  $D$  decreased until all droplets possessed a monolayer of comb polyelectrolytes on their surfaces assuming the interfacial area per coacervate droplets was proportional to  $C_{CPE}$ . Increasing the salt concentration also led to similar, albeit smaller reduction in  $D$  upon stabilization. In other words, in as-mixed dispersions containing a constant concentration of the total polyelectrolytes  $C_{PE}$  and comb polyelectrolyte concentration  $C_{CPE}$ ,  $D$  increased initially before plateauing with increasing salt concentration  $C_{salt}$  (Figure 5-3B). Marginal coarsening and settling of the microdroplets was observed over 24 hours at low salt concentrations (Figure 5-3A, particularly 100 and 200 mM  $C_{salt}$ ), and  $D$  remained nearly constant over 48 hours in these dispersions (Figures 5-3B – D). In contrast, prominent settling was observed in dispersions with medium to high salt concentrations

( $\geq 300$  mM  $C_{salt}$ ) within 24 hours (Figure 5-3A). Surprisingly, the droplet size distribution remained nearly constant in the time frame before settling. This indicates that while the comb polyelectrolytes were able to stabilize a minority of the microdroplets, most coacervate droplets coalesced and settled over time. Moreover, it is consistent with our earlier hypothesis that kinetic barriers imposed on droplet coalescence result in enhanced stability against salt in as-mixed formulations. With time, droplet coarsened by overcoming these barriers, leading to settling. We expect that a higher comb polyelectrolyte concentration may mitigate settling in such high-salt dispersions by reducing the droplet size, and that this critical comb polyelectrolyte concentration required to prevent settling will have to be optimized for individual dispersions to account for increased screening with increasing salt concentration and associated effects on coacervation.

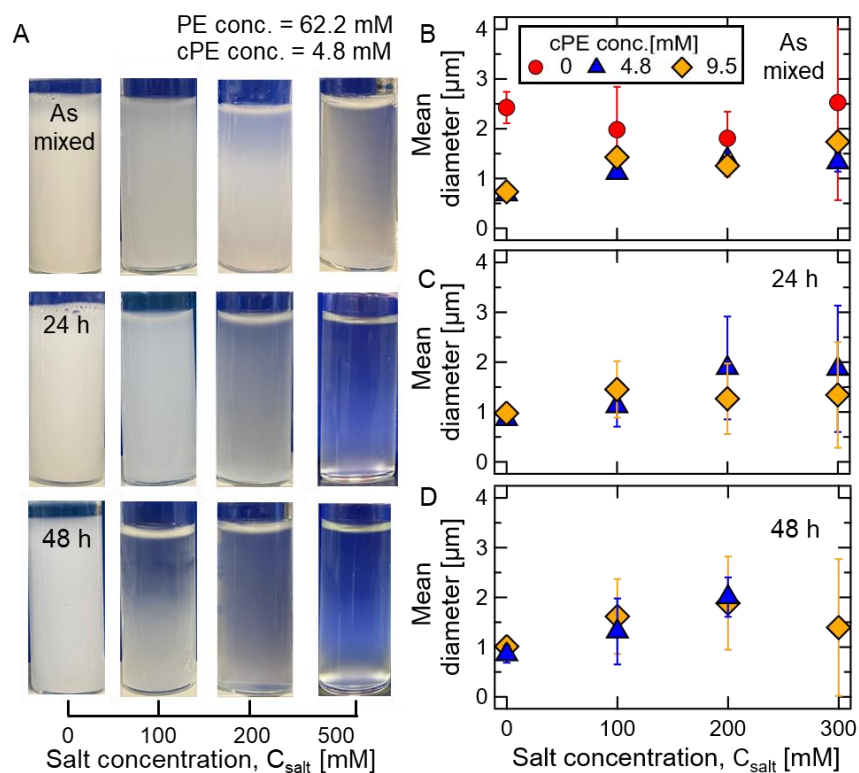


**Figure 5-3: Comb polyelectrolyte stabilized complex coacervate emulsions can withstand addition of salt.** (A) Stable polyelectrolyte complex coacervate emulsions comprising oppositely charged linear polyelectrolytes (1:1 charge ratio, 62.2 mM charge concentration), anionic comb polyelectrolyte (4.8 mM charge concentration) and increasing concentration of salt (NaCl, 0, 100, 200, 500 mM). Photographs taken at different times, indicated as “as mixed”, 24 hours, and 48 hours after mixing. Turbidity in the samples is a key factor for indicating the stability of the emulsions. **Salt can provide another handle to tune microdroplet size in complex coacervate emulsions.** (B-D) The evolution of the mean diameter (by volume) of the complex coacervate microdroplets in formulations comprising oppositely charged linear polyelectrolytes (1:1 charge ratio, 62.2 mM charge concentration), anionic comb polyelectrolyte (0, 4.8 mM or 9.5 mM charge

concentration) and salt. The mean size of the comb polyelectrolyte stabilized coacervate microdroplets increases with increasing salt concentration but remain nearly constant with time up to 48 hours. The microdroplet diameters were measured using dynamic light scattering and averaged from triplicate samples at each concentration and three measurement trials for each sample. Errors are calculated through the mean standard deviations of the measurements. Error bars are shown when they are larger than the symbols.

### 5.2.3. Stabilized Complex Coacervate Emulsions Maintain Their Protein Sequestration Capability in Salt Solutions

We have previously shown that the comb polyelectrolyte-induced stabilization of the complex coacervate droplets withstand the partitioning of proteins in the complex coacervate phase.<sup>27</sup> Here, we show that sequestration of proteins into the stabilized coacervate droplets occurs even in presence of salt. This partitioning of biomacromolecules in the droplets from salty solutions was monitored over time by fluorescence imaging probed with fluorescein isothiocyanate labeled bovine serum albumin (FITC-BSA). Fluorescent labeled proteins were mixed with PDADMAC, followed by addition of PAA to induce coacervation. BSA, with a net negative charge of  $18 e^-$  at pH  $\sim 6$ , was localized in the coacervate microdroplets and distributed uniformly inside the droplets, as indicated by the overlaid brightfield and fluorescent images (Figure 5-4, row 1). However, in the unstable dispersions, droplet coalescence led to macro-phase separation of the coacervate phase within a few hours. Moreover, upon addition of 300 mM salt, no coacervation was observed in protein containing solutions.

The introduction of the PAA-*c*-PEG comb polyelectrolytes to stabilize the coacervate microdroplets in salty solutions resulted in similar localization (Figure 5-4, rows 2-5) and uniform distribution within the coacervate microdroplets. Moreover, in the low  $C_{salt}$  regime, droplet size, morphology, and number density in the stabilized as-mixed dispersions (Figure 5-4, row 2) appeared to be similar to the unstable as-mixed formulations (Figure 5-4, row 1). However, while the unstable protein-loaded coacervate droplets coalesced spontaneously, the stabilized protein-containing coacervate microdroplets maintained their stability over 48 hours (Figure 5-4 row 3). This enhanced stability was accompanied with an apparent reduction in droplet number density

with time, akin to coacervate droplets without proteins (Figure 5-1B) and again ascribable to the comb polyelectrolytes introducing kinetic barriers against coalescence that droplets overcome more readily over time in salty solutions.

While no coacervation occurred at  $\sim 300$  mM  $C_{salt}$ , the enhanced stability against salt by comb polyelectrolytes supported the complexation up to  $C_{salt} \sim 300$  mM. The size of the coacervate droplets reduced in size, indicating a stronger screening effect from salt induced a weaker PE-PE interaction. The addition of salt influenced the comb polyelectrolytes stabilization efficiency by screening the charges on the backbones and reducing the adsorption of comb polyelectrolytes onto the droplet surfaces. FITC-BSA remained localized within the stable droplets (Figure 5-4A row 3, row 5); nominal loss of protein from the stable droplets was observed (as discerned from comparing the fluorescent intensities).

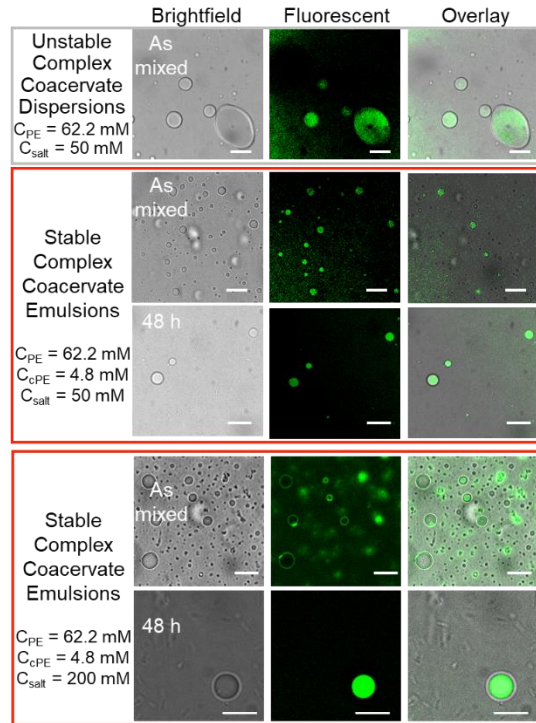


**Figure 5-4: Proteins partition preferentially in coacervate droplets in the comb poyelectrolyte stabilized coacervate emulsions.** Confocal brightfield (left), fluorescence (middle) and overlaid (right) micrographs showing FITC-labelled BSA localized in unstable coacervates droplets in as mixed formulations in 50 mM salt solutions (row 1) and in stabilized complex coacervate droplets in as mixed formulations in 50 mM salt solutions (row 2) and after 48 hours of aging (row 3). While unstabilized coacervate dispersions maintain fast coalescence in 200 mM salt solution, the FITC-labelled BSA localized in stabilized complex coacervate droplets in as mixed formulations in 50 mM salt solutions (row 4) and after 48 hours of aging (row 5). The droplets were visualized upon settling on nonadherent substrates. FTIC-BSA concentration was 1 mM (charge concentration).

### 5.3. CONCLUSIONS

In this chapter, we have demonstrated a methodology for stabilizing coacervate microdroplets in salty solutions by the incorporation of comb polyelectrolytes in the complex coacervate formulations. Our methodology produces stable complex coacervate emulsions comprising microdroplets, composed of oppositely charged linear polyelectrolytes and stabilized by interfacially adsorbed comb polyelectrolytes that exhibit prolonged stability. The microdroplet size remains relatively constant with time and is shown to be regulated by the salt concentrations of the salt in addition to other handles like comb polyelectrolyte concentration and linear polyelectrolyte concentrations (discussed in chapter 4). Our stabilization strategy improves the salt resistance of the complex coacervates while minimally interfering with other desirable attributes of coacervate droplets, including their ability to spontaneously sequester and encapsulate proteins from solution. These attributes of stabilized coacervate microdroplets will be crucial for their development as protein encapsulants that can withstand harsh environments, as well as in their adoption as a viable platform for delivering drugs, enzymes, and nutrients in pharmaceutical, cosmetics, and agricultural formulations.

#### 5.4. REFERENCES

- (1) Gao, S.; Holkar, A.; Srivastava, S. Protein-Polyelectrolyte Complexes and Micellar Assemblies. *Polymers (Basel)*. **2019**, *11* (7). <https://doi.org/10.3390/polym11071097>.
- (2) Li, L.; Srivastava, S.; Andreev, M.; Marciel, A. B.; De Pablo, J. J.; Tirrell, M. V. Phase Behavior and Salt Partitioning in Polyelectrolyte Complex Coacervates. *Macromolecules* **2018**, *51* (8), 2988–2995. <https://doi.org/10.1021/acs.macromol.8b00238>.
- (3) Li, L.; Srivastava, S.; Meng, S.; Ting, J. M.; Tirrell, M. V. Effects of Non-Electrostatic Intermolecular Interactions on the Phase Behavior of PH-Sensitive Polyelectrolyte Complexes. *Macromolecules* **2020**, *53* (18), 7835–7844. <https://doi.org/10.1021/acs.macromol.0c00999>.
- (4) Black, K. A.; Priftis, D.; Perry, S. L.; Yip, J.; Byun, W. Y.; Tirrell, M. Protein Encapsulation via Polypeptide Complex Coacervation. *ACS Macro Lett.* **2014**, *3* (10), 1088–1091. <https://doi.org/10.1021/mz500529v>.
- (5) Mccall, P. M.; Srivastava, S.; Perry, S. L.; Kovar, D. R.; Margaret, L.; Tirrell, M. V. Supplemental Information Partitioning and Enhanced Self-Assembly of Actin in Polypeptide Coacervates. *114*.
- (6) Sokolova, E.; Spruijt, E.; Hansen, M. M. K.; Dubuc, E.; Groen, J.; Chokkalingam, V.; Piruska, A.; Heus, H. A.; Huck, W. T. S. Enhanced Transcription Rates in Membrane-Free Protocells Formed by Coacervation of Cell Lysate. *Proc. Natl. Acad. Sci. U. S. A.* **2013**, *110* (29), 11692–11697. <https://doi.org/10.1073/pnas.1222321110>.
- (7) Douliez, J.-P.; Martin, N.; Gaillard, C.; Beneyton, T.; Baret, J.-C.; Mann, S.; Beven, L. Catanionic Coacervate Droplets as a Surfactant-Based Membrane-Free Protocell Model.

- Angew. Chemie* **2017**, *129* (44), 13877–13881. <https://doi.org/10.1002/ange.201707139>.
- (8) Deng, N. N. Complex Coacervates as Artificial Membraneless Organelles and Protocells. *Biomicrofluidics* **2020**, *14* (5). <https://doi.org/10.1063/5.0023678>.
- (9) Deng, N. N.; Huck, W. T. S. Microfluidic Formation of Monodisperse Coacervate Organelles in Liposomes. *Angew. Chemie - Int. Ed.* **2017**, *56* (33), 9736–9740. <https://doi.org/10.1002/anie.201703145>.
- (10) Nakashima, K. K.; van Haren, M. H. I.; André, A. A. M.; Robu, I.; Spruijt, E. Active Coacervate Droplets Are Protocells That Grow and Resist Ostwald Ripening. *Nat. Commun.* **2021**, *12* (1), 3819. <https://doi.org/10.1038/s41467-021-24111-x>.
- (11) Douliez, J.-P.; Martin, N. Fatty Acid Vesicles and Coacervates as Model Prebiotic Protocells. *ChemSystemsChem* **2021**. <https://doi.org/10.1002/syst.202100024>.
- (12) van Stevendaal, M. H. M. E.; Vasiukas, L.; Yewdall, N. A.; Mason, A. F.; van Hest, J. C. M. Engineering of Biocompatible Coacervate-Based Synthetic Cells. *ACS Appl. Mater. Interfaces* **2021**, *13* (7), 7879–7889. <https://doi.org/10.1021/acsami.0c19052>.
- (13) Mason, A. F.; Yewdall, N. A.; Welzen, P. L. W.; Shao, J.; Stevendaal, M. Van; Hest, J. C. M. V.; Williams, D. S.; Abdelmohsen, L. K. E. A. Mimicking Cellular Compartmentalization in a Hierarchical Protocell through Spontaneous Spatial Organization. *ACS Cent. Sci.* **2019**, *5* (8), 1360–1365. <https://doi.org/10.1021/acscentsci.9b00345>.
- (14) Pir Cakmak, F.; Grigas, A. T.; Keating, C. D. Lipid Vesicle-Coated Complex Coacervates. *Langmuir* **2019**, *35* (24), 7830–7840. <https://doi.org/10.1021/acs.langmuir.9b00213>.
- (15) Hossel, S. N.-K. M. W. Cosmetic and Pharmaceutical Substances Based on

- Polyelectrolyte Complexes, 2006.
- (16) Panova, I. G.; Khaydapova, D. D.; Ilyasov, L. O.; Umarova, A. B.; Yaroslavov, A. A. Polyelectrolyte Complexes Based on Natural Macromolecules for Chemical Sand/Soil Stabilization. *Colloids Surfaces A Physicochem. Eng. Asp.* **2020**, *590* (November 2019), 124504. <https://doi.org/10.1016/j.colsurfa.2020.124504>.
- (17) Panova, I. G.; Ilyasov, L. O.; Khaidapova, D. D.; Bashina, A. S.; Smagin, A. V.; Ogawa, K.; Adachi, Y.; Yaroslavov, A. A. Soil Conditioners Based on Anionic Polymer and Anionic Micro-Sized Hydrogel: A Comparative Study. *Colloids Surfaces A Physicochem. Eng. Asp.* **2021**, *610* (June 2020), 125635. <https://doi.org/10.1016/j.colsurfa.2020.125635>.
- (18) Cooper, C. L.; Goulding, A.; Kayitmazer, A. B.; Ulrich, S.; Stoll, S.; Turksen, S.; Yusa, S.; Kumar, A.; Dubin, P. L. Effects of Polyelectrolyte Chain Stiffness, Charge Mobility, and Charge Sequences on Binding to Proteins and Micelles. *Biomacromolecules* **2006**, *7* (4), 1025–1035. <https://doi.org/10.1021/bm050592j>.
- (19) Comert, F.; Dubin, P. L. Liquid-Liquid and Liquid-Solid Phase Separation in Protein-Polyelectrolyte Systems. *Adv. Colloid Interface Sci.* **2017**, *239*, 213–217. <https://doi.org/10.1016/j.cis.2016.08.005>.
- (20) Yuan, X.; Harada, A.; Yamasaki, Y.; Kataoka, K. Stabilization of Lysozyme-Incorporated Polyion Complex Micelles by the  $\omega$ -End Derivatization of Poly(Ethylene Glycol)–Poly( $\alpha,\beta$ -Aspartic Acid) Block Copolymers with Hydrophobic Groups. *Langmuir* **2005**, *21* (7), 2668–2674. <https://doi.org/10.1021/la0488811>.
- (21) Harada, A.; Kataoka, K. Supramolecular Assemblies of Block Copolymers in Aqueous Media as Nanocontainers Relevant to Biological Applications. *Prog. Polym. Sci.* **2006**, *31*

- (11), 949–982. <https://doi.org/10.1016/j.progpolymsci.2006.09.004>.
- (22) Jaturanpinyo, M.; Harada, A.; Yuan, X.; Kataoka, K. Preparation of Bionanoreactor Based on Core-Shell Structured Polyion Complex Micelles Entrapping Trypsin in the Core Cross-Linked with Glutaraldehyde. *Bioconjug. Chem.* **2004**, *15* (2), 344–348. <https://doi.org/10.1021/bc034149m>.
- (23) Marquié, C. Chemical Reactions in Cottonseed Protein Cross-Linking by Formaldehyde, Glutaraldehyde, and Glyoxal for the Formation of Protein Films with Enhanced Mechanical Properties. *J. Agric. Food Chem.* **2001**, *49* (10), 4676–4681. <https://doi.org/10.1021/jf0101152>.
- (24) Yuan, X.; Yamasaki, Y.; Harada, A.; Kataoka, K. Characterization of Stable Lysozyme-Entrapped Polyion Complex (PIC) Micelles with Crosslinked Core by Glutaraldehyde. *Polymer (Guildf)*. **2005**, *46* (18), 7749–7758. <https://doi.org/10.1016/j.polymer.2005.02.121>.
- (25) Klyachko, N. L.; Manickam, D. S.; Brynskikh, A. M.; Uglanova, S. V.; Li, S.; Higginbotham, S. M.; Bronich, T. K.; Batrakova, E. V.; Kabanov, A. V. Cross-Linked Antioxidant Nanozymes for Improved Delivery to CNS. *Nanomedicine Nanotechnology, Biol. Med.* **2012**, *8* (1), 119–129. <https://doi.org/10.1016/j.nano.2011.05.010>.
- (26) Kuwada, K.; Kurinomaru, T.; Tomita, S.; Shiraki, K. Noncovalent PEGylation-Based Enzyme Switch in Physiological Saline Conditions Using Quaternized Polyamines. *Colloid Polym. Sci.* **2016**, *294* (10), 1551–1556. <https://doi.org/10.1007/s00396-016-3916-5>.
- (27) Johnston, B. M.; Johnston, C. W.; Letteri, R. A.; Lytle, T. K.; Sing, C. E.; Emrick, T.;

Perry, S. L. The Effect of Comb Architecture on Complex Coacervation. *Org. Biomol. Chem.* **2017**, *15* (36), 7630–7642. <https://doi.org/10.1039/c7ob01314k>.

## CHAPTER 6

# INTERACTIONS OF AMPHIPHILIC BLOCK POLYELECTROLYTES WITH COMPLEX COACERVATES

### ABSTRACT

Complex coacervates have been proposed as models for artificial cells owing to their unique capabilities to assemble spontaneously, achieve spatial compartmentalization, and selectively sequester biological molecules. Yet, their use as protocell models and bioreactors have been limited owing to our inability to stabilize the coacervate droplets and prevent their uncontrolled coalescence. Fatty acids, lipid molecules, and amphiphilic triblock polymers have been demonstrated to stabilize coacervate droplets by forming multi-layer membranes around the droplets. However, systematic investigations of the interactions between the amphiphiles and coacervate droplets are still lacking. In particular, the interplay of hydrophobic, solvation, and electrostatic interactions, that dictate self-assembly of amphiphilic diblock polyelectrolytes as well as complex coacervates have not been investigated. Here, we first demonstrate a water-soluble amphiphilic diblock polyelectrolyte that forms micellar assemblies in aqueous environments. Secondly, we analyze the interactions of these micellar assemblies with complex coacervate microdroplets to demonstrate that (i) by following precise mixing protocols, amphiphilic polyelectrolytes can stabilize complex coacervate microdroplets and (ii) this stabilization does not interfere with the spontaneous preferential partitioning of proteins in the coacervate droplets. Alternating the mixing order of the polyelectrolyte constituents of the complex coacervates and the amphiphilic polyelectrolytes is shown to influence the droplet stability and morphology profoundly. Our findings emphasize the importance of non-covalent interactions and hydrophobic

interactions between amphiphiles and polyelectrolytes in dictating their aqueous self-assembly, and present a model system to understand the complex interactions of amphiphiles with proteins that are critical for furthering the development of artificial cells and protocells.

## 6.1. INTRODUCTION

Liquid-liquid phase separation (LLPS) occurs in living cells, which leads to the formation of membraneless organelles, including P bodies, cajal bodies, and nucleolus.<sup>1-3</sup> These intracellular liquid compartments interact with lipid molecules (such as lipid membranes) while performing a variety of cellular functions. For instance, in neurotransmission, the formation of synapsin-rich phase correlates with the existence of the synaptic vesicles at synapses.<sup>4</sup> Similarly, membrane-supported endoplasmic reticulum is found to support the formation of internal intracellular membraneless compartments, including stress granules.<sup>5</sup> As the interactions between lipid amphiphiles and liquid condensates are essential in cell biology, it is imperative to understand an *in vitro* synthetic system of amphiphilic self-assemblies correlating with complex coacervates to inform the design of artificial cells and protocells.<sup>6-8</sup>

Amphiphilic self-assemblies have been reported to enable the emulsification of a typical aqueous two-phase systems, where otherwise vigorous mechanical agitation is required to achieve droplet stabilization. Lipid vesicles or liposomes have been shown to stabilize Pickering emulsions during partitioning in PEG/dextran two aqueous liquid-liquid phase separation via assembling at the droplet interfaces.<sup>9-11</sup> The intact single-layer vesicles coated at the interfaces with effective charge repulsions form discrete interspaces allowing substrate transport in and product diffuse out. This semi-impermeable interface enables the use of PEG/dextran droplets as potential enzyme cargos and bioreactors.<sup>10</sup>

Herein, we investigate the interaction between amphiphilic polyelectrolytes with oppositely charged polyelectrolytes constituting complex coacervate microdroplets. Moreover, we explore avenues to stabilize the coacervate microdroplets by adopting strategies similar to those employed

to stabilize PEG-dextran mixtures. Complex coacervate microdroplets form upon associative phase separation of oppositely charged polyelectrolytes in aqueous solutions. A combination of electrostatic interactions between charged macromolecules and the entropy gains from counterion release drive the complexation and LLPS. Biomacromolecules (such as proteins, enzymes, and nucleic acids) sequester spontaneously into complex coacervate microdroplets, enhancing their utility as artificial protocells and bioreactors.

However, the membraneless interface between the coacervate microdroplets and their surroundings results in rapid coalescence of the droplets, leading to their bulk phase separation and loss of function emerging from the reduced interfacial area. General approaches for stabilization of liquid-liquid interfaces, including the use of short chain amphiphilic surfactants (like sodium dodecyl sulfate that stabilize oil-water emulsions) or nanoparticles (such as nano-scale silica that stabilize Pickering emulsions) are not sufficient to prevent the coalescence of complex coacervate microdroplets. Mann and co-workers demonstrated that the addition of sodium oleate formed multilayers membranes bounded the pre-formed coacervate microdroplets below critical micelle concentrations. The multi-layer architectures modify the permeability of the membraneless coacervates in selective sequestering and excluding molecules further influencing the potential functionality.<sup>12-15</sup> Keating and co-workers coated ~ 90 nm diameter negatively charged PEGylated phospholipid vesicles at the polyuridylic acid/spermine coacervates and demonstrated the single intact lipid vesicles allowing the transportation of small molecules.<sup>10,16,17</sup>

In this study, we aim to understand the interactions between water-soluble amphiphiles and coacervate droplets in synthetic settings, which are of fundamental importance to study interactions of lipid membranes with intracellular liquid phases in cell biology. We anticipate that

the affinities between amphiphiles and polyelectrolyte complex coacervates will influence their respective assemblies markedly, and these interactions should be impacted by mixing sequences. We design a diblock amphiphile PBuMA<sub>40</sub>-*b*-PDMAEMA<sub>40</sub> consisting hydrophobic *n*-butyl methacrylate (BuMA) and ionic 2-dimethyl amino ethyl methacrylate (DMAEMA) blocks, with an estimated hydrophilic-lipophilic balance value ( $HLB = 20 \times M_h/M \sim 10$ ) and investigate its assembly in water and its interactions with complex coacervate microdroplets comprising oppositely charged poly(acrylic acid sodium salt) and poly(diallyldimethylammonium chloride), with a particular focus on the mixing sequence of the constituents. We also introduce fluorescently labelled proteins into the formulations to monitor its partitioning in the coacervate droplets and its evolution upon introduction of the amphiphilic polyelectrolytes.

## 6.2 MATERIALS AND METHODS

### *Polymer Synthesis and NMR Analysis*

PBuMA<sub>40</sub>-*b*-PDMAEMA<sub>40</sub> block polymers were synthesized using a sequential group transfer polymerization (GTP).<sup>9,18,19</sup> DMAEMA and BuMA (both purchased from Millipore Sigma) monomers were passed through basic alumina columns twice to remove inhibitors and protic impurities. Subsequently, a 3-hour stir with CaH<sub>2</sub> was carried out for both monomers in the presence of free radical inhibitor, DPPH (2,2-diphenyl-1-picrylhydrazyl hydrate, Sigma) to remove water followed by distillation to recover purified monomer. Freshly distilled tetrahydrofuran (THF, 30 mL) and methyl trimethylsilyl dimethylketene acetal (MTS, 0.12 mL, 0.1 g, 0.57 mmol, Sigma) were syringed into a 100 mL round-bottom flask containing tetrabutylammonium bibenzoate (TBABB, purchased from Toronto Research Chemicals, Canada, ~2.3 mg) and sealed with a septum in glove box under argon. BuMA (5 mL, 4.46 g, 31.35 mmol)

was added using a syringe fitted with an in-line filter (0.25  $\mu\text{m}$ ). The addition led to a temperature increased from room temperature (21  $^{\circ}\text{C}$ ) to 30  $^{\circ}\text{C}$ . After  $\sim 30$  mins, the temperature slowly decreased to room temperature, indicating the completion of the reaction. Two 0.1 mL aliquots were subsequently collected for THF-GPC and  $^1\text{H}$  NMR analysis. Then, DMAEMA (6.05 mL, 5.65 g, 35.91 mmol) was added through a syringe fitted with an in-line filter causing a temperature increase from 28  $^{\circ}\text{C}$  to 42  $^{\circ}\text{C}$ . After the temperature decreased back to room temperature, two 0.1 mL aliquots of the reaction mixture were extracted to prepare THF-GPC and  $^1\text{H}$  NMR samples. The reactor was exposed to air to terminate the radical reactions. The synthesized copolymers were recovered by precipitation into addition of n-hexane and dried at room temperature for 1 week.

A Bruker AV400 MHz spectrometer instrument was used to obtain the  $^1\text{H}$  NMR spectra of the diblock and linear polymers dissolved in  $\text{CDCl}_3$  (Figure 6-1a). The ratio of the degrees of polymerization of the B and D blocks in the copolymers were determined through NMR data. The six methyl protons at the end block of DMAEMA chains ( $\sim 2.3$  ppm, peak *l*), the two methyl protons next to the amine group in DMAEMA chains ( $\sim 2.5$  ppm, peak *k*), and the two methyl protons next to the ester group in DMAEMA chains ( $\sim 4.1$  ppm, peak *j*) exhibited a peak area ratio *l:k:j*  $\sim 3:1:1$ . Similarly, the two methyl protons next to the ester bond of the BuMA ( $\sim 3.9$  ppm, peak *f*), and the two methyl groups ( $\sim 1.6$  ppm, peak *g*, and  $\sim 1.4$  ppm, peak *h*) exhibited a peak area ratio *f:g:h*  $\sim 1:1:1$ . The degree of polymerization ratio is calculated through the ratio of peak integrals (*k:f*), given  $\sim 1:1$ . The chemical shift of the end methyl group from BuMA chains ( $\sim 0.9$  ppm, peak *i*) shares with the same position with the methyl groups from both side chains ( $\sim 0.9$  ppm, peak *b*), thus determining the exact number of repeating units of each block was not feasible

from the NMR spectra and required a GPC analysis. We note that no double bond peaks corresponding to the radical groups from monomers were observed in the NMR spectra.

The peak integral ratio combined with the number average molecular weight ( $M_n$ ) of the final polymer aliquot measured by the THF-GPC (Figure 1b) are used to obtain the degrees of polymerization of B and D blocks as 40-mers each. THF-GPC also provided information on polydispersity index (PDI, equal to the weight average MW divided by the number average  $M_w/M_n$ ) which was less than  $\sim 1.12$ , characteristic of a narrow chain length distribution and controlled polymerization. The elution time comparison between the intermediate PBuMA, and final B<sub>40</sub>-D<sub>40</sub> diblock copolymers demonstrates the molecular weight differences between the intermediate macromonomers PBuMA and final polymer. FTIR spectra (Figure 1c) demonstrates the presence of typical bonds, including C-H, C=O, C-N, and C-O.

#### *DLS and $\zeta$ -potential Measurements*

A 0.1 wt% B<sub>40</sub>-D<sub>40</sub> polymer solution was prepared for measuring the  $\zeta$ -potential and the particle sizes using Malvern Zetasizer Nano-ZS. 1 mL solution was prepared for the  $\zeta$ -potential and 200  $\mu$ L solutions were measured via dynamic light scattering (DLS).  $\zeta$ -Potential and the size measurements were carried out on triplicate samples, and each sample was measured three times. pH values were varied between 1 and 13 during the size measurements.

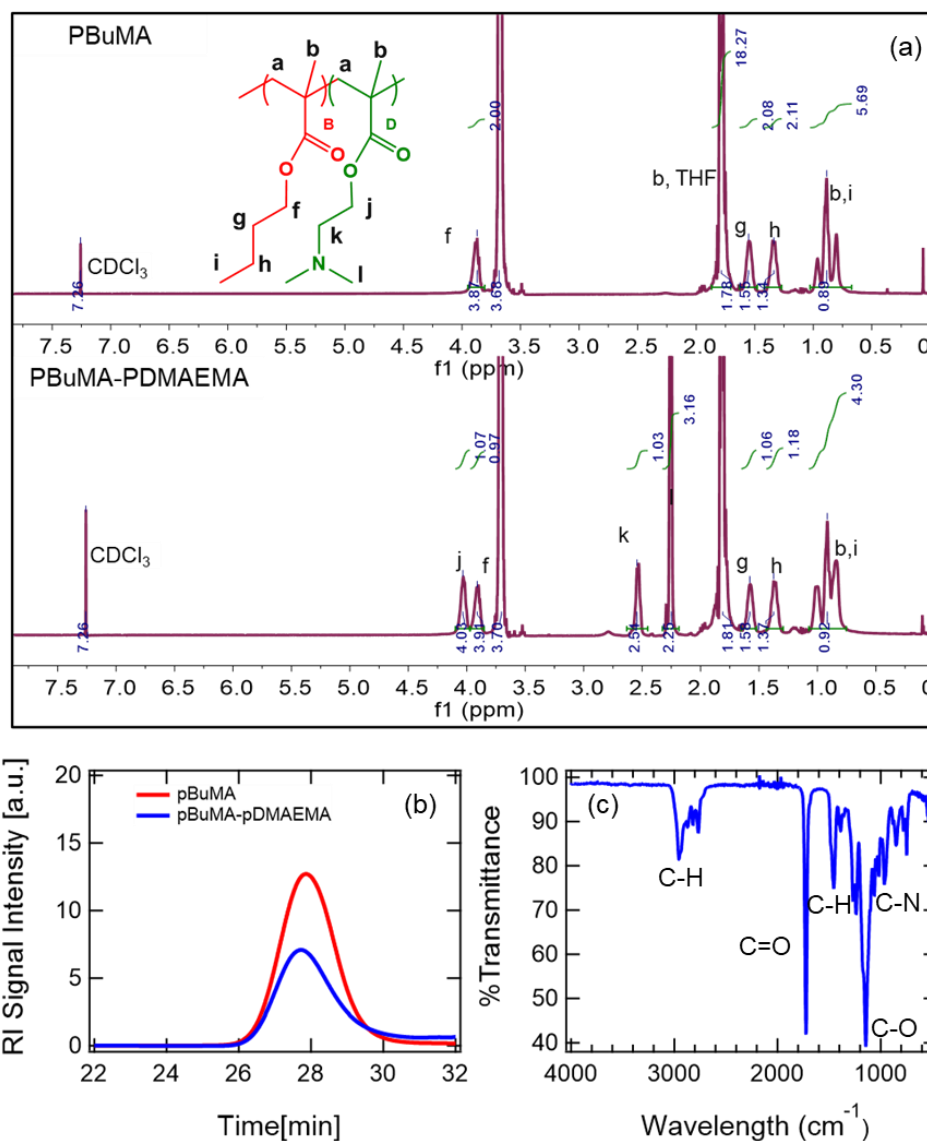


**Figure 6-1 Polymer NMR, GPC, and FTIR characterizations.** (a) <sup>1</sup>H NMR spectra of synthesized PBuMA-PDMAEMA diblock amphiphilic polymer and its precursors. Peaks from different protons were assigned in the spectra, where the protons ratios were indicated as 55:63. Both polymers were dissolved in CDCl<sub>3</sub>. (b) GPC traces of the polymer PBuMA-PDMAEMA and its precursors were shown in blue and red, respectively. FTIR spectra with demonstrated C-H bonds, C=O bonds, C-O bonds, and C-N bonds were shown in (c).

### *Small Angle X-ray Scattering (SAXS)*

Small angle X-ray scattering (SAXS) measurements were performed at the Advanced Photon Source beamline 12-ID-B of Argonne National Laboratory. Amphiphilic polyelectrolyte solutions with fixed polymer concentration at 0.1 wt% (0.1 mM) and varying pH in deionized water were placed in 2 mm thin-walled quartz capillary tubes (Charles Supper Company, Inc), and were kept at room temperature during the loading and measurement times. The capillaries were placed in the path of the beam to obtain the scattering measurements. The scattering intensity,  $I(q)$  was obtained from the two-dimensional data, with the solvent background subtracted, as a function of the wave vector  $q = \frac{4\pi \sin \theta}{\lambda}$ , with  $q$  ranging from  $0.04 \text{ nm}^{-1}$  to  $6 \text{ nm}^{-1}$ .  $I(q)$  depends on the structure factor,  $S(q)$  set by intermicellar interference effects, the form factor,  $P(q)$  determined by intraparticle interference, and the number density of micelles  $\phi$  as  $I(q) \propto \phi P(q)S(q)$ . The structural characteristics and the micellar charges were obtained by fitting the product  $P(q)S(q)$  to the experimental curve  $I(q)$ . Due to the dilute solutions,  $S(q)$  was found to be  $\sim 1$ .

### *Confocal Microimaging of Complex Coacervate Microdroplet Dispersions*

Confocal microscopy (Leica, Confocal SP8-STED/FLIM/FCS) was used to image complex coacervate microdroplet dispersions. A small aliquot ( $\sim 6 \mu\text{L}$ ) of the coacervate dispersions (noted as different time periods after mixing) was pipetted onto a glass slide, immediately sandwiched by a silanized cover glass before sealing, and equilibrated before imaging the droplets at the bottom surface of the coverslips after using the brightfield camera (using 100X oil lenses). To promote the retention of spherical morphology of the coacervate microdroplets upon settling at the bottom surface, the micro cover glasses (No. 1 1/2,  $22 \times 22 \text{ mm}$  square, VWR) were first soaked in a

saturated solution of potassium hydroxide (95%, Sigma-Aldrich) in isopropanol (90%, Fisher Scientific) for 30 minutes followed by water rinsing and drying at 70 °C. Then, the pre-cleaned slides were PEGylated (polyethylene glycol) with a 0.3% solution of N-(triethoxysilylpropyl)-*o*-polyethylene oxide urethane (95%, Gelest, Inc.) in anhydrous toluene (99.8%, Sigma-Aldrich) for 4 hours. After the silanization step, the slides were thoroughly washed with toluene (anhydrous, Fisher Scientific), ethanol (200 proof, Koptec), and Milli-Q water, respectively, with a final drying step at 70°C overnight to further enhance hydrophobicity of the glass slides and inhibit spreading of the droplets, improving the image quality.

#### *Preparation of stock polyelectrolyte solutions*

Poly(acrylic acid sodium salt) (PAA, molecular weight 5100 g/mol, in powder form), bovine serum albumin (BSA, molecular weight 66kDa, lyophilized powder), and fluorescein isothiocyanate (FITC) were purchased from Millipore Sigma. Poly(diallyldimethylammonium chloride) (PDADMAC) (molecular weight 8500 g/mol) was purchased from Polysciences, Inc. as a 28 wt% aqueous solution. FITC-labelled BSA (FITC-BSA) was synthesized following previously published protocols.<sup>20</sup>

#### *Preparation of Complex Coacervate Dispersions*

Stock solutions of the linear polyelectrolytes, the amphiphilic polyelectrolyte and water were mixed in appropriate amounts to produce complex coacervate dispersions. All dispersions contained charge-matched amounts of the oppositely charged linear polyelectrolytes. In dispersions containing proteins (FITC-BSA), protein stock solutions were also added to the dispersions following the adding sequence: PDADMAC, water, protein, and PAA.

Amphiphilic polyelectrolyte stabilized polyelectrolyte complexes were prepared by mixing amphiphilic polycations with charge-matched amounts of PAA<sub>53</sub> and PDADMAC<sub>53</sub>, with a polymer molar ratio between linear polycations (PDADMAC<sub>53</sub>) and amphiphilic polycations (B<sub>40</sub>-D<sub>40</sub>) = 1:0.5 (charge ratio = 3:1). The mixing sequences were following: i) PDADMAC, deionized water, amphiphiles and PAA, ii) PAA, deionized water, amphiphiles and PDADMAC, iii) PDADMAC, deionized water, PAA and amphiphiles. After each addition, samples were vortexed for approximately 10 seconds.

1  $\mu$ M (5  $\mu$ L 36 g/L stock diluted in total volume of 50  $\mu$ L, charge concentration) final concentration fluorescent labelled bovine serum albumin (FITC-BSA) were additionally added to the amphiphilic polyelectrolyte stabilized complex coacervates. We followed the ordering: (A) PDADMAC, deionized water, amphiphiles, BSA, and PAA (DAD + BD + BSA + AA), (B) PAA, deionized water, amphiphiles, BSA and PDADMAC (AA + BD + BSA + DAD), (C) PDADMAC, deionized water, BSA, PAA and amphiphiles (DAD + BSA + AA + BD), and (D) PDADMAC, deionized water, amphiphiles, PAA, and BSA (DAD + BD + AA + BSA). 0.25 wt% complex coacervates were prepared immediately before use and studied at room temperature (25 °C).

### **6.3 RESULTS AND DISCUSSIONS**

#### *Self-assembly of Amphiphilic Polyelectrolytes in Water*

An independent confirmation of the self-assembled structures of amphiphilic polyelectrolytes was obtained using SAXS and DLS. Figure 6-2a presents SAXS spectra  $I(q)$  for 0.1 wt% B<sub>40</sub>-D<sub>40</sub> solutions at various pH (1, 5, 7, 10, 13). Varying the pH was expected to influence the structure of the self-assemblies, varying from large vesicles to micelles during the pH transitions. This was

expected since the area occupied by the amphiphile headgroup is expected to increase with decreasing pH, imposing a stronger repulsion among them resulting from a high degree of ionization of tertiary amines (pKa value  $\sim 10$ ). However, we do not visualize any transitions in the SAXS spectra.

Characteristics dimensions of the self-assembled structures were determined by fitting the SAXS spectra using a polydisperse core-shell form factor model. Fits from the model are depicted as black solid lines in Figure 6-2a. From this analysis, the B<sub>40</sub>-D<sub>40</sub> self-assemblies were found to have a mean total radius (core radius  $r$  + shell thickness  $\delta$ ) of 47 nm with 15% polydispersity at low pH (Figure 6-2b). The core radius of the self-assembly is found to retain the same sizes (Figure 6-2b, light red) over a broad pH range while the shell thickness  $\delta$  in acidic solutions is double as compared to  $\delta$  in the basic environment (Figure 6-2b, in dark red). The decreasing shell thickness is attributed to the weakened repulsion of interchain due to the unionized headgroups in basic solutions.

The sizes of self-assembly measured using DLS agreed with the findings from SAXS analysis. The hydrodynamic radius of self-assembly exhibits  $\sim 40$  nm at low pH. A decrease in mean diameter is observed with increasing pH (Figure 6-2b), consistent with the findings from SAXS investigations.

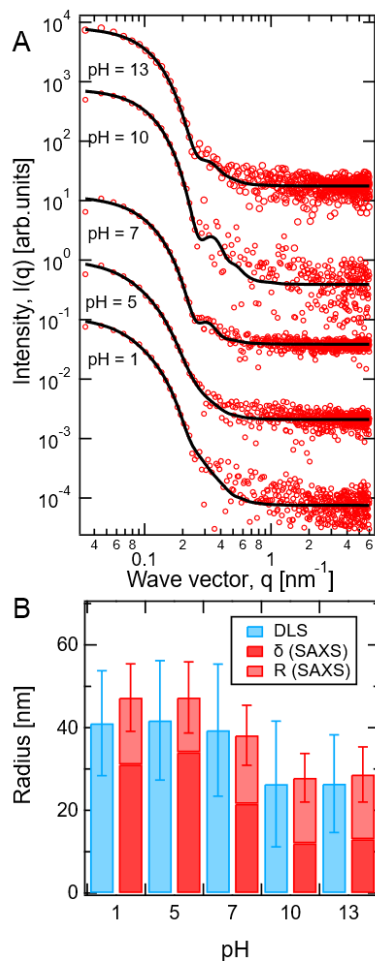


**Figure 6-2 Small angle X-ray scattering (SAXS) results and self-assembly characteristics. (a)** SAXS intensity patterns and the corresponding typical fits for 0.1 wt% PBuMA-PDMAEMA amphiphiles at various pH conditions including 1, 3, 5, 7, 10, and 13. The fits use the form factor for core-shell spheres and structure factor is assumed to be  $\sim$  unity due to the low amphiphilic self-assembly volume fraction, respectively. The profiles are shifted vertically by a factor of 20 for clarity. **(b)** Dimensions of the core-shell self-assemblies interpreted by SAXS profiles: the radius  $R$  shown in light red, and the thickness  $\delta$  shown in dark red respectively. Dimensions of the core-shell self-assemblies interpreted by DLS profiles of same concentration and pH conditions: the mean diameters of self-assembly shown in blue. In basic solutions, self-assemblies with smaller

sizes ( $\sim 26$  nm) are observed, whereas they maintain a size  $\sim 40$  nm when the pH of the solution is above the anionic polyelectrolyte pKa. Error bars depict the size polydispersity of the micelles.

*Interactions between cationic amphiphile micelles with complex coacervates: Influence of mixing sequence*

The amphiphilic polyelectrolytes and their self-assembled micelles are positively charged and are likely to electrostatically interact with polyanions while mixing, competing with linear polycations. Moreover, the addition of linear polycations can be hypothesized to impact the micelles integrity and their size distribution. A systematic investigation on the adding sequences of the amphiphilic polyelectrolytes and linear polyelectrolytes was carried out to examine these effects.

Figure 6-3a shows a comparison of the dispersions wherein the three macromolecular components were added in three different mixing orders: (i) mixing the cationic amphiphilic diblock polyelectrolytes (DBP) with diluted linear polycations (PC) before adding polyanions (PA) [PC + DBP + PA]: column (1), (ii) mixing the amphiphilic polyelectrolytes after forming the complex coacervates [PC + PA + DBP]: column (3), and (iii) mixing the cationic amphiphilic polyelectrolytes with polyanions before adding linear polycations [PA + DBP + PC]: column (5). Amphiphilic polyelectrolytes self-assemble into micelles when dissolved in water prior to the linear polyelectrolytes. In as-mixed dispersions, both coacervate droplets with mixing sequence (i) and (iii) maintain similar turbidity, but a lower turbidity is observed in dispersions obtained from sequence (ii). 48 hours after preparation, the complex coacervate dispersions formed by the mixing orders of (i) and (iii) retained their turbidity (Figure 6-3a, columns 2 and 4), while dispersions obtained from mixing order of (ii) phase separated (Figure 6-3a, column (6)). A turbidity measurement of the dispersions at different times after preparation – as mixed, 3 hours, 24 hours, and 48 hours – indicated that the turbidity of dispersions obtained from orders (i) and (iii) remained

nearly constant over time, while the turbidity decreased markedly in the dispersions obtained from mixing order (ii) comprising the pre-formed coacervate microdroplet (Figure 6-3b).

Microscopy images (Figure 6-3c column (1-6)) further demonstrate the similar morphology of the microdroplets among the adding sequences (i) and (iii). In the post-mixing system (ii), far fewer complex coacervate microdroplets were observed as compared to mixing sequence (i) and (iii) as well as unstable complex coacervates (Figure 6-3c column (7)). We hypothesize that the amphiphilic micelles interact with and participate in the complexation-driven assembly of the oppositely charged polyelectrolytes, leading to stabilization of the coacervate microdroplets. The concentration of amphiphilic polyelectrolytes in solutions is above the critical micelle concentration. Thus, existence of intact amphiphilic micellar self-assemblies is expected in the absence of the linear polyelectrolytes. However, upon introduction of the linear polyelectrolytes, in particular the polyanions, the amphiphilic micelles may disassemble and re-arrange into unilamellar double layer membranes that coat the water-coacervate interfaces. Another possibility is coating of the coacervate microdroplets by the amphiphilic micelles, introducing steric repulsion between them and stabilizing the droplets. However, this would have been expected in the case when the amphiphilic polyelectrolytes were added after the linear polyelectrolytes have complexed. Since droplet stabilization is not observed in this case, we posit that the amphiphilic micelles are not incorporated in the coacervate microdroplets but rather disrupt the complex coacervate droplets.

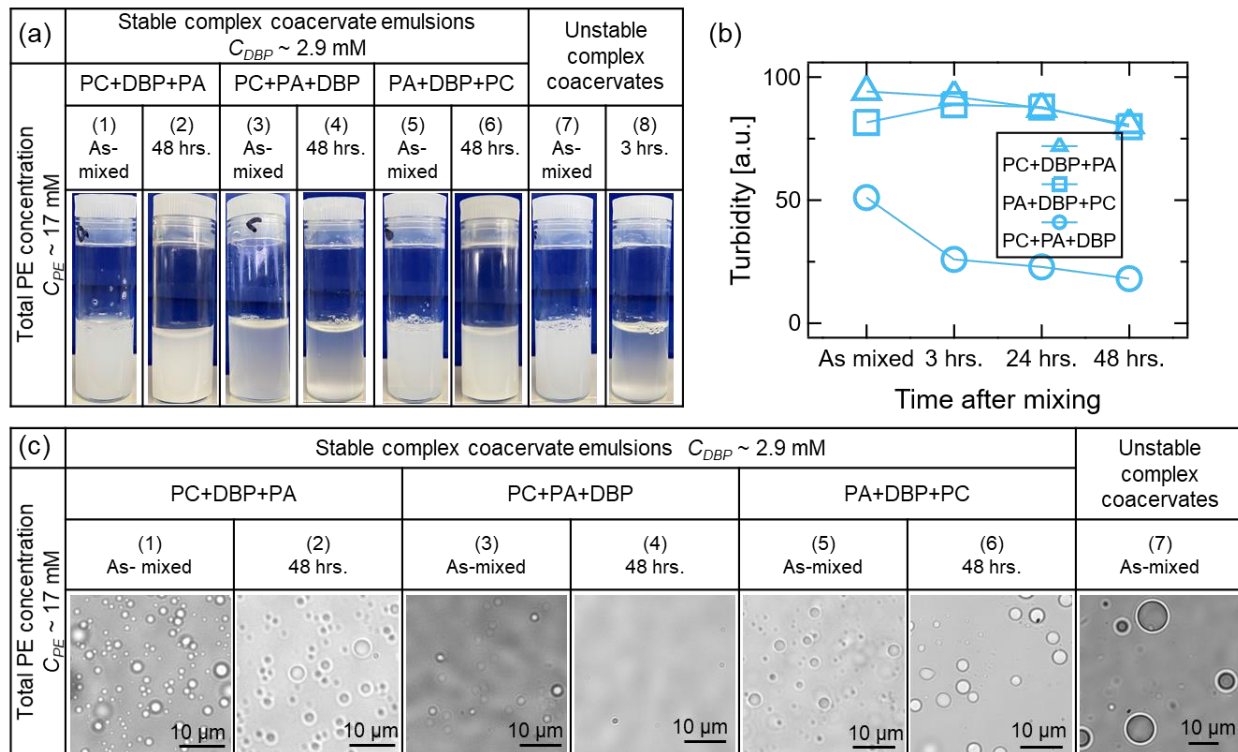


**Figure 6-3** Mixing sequences impact the stability of amphiphilic micelles stabilized complex coacervate droplets. (a) Complex coacervate droplets obtained upon mixing of solutions oppositely charged linear polyelectrolytes (total polyelectrolyte concentrations 17 mM), and 2.9 mM diblock amphiphilic polyelectrolytes. The adding sequences are varying in three scenarios: (column 1) PC+DBP+PA; (column 3) PC+PA+DBP; (column 5) PA+DBP+PC. Turbidity in the as-mixed solutions (column 1, 3, 5) emerges from the presence of complex coacervate microdroplets. Stable complex coacervate emulsions are demonstrated in columns (2, 6) for same samples as columns (1, 5) 48 hours after mixing. These stable complex coacervate emulsions are turbid when prepared and maintain a uniformly turbidity for more than 48 hours. Turbidity in the samples is a key factor for indicating the stability of the emulsions. Columns 7 and 8: Complex coacervate droplets obtained upon mixing of solutions oppositely charged linear polyelectrolytes

(total polyelectrolyte concentrations 17 mM, polyelectrolyte charge matched solutions). These complex coacervate microdroplets are prone to coalescence and merge into a homogenous transparent coacervate phase after ~ 3 hours, with the polymer dense phase coacervate phase at the bottom and the polymer-lean supernatant phase at the top (column **8**). **(b)** Evolution of turbidity intensity monitored with time demonstrates stabilized coacervates maintained at high turbidity over 48 hours of adding sequence (i, iii) while the turbidity of unstabilized coacervates by adding sequence ii tremendously decreased in 3 hours. **(c)** Micrographs of the as-prepared complex coacervates droplets (column **1, 3, 5**), as-prepared unstable complex coacervates droplets (column **7**) and stabilized complex coacervate emulsions after 48 hours (column **2, 6**). The insufficient stabilized emulsions undergo droplet coalescence and phase separate (column **4**). The stabilized emulsions contain 4.8 mM comb polyelectrolyte dispersants in addition to the oppositely charged linear polyelectrolytes. All as-mixed solutions contain micron-sized droplets. Scale bars are shown in each micrograph.

*Protein sequestration in cationic amphiphilic polyelectrolyte-stabilized complex coacervate microdroplets*

Here, we probe the mechanism behind the stabilization of coacervate microdroplets observed in mixing sequences (i) and (iii) and investigate the localization of proteins in complex coacervates interacting with amphiphilic block polyelectrolytes by monitoring the sequestration of fluorescent labeled bovine serum albumin (FITC-BSA) in the coacervate droplets as a function of varying mixing sequences. It is expected that protein sequestration will vary markedly owing to differences in protein diffusion and partitioning depending on the mixing sequence.

Micrographs (Figure 6-4a) obtained from solutions prepared with mixing sequences B (PA+DBP+BSA+PC), C (PC+BSA+PA+DBP), and D (PC+DBP+PA+BSA) demonstrate similar droplet morphologies, which were starkly different from the droplet morphology observed for mixing sequences A (PC+DBP+BSA+PA). In B and D, small coacervate microdroplets encapsulating BSA proteins were observed. Mixing sequence A (PC+DBP+BSA+PA) resulted in clusters of droplets (5-10  $\mu\text{m}$ ) comprising liquid coacervate droplets (1-2  $\mu\text{m}$ ) with encapsulated BSA that did not coalesce in the time frame of observation. It should be noted that in the absence of BSA, mixing sequences A, B, and D would have provided stable microdroplets while C would have provided relatively few unstable microdroplets. Expectedly, larger droplets were observed in C, ascribable to coalescence and insufficient stabilization; these droplets coalesced to form a macro-phase within 48-hour (Figure 6-5a). These observations support the hypothesis that if PA are added post-coacervation, they do not assimilate into the coacervate droplets.

In the droplet clusters observed in solutions obtained from mixing sequence A (PC+DBP+BSA+PA), we find that the fluorescently labeled proteins manifest throughout the

entire droplets, including at the droplet interfaces. Here, we expect minimal interactions between the cationic amphiphilic micelles and the linear polycations upon initial mixing, resulting in well-dispersed micelles and polycation chains. Electrostatic interactions between cationic micelles and FITC-BSA compete with those between FITC-BSA and linear polycations when proteins are introduced into these solutions, such that individual DBP+BSA and PC+BSA complexes form. The complexation of DBP micelles with BSA reduce the surface charges of cationic micelles, limiting their interaction with the PA chains subsequently introduced in the solution. The complexed proteins may also stabilize the micelles against dissociation in presence of the PA chains, affecting their interfacial assembly around the coacervate droplets. Eventually, these competing interactions provoke the de-stabilization of the solutions, resulting in macrophase separation (Figure 6-5a).

Our hypothesis that PA chains disrupt the DBP micellar assemblies and that this disruption is critical for stabilization of the coacervate microdroplets is consistent with our observations in solutions obtained with mixing sequence B wherein PA and DBP were mixed first followed by addition of BSA and PC. In fact, this system exhibited long term stabilization of the coacervate microdroplets, as is evident from turbid solutions even after 48 hours of preparation (Figure 6-5a), as well as an ability to retain proteins in the droplets (Figure 6-5b).

The solutions prepared by mixing sequence D present an interesting scenario. These solutions exhibit comparable FITC-BSA sequestration into the pre-formed stabilized coacervate droplets, implying that (i) proteins can be sequestered into pre-formed coacervate droplets, and (ii) the amphiphilic polyelectrolytes that stabilize the coacervate microdroplets do not entirely impede the transport of proteins into the droplets despite forming the hypothesized amphiphilic membranes.

Partial restriction of protein sequestration efficiency is observed upon qualitative comparison of fluorescence intensity contrast in the aqueous phases in images corresponding to systems B and C, attributable to lower permeability of the stabilized interfaces as well as complexation of the protein molecules with the cationic membrane stabilizing the droplets. The latter can be attributed to result in a deterioration of the stabilization efficiency of the membranes as well, resulting in settling of the microdroplets within 48 hours (Figure 6-5a). Moreover, the macrophase observed in this case resembled solid precipitates instead of liquid phases observed in the unstable systems, further highlighting the interactions and complexation between proteins and the amphiphilic DBPs.

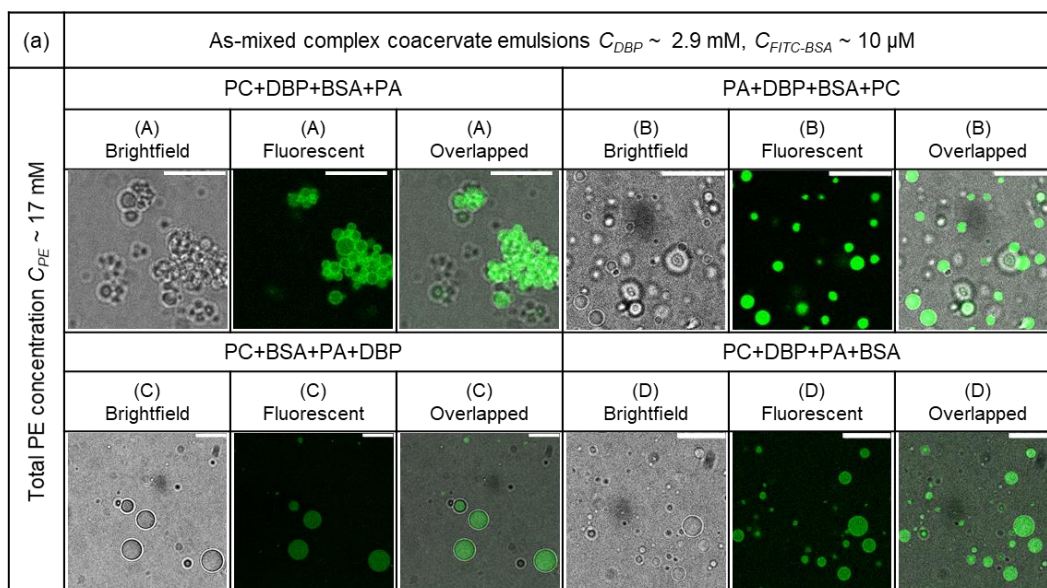


**Figure 6-4 Amphiphilic micelles stabilized complex coacervate droplets encapsulated FITC-labelled BSA.** Complex coacervate droplets encapsulated FITC-labelled BSA (fixed concentration) obtained upon mixing of oppositely charged linear polyelectrolyte solutions (total polyelectrolyte concentrations 17 mM), 10  $\mu$ M FITC-BSA and 2.9 mM diblock amphiphilic polyelectrolytes with varying adding sequences: **(a)** amphiphiles adding into polycation solution before proteins, finally with polyanions; **(b)** amphiphiles adding into polyanion solution before proteins, finally with polycations; **(c)** amphiphiles adding into pre-formed protein encapsulated coacervate solutions; **(d)** amphiphiles adding into polycation solution before polyanions, finally with protein. These coacervate droplets were all visualized as-prepared through silanized glass coverslips via 100X oil lenses confocal microscopy, and channels of micrographs are described as brightfield, fluorescent, and overlapped.

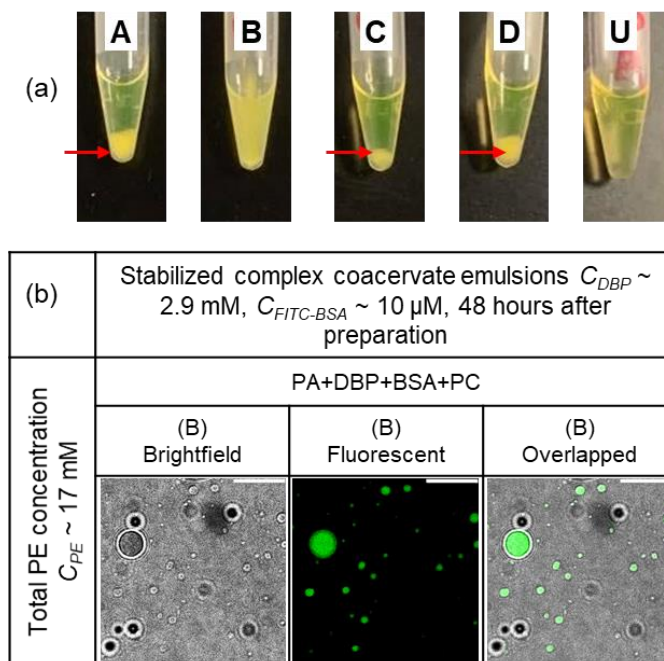


**Figure 6-5 Macroscopic and microscopic views of amphiphilic stabilized complex coacervates with 48 hours after mixing.** (a) Macroscopic views on samples from Figure 5 were recorded 48 hours after mixing, where B maintained the turbidity, while A, C and D phase separated with precipitates at bottom. C had fewer precipitates than A and D, due to the insufficient adsorption of amphiphilic self-assemblies. U showed the unstabilized coacervate droplets without amphiphilic diblock copolymers phase separated with transparent supernatant. (a) Micrographs of (A) demonstrate collected unstabilized complexes in precipitate phase 48 hours after preparation; Micrographs of (B) present stabilized protein encapsulated coacervate droplets 48 hours after preparation.

## 6.4 CONCLUSIONS AND FUTURE DIRECTIONS

Our studies here feature a water-soluble amphiphilic diblock polyelectrolyte that forms micellar assemblies in aqueous environments and provided a methodology to stabilize complex coacervate microdroplets. The mixing sequence has a significant influence on the stability of complex coacervate microdroplets, suggesting the electrostatic interactions between the polycations, the polyanions and the diblock polyelectrolytes determines the phase behaviors of droplets. It is hypothesized that the stabilization of the microdroplets is governed by formation of an amphiphilic membrane around the droplets following disruption of the micellar assemblies by the polyanion chains. Further, the sequestration of charge proteins is observed in both stabilized and unstable droplets, highlighting that the amphiphilic polyelectrolytes do not interfere with the partitioning of the proteins in the coacervate phase. Future work in this research will entail further investigation of the mechanism through which amphiphilic polyelectrolyte self-assemblies interact and stabilize the complex coacervate microdroplets. We will probe whether these self-assemblies retain intact after mixing with the linear oppositely charged polyelectrolytes or disassemble and rearrange into membranes by employing fluorescent modifications on the amphiphilic polyelectrolytes.

## 6.5. REFERENCES

- (1) Brangwynne, C. P.; Mitchison, T. J.; Hyman, A. A. Active Liquid-like Behavior of Nucleoli Determines Their Size and Shape in *Xenopus Laevis* Oocytes. *Proc. Natl. Acad. Sci. U. S. A.* **2011**, *108* (11), 4334–4339. <https://doi.org/10.1073/pnas.1017150108>.
- (2) Parker, R.; Sheth, U. P Bodies and the Control of mRNA Translation and Degradation. *Mol. Cell* **2007**, *25* (5), 635–646. <https://doi.org/10.1016/j.molcel.2007.02.011>.
- (3) Kaiser, T. E.; Intine, R. V.; Dundr, M. De Novo Formation of a Subnuclear Body. *Science* (80-. ). **2008**, *322* (5908), 1713–1717. <https://doi.org/10.1126/science.1165216>.
- (4) Milovanovic, D.; Wu, Y.; Bian, X.; De Camilli, P. CELL BIOLOGY A Liquid Phase of Synapsin and Lipid Vesicles.
- (5) Jain, S.; Wheeler, J. R.; Walters, R. W.; Agrawal, A.; Barsic, A.; Parker, R. ATPase-Modulated Stress Granules Contain a Diverse Proteome and Substructure. *Cell* **2016**, *164* (3), 487–498. <https://doi.org/10.1016/J.CELL.2015.12.038>.
- (6) Ivanov, I.; Lira, R. B.; Tang, T. Y. D.; Franzmann, T.; Klosin, A.; da Silva, L. C.; Hyman, A.; Landfester, K.; Lipowsky, R.; Sundmacher, K.; Dimova, R. Directed Growth of Biomimetic Microcompartments. *Adv. Biosyst.* **2019**, *3* (6), 1–9. <https://doi.org/10.1002/adbi.201800314>.
- (7) Zhu, T. F.; Szostak, J. W. Coupled Growth and Division of Model protocell membranes. *J. Am. Chem. Soc.* **2009**, *131* (15), 5705–5713. <https://doi.org/10.1021/ja900919c>.
- (8) Inaoka, Y.; Yamazaki, M. Vesicle fission of giant unilamellar vesicles of liquid-

- Ordered-Phase Membranes Induced by Amphiphiles with a Single Long Hydrocarbon Chain. *Langmuir* **2007**, *23* (2), 720–728. <https://doi.org/10.1021/la062078k>.
- (9) Buzza, D. M. A.; Fletcher, P. D. I.; Georgiou, T. K.; Ghasdian, N. Water-in-Water Emulsions Based on Incompatible Polymers and Stabilized by Triblock Copolymers-Templated Polymersomes. *Langmuir* **2013**, *29* (48), 14804–14814. <https://doi.org/10.1021/la403356j>.
- (10) Dewey, D. C.; Strulson, C. A.; Cacace, D. N.; Bevilacqua, P. C.; Keating, C. D. Bioreactor Droplets from Liposome-Stabilized All-Aqueous Emulsions. *Nat. Commun.* **2014**, *5* (May), 1–9. <https://doi.org/10.1038/ncomms5670>.
- (11) Sadeghpour, A.; Pirolt, F.; Glatter, O. Submicrometer-Sized Pickering Emulsions Stabilized by Silica Nanoparticles with Adsorbed Oleic Acid. *Langmuir* **2013**, *29* (20), 6004–6012. <https://doi.org/10.1021/la4008685>.
- (12) Koga, S.; Williams, D. S.; Perriman, A. W.; Mann, S. Peptide-Nucleotide Microdroplets as a Step towards a Membrane-Free Protocell Model. *Nat. Chem.* **2011**, *3* (9), 720–724. <https://doi.org/10.1038/nchem.1110>.
- (13) Dora Tang, T. Y.; Rohaida Che Hak, C.; Thompson, A. J.; Kuimova, M. K.; Williams, D. S.; Perriman, A. W.; Mann, S. Fatty Acid Membrane Assembly on Coacervate Microdroplets as a Step towards a Hybrid Protocell Model. *Nat. Chem.* **2014**, *6* (6), 527–533. <https://doi.org/10.1038/nchem.1921>.
- (14) Booth, R.; Qiao, Y.; Li, M.; Mann, S. Spatial Positioning and Chemical Coupling in Coacervate-in-Proteinosome Protocells. *Angew. Chemie - Int. Ed.* **2019**, *58* (27), 9120–

9124. <https://doi.org/10.1002/anie.201903756>.
- (15) Srivastava, S.; Andreev, M.; Levi, A. E.; Goldfeld, D. J.; Mao, J.; Heller, W. T.; Prabhu, V. M.; De Pablo, J. J.; Tirrell, M. V. Gel Phase Formation in Dilute Triblock Copolyelectrolyte Complexes. *Nat. Commun.* **2017**, *8*, 1–9. <https://doi.org/10.1038/ncomms14131>.
- (16) Pir Cakmak, F.; Grigas, A. T.; Keating, C. D. Lipid Vesicle-Coated Complex Coacervates. *Langmuir* **2019**, *35* (24), 7830–7840. <https://doi.org/10.1021/acs.langmuir.9b00213>.
- (17) Aumiller, W. M.; Pir Cakmak, F.; Davis, B. W.; Keating, C. D. RNA-Based Coacervates as a Model for Membraneless Organelles: Formation, Properties, and Interfacial Liposome Assembly. *Langmuir* **2016**, *32* (39), 10042–10053. <https://doi.org/10.1021/acs.langmuir.6b02499>.
- (18) Georgiou, T. K.; Patrickios, C. S. Synthesis, Characterization, and Modeling of Double-Hydrophobic Model Networks Based on Cross-Linked Star Copolymers of n-Butyl Methacrylate and Methyl Methacrylate. *Macromolecules* **2006**, *39* (4), 1560–1568. <https://doi.org/10.1021/ma051360f>.
- (19) Patrickios, C. S.; Sharma, L. R.; Armes, S. P.; Billingham, N. C. Precipitation of a Water-Soluble ABC Triblock Methacrylic Polyampholyte: Effects of Time, PH, Polymer Concentration, Salt Type and Concentration, and Presence of a Protein. *Langmuir* **1999**, *15* (5), 1613–1620. <https://doi.org/10.1021/la970662a>.
- (20) Ke, C. Y.; Wu, Y. T.; Tseng, W. L. Fluorescein-5-Isothiocyanate-Conjugated Protein-Directed Synthesis of Gold Nanoclusters for Fluorescent Ratiometric Sensing of an

Enzyme-Substrate System. *Biosens. Bioelectron.* **2015**, *69*, 46–53.

<https://doi.org/10.1016/j.bios.2015.02.002>.

## CHAPTER 7

### CONCLUSIONS

Interfacially active molecules own unique bifunctional groups with different preferences and contrasting affinities when adsorbing at interfaces. Liquid foams formed by tracking gas pockets in liquid-phase colloidal dispersions separated by the thin foam films consist of water-air interfaces. Polyelectrolyte complex coacervates formed by oppositely charged polyelectrolytes condensing into microdroplets consist of water-water interfaces. An approach of manipulating interfacially active molecules with bifunctionalities is proposed to stabilize these interfaces. Developing and optimizing the structures, associative interactions, and adsorption mechanism of the bifunctional molecules are imperative for broadening their applications.

A reasonable agreement between the concentration-dependent changes in  $\overline{\Delta h}$  measured in stratification studies with intermicellar distances  $d$  in bulk solutions obtained using small angle X-ray scattering (SAXS) for aqueous solutions of sodium dodecyl sulfate (SDS) is observed, consistent with earlier hypotheses that both lengths are dictated by intermicellar interactions and micelle number density suggesting that even though the confining interfaces in thin films lead to micelle layering and stratified drainage, the interlayer spacings are dictated largely by the repulsive intermicellar interactions in thin surfactant films without added salt.

We further investigate the influences of ionic strength on these self-assemblies formed in bulk by an ionic surfactant using small-angle X-ray scattering (SAXS), where both  $d$  and  $\overline{\Delta h}$  of the stratified drainage of thin SDS films decrease steadily but the agreement worsens with increasing salt, where screening of the intermicellar interactions upon addition of salt decreases both the

amplitude and the decay length of the disjoining pressure, and the structural forces contributed by the self-organization of micelles within nanoscopic confinement are impacted by the influence of salt. Moreover, we establish an equivalent hard-sphere model to estimate the screened intermicellar interactions where the standard approach (Hayter-Penfold structure factor model) to elucidate interparticle correlations fail in high salt concentration regime.

After surveying on interfacially active surfactant molecules, we follow up with understanding the interfacial phenomena of polyelectrolyte complex coacervates aiming at building up a strategy to stabilize these membraneless microdroplets. We demonstrate a methodology for stabilizing coacervate microdroplets by the incorporation of PAA-*co*-PEG comb polyelectrolytes in the complex coacervate formulations. Our methodology produces stable complex coacervate emulsions comprising microdroplets, composed of oppositely charged linear polyelectrolytes and stabilized by interfacially adsorbed comb polyelectrolytes, that exhibit long-term (> 4+ months) stability. The microdroplet size remains relatively constant with time and is shown to be regulated by the concentrations of the comb and linear polyelectrolytes. Our stabilization strategy improves the salt resistance of the complex coacervates while minimally interfering with other desirable attributes of coacervate droplets, including their ability to sequester and encapsulate proteins from solution and their membraneless interface that allows for fast transport of small molecules across them. The PAA-*co*-PEG dispersant also well-performs in stabilizing the PEC coacervate emulsions formed by the rehydration of miscible polyelectrolytes indicates the dispersant capability are not screened by water as a key player in current compositions. Further, an expedited enzymatic reaction is achieved by the PAA-*co*-PEG stabilized coacervate droplets even when

stored for up to 48 hours. These findings are expected to broaden the applications of complex coacervate droplets as artificial cells and bioreactors.

Moreover, our PAA-*co*-PEG comb-polymer stabilized PEC coacervate emulsions are stable against the addition of salt above the critical salt concentration corresponding to the unstable coacervates with remaining their morphology. Consequently, the critical salt concentration and the critical total linear polyelectrolyte concentration at which the complex coacervate phase vanishes both increases upon incorporation of comb polyelectrolytes in the formulations. The encapsulation capability of loading the natural model proteins bovine serum albumin (BSA) is not impeded up to 200 mM salt concentrations. Enabled by the comb polyelectrolyte stabilizers, such stable complex coacervate emulsions that can withstand salt may broaden the applications of coacervates in the fields of biotechnology and pharmaceutical sciences.

Applying PAA-*co*-PEG comb polymers in stabilizing complex coacervate droplets provides a steric layer onto the interfaces of water-water emulsions. Further, fatty acids, lipid molecules, and amphiphilic triblock polymers have been demonstrated to stabilize coacervate droplets by forming multi-layer membranes around the droplets. However, no systematic investigations of the interactions between the amphiphiles and coacervate droplets have discussed. We first demonstrate a water-soluble amphiphilic diblock polyelectrolyte that forms micellar assemblies in aqueous environments, and by following precise mixing protocols, amphiphilic polyelectrolytes can stabilize complex coacervate microdroplets. Further, we elucidate the interactions of these micellar assemblies with complex coacervate microdroplets demonstrates that the interplay of hydrophobic, solvation, and electrostatic interactions, that dictate self-assembly of amphiphilic diblock polyelectrolytes as well as complex coacervates. This stabilization does not interfere with the

spontaneous preferential partitioning of proteins in the coacervate droplets. Our findings highlight the importance of non-covalent interactions and hydrophobic interactions between amphiphiles and polyelectrolytes and present a model system to understand the complex interactions of amphiphiles with proteins that are critical for furthering the development of protocells.